



Nonlinear quantum optics with a single Rydberg superatom coupled to a medium-finesse cavity

Julien Vaneecloo

► To cite this version:

Julien Vaneecloo. Nonlinear quantum optics with a single Rydberg superatom coupled to a medium-finesse cavity. Optics [physics.optics]. Sorbonne Université, 2022. English. NNT: 2022SORUS089 . tel-03701968

HAL Id: tel-03701968

<https://theses.hal.science/tel-03701968>

Submitted on 22 Jun 2022

HAL is a multi-disciplinary open access archive for the deposit and dissemination of scientific research documents, whether they are published or not. The documents may come from teaching and research institutions in France or abroad, or from public or private research centers.

L'archive ouverte pluridisciplinaire **HAL**, est destinée au dépôt et à la diffusion de documents scientifiques de niveau recherche, publiés ou non, émanant des établissements d'enseignement et de recherche français ou étrangers, des laboratoires publics ou privés.



COLLÈGE
DE FRANCE
1530

S SCIENCES
SORBONNE
UNIVERSITÉ

THÈSE DE DOCTORAT DE SORBONNE UNIVERSITÉ

Préparée par

JULIEN VANEECLOO

Nonlinear quantum optics with a single Rydberg superatom coupled to a medium-finesse cavity

Soutenue le 11 mars 2022 devant le jury composé de :

Aurélien Dantan	Rapporteur
Sebastian Hofferberth	Rapporteur
Jacqueline Bloch	Présidente du Jury
Jakob Reichel	Examinateur
Philippe Grangier	Examinateur
Alexei Ourjoumtsev	Directeur de thèse

Travail réalisé dans l'équipe de photonique quantique des Jeunes Equipes de l'Institut de Physique du Collège de France.

Remerciements

Je veux exprimer ici mes remerciements aux personnes qui m'ont accompagné pendant ces années de doctorat au Collège de France et qui ont contribué à rendre si agréable cette période singulière de ma vie.

J'adresse ma pleine gratitude aux membres du jury qui ont généreusement accepté de donner de leur temps pour évaluer mon travail. Mes premiers remerciements vont aux deux rapporteurs Sébastien Hofferberth et Aurélien Dantan, pour avoir accepté de lire en profondeur ce manuscrit, ainsi que pour cet agréable échange pendant la soutenance de thèse. Immédiatement après viennent les examinateurs, merci donc à Jakob Reichel ainsi qu'à Philippe Grangier pour l'acuité de leurs remarques et interrogations, et enfin, je remercie Jacqueline Bloch, la présidente du Jury, pour sa curiosité envers mes travaux de thèse pourtant quelque peu éloignés des semi-conducteurs.

Je tiens ensuite à remercier chaleureusement mon directeur de thèse, Alexei Ourjoumtsev. J'ai eu la vie facile au laboratoire grâce à ta patience, ta confiance et ton écoute dans nos échanges quotidiens, aidé aussi, il faut le dire, par ton goût pour la transmission. Je garde de mon temps passé dans ton équipe l'exemple de ta rigueur, ton talent scientifique couplé à une pugnacité pour porter un projet scientifique si ambitieux; des qualités qui m'ont laissé une forte impression et dont je tâcherais de m'inspirer autant que possible.

Quelques mots aussi pour l'équipe de photonique quantique. TMerci à Sébastien Garcia avec qui j'ai partagé toutes ces années, du montage de l'expérience à nos discussions interminables à n'importe quelle heure de la journée et n'importe quel jour de la semaine. Merci pour ton investissement sur le projet, pour ta transmission, ton imagination, ta bonne humeur et enfin, ou surtout, ta patience à mon égard. Je suis très heureux de savoir que tu es maintenant chargé de recherche au CNRS ! Merci aussi à Valentin Magro qui prend la suite, pour la presque année que nous avons passée ensemble. Je suis content de voir que la relève est bien assurée. Sache que je retiens nos galères quasi-quotidiennes d'expérimentateurs et c'est pourquoi je te souhaite bon courage, évidemment, mais surtout de belles réussites. Merci aussi aux plus anciens pour les échanges passionnants, Merlin Enault-Dautheribes avec qui j'ai passé deux années à construire l'expérience et tout ce qui l'entoure, et Nicolas Vitrant qui m'a beaucoup appris pendant ma première année au Collège de France.

Je veux par ailleurs souligner le cadre exceptionnel dans lequel j'ai eu la chance de travailler pendant ces années. Je tiens à remercier les membres de l'Institut de physique du Collège de France dirigé par Jean Dalibard, l'atelier de mécanique et en particulier Pascal Travers sans qui la plateforme expérimentale sous vide n'existerait pas, la partie administrative et l'aide particulière de Carmen Toderasc. Merci aussi à Michel Brune, le directeur du Laboratoire de Jeunes Equipes du Collège de France qui accueille l'équipe d'Alexei et aux équipes voisines qui ont toujours répondu présent pour prêter du matériel et discuter physique.

Que Brassens ne s'en retrouve pas offensé si, malgré l'évidente force des sentiments, on n'y retrouve pas tout à fait les copains d'abord. A tous ces oiseaux de passage, que je croisai pendant mon enfance au bord de l'eau à la Forêt Fouesnant, des années après au Likès à Quimper pendant le lycée, puis à Chatô en prépa à Rennes, au sud de Paris jusqu'au Collège de France, je veux dire merci pour tous les bons moments passés et, par avance, à venir. Je ne prendrai pas le risque de donner des noms, de peur de froisser ceux que, par malheur, j'aurais la maladresse d'oublier.

Je dois aussi énormément à ma grande famille. Ma reconnaissance va à mes parents, merci à mes frères et ma sœur, et j'ai une pensée particulière pour mes deux grands-mères

qui, chacune à leur manière, m'ont beaucoup apporté. Il y eut nécessairement des doutes, de la fatigue, ou même par moment de la lassitude pendant cette période intense, merci à Clémence pour sa patience et son soutien indéfectible.

Enfin, je ne peux conclure sur cette aventure, puisque c'est bien de ça dont il s'agit, sans évoquer l'édition 2020-2021 du Vendée Globes. Merci Jean le Cam pour le panache, la bouffée d'air frais, la détermination et la visite de ton navire enfant, je n'oublierai pas. Après avoir fait le tour du monde seul avec une avarie et sauvé un homme, ton mantra laconique " Bien dire fait rire, bien faire fait taire" me laisse également amusé et admiratif.

Abstract

Producing interactions between optical photons is a major concern for the implementation of quantum communication protocols, for photonic quantum computing, as well as for the exploration of interacting photonic fluids. This thesis presents a new experimental platform designed to obtain such interactions via a small atomic ensemble ($\sim 10 \mu\text{m}$) coupled to a cavity. The photons injected through the cavity are transiently converted into Rydberg excitations, characterized by strong van der Waals interactions spanning the whole atomic cloud. This hybridization between photons and atomic excitations, also called polariton, allows us to achieve strong optical nonlinearities at the single-photon level.

The first part of this thesis presents the new experimental setup, its construction and the technical choices. The second part then focuses on the characterization of the experiment and the different steps required to achieve strong interactions between photons: the preparation of a small atomic cloud in the cavity, the strong collective coupling with the cavity mode and the hybridization between photons and atomic excitations. The last part covers two experiments conducted with the platform. First, the strong interactions provided by Rydberg excitations are used to realize a nonlinear quantum memory. This mechanism is an efficient way to produce single photons and allows us to truncate a coherent state. The second experiment addresses the control and single-shot detection of a single Rydberg excitation in the cloud. In particular, one Rydberg atom is enough to induce a sign flip of the electromagnetic field reflected on the cavity. These techniques constitute a toolbox for quantum engineering of light with our platform and should allow us to perform more sophisticated protocols in the years to come: the generation of nonclassical states of light, the realization of photonic gates, etc.

Résumé

La production d'interactions entre photons optiques est une préoccupation majeure pour la mise en œuvre de protocoles de communication quantique, pour le calcul quantique photonique, ainsi que pour l'exploration de fluides photoniques en interaction. Cette thèse présente une nouvelle plateforme expérimentale conçue pour obtenir ces interactions par l'intermédiaire d'un petit ensemble d'atomes ($\sim 10 \mu\text{m}$) couplé à une cavité. Les photons injectés à travers la cavité sont transitoirement convertis en excitations de Rydberg, caractérisées par de fortes interactions de van der Waals couvrant l'ensemble des atomes. Cette hybridation entre photons et excitations atomiques, communément appelé polariton, permet d'obtenir de fortes non-linéarités optiques entre quelques photons.

La première partie de cette thèse présente le nouveau dispositif expérimental, discute la construction et les choix techniques. La deuxième partie se concentre ensuite sur la caractérisation de l'expérience et les différentes étapes nécessaires pour atteindre de fortes interactions entre photons : la préparation d'un petit nuage atomique dans la cavité, le fort couplage collectif avec le mode du résonateur et l'hybridation entre photons et excitations atomiques. La dernière partie présente deux expériences menées avec la plateforme. Dans la première, les fortes interactions obtenues par les excitations de Rydberg sont utilisées pour réaliser une mémoire quantique non linéaire. Ce mécanisme fournit un moyen efficace de produire des photons uniques et nous permet de tronquer un état cohérent. La deuxième expérience porte sur le contrôle et la détection à mesure unique d'une excitation Rydberg unique dans le nuage. En particulier, un seul atome de Rydberg est nécessaire pour induire un changement de signe du champ électromagnétique réfléchi sur la cavité. Ces techniques sont des outils essentiels pour l'ingénierie quantique de la lumière avec notre plateforme, et devrait permettre de réaliser des protocoles plus sophistiqués dans les années à venir : la génération d'états non classiques de la lumière, la réalisation de portes photoniques, etc.

Contents

1 Theoretical framework	7
1.1 Strong light-matter interactions (cavity QED)	8
1.1.1 A classical approach to the atom-cavity coupling	8
1.1.2 Quantum description for two-level atoms	11
1.2 Coupling to Rydberg states	16
1.2.1 Rydberg atoms	16
1.2.2 Electromagnetically induced transparency	20
1.2.3 Photon-photon interactions	24
2 Experimental setup	31
2.1 Experimental platform	32
2.1.1 Science cavity	35
2.1.2 Build-up cavities	41
2.2 Laser bench	44
2.2.1 Lasers	44
2.2.2 Frequency locking chain	46
2.2.3 Optical modulator: frequency control and switch	49
2.3 Control setup	51
2.3.1 Hardware	51
2.3.2 Software	52
3 Preparation of an atomic ensemble inside the science cavity	55
3.1 Magneto-optical traps	57
3.1.1 Atomic beam: 2D MOT	58
3.1.2 3D Magneto-optical trap	59
3.2 Optical dipole traps	64
3.2.1 Conveyor belt	65
3.2.2 Crossed-dipole trap	67
3.3 Degenerate Raman sideband cooling	69
4 Detection of the atom-cavity coupling	75
4.1 Detection setup	76
4.1.1 Intensity measurements	76
4.1.2 Balanced homodyne detection	79
4.1.3 Optical setup	84
4.2 Collective strong coupling regime	86
4.2.1 Optical pumping	86
4.2.2 Coupling to $ 5S_{1/2}, F = 1, m_F = 1\rangle \rightarrow 5P_{1/2}, F' = 2, m_{F'} = 2\rangle$.	89

5 Rydberg EIT with polariton blockade	93
5.1 Rydberg EIT in the linear regime	95
5.1.1 EIT spectrum: experimental implementation	95
5.1.2 Coupling to the Rydberg state	97
5.2 Strongly interacting photons	103
5.2.1 Saturation	103
5.2.2 Photon statistics	107
5.3 Conclusion	114
6 Deterministic generation of nonclassical light	115
6.1 Nonlinear quantum memory	117
6.1.1 Presentation	117
6.1.2 Model for the pulsed regime	119
6.2 Efficient single-photon source	123
6.2.1 Experimental setup	123
6.2.2 Characterization	125
6.3 Study of the continuous variables of the field	131
6.3.1 Theoretical considerations and simulation	131
6.3.2 Output mode and homodyne signal	134
6.3.3 Experimental results	136
7 Coherent control and optical detection of a Rydberg superatom.	141
7.1 Collective Rabi oscillations	144
7.1.1 Rabi oscillations of a single Rydberg superatom	145
7.1.2 Experimental implementation	150
7.1.3 Characterization of the collective driving	154
7.2 Detection of a Rydberg atom	158
7.2.1 Fidelity of a detector	158
7.2.2 Transmission switch	159
7.2.3 Detection via the reflected field	167
Bibliography	178

Introduction

At the smallest scale, the laws of nature are described by the physical theory of quantum mechanics, famous for its unprecedented precision. The first successes of this theory concerned the explanation of macroscopic phenomena by the quantization of light and matter: the ultraviolet catastrophe predicted by the Rayleigh-Jeans law for the black-body radiation in thermodynamics [1], the photoelectric effect [2] or the stability of matter [3].

In the second part of the 20th century, the technical progress, in close connection with quantum mechanics, brought a new impulse to the research in this field. The realization of the laser in 1960 opened the way, among other things, for the in-depth study of atomic and molecular spectra. At the end of this century, marked by the achievement of the Bose-Einstein condensation [4], it also contributed to the discovery of new methods to trap and cool down atoms. In the same way, the development of the scanning tunneling microscope in 1981 [5] led to the first observations of the crystallographic structures of materials. Simultaneously, the boom of semiconductor-based technologies, for example digital computers developed from the transistor [6], but also new detection methods such as the Zener diode, radically changed the way to carry out a physics experiment.

These technical breakthroughs helped physicists to isolate, control and detect single quantum systems: an atom, a photon, an ion... In turn, the experiments of this period emphasized the accuracy of the quantum theory with more and more precision, but also observed puzzling phenomena. There are many examples, but one of the most remarkable results is the violation of Bell's inequalities observed experimentally by Alain Aspect's team [7, 8] to settle the completeness of quantum mechanics questionned by the EPR paradox [9].

The techniques for the control and detection of isolated quantum objects have continued to develop and improve in recent decades, resulting in more and more sophisticated experiments, expanding the scope of investigations:

- One of the motivations behind the current research is related to some fundamental questions in physics. This is for example the case of the projects GBAR, ALPHA or AEGIS [10–12] that aim at studying the equivalence principle with anti-hydrogen, requiring the trapping of the antihydrogen ions. The detection of gravitational waves with the gigantic optical interferometers of LIGO and VIRGO is another example, through the use of squeezed vacuum to reduce noise. The increasing precision of atomic clocks could allow, in the decades to come, to detect gravitational waves below 10 kHz signals, the current limitation with optical interferometers [13], or to look for the hypothetical dark matter [14] and the variation of the fundamental constants. Many other applications are discussed in the review of Ludlow *et al.* [15]. Other experiments are examining the value of the dipole moment of the electron in the hope of finding a flaw in the standard model [16]. Further future experiments or proposals based on atoms or molecules to search for new physics are discussed in a review by Safronova *et al.* [17].

- Another research direction is to use the control of elementary constituents to study more complex and richer composite systems, while keeping a high level of control over the individual components. This allows for example the study of phase transitions, with ions [18] or superconducting circuits [19] and numerous approaches and platforms are presented in the review of Georgescu *et al.* [20]. The aim of these investigations is to reproduce a complex Hamiltonian, to study the evolution of the system or its steady state. This is for instance relevant for condensed matter physics where the in-depth study of real materials is sometimes challenging due to noise or lack of control over the parameters.
- These “analog” quantum simulators could ultimately lead to a yet speculative goal: the quantum computer. In the realm of quantum computing, a quantum two-level system is used as an information carrier named qubit. It is the quantum analogue of a bit in classical computing which state is either 0 or 1, but here, a qubit can be in any superposed state:

$$a |0\rangle + b |1\rangle \quad (1)$$

where a and b are two complex numbers verifying $|a|^2 + |b|^2 = 1$ and $|0\rangle$, $|1\rangle$ are two states.

The interest of this approach comes from the fact that some problems can be solved considerably more quickly than with standard calculators, for instance finding an element among N unranked elements via Grover’s algorithm [21]. It is also suspected that the prime factorization can be obtained faster: Shor demonstrated that this task takes a polynomial time with a quantum computer while there is, until now, no equivalent with standard computing [22]. It is this quantum advantage that has attracted so much interest, pushing companies such as Google or IBM to invest in this field. However, there are still many open questions: the robustness of this method of calculation with regard to errors is an example, even if error correction codes are developed to fight this problem [23]. It requires so far an incredibly large number of qubits, at least millions, while the best Noisy Intermediate Scale Quantum computers (NISQ) are only at a hundred qubits, see Dyakonov’s articles for some other arguments [24] and the review of Preskill on quantum computing with NISQ calculators [25].

- In the same vein, the creation and increased control of entanglement between quantum objects have contributed to the development of new communication and cryptography schemes. For the latter case, the “distribution” of an encryption key by quantum means, for instance with the BB84 protocol [26], is protected against eavesdropping on the communication line by the non-cloning theorem [27], see the review of Pirandola *et al.* [28]. In this large-scale communication framework, one quantum object stands out from the rest: the optical photon. It propagates as fast as the laws of the universe allow, can be easily guided by optical fibers and has several degrees of freedom to carry information. There are nevertheless some major challenges: although photons experience limited losses, current classical fiber networks need amplifiers to ensure the transmission of reliable information over large distances. For qubits, it is more subtle since the non-cloning theorem prevents here the amplification of the quantum signal by classical means. One way to exchange qubits over a large distance is to use the teleportation of a quantum state through entanglement with what is called a quantum repeater [29], requiring two-photons gates which, to function deterministically, necessitate efficient and strong interactions. These operations would be, of course, also interesting for quantum computation. In most of these quantum communication protocols, it is essential to have a way to generate photons and this with a high efficiency, on demand

and with controlled properties. There has been a lot of progress in the last few years, especially with quantum dot technologies in the optical domain with on-demand sources reaching 57% efficiency [30]. The other cornerstone is the detection of single photons, which is now very mature with 98% efficiency for the detection of photons at telecom wavelengths via superconducting nanowire detectors [31].

Of course, the experiments carried out in laboratories are not necessarily directed towards one of these arbitrary axes and this introduction is by no mean an exhaustive inventory of all the research currently conducted in quantum physics. The experimental platform we are concerned with in this thesis belongs to this branch of experiments exploiting the increased control of quantum systems. More specifically, this project focuses on photons and quantum optics experiments.

Interactions between photons

One of the main drawbacks of photons is the absence, or at least the very weak strength of their interactions at the scales of our experiments. Fortunately, it exists several methods to induce strong interactions through the coupling to matter.

Achieving optical nonlinearities with matter is not something new. These nonlinearities have been studied since the emergence of the laser: it is for instance a standard way to provide a frequency doubling of a laser. However, we do not seek for interactions within a macroscopic collection, but between only few photons. In fact, an alternative way to proceed is to use linear optics combined with measurements to obtain a nonlinear operation by post-selecting events: this trick allowed for instance the realization of a CNOT photonic gate [32]. This method has however a low probability of success. Scaling it up to build a complex quantum network requires quantum memories capable of storing the result of a successful operation until all other operations required before the next logic step succeed as well. Despite significant progress in this direction, this goal remains to be reached.

One alternative option to implement strong interactions between photons is to use a quantum of matter, i.e an atom, or its artificial counterpart, and in particular the nonlinearity of its spectrum. The atom can only absorb one photon at a given frequency and thereby provides a coupling that strongly depends on the number of photons it encounters. Unfortunately, the probability for a single photon to be absorbed by an atom is very low. Important developments have allowed to increase this interaction between a photon and a single two-level emitter over the last decades. One of the most popular methods to obtain strong light-matter coupling is to use facing mirrors to trap photons. By placing the atom inside, the possibilities of having an interaction between the photon and the emitter are increased because of the numerous round-trips traveled by light. Other methods are studied to couple light and matter: through an evanescent field around a fiber [33], with whispering-gallery modes [34], via photonic crystals [34]... All this by broadly exploiting the electromagnetic spectrum domains among the optical, microwave or infrared ones with different platforms and techniques [35–37]. A large proportion of these approaches allows experimentalists to reach the so-called strong coupling: the energy exchange time between light and the emitter is shorter than the lifetime of the two quantum objects. In this case, the physics become strongly nonlinear for light at the single-excitation level.

For this purpose, it is necessary to focus the light in the resonator and to use mirrors with very high reflectivity in order to obtain a high number of round trips traveled by light, while keeping the optical losses at a low level to have both strong and efficient interactions. The latest results are very encouraging with, for instance, the on-demand generation of optical Schrödinger cat states [38]. This standard is however challenging to reach and the reduction

of losses in mirrors, to go further, mainly relies on the development of advanced engineering techniques.

A third approach is to inject optical photons into a cold atomic cloud and to use the interactions between atoms to achieve optical nonlinearities. A widespread method consists in mapping photons onto Rydberg excitations, via electromagnetically induced transparency (EIT) [39], to allow for a low-loss propagation of photons in the medium while benefiting from the strong dipole-dipole interactions of Rydberg atoms, perceptible over large distances $\sim 10 \mu\text{m}$ [40]. The response of a medium smaller than this $\sim 10 \mu\text{m}$ scale is then strongly dependent on the number of excitations that propagate through it. For instance, one photon is able to change the absorption of the medium, resulting in single-photon blockade [41] that can be used to make single-photon switches [42] or transistors [43, 44]. In this limit, the atomic ensemble behaves as a two-level system called a Rydberg superatom. In the dispersive regime, this EIT mapping together with Rydberg interactions leads to a nonlinear variation of the group index. This nonlinearity is used, for instance, to obtain attractive interactions between photons [45] or photonic molecules [46]. Another interesting approach is to take advantage of the dispersion to achieve a π phase shift between photons [47] to get efficient interactions. Unfortunately, the interaction strength is too weak in this regime and cannot be compensated by the atomic density without increasing the collisions between Rydberg excitations and ground-state atoms [48]. There are two comprehensive reviews on this topic by Firstenberg *et al.* [49] and Murray *et al.* [50].

A new hybrid platform

Nowadays, a lot of research projects are using hybrid systems mixing different quantum objects to benefit from the assets of each component [51–53]. This is precisely the approach followed by the project presented in this thesis. The aim is to combine a cavity, made of almost standard mirrors, with Rydberg excitations in an atomic ensemble.

On the one hand, the use of an atomic ensemble rather than one atom provides a magnified coupling between the light and the atomic cloud, without having to rely on state-of-the-art mirrors. On the other hand, thanks to the cavity, in a well-chosen parameter regime exploited in our setup, the dissipation induced by an atomic ensemble translates into a sign change on light fields reflected off the resonator rather than absorption. Consequently, it is possible to work directly in the dissipative regime to obtain strong interactions from the Rydberg excitations but with low losses.

Our experimental platform is a sequel to the experiment conducted in Palaiseau [54] (2010-2015), where the first signals of dispersive and dissipative nonlinearities were obtained with Rydberg excitations in a cavity, at a level of approximately a thousand photons [55, 56]. In 2018, Jonathan Simon’s team observed strong interactions between photons by coupling an atomic ensemble with a cavity in the dissipative regime [57].

This new experimental platform is also designed to be as versatile as possible. This is certainly a specificity of cold atoms experiments: an experimental setup as presented in this thesis requires several years of design and in general, once the vacuum is made, experiments are conducted for five to ten years before any change inside the vacuum enclosure. It is however impossible to have a prior answer to all the technical and experimental challenges in such a new project; this flexibility in the design of the platform allows us to navigate with these constraints to explore different phenomena and parameter regimes.

Because of the choice of versatility and the many unknowns, the aim of this new project is to make one step forward in some of the topics exposed above, and to show that a hybrid approach is indeed appropriate to address some of the current technical and physical challenges but not to realize an ideal quantum repeater nor to focus on getting a perfect photon source. In the long run, the strong interactions between photons in this platform should allow

to explore uncharted areas of nonlinear quantum optics. In addition, it will be possible to carry out quantum emulation experiments by acting on the optical modes of the cavity with Rydberg interactions, as demonstrated by Jonathan Simon and his team with their similar platform [58].

This manuscript reports on the main results obtained during the thesis. It begins with the assembly of the experimental platform along with its characterization, reviews the main steps required for the preparation of a small atomic ensemble and the achievement of electromagnetically induced transparency via the coupling to Rydberg excitations. We then demonstrate that this system provides strong optical nonlinearities by observing the saturation of the transmission rate and a strong photon antibunching. The platform is finally used to perform two experiments. The first one consists in realizing an efficient and on-demand single-photon source and to characterize the resulting truncated coherent state. The other experiment focuses on the control and detection of a Rydberg superatom coupled to the cavity. Among other things, we observe a sign flip of the electromagnetic field induced by a change of the state of our superatom.

Outline of the thesis

A brief description of the 7 chapters that articulate this thesis is given here.

Chapter 1 is dedicated to the introduction of the key theoretical concepts, briefly mentioned in this introduction, regarding the achievement of strong interactions between optical photons through the mapping with Rydberg excitations in a cold atomic ensemble strongly coupled to a cavity.

Chapter 2 is a presentation of the experimental platform, especially the vacuum enclosure and all the related equipment. The objective here is to discuss the design of the apparatus and to motivate the technical choices with regard to what is established in chapter 1.

Chapter 3 discusses the preparation of a small cold and dense atomic ensemble inside the optical cavity. We describe the different stages of trapping and cooling, based on the insights provided in Chapters 1 and 2.

Chapter 4 gives the detection methods used to probe our platform and introduces the dedicated optical setup built around the vacuum chamber. These techniques are then employed to characterize the coupling between the cavity and the atomic cloud.

Chapter 5 focuses on the strong interactions between optical photons. For this purpose, we introduce the coupling to Rydberg states and start by discussing the phenomenon of electromagnetically induced transparency in the linear regime. We then present our observations in the strongly interacting regime, in particular the saturation of the transmission and a strong photon antibunching.

Chapter 6 describes a first quantum optics experiment with the platform. The system is used as a nonlinear quantum memory which allows to truncate a coherent state at one photon. We show that this also constitutes an efficient single-photon source and we present a study of the field quadratures.

Chapter 7 tackles the coherent control and the single-shot detection of a single Rydberg excitation. The control is achieved through a two-photon Rabi driving while the detection is done via the blockade of the transmission. We use this control to prepare a Rydberg state in a deterministic way to characterize our detection. Finally, we study the reflection of the cavity and demonstrate a state dependent π phase shift.

Chapter 1

Theoretical framework

Contents

1.1 Strong light-matter interactions (cavity QED)	8
1.1.1 A classical approach to the atom-cavity coupling	8
Spectrum of a cavity	9
Coupling the cavity to a dielectric medium	10
1.1.2 Quantum description for two-level atoms	11
Field quantization and driving	11
One atom inside the resonator	13
From one atom to many: Dicke basis	13
Cooperativity	14
1.2 Coupling to Rydberg states	16
1.2.1 Rydberg atoms	16
Spectrum and lifetime	16
Dipole moment	17
1.2.2 Electromagnetically induced transparency	20
Free space and dark state of the Hamiltonian	20
Cavity spectrum with EIT	21
Rydberg polaritons	22
1.2.3 Photon-photon interactions	24
Rydberg blockade	24
EIT with interacting Rydberg atoms	25
Photon blockade in a cavity	27

This chapter is a brief introduction to the theoretical ideas and equations driving this new project. This theoretical framework will support and motivate our technical choices, which are presented in the second and third chapter of this thesis. The equations derived here will be used as from chapter 4 to model our experimental results.

The first section of this chapter is a presentation of the collective strong coupling regime between the optical mode of a cavity and a cold atomic ensemble. In this case and in the limit of a few excitations inside the resonator, the atom-cavity system is equivalent to two coupled harmonic oscillators that can therefore be described by a purely classical approach. This is quite different from the strong coupling between light and a single atom where the saturation is reached with a single excitation in the system.

In the following section, we discuss the coupling to Rydberg states with the aim of achieving strong photon-photon interactions with our atom-cavity platform. We start by introducing Rydberg atoms and their properties, in particular their large van der Waals interactions, to then tackle the excitation scheme to map Rydberg states onto photons. Finally, we introduce the regime of strong interactions where the atomic ensemble boils down to a single two-level system called a Rydberg superatom.

1.1 Strong light-matter interactions (cavity QED)

One of the long-standing issues of quantum optics is that optical photons do not interact with each other. The only way to obtain optical nonlinearities is then to mediate interactions via the coupling to matter. Unfortunately, the interaction strength between a photon in free space and a two-level system is very weak. This has led to the development of cavity quantum electrodynamics (cavity QED) in the past decades, with the idea of strengthening the light-matter coupling by surrounding the single emitter with mirrors, in other words an optical resonator. The challenge is then to sufficiently increase the number of round-trips for light, using highly reflective mirrors, together with a small mode volume to enhance the electric field amplitude. Eventually, the coupling strength between a cavity photon and the two-level system overcomes the losses of both the mirrors and the emitter. In this regime, the single two-level system is said to be strongly coupled to the cavity field.

For instance, the anharmonicity of the atomic spectrum provides an almost ideal two-level system that was exploited in many experiments at the early development of this field [59–63]. Others methods have been employed since then to obtain strong interactions between light and artificial two-level systems by using quantum dots, Josephson junctions, etc [64–66]. However, building a high-finesse resonator is an arduous task, even more to get a low-loss system for efficient optical nonlinearities. One of the challenges comes from the mirrors imperfections, as it will be discussed in more detail in chapter 2. Another concern is to ensure a stable coupling between the optical mode and the emitter while maintaining a small mode volume.

In our experiment, our approach focuses on the coupling of a medium-finesse cavity with an atomic ensemble. The platform is then less sensitive to mirror losses and does not require a low-mode volume, but this choice naturally suffers from the loss of nonlinearity as the atomic ensemble can absorb many photons before being saturated. In the last section of this chapter, we will see that it is still possible to obtain strong nonlinearities by coupling the ensemble to Rydberg states.

1.1.1 A classical approach to the atom-cavity coupling

Before going into a quantum description of the coupling between atoms and a resonator, we can have a good understanding of the atom-cavity system through a simple classical model.

The atomic ensemble is described as a generic dielectric medium with a complex refractive index n and a length l_0 , small compared to the cavity length. For clarity and simplicity, we will assume that the cavity is made of only two mirrors, placed in vacuum (refractive index $n_v = 1$) and separated by a distance d . This derivation can then be easily extended to an arbitrary number of mirrors. A light beam of amplitude E_{in} at a frequency ω is injected from a mirror with a reflectivity r_0 and a transmission $t_0 = \sqrt{1 - r_0^2}$. The second mirror is characterized by a reflectivity $r'_1 = r_1 e^{-L_m/2}$ such that $t_1 = \sqrt{1 - r'_1^2}$. Here, the term $L_m \ll 1$ encompasses the losses of the two mirrors (but not the transmission), that we put at

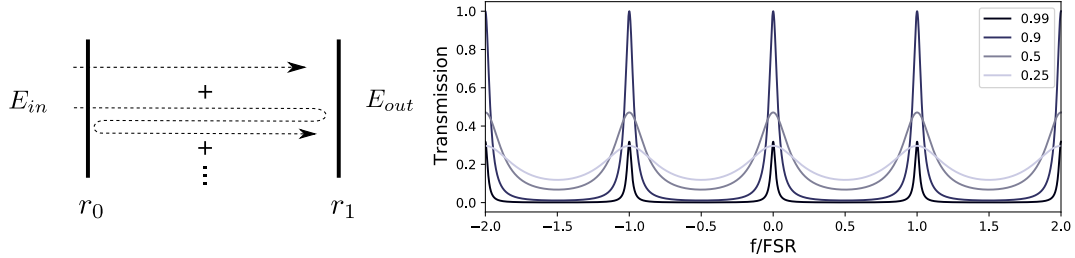


Figure 1.1: Cavity spectrum. Left - Buildup of the electromagnetic field. The light injected from the left (E_{in}) is reflected many times inside the cavity and the intra-cavity field is the sum of these reflections. Right- Cavity transmission spectra when we vary the reflectivity of the first mirror (legend panel) while the second one has a reflectivity set to 0.9. The frequency is normalized by the Free Spectral Range (FSR) c/ℓ , see text. The cavity transmission is maximal when the two reflectivities are equal, corresponding to an impedance matched cavity. The increase of the reflectivity leads to a refinement of the linewidth.

the intra-cavity surface of the second mirror⁽¹⁾. A more accurate derivation for the resonator of this experimental platform is presented in Appendix 7.2.3, but the two are equivalent in the limit of small transmissions and losses.

Spectrum of a cavity

The progressive-field amplitude inside the cavity, E_{cav}^+ , is given by the input amplitude transmitted through the first mirror $t_0 E_{in}$ added to the amplitude after one round-trip inside the resonator $r_0 r'_1 t_0 E_{in} e^{i\omega\ell/c}$, plus the contribution after two round-trips and so on. Here, $\ell = 2d$ is the distance traveled after one round-trip and c is the speed of light in vacuum. This buildup is illustrated in figure 1.1 and leads to the expression of the intra-cavity field:

$$E_{cav}^+ = \sum_n (r_0 r'_1 e^{i\phi})^n t_0 E_{in} = \frac{t_0}{1 - r_0 r'_1 e^{i\phi}} E_{in} \quad (1.1)$$

where $\phi = \omega\ell/c$. The transmitted field after the second mirror is then $E_t = t_1 E_{cav}^+$. We can rewrite this expression for the intensity to get the Airy function:

$$I_t = I_{in} \frac{t_0^2 t_1^2}{(1 - r_0 r'_1)^2 + 4r_0 r'_1 \sin^2 \frac{\phi}{2}} \quad (1.2)$$

We see that the cavity spectrum is made of two characteristic frequencies. First, the transmitted intensity is a periodic function of the frequency with a periodicity given by $\nu_{FSR} = \ell/c$, that is called the Free Spectral Range (FSR). As a result, $1/\nu_{FSR}$ is the time taken by light to make a round-trip. When the reflectivity of the two mirrors are close to one, the sine function can be approximated by its first order expansion around a resonance. We recover a Lorentzian shape with a full width at half maximum given by:

$$K = 2\nu_{FSR} \frac{1 - r_0 r'_1}{\sqrt{r_0 r'_1}} \simeq \nu_{FSR} (t_1^2 + t_0^2 + L_m) \quad (1.3)$$

where K is an angular frequency.

In this limit, it then convenient to introduce the optical losses of the resonator $L = t_1^2 + t_0^2 + L_m$. Because we have a Lorentzian, the lifetime of photons inside the cavity is

⁽¹⁾One is free to arbitrary weight optical losses on the two mirrors but the result is almost identical and we can shorten the notation in this way.

$\tau = 1/K = 1/(L\nu_{FSR})$ while the field damping rate is $\kappa = K/2$. The ratio between these two frequencies is called the finesse of the optical cavity. It characterizes the separation between two resonances. In our example, the finesse is then:

$$\mathcal{F} = \frac{2\pi\nu_{FSR}}{K} = \pi \frac{\sqrt{r_0 r_1}}{1 - r_0 r_1} \simeq \frac{2\pi}{L} \quad (1.4)$$

One can also see the finesse as the ratio between the photon lifetime and the time required to make a round-trip. The finesse is thus the average number of round-trips N that light travels before it leaves the resonator, up to a factor 2π : $\mathcal{F} = 2\pi N$.

Coupling the cavity to a dielectric medium

Now that we have the spectrum of an empty cavity, we can look at its evolution in the presence of a thin dielectric medium characterized by a complex reflective index $n(\omega)$ and a length l_0 . The refractive index captures the response of the medium to an external electromagnetic field E through its polarization $P = \chi\epsilon_0 E$ with the relation $\chi = n^2 - 1$, where ϵ_0 is the vacuum permittivity. Starting from equation 1.1, we only have to change the accumulated phase by:

$$\phi' - \phi = \omega[n(\omega) - 1] \frac{2l_0}{c} \simeq kl_0\chi(\omega) \quad (1.5)$$

where $k = \omega/c$ and assuming $\chi \ll 1$.

This coupling has two consequences on the spectrum: on one hand, the real part of the refractive index shifts the resonance of the empty cavity since the effective length of the cavity is modified by the medium. On the other hand, the imaginary component corresponds to the absorption of light and leads to a decrease of the transmission as depicted in figure 1.2. In the limit $kl_0|\chi(\omega)|, t_0, t_1 \ll 1$, the transmission spectrum is:

$$\mathcal{T} = \frac{I_t}{I_{in}} = \frac{t_0^2 t_1^2}{(L/2 + kl_0 \text{Im}(\chi))^2 + 4 \sin^2\left(\frac{\phi + kl_0 \text{Re}(\chi)}{2}\right)} \quad (1.6)$$

This coupling between a dielectric medium and a cavity is well known in physics and is a standard method to measure the susceptibility of a medium [67].

From the equation 1.6, one can obtain the spectrum of the coupled system with only classical physics. The susceptibility of a dilute atomic medium can be calculated via the Drude model [68]:

$$\chi \simeq \frac{\rho e^2}{2m\omega_0\epsilon_0} \frac{1}{(\omega_0 - \omega) + i\gamma/2} \quad (1.7)$$

This model considers each atom as a damped harmonic oscillator with a resonant angular frequency ω_0 , driven close to this frequency at ω , with a damping rate γ and an atomic density ρ .

We can now describe how the spectrum evolves as the cavity starts to couple with atoms. Let us assume that the frequency ω_0 is equal to that of the cavity mode, which is always possible by tuning the cavity length. We will only consider here the case where the atomic linewidth γ is much smaller than the cavity linewidth κ (a more rigorous and general derivation without this assumption is given later on). When we progressively increase the atom number, the absorption reduces the transmission on resonance, but on a narrow window compared to the bare cavity mode. On the other hand, the real part of the susceptibility (dispersion) is an odd function, with respect to $\omega = \omega_0$, pushing the resonance in two opposite

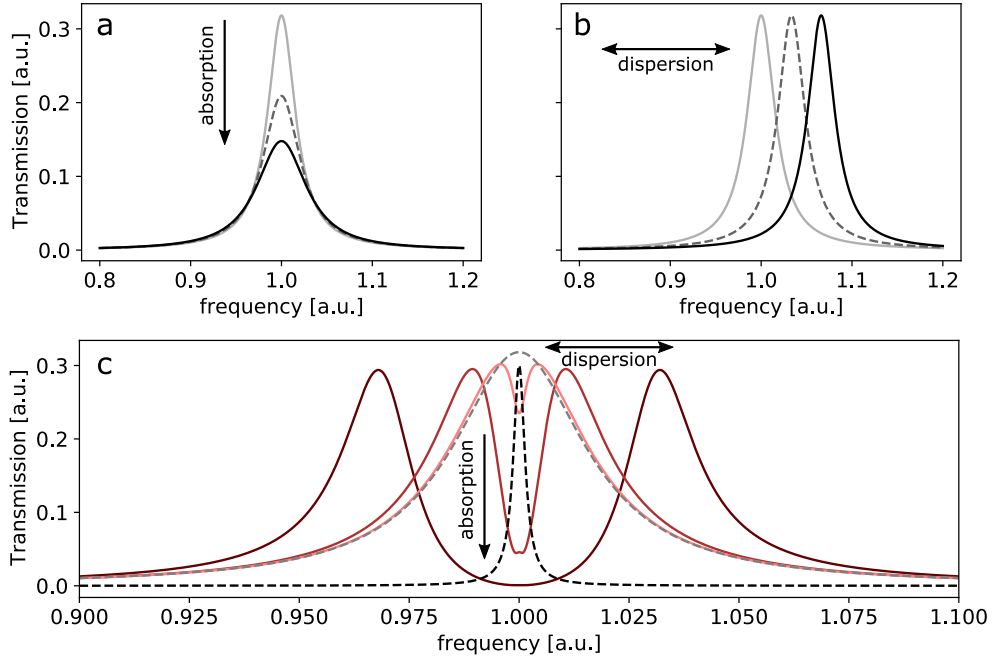


Figure 1.2: Spectrum in the presence of a dielectric medium. a- The absorption inside the cavity reduces the amplitude of the intra-cavity field and induces a drop of the transmission level. b- The dispersion causes a shift of the cavity resonance, see text. c- Atom-cavity spectra (shades of red) obtained from the Drude model for a cavity linewidth (grey dashed line) much larger than the atomic linewidth (black dashed line). From light red to dark: the atomic susceptibility $\times 1, 10, 100$.

directions. For a high enough atomic density, this eventually leads to two separate transmission modes, which is just the consequence of coupling two harmonic oscillators together. This transition from the empty cavity to the mode splitting is shown in figure 1.2.

This approach allows one to compute the coupling between a cavity and a dilute medium as long as the atomic ensemble can be captured by a semi classical model through its susceptibility. Since our experimental platform aims at reaching interaction down to few photons, a full quantum treatment is required to describe this quantum correlated system.

1.1.2 Quantum description for two-level atoms

We now focus on a quantum description of the atom-cavity system that will be needed for the description of optical nonlinearities. As a first step, we focus on a quantum description of the atom-cavity system, without interactions, to recover the mode splitting. On one hand, we will use the second quantization of light to introduce creation and annihilation operators: \hat{a}^\dagger, \hat{a} . On the other, atoms will be described as discrete quantum objects, here simplified to a collection of two-level systems: a ground state $|g\rangle$ and an excited state $|e\rangle$.

Field quantization and driving

The expression of the electric field operator is obtained from the method of second quantization developed by Dirac in 1927. In all generality, this operator is given by [69]:

$$\hat{\mathbf{E}}(\mathbf{r}) = \sum_i \mathcal{E}_i \left(\mathbf{f}_i(\mathbf{r}) \hat{a}_i + \mathbf{f}_i^*(\mathbf{r}) \hat{a}_i^\dagger \right) \quad (1.8)$$

where the field is decomposed in an arbitrary set of modes characterized by a spatial envelope \mathbf{f}_i taking into account the polarization, annihilation and creation operators respectively \hat{a}_i , \hat{a}_i^\dagger ; and \mathcal{E}_i is the electric field amplitude associated to a given mode.

In the case of a cavity, the envelope functions naturally correspond to the cavity eigenmodes. When their resonances are sufficiently non-degenerate with respect to other physically relevant frequencies, the problem can be simplified to account for a single mode. This experimental platform is also adapted to the study of multimode phenomena [58, 70, 71], but the work of this thesis focuses only on the coupling between the atomic ensemble and a single cavity mode. The electric field operator for a single mode has then a very simple expression:

$$\hat{\mathbf{E}}(\mathbf{r}) = \mathcal{E} \mathbf{f}(\mathbf{r})(\hat{a}^\dagger + \hat{a}) \quad (1.9)$$

where \mathcal{E} is the electric field amplitude and \mathbf{f} the spatial mode with $\max |\mathbf{f}|^2 = 1$ and $\nabla \cdot \mathbf{f} = 0$. This mode envelope \mathbf{f} defines the mode volume of the electric field via the relation:

$$V = \int_{\mathcal{V}} |\mathbf{f}(\mathbf{r})|^2 d\mathbf{r} \quad (1.10)$$

This volume sets the maximum value of the electromagnetic field amplitude in order to recover the circulating power inside the resonator. One deduces the expression of the field amplitude:

$$\mathcal{E} = \sqrt{\frac{\hbar\omega}{2\epsilon_0 V}} \quad (1.11)$$

where \hbar is the reduced Planck's constant. As mentioned in the introduction, it is then possible to reach a high amplitude by using a low mode volume.

Now that we have the expression of the field inside the resonator, we must take into account an external bath to feed the cavity. In order to obtain such driving, we consider that light is injected from one mirror with a transmission T . This parameter defines a photon feeding rate $K_0 = T\nu_{FSR}$ that can be understood as the probability to be transmitted by this mirror divided by the round-trip duration. The field feeding rate is then $\kappa_0 = K_0/2$ and the operator describing the driving of the cavity is provided by the input/output theory [72]:

$$\hat{F}/\hbar = i\alpha\sqrt{2\kappa_0}(\hat{a}^\dagger e^{-i\omega t} - \hat{a}e^{i\omega t}) \quad (1.12)$$

where $|\alpha|^2$ is the coherent input flux in front of the resonator. The Hamiltonian of the quantum field is:

$$\hat{H}_a = \hbar\omega_a \hat{a}^\dagger \hat{a} + \hat{F} \quad (1.13)$$

and the dynamics of the density matrix $\hat{\rho}$ is given by the master equation:

$$\begin{aligned} \hbar \frac{d\hat{\rho}}{dt} &= i[\hat{\rho}, \hat{H}_a] + \mathcal{D}[\hat{L}_a](\hat{\rho}) \\ \mathcal{D}[\hat{L}](\hat{\rho}) &= \hbar(\hat{L}\hat{\rho}\hat{L}^\dagger - \frac{1}{2}\{\hat{L}^\dagger\hat{L}, \hat{\rho}\}) \end{aligned} \quad (1.14)$$

where the Lindblad operator $\hat{L}_a = \sqrt{2\kappa}\hat{a}$ is there to account for the photon leaks out of the cavity, induced by the defects on the mirrors and their residual transmission. These losses are described by the coefficient L introduced in the previous subsection and define a field damping rate $\kappa = K/2 = cL/2\ell$. Finally, the operator acting on the system for a given Lindblad operator \hat{L} is defined by the superoperator \mathcal{D} .

One atom inside the resonator

The second step consists in a quantum description of both the atomic ensemble and the light-matter interaction. As mentioned earlier, atoms are described as two-level systems composed of a ground state $|g\rangle$ and an excited state $|e\rangle$. The energy in the excited state is $\hbar\omega_e$ and the Hamiltonian for one atom reads $H_{\text{atom}} = \hbar\omega_e\hat{\sigma}_{ee}$, where $\hat{\sigma}_{ee} = |e\rangle\langle e|$.

In the limit where the wavelength λ is large compared to the typical size of an atom, the light-matter interaction is given by the coupling between the dipole operator $\hat{\mathbf{d}} = \mathbf{d}(|g\rangle\langle e| + |e\rangle\langle g|)$ and the electric field operator $\hat{\mathbf{E}}$. Then, the interaction Hamiltonian for one atom coupled to light is:

$$\hat{H}_{\text{int}} = -\hat{\mathbf{d}} \cdot \hat{\mathbf{E}} = \hbar g_0(\hat{a}^\dagger + \hat{a})(\hat{\sigma}_{eg} + \hat{\sigma}_{ge}) \quad (1.15)$$

where $g_0 = -\mathcal{E}\mathbf{d} \cdot \mathbf{f}(\mathbf{r})$ with \mathbf{r} the position of the atom, $\hat{\sigma}_{eg} = |e\rangle\langle g|$ and $\hat{\sigma}_{eg}^\dagger = \hat{\sigma}_{ge}$.

Again, we need to take into account the coupling of the atom with an external bath. This time, it is given by the spontaneous emission via a field damping rate γ and the Limblad operator is $\hat{L}_e = \sqrt{2\gamma}\hat{\sigma}_{ge}$. The full dynamics of the atom-light system inside the resonator is then:

$$\hbar \frac{d\hat{\rho}}{dt} = i[\hat{\rho}, \hat{H}_{JC}] + \mathcal{D}[\hat{L}_e](\hat{\rho}) + \mathcal{D}[\hat{L}_a](\hat{\rho}) \quad (1.16)$$

where the total Hamiltonian corresponds to the Jaynes-Cummings model: $\hat{H}_{JC} = \hat{H}_a + \hat{H}_{\text{atom}} + \hat{H}_{\text{int}}$.

In our case, the coupling strength remains small compared to the photon frequency ($\omega \gg g_0$) such that counter-rotating terms in equation 1.15 can be neglected in the rotating frame. The final light-matter Hamiltonian for one atom reads:

$$\hat{H}_{JC} = -\hbar\delta_e\hat{\sigma}_{ee} - \hbar\delta_a\hat{a}^\dagger\hat{a} + g_0(\hat{a}^\dagger\hat{\sigma}_{ge} + \hat{a}\hat{\sigma}_{eg}) \quad (1.17)$$

where $\delta_a = (\omega - \omega_a)$ and $\delta_e = (\omega - \omega_e)$

From one atom to many: Dicke basis

For an atomic ensemble, one simply has to make the sum of the single-atom operators in equation 1.16 over all the atoms. Individual operators and couplings become $\hat{\sigma}_{ij} \rightarrow \hat{\sigma}_{ij}^{(n)}$ and $g_0 \rightarrow g_0^{(n)}$ where the subscript n refers to the n^{th} atom and i, j to the two states g, e . The complete Hamiltonian and decay terms, involving atoms, are:

$$\begin{aligned} \hat{H}_{\text{cloud}} &= \sum_n \left(\hat{H}_{\text{atom}}^{(n)} + \hat{H}_{\text{int}}^{(n)} \right) \\ \mathcal{D}[\hat{L}_{\text{cloud}}](\hat{\rho}) &= \sum_n \mathcal{D}[\hat{L}_e^{(n)}](\hat{\rho}) \end{aligned} \quad (1.18)$$

It is interesting to notice that each two-level atom is equivalent to a spin-1/2, with the spin up defined by $|\uparrow\rangle = |e\rangle$ and down by $|\downarrow\rangle = |g\rangle$. Therefore, a convenient way to describe the atomic ensemble is to consider the basis given by the combination of N spin-1/2:

$$\{|J, J_z\rangle\}, \text{ where } 0 \leq J \leq N/2 \text{ and } -J \leq J_z \leq J \quad (1.19)$$

The atomic ensemble can thus be seen as a spin J and for instance, its ground state corresponds to the state $|g, \dots, g\rangle = |N/2, -N/2\rangle$. This formalism was introduced by Dicke [73] to describe superradiant emissions occurring when an atomic ensemble is confined in a volume much smaller than the wavelength [74].

One interesting subspace of this Dicke basis is formed by states that are invariant under the permutation of any atom pair. The states in this subspace are called “symmetric” Dicke states and are given by:

$$|n_D\rangle = |J = N/2, J_z = n_D - N/2\rangle \quad (1.20)$$

This subset, made of N states, can be generated by the ladder operator of the total spin:

$$\hat{J}^\dagger = \frac{1}{\sqrt{N}} \sum_n \sigma_{eg}^{(n)} \quad (1.21)$$

For instance, the first excited state in this “symmetric” subspace is obtained by applying this operator to the ground state and corresponds to the W state in the context of quantum information [75, 76]:

$$|W\rangle = |n_D = 1\rangle = \frac{1}{\sqrt{N}} \sum_n |g, \dots, e_n, \dots, g\rangle \quad (1.22)$$

All the other states of the Dicke basis are referred to as the “asymmetric” Dicke states.

Cooperativity

The atom-cavity system for N atoms is described by the open Tavis-Cummings model:

$$\hbar \frac{d\hat{\rho}}{dt} = i[\hat{\rho}, \hat{H}_{\text{TC}}] + \mathcal{D}[\hat{L}_a](\hat{\rho}) + \sum_n \mathcal{D}[\hat{L}_e^{(n)}](\hat{\rho}) \quad (1.23)$$

where the Hamiltonian is $\hat{H}_{\text{TC}} = \hat{H}_{\text{cloud}} + \hat{H}_a$. The relevant steady-state solutions, in the rotating frame, are:

$$\begin{aligned} \langle \hat{a} \rangle &= \frac{1}{\delta_a + i\kappa} \left(i\alpha\sqrt{2\kappa_0} + \sum_n g_0^{(n)} \langle \hat{\sigma}_{ge}^{(n)} \rangle \right) \\ \langle \hat{\sigma}_{ge}^{(n)} \rangle &= \frac{g_0^{(n)}}{\delta_e + i\gamma} \langle \hat{a} (\hat{\sigma}_{gg}^{(n)} - \hat{\sigma}_{ee}^{(n)}) \rangle \end{aligned} \quad (1.24)$$

One should in principle also compute the correlators between the operator \hat{a} and $\hat{\sigma}_{ee}^{(n)}$, $\hat{\sigma}_{gg}^{(n)}$ to solve this set of equations, which turn out to depend on higher-order correlators and so on indefinitely. These terms are for instance responsible for optical bistabilities in the atom-cavity system [77, 78]. In the limit of a small input rate, it is however possible to approximate the atomic population by assuming that most of the atoms stay in the ground state: $\langle \hat{\sigma}_{gg}^{(n)} \rangle \simeq 1$.

Then, equation 1.24 can be re-expressed with the operator \hat{a} and a collective operator \hat{P} only:

$$\hat{P} = \frac{1}{g} \sum_n g_0^{(n)} \hat{\sigma}_{ge}^{(n)} \quad (1.25)$$

where g is the collective coupling strength, $g^2 = \sum_n |g_0^{(n)}|^2$.

This operator is very reminiscent of the Ladder operator for the Dicke basis (equation 1.21, \hat{J}) and the two are equal for a homogeneous coupling. Notice that the evolution of the operator \hat{P} is influenced by the motion of atoms due to the coupling with light: each atom acquires a different phase factor $e^{i\mathbf{k}\mathbf{d}_n}$ contained in the individual coupling $g_0^{(n)}$, with \mathbf{k} the wave vector and \mathbf{d}_n the displacement of the n^{th} atom. In the limit of a small number of excitations, the commutation relation of the collective operator is simplified because one has $[\hat{P}, \hat{P}^\dagger] \simeq \mathbb{1}$. The atomic ensemble is then equivalent to a harmonic oscillator with an energy spacing $\hbar\omega_e$, and the coupling between two-level atoms and light can be seen as the coupling

between two harmonic oscillators. This justifies our ability to correctly describe the system by a purely classical approach, as explained earlier.

From this set of equations, one can for instance compute the transmission of the resonator in the presence of atoms, normalized to the empty cavity transmission:

$$\mathcal{T} = \frac{1}{(1 + \frac{2C}{1+\delta_e^2/\gamma^2})^2 + (\delta_a/\kappa - \delta_e/\gamma \frac{2C}{(1+\delta_e^2/\gamma^2)^2})^2} \quad (1.26)$$

where $C = \sum_n g_n^2/(2\gamma\kappa) = g^2/(2\gamma\kappa)$ is called the cooperativity of the system.

This parameter characterizes the strength of the collective coupling g with respect to the spontaneous emission γ and the damping of the cavity field κ . When $g \gg \kappa, \gamma$ the system enters the collective strong coupling regime where the losses κ, γ are smaller than the coupling g . The strength of the interaction between light and atoms is amplified by the atom number and for a homogeneous driving, the collective coupling is simply $g = \sqrt{N}g_0$. It is therefore possible to stand in the collective strong coupling regime with the atomic ensemble while atoms at the individual level are not strongly coupled to the resonator: $C_0 = g_0/(2\kappa\gamma) \ll 1/2$. This is one of the main advantage of our approach, due to this \sqrt{N} increase in the coupling and to the Rydberg blockade mechanism described below, it is possible to reduce the strength of the individual coupling g_0 compared to experiments with a single atom coupled to a resonator. More importantly, we will only need to use a medium-finesse cavity to reach the collective strong coupling.

Several regimes can be distinguished within the collective strong coupling limit. First, we can assume that the cavity is resonant with the atomic transition ($\delta_e = \delta_a$). Then, the coupled system stands in the dissipative regime, dominated by the atomic absorption in the vicinity of the zero-detuning region. In this case, the Lorentzian shape of the empty cavity is split in two modes separated by $2g$. This corresponds to the figure 1.3, with a very low transmission at zero detuning as also described in the previous subsection. For an atom-cavity detuning ($|\omega_a - \omega_e|$) bigger than the collective coupling strength, the coupled system is then in the dispersive regime where almost only one of the two Rabi modes is visible in the spectrum, shifted with respect to the cavity resonance because of the atomic dispersion. In this thesis, we will mostly focus on the dissipative regime.

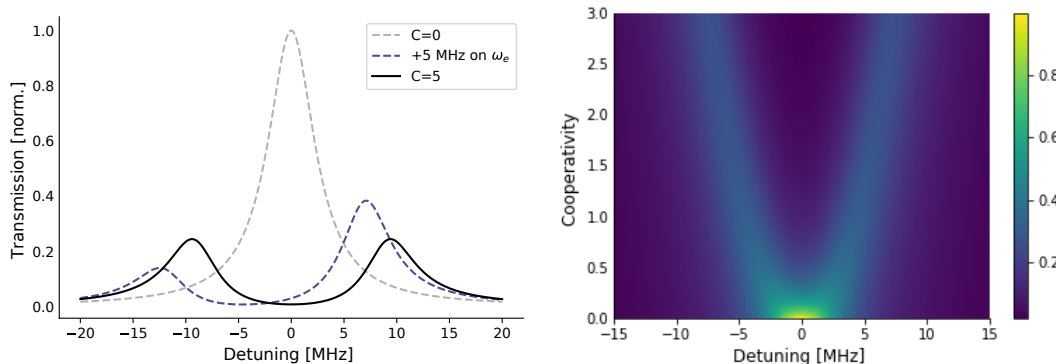


Figure 1.3: Rabi Splitting. Left- Cavity transmission spectra with $\omega_a = \omega_e$, $\gamma = 2\pi \times 3 \text{ MHz}$, $\kappa = 2\pi \times 2.7 \text{ MHz}$. Without atoms (grey line), we recover the bare cavity resonance. When we put atoms with $C=5$ (black line), the strong absorption reduces the transmission at resonance while two peaks appear for a detuning of $\pm 10 \text{ MHz}$. The last line is an illustration of the splitting when $\omega_a \neq \omega_e$. Right- Transmission of the cavity as a function of the cooperativity assuming $\omega_a = \omega_e$.

1.2 Coupling to Rydberg states

In the first part of this chapter, we described the coupling between an atomic cloud and an optical resonator to reach strong light-matter interactions. However, this mechanism is completely linear when the number of excitations is much smaller than the number of atoms.

In our approach, we use a third ingredient to provide strong optical nonlinearities in the atom-cavity system: the coupling to a Rydberg state. We start by briefly discussing the properties of Rydberg atoms in this section, in particular their strong dipole-dipole interactions. Next, we will explain how electromagnetically induced transparency allows to map photons onto these Rydberg excitations in the context of our atom-cavity platform. We finally discuss the conversion of van der Waals interactions into photon-photon nonlinearities at the quantum level.

1.2.1 Rydberg atoms

Rydberg states are highly excited atoms characterized by a high principal quantum number n . These excitations are promising tools for quantum technologies [79], for instance, considerable efforts are made to develop tunable atomic lattices with site-to-site interactions provided by Rydberg atoms [80, 81]. Rydberg excitations were also involved in the early development of cavity quantum electrodynamics (QED). The 2012 Nobel prize rewarded the work of Serge Haroche and his team on microwave cavity QED with circular Rydberg states [82]. These are only few examples out of numerous investigations currently conducted with Rydberg atoms [83–85].

We now briefly emphasize their unique and outstanding properties. More specifically, we focus on alkali atoms as they present a simple spectrum, very close to the textbook hydrogen atom in this limit of highly excited states. Furthermore, we will discuss the lifetime of these states with respect to low excited atoms and their high sensitivity to external fields due to their large dipole moments. We will then turn to the key property for our experiment: the strong dipole-dipole interactions existing between Rydberg atoms.

Spectrum and lifetime

Alkali atoms stand in the first column of the Mendeleev periodic table with a unique electron in their outer shell. This electronic configuration makes them close to the hydrogen atom and the spectrum of a given alkali Rydberg atom can be calculated by adding some corrections to the energy levels of hydrogen. These corrections are obtained by the quantum defects theory [86] to take into account the interactions of inner electrons with the outer electron. The energy ladder for alkali atoms can thus be expressed as:

$$E_{n,l,j} = -\frac{m_c}{m_c + m_e} \frac{hcR_\infty}{n_{n,l,j}^{*2}}, \text{ with } n_{n,l,j}^* = n - \delta_{n,l,j} \quad (1.27)$$

where n is the principal quantum number, m_c is the nucleus mass, m_e the electron mass and R_∞ is the Rydberg constant [87]:

$$R_\infty = \frac{m_e e^4}{8\epsilon_0^2 h^3 c} = (10\,973\,731.568\,160 \pm 0.000\,021) \text{ m}^{-1} \quad (1.28)$$

This Rydberg constant can also be expressed in unit of energy, $R_y = hcR_\infty$. Finally, $\delta_{n,l,j}$ is the quantum defect indexed by the angular orbital momentum l and the fine structure j . Note that these corrections decline rapidly with l as they originate from the interaction between the external electron and the others. These quantum defects are estimated with microwave

spectroscopy or electromagnetically induced transparency [88, 89] and can be computed by perturbation with the following model [90]:

$$\delta_{n,l,j} = \delta_{0,l,j} + \frac{\delta_{2,l,j}}{(n - \delta_{0,l,j})^2} + \frac{\delta_{4,l,j}}{(n - \delta_{0,l,j})^4} + \dots \quad (1.29)$$

Since the distance between the outer electron and inner electrons grows with the principal quantum number, $\langle \hat{r} \rangle \propto n^{*2}$, these corrections rapidly saturate for highly excited states [86, 88]. Consequently, the first two correction terms are sufficient for highly excited states.

Our experiment is conducted with Rubidium 87, the biggest quantum defect in this case is obtained for the $nS_{1/2}$ state, valid when $n \gg 5$ and corresponds to 3.1311804(10) [88]. Thereby, the Hydrogen spectrum is recovered in the limit of a high principal quantum number up to a small shift on the latter. Finally, notice that for highly excited states the important distance between the outer electron and the nucleus makes the coupling between the nuclear spin I and the electronic angular momentum J almost negligible, but this will be discussed in chapter 5.

Another interesting property of Rydberg atoms is their extended lifetime with respect to low excited states. This increase comes from the reduced overlap between the wave functions of the excited state and the ground states. The Fermi golden rule provides an interesting insight on its scaling law with respect to the principal quantum number. The emission rate from an excited state, here the Rydberg state r , to a lower level g is given by:

$$\Gamma_{g,r} = \frac{\omega_{g,r}^3 d^2}{3\pi\epsilon_0\hbar c^3} \quad (1.30)$$

where $\omega_{g,r}$ is the atomic angular frequency between r and g , d is the dipole of the transition taking into account the spatial overlap of the wave functions. In order to compute the effective lifetime of a given state, one simply has to take into account all the lower states. The lifetime of the state r is then:

$$\tau_r = \frac{1}{\sum_i \Gamma_{g_i,r}} \quad (1.31)$$

with a summation of the states with a lower energy: $E_{g_i} < E_e$ and assuming a 0 K temperature.

The main contributions come from transitions with very low excited states where $\hbar\omega_{g,r} \approx |E_{g_i}| \gg |E_r| \propto n^{*-2}$ while $\langle d \rangle^2 \propto n^{*-3}$ for a low- l Rydberg state from a direct calculation of the integral [91]. On the contrary, transitions with neighboring Rydberg states have an increased transition dipole $\langle d \rangle^2 \propto n^{*4}$ but the energy spacing is much smaller $\omega_{g,r} \propto n^{*-3}$. As a result, the lifetime scales as n^{*3} for low angular momenta and up to n^{*5} for circular Rydberg states ($l = n - 1$).

At ambient temperature, the black body radiation favors transitions in the $\sim GHz - THz$ range with a peak emission around $\simeq 30$ THz close to the energy between neighboring Rydberg states for $n \approx 100$ (few GHz). In this case, the lifetime is shortened and can be estimated by taking into account the population occupancy at finite temperature. For instance, the lifetime for the 100S Rydberg state⁽²⁾ is 1.1 ms at 0 K and falls to 0.4 ms when $T = 300$ K⁽³⁾.

Dipole moment

Since the typical radius of Rydberg atoms scales as $\langle \hat{r} \rangle \propto n^2$, these states have a large dipole moment $\langle \hat{\mu} \rangle = q \langle \hat{r} \rangle$. This makes Rydberg atoms very sensitive to external electric fields and

⁽²⁾For Rubidium 87.

⁽³⁾Estimated using ARC (Alkali.ne Rydberg Calculator) [92].

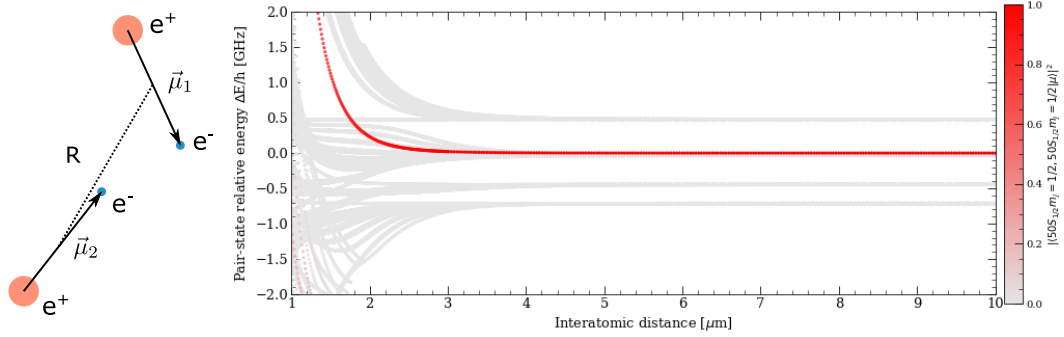


Figure 1.4: Dipole-Dipole interaction. Left- Two Rydberg atoms separated by a distance R . Right- Energy cost as a function of the separation between two $50S$ Rydberg states. Each line corresponds to a final pair state with the relative contribution colored from zero (white) to 1 (red). The dominant contribution is a van der Waals potential for $R > 1 \mu\text{m}$. Beyond this limit, the interaction potential is very complex and often called the “Spaghetti” regime.

they are thus an interesting sensor [93], for instance as a near-field detector of gigahertz and terahertz signals [94, 95].

For a static external field \mathcal{E} , the dc shift can be calculated from the quantum perturbation theory. The first order correction to the Rydberg energy is zero by symmetry of the wave function. As a result, the external field leads to a quadratic energy shift:

$$\Delta E = -\frac{1}{2}\alpha_0\mathcal{E}^2 = \sum_{n',l',j',m'_j \neq n,l,j,m_j} \frac{|\langle n',l',j',m'_j | q\hat{r} | n,l,j,m_j \rangle|^2}{E_{n,l,j,m_j}^0 - E_{n',l',j',m'_j}^0} \mathcal{E}^2 \quad (1.32)$$

where α_0 is the scalar polarizability with a scaling in n^7 , $|n,l,j,m_j\rangle$ is the initial Rydberg state at zero electric field with an unperturbed energy E_{n,l,j,m_j}^0 and $\{|n',l',j',m'_j\rangle\}$ are the other Rydberg states with an energy E_{n',l',j',m'_j}^0 .

This strong polarizability can be an important source of trouble for the kind of experiments we aim to conduct. An external electric field causes an important shift of the Rydberg resonance and can induce a mixing between Rydberg states of the fine structure, resulting in a significant broadening of the Rydberg linewidth. In this respect, electric field gradients over the atomic ensemble, such as those created by localized electrostatic charges close to the atoms, are even more troublesome.

Note that Rydberg atoms are not only very sensitive to external electric fields, but also to magnetic fields when excited in a circular state ($l = n - 1$) [96]. It is however not the case for us as we only want to address low- l momentum states.

Another consequence of these large dipole moments is the strong dipole-dipole interaction between Rydberg atoms. Rydberg interactions are a key ingredient for numerous proposals and experiments. The dipole interaction potential between two Rydberg atoms is given by:

$$\hat{V} = \frac{1}{4\pi\epsilon_0} \frac{\hat{\mu}_1 \hat{\mu}_2}{\|\hat{\mathbf{R}}\|^3} - \frac{3(\hat{\mu}_1 \cdot \hat{\mathbf{R}})(\hat{\mu}_2 \cdot \hat{\mathbf{R}})}{\|\hat{\mathbf{R}}\|^5} \quad (1.33)$$

where $\hat{\mu}_{1,2}$ are the dipole moment operators associated to the two Rydberg atoms, $\hat{\mathbf{R}} = \hat{\mathbf{r}}_1 - \hat{\mathbf{r}}_2$ and $\hat{\mathbf{r}}_{1,2}$ are the position operator for each atom, illustrated in figure 1.4 (left schematic).

This dipolar approximation remains valid as long as the spatial extension of the two wave functions is smaller than the distance between the two atoms. This limit is called the Leroy

radius which is for instance 3.1 μm for the 100S Rydberg state of Rubidium 87. Below this limit, the initial pair is strongly mixed and mostly results in a molecular bound state or ionization.

This dipole-dipole potential has two effects on the initial Rydberg atoms: an attractive or repulsive potential between the two highly-excited atoms and a mixing between states via dipole operators. In the latter case, the transitions between different Rydberg states can be seen as a chemical process $n_1 + n_2 \rightarrow n_3 + n_4$ with an energy budget $\Delta = E_3 + E_4 - E_2 - E_1$. If this energy cost is large compared to magnitude of the dipole-dipole potential, these transitions are unlikely to occur and the effective potential can be computed from perturbation theory:

$$\delta E \simeq C_6/R^6 \quad (1.34)$$

where the first order correction vanishes due to the odd parity of the dipole operators. The effective interaction between two Rydberg atoms is then given by a van der Waals potential with a C_6 coefficient taking into account all the final pair states:

$$C_6 = \frac{1}{(4\pi\epsilon_0)^2} \sum_{r_3, r_4} \frac{|\langle r_3 | \hat{\mu}_1 | r_1 \rangle \langle r_4 | \hat{\mu}_2 | r_2 \rangle - 3 \langle r_3 | \hat{\mu}_1 \cdot \hat{\mathbf{u}} | r_1 \rangle \langle r_4 | \hat{\mu}_2 \cdot \hat{\mathbf{u}} | r_2 \rangle|^2}{E_1 + E_2 - E_3 - E_4} \quad (1.35)$$

where $\hat{\mathbf{u}} = \hat{\mathbf{R}}/\|\hat{\mathbf{R}}\|$. Consequently, the sign of the C_6 coefficient is set by the contributions from the closest pair states. To shorten the previous expression, a given Rydberg state $|r\rangle$ implicitly refers to the set of quantum numbers: n, l, j, m_j . The complete energy spectrum of the 50S Rydberg pair is shown in figure 1.4 as a function of the distance. The main contribution, in red, is indeed a van der Waals potential for a large interatomic distance while the short range energy spectrum is much more complex.

The energy spacing between closest states is typically $R_y n^{-3}$ while the order of magnitude for the dipole is $ea_0 n^{*2}$. As a result, the C_6 van der Waals coefficient varies drastically with the principal quantum number and an order of magnitude for this coefficient is:

$$C_6 \simeq \frac{e^4 a_0^4}{(4\pi\epsilon_0)^2 R_y} n^{*11} \quad (1.36)$$

For $n = 100$, this naive calculation gives a ~ 2 MHz frequency shift for a 10 μm separation between the two atoms. As a comparison, a more rigorous derivation for the 100S Rydberg state of Rubidium 87 yields a 56 MHz frequency shift at a distance of 10 μm. This difference comes from two factors. First, when the pair is close to a resonance, called Förster resonance, the interaction strength is drastically enhanced. Note that close to such a resonance, the interaction between Rydberg atoms can be further increased by the use of an external static electric fields to bring the missing energy Δ to the Rydberg pair in order to directly benefit from the dipole interaction \hat{V} instead of the Van der Waals potential [43, 97]. On the other end, the C_6 coefficient is the result of an interference between several contributions that can either be rather constructive, leading to an increase of this coefficient, or can sometimes almost cancel the interaction strength.

In 2013, Béguin *et al.* performed a direct measurement of this van der Waals potential with two atoms trapped in optical tweezers [98]. They were able to measure the energy shift between two Rydberg atoms as a function of the distance between the two dipole traps, and estimated the value of the C_6 coefficient.

To conclude on Rydberg atoms, the main scaling of their properties, with respect to the principal quantum number, are summarized in table 1.1.

Energy from ground state	n^{*-2}
Lifetime (0K)	n^*3
Radius	n^{*2}
Dipole from a low-excited state (d)	$n^{*-3/2}$
Dipole moment (μ)	n^{*2}
Polarizability (α_0)	n^{*7}
Van der Waals coefficient (C_6)	n^{*11}

Table 1.1: Scaling for low-momentum Rydberg atoms.

1.2.2 Electromagnetically induced transparency

In the first section, we derived the Hamiltonian describing the collective strong coupling between two-level atoms and a resonator. We now push this approach one step further by considering the coupling to a Rydberg state via a control beam. In this case, the system is addressed in an electromagnetically induced transparency (EIT) scheme that enables us to restore the transmission in a narrow window of the atom-cavity spectrum. In this way, Rydberg excitations are mapped onto photons inside the resonator and offer a mechanism to achieve strong nonlinearities with our platform, as will be discussed later on.

Free space and dark state of the Hamiltonian

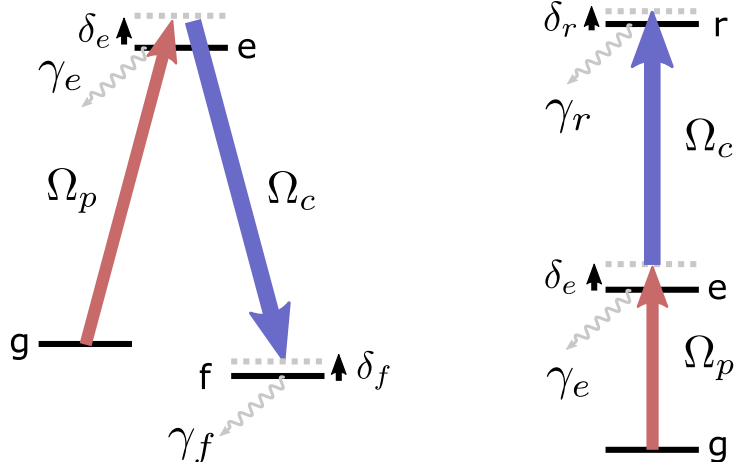


Figure 1.5: Electromagnetically induced transparency. Excitation schemes for electromagnetically induced transparency: a lambda configuration to a third state $|f\rangle$ (left) or a ladder excitation scheme via a Rydberg state $|r\rangle$ (right).

We start by considering a free space configuration with one atom to understand the basic process involved in electromagnetically induced transparency. We now describe this atom as a three-level system made of a ground state $|g\rangle$, an excited state $|e\rangle$ and a Rydberg state $|r\rangle$. Most of the time, EIT is described with a third state in one of the ground state of the atom, in a lambda excitation scheme as shown in figure 1.5 (left). For instance, the first demonstration of this technique was performed in this configuration by Boller *et al.* [39]. Since Rydberg atoms feature a long lifetime compared to the intermediate state, it is also possible to implement EIT in a ladder excitation scheme. This ladder EIT with Rydberg atoms was first obtained by Mohapatra *et al.* and used as a non-destructive probe for the detection of Rydberg states [99]. In both cases, a weak coherent probe is sent to address the $|g\rangle$ to $|e\rangle$ transition while a strong field, called control field, is set between $|e\rangle$ and $|r\rangle$ states.

The Hamiltonian of the system, in the rotating frame, is then:

$$\hat{H}_{\text{FS}}/\hbar = -\delta_p \hat{\sigma}_{ee} - \delta_c \hat{\sigma}_{rr} + \frac{\Omega_p}{2} (\hat{\sigma}_{eg} + \hat{\sigma}_{ge}) + \frac{\Omega}{2} (\hat{\sigma}_{re} + \hat{\sigma}_{er}) \quad (1.37)$$

where the notations follow what was defined in the first section: $\hbar\omega_r$ is the energy for the state $|r\rangle$, $\hbar\omega_e$ for the state $|e\rangle$, Ω_p is the Rabi frequency of the probe at a frequency ω addressing the ground-intermediate transition while Ω is the Rabi frequency for a beam at a frequency ω_c driving the $|e\rangle \rightarrow |r\rangle$ transition (called control beam), $\delta_e = \omega - \omega_e$ and $\delta_c = \omega_c + \omega - \omega_r$.

When the two-photon detuning is zero ($\delta_r = 0$), this Hamiltonian features a zero-energy eigenstate:

$$|d\rangle = \cos(\theta) |g\rangle + \sin(\theta) |r\rangle \quad (1.38)$$

where $\tan \theta = -\Omega_p/\Omega$. This corresponds to a dark state, uncoupled to the electromagnetic field. If the probe beam (Ω_p) is turned on adiabatically, the atom initially in the ground state is coherently transferred to this dark state without populating the intermediate state. In other words, the absorption of the $|g\rangle - |e\rangle$ transition is almost suppressed by this mechanism and a probe photon is subject to very low losses due to the coupling with the control beam.

Cavity spectrum with EIT

We now describe the phenomenon of electromagnetically induced transparency in a cavity, with an atomic ensemble and taking into account the decoherence from the excited state and the Rydberg state.

We want to compute the cavity spectrum with the excited state $|e\rangle$ coupled to a third state $|r\rangle$ at a Rabi frequency Ω . We already have all the ingredients for this derivation, we start from equation 1.16 and add the coupling term to the Rydberg state for each atom in the rotating frame:

$$\hat{H}_c/\hbar = \sum_n^N -\delta_r \hat{\sigma}_{rr}^{(n)} + \frac{\Omega^{(n)}}{2} (\hat{\sigma}_{er}^{(n)} + \hat{\sigma}_{re}^{(n)}) \quad (1.39)$$

The full Hamiltonian is then $\hat{H}_{\text{EIT}} = \hat{H}_c + \hat{H}_{\text{cloud}} + \hat{H}_a$, where \hat{H}_{cloud} was introduced in equation 1.18 and \hat{H}_a in equation 1.13. Finally, we take into account the finite lifetime of the n^{th} atom in the state $|r\rangle$ via the following Lindblad operator: $\hat{L}_c^{(n)} = \sqrt{2\gamma_r} \hat{\sigma}_{gr}^{(n)}$. The complete dynamics of the system is then:

$$\hbar \frac{d\hat{\rho}}{dt} = i[\hat{\rho}, \hat{H}_{\text{EIT}}] + \mathcal{D}[\hat{L}_a](\hat{\rho}) + \sum_n (\mathcal{D}[\hat{L}_c^{(n)}](\hat{\rho}) + \mathcal{D}[\hat{L}_e^{(n)}](\hat{\rho})) \quad (1.40)$$

The derivation now consists in reproducing the steps followed in equation 1.24. We use the collective operator \hat{P} that was defined in equation 1.25 and we introduce a second operator \hat{S} between the ground and Rydberg states:

$$\hat{S} = \frac{1}{g\Omega} \sum_n g_0^{(n)} \Omega^{(n)} \sigma_{gr}^{(n)} \quad (1.41)$$

where $\Omega^2 = 1/g^2 \sum_n (g_0^{(n)} \Omega^{(n)})^2$ is the effective control Rabi frequency.

Again, we assume a small coherent feeding rate in order to neglect the population of both the excited and the Rydberg state compared to the ground state population. In this approximation, we can neglect the contribution of the correlation term $\langle \hat{a} \hat{\sigma}_{er}^{(n)} \rangle \simeq 0$ since it is at least proportional to α^2 . This correlator is for instance responsible for nonlinearities at

high input rates [100]. These approximations result in very simple steady states equations:

$$\begin{aligned}\langle \hat{a} \rangle &= \frac{1}{\delta_a + i\kappa} \left(i\alpha\sqrt{2\kappa_0} + g\langle \hat{P} \rangle \right) \\ \langle \hat{P} \rangle &= \frac{1}{\delta_e + i\gamma} \left(g\langle \hat{a} \rangle + \frac{\Omega}{2}\langle \hat{S} \rangle \right) \\ \langle \hat{S} \rangle &= \frac{\Omega}{2(\delta_r + i\gamma_r)} \left(\langle \hat{P} \rangle + \sum_n \frac{g_0^{(n)}(\Omega^{(n)2} - \Omega^2)}{g\Omega^2} \langle \hat{\sigma}_{ge}^{(n)} \rangle \right)\end{aligned}\quad (1.42)$$

The last term of the third equation describes the coupling out of the “symmetric” Dicke states. This effect is induced by the inhomogeneities of the control beam and will be discussed later, for now we will assume that the field is homogeneous all over the atomic sample.

This approximation on the last equation allows to compute the mean value of the collective operator \hat{P} with respect to the cavity photon field:

$$\langle \hat{P} \rangle = \frac{g}{\delta_e + i\gamma - \frac{\Omega^2}{4(\delta_r + i\gamma_r)}} \langle \hat{a} \rangle \quad (1.43)$$

At $\delta_r = 0$, the modulus of this term reaches its minimal value. On top of this, if we assume that $\Omega^2/\gamma_r \gg \gamma, g$, we get $\langle \hat{P} \rangle / \langle \hat{a} \rangle \simeq 0$. Concretely, it corresponds to the drop of absorption between the ground and the excited state induced by the coupling to a Rydberg state. In this limit, the intra-cavity field is almost equivalent to the empty cavity case ($g = 0$) and we recover the transparency window discussed in free space.

We can again compute the transmission of the resonator (normalized by the empty cavity transmission):

$$\mathcal{T} = \left| \delta_a/\kappa + i - \frac{2C}{\delta_e/\gamma + i - \frac{B}{\delta_r/\gamma_r + i}} \right|^{-2} \quad (1.44)$$

where $B = \Omega^2/(4\gamma\gamma_r)$ is a cooperativity-like parameter to characterize the control driving strength. This is again a comparison between the coupling Ω and the damping of the system given by two coupled states (γ_r, γ). The transmission on resonance ($\delta_e = \delta_r = \delta_a = 0$) has then a simple expression:

$$\mathcal{T}_0 = \left| 1 + \frac{2C}{1 + B} \right|^{-2} \quad (1.45)$$

Since we recover the empty cavity mode for $B \rightarrow +\infty$, the transparency window is limited by the linewidth of the cavity mode set by κ .

Rydberg polaritons

Let us assume that the cavity mode is adjusted on one of the atomic resonance $\delta_a = \delta_e$ and that the control beam is also resonant with the intermediate-Rydberg transition such that $\delta_a = \delta_r = \delta$ (dissipative regime). In this case, and if further assume that $B \gg 1$, one recovers a Lorentzian for the transparency window:

$$\mathcal{T}_{\text{EIT}} = \mathcal{T}_0 \frac{1}{(\delta/\gamma_{\text{EIT}})^2 + 1} \quad (1.46)$$

where the transparency linewidth is:

$$\gamma_{\text{EIT}} = \frac{1 + \frac{2C}{B}}{\frac{1}{\kappa} + \frac{2C}{B\gamma_r} \frac{1}{\gamma_r}} \quad (1.47)$$

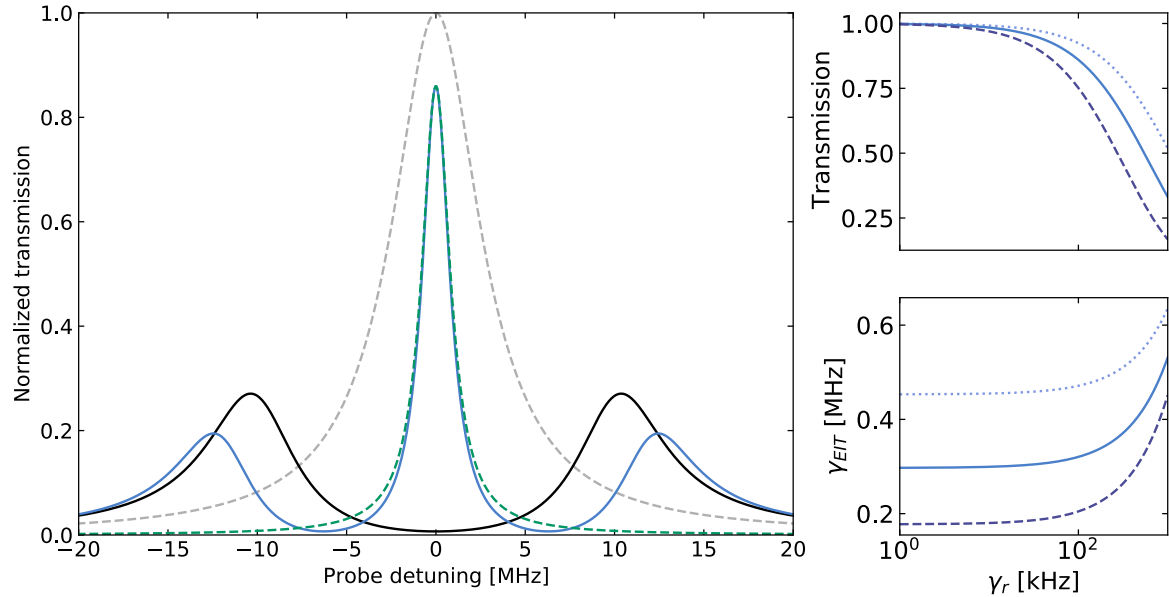


Figure 1.6: Electromagnetically induced transparency. Left- Transmission cavity spectra with $\gamma = \kappa = 2\pi \times 3 \text{ MHz}$, $\gamma_r = 2\pi \times 0.1 \text{ MHz}$, $\Omega = 2\pi \times 13 \text{ MHz}$, $g = 2\pi \times 10 \text{ MHz}$ and $\omega_a - \omega_e = 0$, $\omega_a + \omega' - \omega_e - \omega_r = 0$. The EIT window is shown in blue, the vacuum Rabi splitting spectrum in black, the bare cavity resonance in grey (dashed line) while the Lorentzian approximation for the EIT transmission peak is plotted in green. Right- Transmission at resonance (top) and EIT linewidth (γ_{EIT} , bottom) as a function of γ_r for: the configuration on the left (solid line), $B/2$ (dotted) and $2 \times C$ (dashed).

One finds that $\gamma_{\text{EIT}} \simeq \kappa$ when $B \gg C$ and $\gamma_{\text{EIT}} \simeq \gamma_r$ in the other limit $C \gg B$. This discussion could be extended to the dispersive regime for a non-zero detuning between the cavity mode and the intermediate state, we do not discuss it further as this work focuses on the dissipative regime.

The dark state of the atom-cavity Hamiltonian is given by the creation operator:

$$\hat{D}^\dagger = \cos \theta \hat{a}^\dagger + \sin \theta \hat{S}^\dagger \quad (1.48)$$

where $\tan(\theta) = -2g/\Omega$. This dark state is therefore a polariton: an hybridization between a cavity photon and an atomic excitation. As a result, this quasiparticle inherits the properties of light and matter. For instance, the effective field decay rate of this dark polariton is given by the EIT window 1.47, that can be rewritten as:

$$\gamma_{\text{EIT}} = \kappa \cos^2 \theta + \gamma_r \sin^2 \theta \quad (1.49)$$

and the polariton lifetime is $\tau = 1/(2\gamma_{\text{EIT}})$.

This linewidth is simply the probability to be a photon times the cavity decay rate plus the probability to be a Rydberg atom times its damping. The polariton damping rate, for the population, is then $2\gamma_{\text{EIT}}$. The same argument holds for the transparency level:

$$\mathcal{T}_0 = \kappa^2 \cos^4 \theta / \gamma_{\text{EIT}}^2 \quad (1.50)$$

corresponding to the ratio between the photonic rate and the dark polariton damping rate, squared. Notice that this narrow transparency window allows one to control the group velocity of a light pulse and this EIT mapping is employed to slow down light drastically or even to store it, see the review of Fleischhauer *et al.* on this topic [101].

Let us discuss now the role of the inhomogeneous terms in equation 38. This factor tends to couple the system out of the “symmetric” Dicke states and can therefore be seen as losses for the photons since this driving populates many “asymmetric” states. One way to understand this is to look at the population in the Rydberg states on resonance when $B \gg 1$:

$$\sum_n \langle \hat{\sigma}_{rr}^{(n)} \rangle = \frac{8\alpha^2\kappa_0}{\kappa^2} \frac{g^2}{N} \sum_n \frac{1}{\Omega^{(n)2}}. \quad (1.51)$$

which is minimal when $\Omega^{(n)}$ is homogeneous since $1/x$ is convex. This simple argument reveals an increase of the Rydberg population compared to the homogeneous case and since the number of “asymmetric” states is huge with respect to “symmetric” ones, these excitations are somehow stuck in the atomic ensemble and are not recovered as a coherent photon at the output. This motivates us to work with a control field homogeneous over the atomic ensemble in order to suppress, or at least to significantly reduce this leakage.

The transmission spectrum of the cavity is plotted on the left panel in figure 1.6. We took realistic parameters close to what we expect to observe in our experiment. In this configuration we reach a quite high transparency, at $> 80\%$ of the empty cavity mode. This spectrum also reveals the light shift of the two vacuum-Rabi modes induced by the presence of the control beam, resulting in an effective coupling factor $g_{\text{eff}} = \sqrt{g^2 + \Omega^2/4}$. This shift is useful to estimate the effective Ω in our experiments. Finally, our dark polaritons are characterized by two quantities: the EIT linewidth and the transparency level. The two are plotted as a function of the Rydberg damping rate to illustrate the crucial role played by this parameter on the polaritons, everything else remaining constant. It seems that working with a linewidth below 100 kHz is sufficient to achieve a high transparency.

1.2.3 Photon-photon interactions

With the mechanism of electromagnetically induced transparency, we have an efficient way to transfer Rydberg properties onto photons. One illustration of this is the reduced damping rate of Rydberg polaritons compared to bare cavity photons, originating from the long lifetime of Rydberg states. We go one step further by discussing the consequences of the van der Waals interactions and several approaches to achieve interactions between optical photons.

Rydberg blockade

As discussed at the beginning of this section, Rydberg atoms are characterized by strong, long-range, dipole-dipole interactions. When atoms are sufficiently separated from each other, i.e. no overlap between the two wave functions, the dipole-dipole interaction is simply given by a van der Waals potential $V(R) = C_6/R^6$, where R is the distance between the two atoms. In this case, the energy required to excite the two atoms toward their Rydberg state is shifted by the interaction potential $V(R)$. Of course this additional energy fades away at long distances and the system becomes linear. The question that naturally arises is: when does this potential have significant consequences on the energy spectrum? If one imagines that the atoms are directly excited by a laser from the ground to the Rydberg state, with a Rabi frequency Ω , it will not be possible to excite both atoms at the same time if the energy shift due to the interactions is larger than the broadening induced by the driving⁽⁴⁾: Ω . This is illustrated in figure 1.7 and the limit is therefore given by $R_B = (C_6/\Omega)^{-1/6}$. In practice this distance can be quite large: if we suppose a driving with a Rabi frequency of $\Omega = 2\pi \times 1 \text{ MHz}$ for the 100S Rydberg state, this separation is then $R_B = 20 \mu\text{m}$. At smaller

⁽⁴⁾It is assumed here that the linewidth is dominated by the Rabi frequency, ultimately the limit is given by the linewidth of the Rydberg state $2\gamma_r$

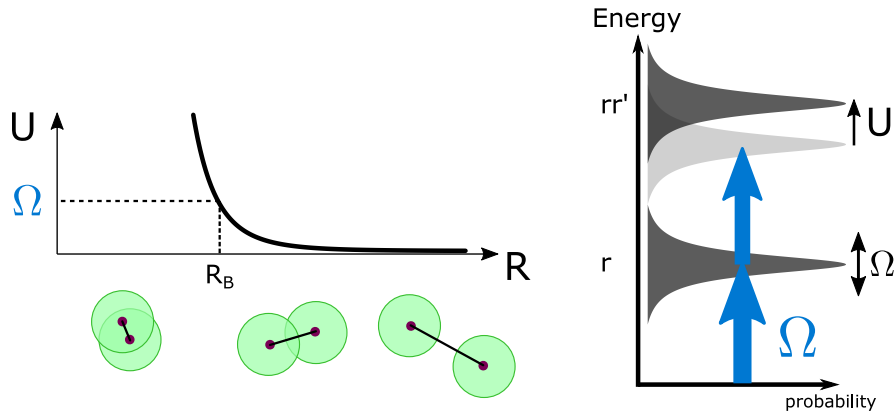


Figure 1.7: Rydberg Blockade. Left- The van der Waals potential as a function of the distance between two Rydberg atoms. When the separation between the two atoms R is smaller than the blockade radius R_B , the system is dominated by interactions. Right- Spectrum of the two atoms for a driving at a Rabi frequency Ω between the ground and the Rydberg state. The van der Waals interaction shifts the energy of the pair, resulting in a blockade of the driving if $U > \Omega$.

distances the van der Waals interaction increases monotonously, which allows one to define a blockade volume [102, 103] around a Rydberg excitation, of radius R_b , where it is not possible to drive another atom in a Rydberg state.

This Rydberg blockade was demonstrated by Gaëtan *et al.* [104] and Urban *et al.* [105] more than ten years ago and it is now one of the building blocks for quantum simulation with atomic arrays [81]. When this scheme is implemented with an atomic ensemble smaller than the blockade radius, the atomic cloud can be described as a single two-level system called a Rydberg superatom, made of a ground state and one collective Rydberg excitation. This was first highlighted by Dudin *et al.* [106], through the observation of collective Rabi oscillations.

EIT with interacting Rydberg atoms

The Rydberg EIT scheme that we discussed earlier in this chapter allows to transiently convert a photon into a Rydberg excitation. With this mapping, the Rydberg blockade mechanism can be transposed into a photon blockade, see figure 1.8. In this case, the propagation of a Rydberg polariton through an atomic ensemble can prevent the hybridization of other photons because of the van der Waals interactions, resulting in their absorption in the dissipative regime. It is then necessary to have an optically dense atomic ensemble to obtain a probability of absorption close to 1 in the absence of EIT, and of course to work with an atomic cloud smaller than the blockade radius in order to reach a nonlinearity at the single-excitation level. In this framework, the relevant energy for the blockade volume is given by the linewidth of the Rydberg polariton Γ_{EIT} and thus the radius is $R_B = (C_6/\Gamma_{EIT})^{1/6}$.

This photon blockade mechanism is a very successful method to achieve strong interactions between photons, many groups obtained this photon blockade in free space and observed a strong photon antibunching in transmission [40, 41, 97, 107]. Other implementations of this photon blockade allowed experimentalists to realize single-photon switches, or transistors [42, 44].

Other nonlinearities can be accessed by working in the dispersive regime. In this case, the probe photons are off resonant with respect to the ground-intermediate transitions and the interactions causes a change of the group index of the medium. This results in attractive interactions between photon [45] or even photonic molecules [46]. One of the concern in these

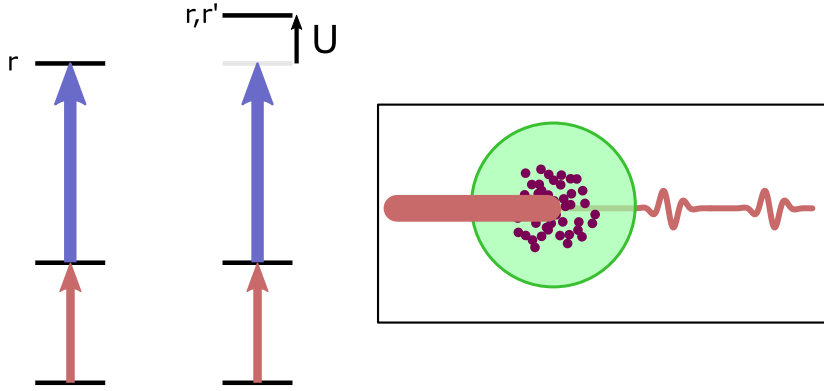


Figure 1.8: EIT with Rydberg blockade. Left- Electromagnetically-induced transparency when interactions are taken into account. The control field (in blue) induces a transparency window for a single photon (red) but the mixing of a second excitation is impossible because of the van der Waals interaction U . Right- For a dense atomic ensemble (dots), smaller than the blockade volume (green sphere), only single photons (red) are transmitted in the dissipative regime.

approaches is to keep strong interactions, requiring to work close to resonance, which induces significant losses.

In principle, one can also use this change of dispersion to achieve low-loss interactions via a phase shift between photons. If this phase shift reaches π , this allows the implementation of a controlled-phase gate:

$$\begin{aligned} |00\rangle &\rightarrow +|00\rangle \\ |01\rangle &\rightarrow +|01\rangle \\ |10\rangle &\rightarrow +|10\rangle \\ |11\rangle &\rightarrow -|11\rangle \end{aligned} \quad (1.52)$$

where $|a, b\rangle$ is the state for a first photon in the Fock state $|a\rangle$ and a second one in the Fock state $|b\rangle$.

The phenomenon at stake can be understood by looking at the susceptibility of the medium with EIT [49]:

$$\chi \propto N \left(i\gamma + \delta_e - \frac{\Omega^2}{4(i\gamma_r + \delta_r)} \right)^{-1} \quad (1.53)$$

It is clear from this equation that in the dissipative regime $\delta_e \gg 1$, one could in principle make the absorption negligible ($\text{Im}\{\chi\} \propto 1/\delta_e^2$) in front of the dispersion ($\text{Re}\{\chi\} \propto 1/\delta_e$) but this inevitably reduces the magnitude of phase shift. The only option to reach a π phase shift is then to rise the atomic density per blockade volume (N). Unfortunately, there is a fundamental limit for the density, that originates from the typical size of Rydberg atoms ($\sim 1 \mu\text{m}$). Beyond a $\sim 1 \mu\text{m}^{-3}$ density, the probability to have a ground state atom lying in between the core and the outer electron of a Rydberg atom is no longer negligible, resulting in ionization and molecular bound states that are detrimental to this kind of protocols, see the study of Pfau and his team [48, 108]. For instance, the team of Gerhard Rempe demonstrated a π phase shift between single-photon pulses [47] and implemented a first Rydberg-based phase gate but at the cost of a post-selection upon survival of both photons, only happening with a probability on the order of 1% [109]. Because of the physical limit associated to the atomic density, it seems difficult to obtain efficient conservative interactions with this free space method.

Photon blockade in a cavity

We briefly expose the benefits of using a medium finesse resonator compared to the free space approach in order to achieve unitary operations between optical photons. When the photon blockade mechanism is operating inside a resonator, it is possible to convert the dissipation into a dispersive response for photons. In order to get a low-loss nonlinearity with a cavity, it is essential to extract as efficiently as possible photons out of the resonator. This constraint motivates the use of a single-ended resonator, where light is injected and collected from the same coupler with a transmission much more important than the others mirrors. The output field in reflection is then the interference between the field directly reflected off from the coupler and the intra-cavity field escaping from the resonator. This can be understood quite simply by looking at the cavity as a folded beam splitter where one of the output channels is reinjected through one of the input modes, see figure 1.9. One can understand this effect classically; the output field is then: $E_{out} = tE_{cav} - rE_{in}$, with $|t|^2 \ll 1$. The absorption from an atomic ensemble can be seen as an attenuation factor (Beer-Lambert law) for the electric field. This is equivalent to what we did when we introduced mirror losses during the derivation of the cavity spectrum, section 1.1. As a consequence, the intra-cavity field is identical, up to a change in the cavity losses $L' = L + OD$, where $OD = kl|\text{Im}\{\chi\}|$ is the optical depth of the atomic ensemble. For a single-ended resonator it is convenient to distinguish the transmission of the input/output mirror t^2 , what we collect from the cavity, from the other sources of losses $L'_0 = OD + L_0$ such that the total losses are $L' = L'_0 + t^2$. In this case, the output field is simply:

$$E_{out} \simeq \frac{t^2 - L'_0}{t^2 + L'_0} E_{in} \quad (1.54)$$

If the transmission of the first mirror is well above the losses L_0 , one has $L'_0 \simeq OD$. From this equation, we see that it is possible to obtain a π phase shift when the threshold $OD = t^2$ is crossed.

This is precisely what our approach provides: the EIT mapping allows for a low-loss propagation of photons ($OD_{\text{EIT}} \ll t^2$) that should lead to an output field close to E_{in} , while the blockade in the dissipative regime brings a strong absorption that can flip the sign of the electric field with a high-reflectivity level if $OD_B \gg t^2$, as depicted in figure 1.9. In this method, as long as $t^2 \gg L_0$, the density limit is not a problem since we are free to choose the value of the transmission parameter to obtain an efficient reflectivity in both regimes.

One can compute the reflectivity spectrum of the resonator with linear EIT from the optical Bloch equations (1.40), in the same vein as the transmission, to recover the result discussed here with classical physics:

$$\mathcal{R}(\delta) = \left| -1 + \frac{i2\kappa_0}{\delta + i\kappa - g^2/(\delta + i\gamma - \frac{\Omega^2}{4(\delta+i\gamma_r)})} \right|^2 \quad (1.55)$$

where the reflectivity on resonance is simply $\mathcal{R}_0 = |-1 + 2\sqrt{\mathcal{T}_0}T/L|^2$, while the reflection coefficient on resonance is:

$$r_0 = -1 + 2\sqrt{\mathcal{T}_0}T/L \quad (1.56)$$

One sees that if the transparency drops to zero then $r_0 \simeq 1$, while it is possible to reach $r_0 \simeq -1$ for a high transparency. Quantitatively, the role of mirrors losses and the precise choice of the transmission parameter will be addressed during the presentation of our resonator in chapter 2.

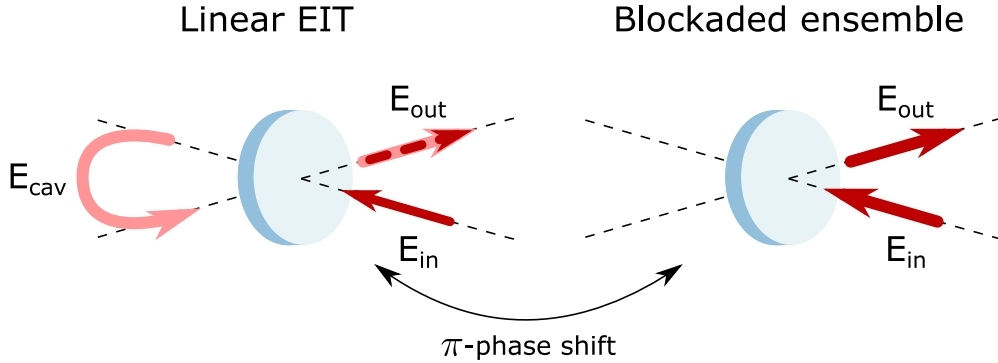


Figure 1.9: π phase shift with a cavity. A single-ended resonator can be seen as a folded beam splitter. The output field E_{out} is therefore the interference between the field directly reflected on the plate and the transmitted intra-cavity field. Left- In the linear EIT regime, light can propagate through the resonator via the transparency window with low optical losses. In this case the output field is $+E_{in}$. Right- When a Rydberg polariton is present inside the resonator, the intra-cavity is close to zero and the output field is then $-E_{in}$ yielding a π phase shift.

In the regime where the size of the atomic ensemble is smaller than the blockade volume, the atomic cloud can be described as a Rydberg superatom. If the interaction energy shift is very large compared to the other energy scales, the description of our system is greatly simplified as one can assume two Rydberg excitations are energetically impossible and thus $(\hat{S}^\dagger)^2 = 0$. Then, $\hat{S}^\dagger = |R\rangle \langle G|$ where $|R\rangle = 1/g \sum_n g_0^{(n)} |g, \dots, r_n, \dots, g\rangle$ is the collective single Rydberg state introduced in equation 1.22. For a small excitation number, one can rewrite the Hamiltonian \hat{H}_{EIT} with collective operators only [110]:

$$\begin{aligned} H_{\text{EIT}} \simeq & -\delta_a \hat{a}^\dagger \hat{a} - \delta_e \hat{P}^\dagger \hat{P} - \delta_r |R\rangle \langle R| + \frac{\Omega}{2} (|R\rangle \langle G| \hat{P} + |G\rangle \langle R| \hat{P}^\dagger) \\ & + g (\hat{P}^\dagger \hat{a} + \hat{P} \hat{a}^\dagger) + i\sqrt{2\kappa_0}\alpha(\hat{a}^\dagger - \hat{a}) \end{aligned} \quad (1.57)$$

We showed that the EIT Hamiltonian has a dark state in the linear regime. When at most one photon is injected inside the resonator, the system remains linear and the polariton propagates through the resonator. On the contrary, if the Rydberg state $|R\rangle$ is already populated, this Hamiltonian becomes equivalent to the vacuum Rabi splitting Hamiltonian, equation 1.24, and the intra-cavity field almost vanishes on resonance. Several theoretical models were developed for the free space approach [111–113] using a propagative description that is not appropriate for a cavity. In order to describe the system beyond two excitations, Grankin *et al.* developed tools to compute correlations and squeezing factors for Rydberg blockade in cavity [114–116].

One of the technical challenges in this Rydberg-based approach is the scaling of the parameters with respect to the principal quantum number n : strengthening the interaction is possible by increasing n ($C_6 \propto n^{*11}$) but it also reduces the magnitude of the transition dipole moment ($d \propto n^{*-3/2}$). On the other hand, the control beam has to be homogeneous over the atomic ensemble, as we pointed out in the previous subsection, which rules out the option of a strong focus to gain in intensity. This motivated us to integrate build-up cavities in the experimental platform to address $n \simeq 100$ Rydberg states with the control beam while maintaining a high transparency level. The apparatus and especially these cavities are presented in more detail in chapter 2.

It is also important to note that the nonlinearity is lost when the control Rabi frequency is large compared to all other parameters. For a finite interaction strength, the interaction energy between two polaritons is given by the van der Waals potential re-scaled by the

probability to have the two polaritons in the Rydberg state:

$$U_{\text{eff}} \simeq V_{vdW} \sin^4 \theta \quad (1.58)$$

This precludes the naive idea of using a very high control Rabi frequency to reach a high transparency level (equation 1.50), because the population in the Rydberg state ($\sin^2 \theta$) is zero in this limit. The Rydberg linewidth γ_r is a crucial parameter that cannot be fully compensated by the control frequency, while maintaining strong optical nonlinearities.

The strong interactions at the single-polariton level will first be stressed in chapter 5, where we will show a saturation of the transmission at half an excitation by continuously driving the atom-cavity system, but also the strong photon antibunching achieved in transmission. This is precisely what Jonathan Simon and his team observed with Rydberg blockade in cavity a few years ago [57]. One of the interesting feature of the Rydberg superatom is obviously its collective coupling with the resonator that is increased by a factor \sqrt{N} . If we make the parallel with single-atom cavity QED experiments, this approach allows to reduce the mode volume constraint and more importantly to only use a medium-finesse resonator. While moving over the chapters, we will discuss others properties of the superatom. For instance, we will see in chapter 7 the coherent control of this Rydberg superatom as initially demonstrated by Dudin *et al.* [106] with a collective enhancement of the Rabi frequency.

Conclusion

This chapter described the general ideas behind our new project in order to obtain photon-photon interactions with an atomic cloud strongly coupled to a medium-finesse resonator. Along this presentation, we stressed the critical role of several parameters to achieve strong and efficient interactions.

First of all, we discussed the high sensitivity of Rydberg states to stray electrical fields. The design of this new platform takes this constraint into account, by keeping surfaces at a few centimeters from the atomic ensemble and by using eight electrodes for the compensation of electric fields. We also briefly exposed some arguments to obtain a π phase shift between optical photons with a single-ended resonator. We continue this discussion in chapter 2 to justify the design of our optical cavity.

The drawback of working with huge principal quantum numbers is the decrease of the dipole strength for the coupling to the Rydberg states with a control beam. The only way to compensate for this loss is to work with a very intense laser beam for this driving. Our solution to this problem is to use buil-up resonators inside the vacuum enclosure to increase this intensity. The geometry and performance of these cavities are discussed in the next chapter.

Of course, we need a Rydberg blockade radius larger than the atomic ensemble to reach strong interactions between optical photons. We aim to couple our atom-cavity system to $n \sim 100$ Rydberg states to achieve blockade radius of the order of $20 \mu\text{m}$. For this purpose, we present the preparation of a $\sim 10 \mu\text{m}$ -radius atomic ensemble in chapter 3.

We also insisted on the importance of keeping the Rydberg linewidth as small as possible. To this end, several sources of noise have to be controlled to some extent. We already mentioned the role of electric fields but the linewidth of our lasers and the temperature of the atomic cloud are other relevant examples. We discuss the cooling steps in chapter 3, whereas we give an estimation of the effective Rydberg linewidth in chapter 5.

Chapter 2

Experimental setup

Contents

2.1 Experimental platform	32
Ultra-high vacuum	33
Assembly and overview	33
2.1.1 Science cavity	35
Reflectivity of the cavity	36
Optical modes of a twisted cavity	38
Cavity length locking	40
2.1.2 Build-up cavities	41
Confocal cavities	41
Presentation of the two resonators	42
Build-up factors	43
2.2 Laser bench	44
2.2.1 Lasers	44
DL pro and TA pro	44
Titanium-Sapphire Laser and External Cavity Doubler	45
High Power 1064 nm fiber laser	46
2.2.2 Frequency locking chain	46
Methods	47
Ultra-stable cavity and Transfer cavity	48
2.2.3 Optical modulator: frequency control and switch	49
2.3 Control setup	51
2.3.1 Hardware	51
2.3.2 Software	52

In this chapter, we go into the details of the experimental platform and the technical means employed to perform experiments with Rydberg atoms in an optical cavity, as it was introduced in chapter 1. The atomic source and atomic setup are discussed in more detail in the next chapter.

The first section is devoted to the components of the main vacuum chamber. We start by a description of the protocol used for the assembly of the experimental platform and discuss the main constraints for this new apparatus: vacuum quality, electric field control, versatility. We then focus on our science cavity and present several aspects of the resonator, for instance its geometry or its reflectivity. Then, we introduce the build-up cavities for the amplification of control beams (474-480 nm) with the aim to improve Rydberg electromagnetically induced transparency as explained in chapter 1.

The following section describes our lasers and the locking chain that we employ to stabilize the frequency of our cavities and lasers. This is an important step to precisely address Rydberg atoms because of their narrow spectral linewidth, about a few kilohertz.

In the last section of this chapter, we give a brief overview of the control of this experiment. This part covers data acquisition, the control of the laser beams and our RF generators.

2.1 Experimental platform

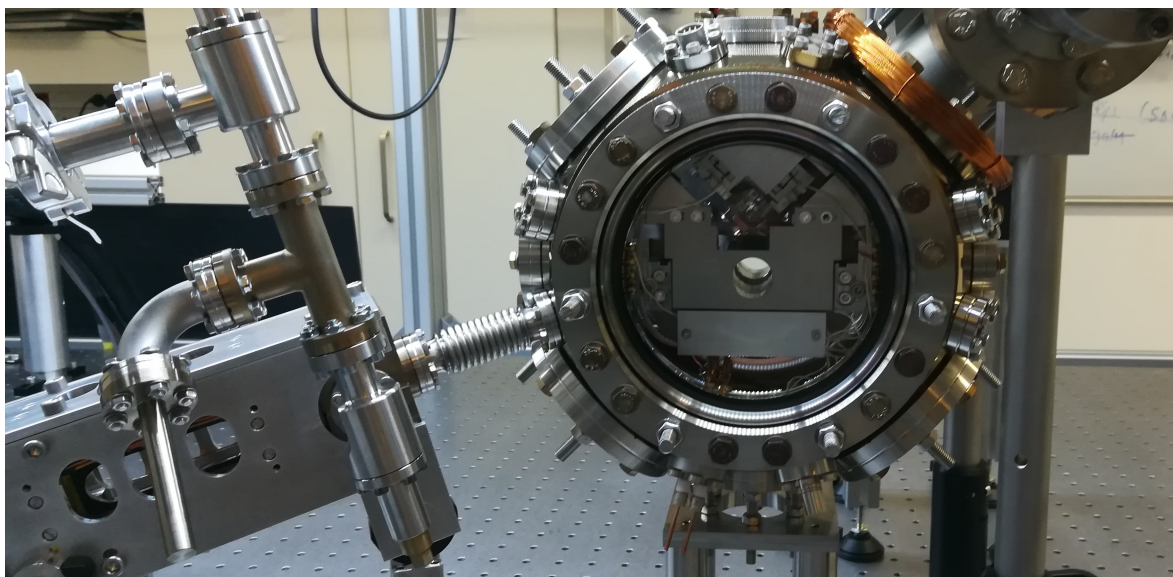


Figure 2.1: Rydberg vacuum chamber. The 2D MOT (our source of atoms, on the left) is linked to the main vacuum chamber (cylinder shaped) where experiments are carried out. The photography was taken right after the assembly; at that moment the platform was still at ambient pressure.

Cold atoms are impossible to observe at ambient pressure because of collisions with the hot surrounding gas. When building this kind of experiment, the very first issue is to reach an ultra-high vacuum regime (a pressure below 1×10^{-8} mbar) to significantly suppress collisions and increase the lifetime of the atomic cloud. The experiment is thus surrounded by a spherical square vacuum chamber made of stainless steel (316 L) with a 10 cm radius and a length of 15 cm⁽¹⁾, see figure 2.1. This vacuum enclosure is linked to an ion pump⁽²⁾ and a non-evaporable getter⁽³⁾ to maintain the pressure level. The chamber is also connected to the source of atoms, the two dimensional Magneto-optical trap (2DMOT) through a 1 mm radius hole. This geometry induces a differential pressure ratio of ~ 1000 between the two parts of the experiment and protects the vacuum inside the main chamber from the 2DMOT

⁽¹⁾MCF800M-SphSq-G2E4C4A16 from Kimball Physics

⁽²⁾Agilent VacIon Plus 55 Pump, 55L/s

⁽³⁾SAES CapaciTorr Z100

where the hot rubidium vapor is located. This section focuses on the inside of the main vacuum chamber. Before going into the details of the platform, it is worth mentioning that putting the overall system under high vacuum requires some precautions.

Ultra-high vacuum

In the low pressure regime, vacuum is limited by outgassing processes, hence the crucial character of the choice of materials [117]. This is well documented by the LIGO Scientific Collaboration: they tested a huge amount of materials for ultra-high vacuum and also gave their cleaning protocol for each component [118]. As an example, we give our cleaning process for one of the most sensitive materials inside the vacuum chamber:

Viton (synthetic rubber) : The first stage is a rough cleaning to remove most of the grease and oil with wipes. It is then repeated in a bath of hot water mixed with Liquinox detergent to help scrub surfaces. It is followed by an ultrasonic bath in Liquinox to remove inaccessible dirt. Viton parts are then put into a pressure cook with deionized water at a pressure of 2 bar during 2 hours. This cooking is repeated four times interspersed by a rinsing step with deionized water. The last step consists in a bake at a temperature of 120 °C during 48 hours, see figure 2.2. In practice, the bake was repeated until no deposits were visible in the test chamber. We cleaned parts with wipes and an ultrasonic bath before restarting a bake.

This protocol is adapted to each part, from electrical wires to the main vacuum chamber itself. The vacuum inside the chamber was achieved by a turbo pump coupled to a primary pump⁽⁴⁾ to go from ambient pressure to ultra-high vacuum. One final bake of the entire platform was carried out during 2 weeks to reach a pressure of 7.10^{-10} mbar inside the main vacuum chamber, which rose to the current level of 2.10^{-9} mbar after the rubidium ampoule was opened inside the 2DMOT. Once the desired pressure had been reached, an ion pump⁽⁵⁾ and a non-evaporable getter pump⁽⁶⁾ took over in the long term to avoid the important mechanical vibrations of the primary pump.

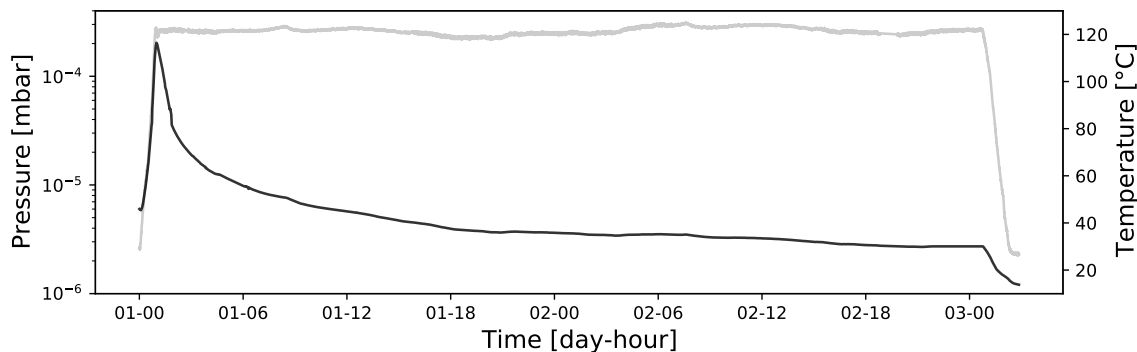


Figure 2.2: Bake of Viton. An example of baking during 48 hours with Viton parts. In black the pressure monitored by the turbo pump and in grey the temperature measured on the bake chamber with a thermo sensor. We observe a 6-fold decrease of the pressure after the bake.

Assembly and overview

The science platform can be split in three parts, from bottom to top: the magneto-optical trap coils support, the blue cavities holder and the science cavity support, see figure 2.3.

⁽⁴⁾Pfeiffer Pumping Station TSH 071E

⁽⁵⁾Agilent VacIon Plus 55 L/s

⁽⁶⁾SAES Getters CapaciTorr Z 100

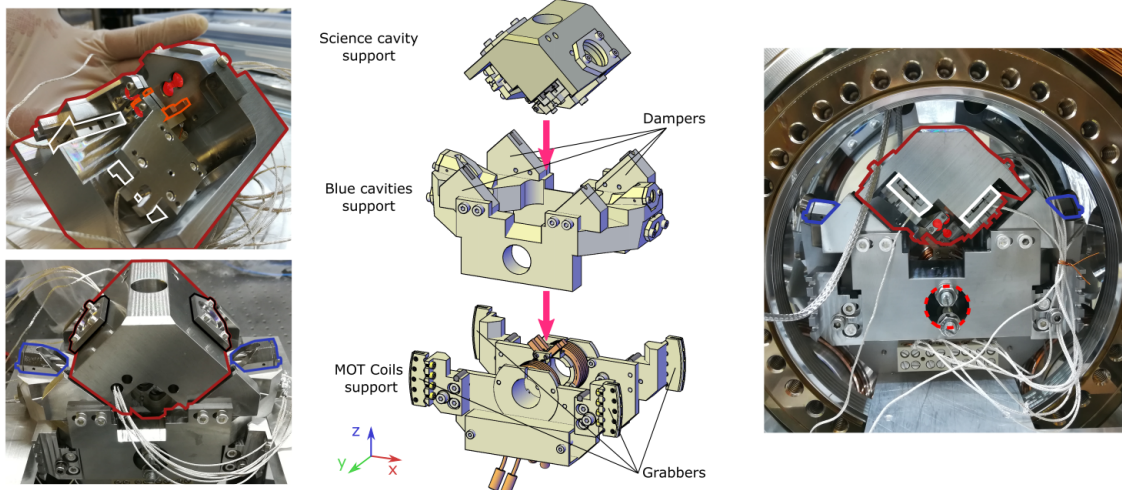


Figure 2.3: Platform assembly. Top left- Our science cavity and its four mirrors are in red, electrodes are circled in orange, translation stages and the science cavity support are respectively circled in white and red. Notice that in the top left image, our science cavity support is upside-down for alignment tests. Down left- On top of the science support, circled in red, two +50 mm achromatic lenses are attached, circled in black, and the two blue cavity high-reflectivity mirrors are circled in blue on their own support. Center - Drawings of the three parts, spaced for clarity. As described in the text, the science support lies on the build-up cavities supports via dampers and the whole is placed on the MOT coils support attached to the chamber. Right- The science platform inside the vacuum chamber, the dashed red circle is the entrance of the horizontal MOT beam where atoms are located before transport to the cavity.

These three supports are stacked one on top of the other separated by small Viton cylinders ($r=2$ mm, $l=10$ mm) to stabilize them. The Viton pieces ensure the thermal and mechanical isolation of the setup. The whole platform lies on the MOT coils support which is hung on the main vacuum chamber by four grabbers. Each support is made of stainless steel (316 L) to avoid magnetization as it is the case for the chamber itself.

The science cavity is a four mirror twisted resonator with a tunable geometry. The position of two mirrors can be adjusted independently by two translation stages (more about it subsection 2.1.1). Two 50 mm-focal aspheric lenses are attached on top of this support with a 0.20 numerical aperture⁽⁷⁾ in order to trap atoms in highly focused laser beams ($\approx 10 \mu\text{m}$) and to make a high resolution characterization of the cloud. For instance, the number of atoms or the temperature can be measured by means of the absorption imaging technique detailed in chapter 3, section 3.1.2.

The other main component of the setup is the pair of build-up cavities to amplify the power of our control beams to address Rydberg states at the science cavity level. The control of the size and position of the beam inside both resonators is made possible by the confocal geometry, see subsection 2.1.2. Steering of electrical components such as piezoelectric actuators for cavities or MOT coils are carried out by feedthroughs placed at the top and at the bottom of the vacuum chamber. Shielded wires were used and electrical connectors were insulated by a metal sheath to prevent the spread of electric fields. This is a critical parameter to control when dealing with high Rydberg states because of their high polarizability (equation 1.32). In addition, an aluminum electric shield was put in front of the mirror support containing piezoelectric actuators and 8 electrodes were placed in the middle of the science cavity to further control electrical fields during the experiment.

⁽⁷⁾Thorlabs AL2550H-B

2.1.1 Science cavity

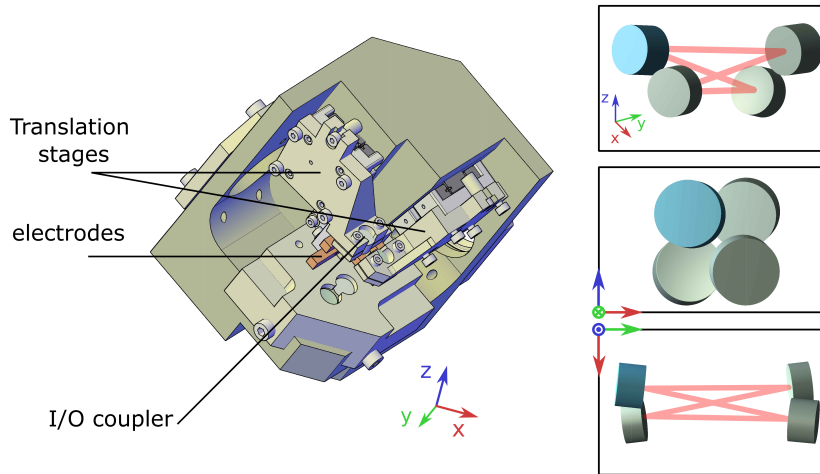


Figure 2.4: Twisted cavity. Left- Science cavity support. The four-mirror cavity is visible in the center of its support. Two mirrors are attached to two translation stages in order to adjust the length of the resonator and four electrodes are visible in the middle of the resonator to control stray electric fields. Right- Science cavity. The Input/Output mirror is tinted in light blue and high-reflectivity mirrors are colored in grey. Mirrors are approximately 21 mm apart along the y axis and the incident angle of light on a mirror is about 9.3° .

The science cavity is at the center of this Rydberg platform to shape interactions between optical photons. In the context of Rydberg blockade, at least two regimes are interesting to investigate. The first one converts dissipation inside the cavity into a photonic dispersive response outside of it. This effect translates into a nonlinear π phase shift for the interacting photons, as it was explained in chapter 1. The other regime corresponds to intra-cavity interactions where several excitations are propagating through the resonator. Both of them rely on the ability to have a beam size of the order of the blockade sphere or smaller inside the resonator. In practice, it is hard to go far beyond $n = 100$ for the Rydberg state because ionization becomes non-negligible (ionization energy about $h \times 350$ GHz) and the sensitivity to electric fields too important. This limit sets the waist⁽⁸⁾ of our optical resonator to 21 μm .

On top of that, the cavity field must be strongly coupled to a thousand atoms with a collective coupling factor g inversely proportional to the mode volume, equation 1.11. For instance, Gerhard Rempe’s team works on similar topics with a single atom coupled to a high-finesse resonator and their cavity has a 30 μm waist and a 500 μm length [38, 119]. In our case, it is very problematic to have dielectric media (mirrors) at this distance from the atomic cloud because of the high polarizability of Rydberg atoms (equation 1.32). Fortunately, we do not seek for a strong coupling at the single atom level but a collective strong coupling regime which allows the cavity length to be extended and the finesse to be reduced. We opted for a bow-tie resonator which has the advantage of separating the output mode from the input mode but also to avoid standing waves that cause abrupt changes in the coupling over the atomic ensemble. Planar configurations are prone to strong astigmatism which led us to adopt a non-planar geometry to counter this effect. A non-planar cavity is also interesting because it supports circularly polarized modes to address stretched states. These considerations will be discussed further in the following.

⁽⁸⁾Half width at $1/e^2$ of the intensity.

Our resonator is thus a four-mirror twisted cavity composed of two planar mirrors in its upper part plus two concave mirrors in the lower part both with a 20 mm radius of curvature, see figure 2.4. The angle of incidence on a mirror is approximately 9.3° and our 6.35 mm-diameter mirrors are separated by a 21 mm distance along the y axis. This length is not fixed and can be adjusted independently over ± 3 mm with two independent translation stages placed on the side of our input/output mirror ($y < 0$). This flexibility combined with the non-planar geometry allows to reach several kinds of mode degeneracies interesting to emulate condensed-matter Hamiltonians [58, 120].

Reflectivity of the cavity

We aim to couple light to a rubidium cloud and extract photons from the cavity in the most efficient way possible. The best configuration is to consider a one-end cavity, i.e. a resonator where one mirror has a much higher transmission T than the others mirrors. This mirror is called the input/output coupler because light is usually injected through it and most of the field escapes from the cavity via this mirror. In such configuration, the resonator reflection coefficient on resonance is given by (equation 1.54):

$$r_{cav} = \frac{E_{out}}{E_{in}} \approx \frac{T - L_0}{T + L_0} \text{ in the limit } T, L_0 \ll 1 \quad (2.1)$$

where the total losses of the resonator are $L = T + L_0$. In the following, we will simply refer to L_0 as losses because the light escaping from the input/output coupler corresponds to the field that we collect in practice. More precisely, the term L_0 encompasses different kinds of losses:

- **Transmission:** Each of the three high-reflectivity mirrors has a residual transmission, with a value of ~ 30 ppm⁽⁹⁾ estimated by a direct measurement at 780 nm.
- **Absorption:** Light always propagates over a short distance inside a Bragg mirror. This propagation in the material induces a weak light absorption, typically < 20 ppm per mirror⁽¹⁰⁾.
- **Diffusion:** Diffuse reflections on the mirror are possible because of nano-metric defects on the surface, this term can be very small for super polish mirrors, < 10 ppm. Our cavity is made of standard substrates and our supplier guarantees values below < 150 ppm per mirror. This effect is probably one of the dominant sources of optical loss in our resonator.
- **Mirror size:** This term is a geometric factor taking into account the spatial cut-off caused by the finite size of our mirrors. This loss factor depends on the specific mode, it is completely negligible for the fundamental mode of our cavity as it is given by $L_{\text{cut-off}} = e^{-d^2/(2w^2)}$ where d is the mirror diameter (~ 6 mm) and w is the waist. However, this term could become visible for high order modes described in subsection 2.1.1.

We estimated the sum of losses to be $L_0 \approx 300$ ppm before the bake of the entire platform. As previously mentioned, one option towards effective interactions between photons is to use dissipation inside the cavity to induce a dispersive response outside of it. This can be understood by adding a term to L_0 to take into account losses induced by the presence of atoms inside the resonator.

⁽⁹⁾Part per million, 10^{-6}

⁽¹⁰⁾from Laseroptik website.

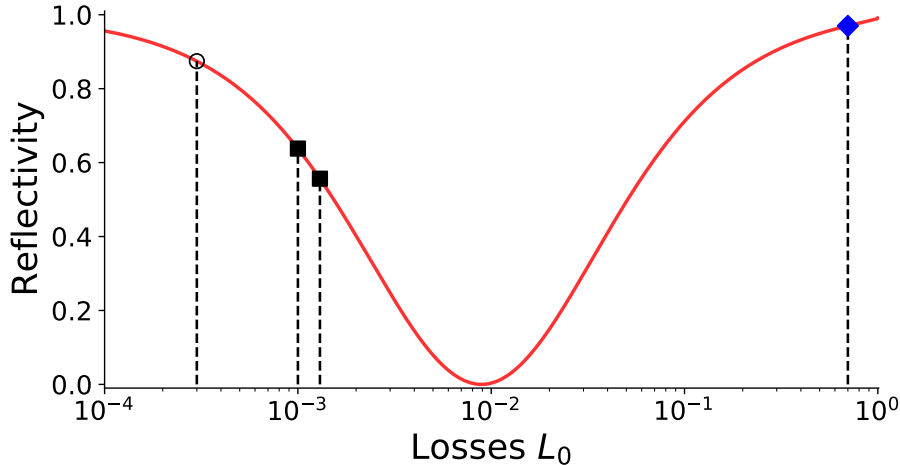


Figure 2.5: Reflectivity vs losses. The reflectivity of the cavity $|r_{cav}|^2$ is plotted for $T=0.90\%$ as a function of the losses L_0 (red curve). $L_0 = 300$ ppm (black circle) are the losses before degradation while the current level is: $L_0 = 1000$ ppm at 795 nm and $L_0 = 1300$ ppm at 780 nm (dark square), giving respectively $R_{795} = 64\%$ and $R_{780} = 55\%$, see text. The phase of the beam is π -shifted when the point $L_0 = T$ is crossed. The reflectivity for a small blockaded ensemble ($L_0 = 70\%$, in blue) is $|r_{cav}|^2 = 0.97$, see text.

Without atoms, the system is such that the total losses are just the intrinsic losses of the cavity $L_0 \ll T \ll 1$. In this case, the reflectivity of the system is simply given by $|r_{cav}|^2 \approx 1 - 4L_0/T = R_0$ and $r_{cav} > 0$. In a strongly dissipative regime, absorption is much more important than T such that the reflectivity goes asymptotically to $|r_{cav}|^2 = 1 - T = R$, $r_{cav} < 0$. The phase of the field is then π -shifted with respect to the initial case. We see here one role of the transmission coefficient to obtain this phase shift.

The rate at which photons leave the cavity is also set by the transmission of the input/output mirror: $K_0 = KT/(T + L_0)$, where K is the cavity damping rate from equation 1.3. It accordingly affects the value of the cooperativity, $C = g^2/(2\kappa\gamma)$, for the coupling with rubidium atoms. Therefore, the value of the transmission is a trade-off between several quantities. First, the need for a low loss system to achieve high-fidelity operations between photons, meaning $L_0 \ll T \ll 1$. Moreover, a fast response of the system, particularly interesting for quantum communication aspects and finally, a high cooperativity $C \gg 1$.

A good compromise is to set the value of the photon rate close to the decay rate of rubidium 87 D lines $\gamma \simeq 2\pi \times 3.0$ MHz⁽¹¹⁾ such that $T \approx 2\gamma\ell/c \approx 10^{-2}$. In practice, we estimated the transmission of our cavity to be $T = 0.90\%$ ⁽¹²⁾, giving $R_0 = 90\%$ and $R = 99\%$. The cavity reflectivity is plotted with this value as a function of losses in figure 2.5. The coating made by Laseroptik is optimized at 780 nm and 795 nm⁽¹³⁾, where experiments are carried out, but also at 1064 nm to lock the cavity length, see subsection 2.1.1. More precisely, mirror coatings are alternations of Ta_2O_5 and SiO_2 with one last SiO_2 layer to prevent vacuum degradation due to oxygen depletion [121]. The transmission parameter T also sets the value of other quantities such as the finesse of the cavity, $F = 2\pi/(T + L_0) = 675$ at 795 nm (equation 1.4).

As a last step, we can estimate the reflectivity in the presence of a small blockaded rubidium cloud to check that 0.9% of transmission is not too important. We take a Gaussian rms

⁽¹¹⁾Full width at half maximum of the D_2 line. For the D_1 line: $\gamma \simeq 2\pi \times 2.9$ MHz.

⁽¹²⁾0.89% at 780 and 0.91% at 795 nm.

⁽¹³⁾We work with the cavity locked on a hyperfine transition from one of the rubidium 87 fine doublet: D_1 , $5S_{1/2} \rightarrow 5P_{1/2}$ at 795 nm and D_2 $5S_{1/2} \rightarrow 5P_{3/2}$ at 780 nm.

of $\sigma_c = 5 \mu\text{m}$ for our cloud to fit inside a Rydberg blockade sphere for the 100S state⁽¹⁴⁾ and a typical peak atomic density of $n_0 = 5 \times 10^{11} \text{ cm}^{-3}$. The optical depth is $OD = n_0 \sqrt{2\pi} \sigma_c \sigma$ with the scattering cross section $\sigma \simeq 2 \times 10^{-9} \text{ cm}^{-2}$. It gives $L_{at} = 1 - \exp(-OD) \approx 0.7 \gg T$ and corresponds to $r_{cav}^2 \approx 97\%$.

The value of L_0 is critical to have high-fidelity photonic interactions. This is one of the main issue for cavity QED with single atoms because losses induced by a single atom have to be much more important than the transmission. It means going to very low transmission for the I/O coupler in the high-finesse regime and to low mode volume cavity to reach the strong coupling regime. In this case, reducing the intrinsic losses is a challenging task [38]. After we started to run experiments with atoms, we observed a decrease of the finesse that we attribute to a rubidium deposit on our mirrors. The finesse is now 620 at 780 nm and 590 at 795 nm. We estimated the value of L_0 to be ~ 1000 ppm at 795 nm and ~ 1000 ppm at 780 nm. With this change, the reflectivity for an empty cavity is now 64% at 795 nm. We did not focus yet on this problem but we did not manage to get rid of it with UV light, nor with a night of high intracavity circulating power at 780 nm to induce local heating of the coating by absorption. The next step is probably to heat the structure close to the mirrors.

Optical modes of a twisted cavity

We now discuss the propagation of light through our four-mirror twisted resonator to find the optical modes. Let us limit ourselves to the study of monochromatic beams propagating along \mathbf{z} so that, in the appropriate basis, the complex field can be written as $\mathbf{E}(x, y, z) = E_0(x, y, z)e^{i(wt-kz)}\mathbf{e}$ where \mathbf{e} is the polarization vector orthogonal to \mathbf{z} . We further assume that the envelope E_0 slowly varies with z compared to the exponential term. In this limit, also called paraxial approximation, the scalar wave equation $(\nabla^2 + k^2)E(x, y, z) = 0$ becomes:

$$\frac{1}{2k}\nabla_\perp^2 E_0(x, y, z) = i\frac{\partial}{\partial z}E_0(x, y, z) \quad (2.2)$$

This expression is valid for a homogeneous and isotropic dielectric medium.

Several orthogonal bases exist to compute a general solution of this equation. In a planar running-wave cavity, we must take into account non-normal reflection on mirrors. For a spherical mirror of focal length f making an angle θ with an incident light beam, the effective focal length is different along the tangential ($f \cos(\theta)$) and sagittal ($f / \cos(\theta)$) directions. Adding a second spherical mirror in a planar cavity can only worsen this astigmatism. Therefore, the mode factorizes into a Hermite-Gauss mode of the sagittal variable and another of the tangential variable. On the contrary, this effect can be suppressed by twisting the resonator out of the plane with two curved mirrors. In this case, the astigmatism induced by the first curved mirror can be compensated by the second one [122–124]. We are then looking for a set of modes that preserves the cylindrical symmetry [125]. The natural basis which has this symmetry is given by the Laguerre-Gaussian modes, as shown in figure 2.6. Its formal expression in cylindrical coordinates is:

$$u_{l,n}(r, \phi, z) = C_0 \frac{w_0}{w(z)} \left(\frac{r\sqrt{(2)}}{w(z)} \right)^{|l|} L_n^{|l|} \left(\frac{2r^2}{w(z)^2} \right) e^{-\frac{r^2}{w(z)^2}} e^{-\frac{ikl^2}{R(z)^2}} e^{i(l\phi + \psi(z))} e^{ikz} \quad (2.3)$$

where C_0 is a normalization constant, l and n are integers respectively named azimuthal and radial index.

⁽¹⁴⁾At $n=100$, the blockade radius is about $R=16 \mu\text{m}$ for a linewidth of $\gamma = 3 \text{ MHz}$, $R = (C_6/\gamma)^{1/6}$.

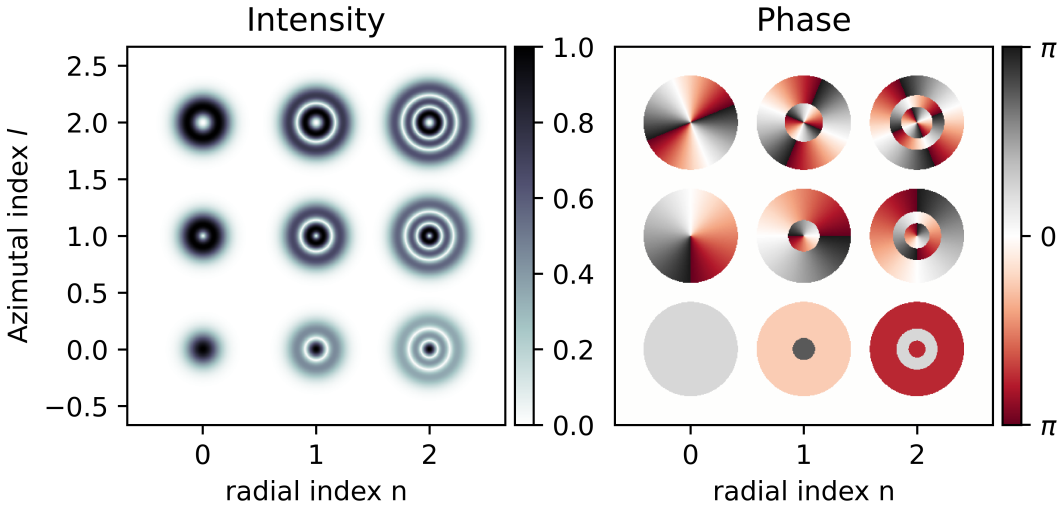


Figure 2.6: Laguerre-Gaussian modes. The intensity (Left) and phase (right) of LG modes are shown a function of the azimuthal index l and the radial index n .

$L_n^{|l|}$ is the Generalized Laguerre-Gauss polynomials given by:

$$L_n^{|l|}(t) = \frac{t^{-|l|} e^t}{n!} \frac{d^n}{dt^n} (e^{-t} t^{n+|l|}) \quad (2.4)$$

Along the transverse plane, the beam is characterized by the spot size parameter w :

$$w(z) = w_0 \sqrt{1 + \left(\frac{z - z_0}{z_r} \right)^2} \quad (2.5)$$

The quantity w_0 is called the waist of the beam at position z_0 while $z_r = \pi w_0^2 / \lambda$ is the Rayleigh length. It characterizes the typical distance over which the beam keeps its shape. In addition, a radius of curvature R is associated to the Gaussian mode:

$$R(z) = (z - z_0) \sqrt{1 + \left(\frac{z_r}{z - z_0} \right)^2} \quad (2.6)$$

Finally, the mode is characterized by a Gouy phase ψ :

$$\psi(z) = (1 + |l| + 2n) \arctan \left(\frac{z - z_0}{z_r} \right) \quad (2.7)$$

The fundamental mode, also called TEM_{0,0} for Transverse ElectroMagnetic mode, is a Gaussian fully characterized by two quantities: the waist w_0 and its position z_0 . For practical reason, these two parameters are often gathered in a unique complex number $q(z) = (z - z_0) + iz_r$.

The paraxial equation may seem complicated to solve for a given resonator geometry. It is in fact equivalent to a simpler method: ABCD matrix from ray optics [122]. In one dimension, the output position and angle (h_{out}, θ_{out}) is a linear transformation of the input parameters (h_{in}, θ_{in}) for any thin optical element. It is given by what is called an "ABCD" matrix:

$$\begin{pmatrix} h_{out} \\ \theta_{out} \end{pmatrix} = \begin{bmatrix} A & B \\ C & D \end{bmatrix} \begin{pmatrix} h_{in} \\ \theta_{in} \end{pmatrix} \quad (2.8)$$

The propagation of light through the cavity is then fully captured by a matrix M . By

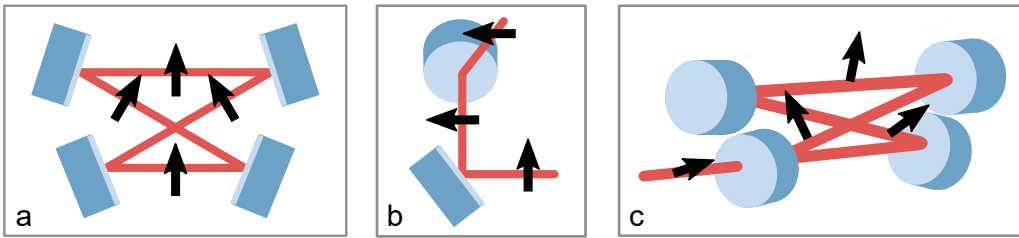


Figure 2.7: Image rotation. Illustration of the image rotation induced by the geometry of the resonator (mirrors are supposed flat here). a- For a planar resonator, the image (black arrow) is not rotating. b- One simple example of image rotation with two mirrors. c- We obtain a rotation along the optical path for our four mirrors twisted cavity.

generalizing this approach to the two transverse axes, one can compute the eigenmodes of our twisted resonator, with a roundtrip phase:

$$\phi = \frac{2\pi\ell_{rt}}{c}\nu + \left(\frac{1}{2} + m\right)\chi_1 + \left(\frac{1}{2} + l\right)\chi_2 = 2\pi n \quad (2.9)$$

where n, m, l are integers corresponding respectively to the longitudinal and the transverse modes. The twisted geometry induces a rotation of the polarization inside the cavity, shown in figure 2.7. The eigenmodes of our resonator are then circularly polarized Laguerre-Gaussian modes where right and left-handed modes are split [122, 123, 126]. Transverse modes indices m, l are related to right and left circularly polarized modes. Finally, $\chi_{1,2}$ are two parameters taking into account Gouy phase factors and depend on the distance between mirrors.

In practice, we control the two parameters χ_1, χ_2 through the two Smaract translation stages with a few nanometers resolution⁽¹⁵⁾. Thanks to this high precision, it is possible to fully control the degeneracy of the transverse modes. Let us consider for instance a configuration such that $\chi_1 = p/q$ where p and q are coprime integers. The mode $u_{l,m,n}$ is resonant if:

$$\nu_{l,m,n} = \frac{2\pi\ell_{rt}}{c}[(\frac{1}{2} + m)\chi_1 + (\frac{1}{2} + l)\chi_2 + 2\pi n] \quad (2.10)$$

We see that this mode is degenerated with the mode $u_{l,m+qj,n-jp}$ where j is an integer. We have then a p/q degeneracy between modes $u_{l,m+qj,n+jp}$ for any integer j . This degeneracy were exploited recently in the group of Jonathan Simon to emulate a 2D gas of electrons in a magnetic field [58, 120]. Our control of the transverse degeneracy will allow us to investigate this kind of system in the coming years.

Cavity length locking

The science platform and supports were designed to reduce as much as possible thermal fluctuations and mechanical vibrations by isolating each support with Viton cylinders as mentioned in the introduction of this section. Despite these precautions, the cavity length is locked to avoid inherent drift caused by slow dynamics (\sim kHz). Furthermore, the cavity must be coupled to an atomic transition which is only possible by a control of the cavity length. This is made possible by three piezoelectric actuators placed inside the holder of the two high-reflectivity mirrors located opposite to the input-output mirror (shown in figure 2.3). The feedback voltage is obtained by the standard Pound-Drever-Hall technique (discussed in subsection 2.2.2) where the cavity length is locked on a reference laser. We had initially planned to use a far-off-resonant 1064 nm laser but we did not manage to keep this laser

⁽¹⁵⁾Smaract translation stages are based on the stick-slip phenomenon.

stable enough. We then turned to a 783 nm beam much closer to the rubidium lines. We had to reduce its power down to 1 nW in front of the cavity to protect our atoms from the residual spontaneous emission induced by this locking beam. We used a specific Thorlabs APD (430 A/M) for this locking at weak intensity.

2.1.2 Build-up cavities

The dipole matrix elements for the coupling between a low excited state of rubidium ($5P_{1/2}$ or $5P_{3/2}$) and a Rydberg state (nS) are very weak, scaling as $n^{*-3/2}$. For instance, at $n = 100$, with 1 W of light and a 100 μm waist, the Rabi frequency has a value of $2\pi \times 4 \text{ MHz}$ ⁽¹⁶⁾. On top of that, some of the experimental protocols we aim for require the use of two different Rydberg states. We have thus two lasers for control beams (Ti-sapphire laser + External Cavity Doubler from Msquared, see section 2.2.1), each can at most deliver 1 W and two build-up cavities increase this power. The two resonators were put inside the vacuum chamber to obtain a small waist (about 100 μm) and to ensure a high stability. They are almost perpendicular⁽¹⁷⁾ to the science cavity optical axis and tilted by 8° with respect to the horizontal axis, shown in figure 2.8.

Confocal cavities

The optimal value of the waist is a trade-off between a high control Rabi frequency and the inhomogeneous broadening induced by the variation of the intensity on the atomic sample. On the other hand, the small atomic sample (few tens of micrometers) must be well coupled to both the science cavity mode (20 μm waist) and our two control beams (about 100 μm). The position of the modes of our cavities and their size are therefore sensitive parameters for our experiment that we have to control to some extent.

A confocal cavity is a simple solution to both problems. In this configuration, two mirrors are separated by a distance equal to the radius of curvature of the two mirrors. The confocal ABCD matrix after one round-trip (equation 2.8) is simply:

$$M_{\text{confocal}} = \begin{bmatrix} -1 & 0 \\ 0 & -1 \end{bmatrix} \quad (2.11)$$

where we notice that $M_{\text{confocal}}^2 = \mathbb{1}$. It means that there is no constraint on the beam input angle or initial position. Any mode goes back to its initial configuration after at most two round-trips. Thereby, it is possible to make a fine alignment of the control beam on the atomic sample to optimize the overlap but also to adjust the size of the beam to maximize the control Rabi frequency. This is even more interesting because it is possible to inject light out of the optical axis of the cavity to avoid inhomogeneities caused by a standing-wave configuration. The waist of the $\text{TEM}_{0,0}$ mode is given by $w = \sqrt{\lambda R/\pi}$, consequently the Rayleigh length is $z_r = R$ and the frequency of a resonant mode can be expressed as:

$$\nu_{n,p} = \frac{c}{4R}(2n + m) \quad (2.12)$$

where m is the transverse mode index and n the longitudinal index (both integers).

⁽¹⁶⁾The dipole is calculated between $5P_{1/2}, F = 2, m_F = +2$ and the $100S$ Rydberg state with linearly polarized light.

⁽¹⁷⁾There is a 102° angle between the two.

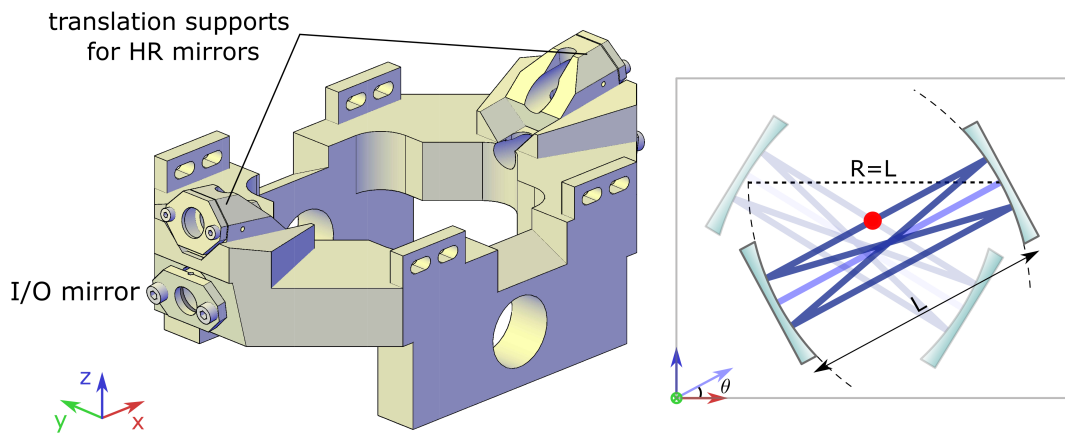


Figure 2.8: Build-up cavities. The two confocal cavities are perpendicular to the science cavity optical axis (y). Left- Our build-up cavities support where the two I/O mirrors can be translated to adjust the length of the resonators. Right- Sketch of the two resonators. A confocal cavity is characterized by a distance between mirrors equal to the radius of curvature, $R = L$. The $\text{TEM}_{0,0}$ mode is represented in light blue while a bow-tie mode is drawn in deep blue and crosses the cloud, red dot.

Presentation of the two resonators

Our build-up cavities are single-ended resonators with an Input/Ouput mirror transmission of 1%. The radius of curvature is $R=150\text{ mm}$ giving a free spectral range of 1 GHz and a $\text{TEM}_{0,0}$ waist of $107\text{ }\mu\text{m}$. We call the resonator with the I/O mirror on the left of figure 2.8 the Left cavity and the other one the Right cavity. The finesse of the cavity is estimated from the full width at half maximum of the $\text{TEM}_{0,0}$ mode: $K_{\text{Right}} = 2\pi \times 2.4\text{ MHz}$ and $K_{\text{Left}} = 2\pi \times 2.0\text{ MHz}$ giving $F_{\text{Right}} = 416$ and $F_{\text{Left}} = 500$. During the assembly, we had to carefully align each cavity to match the condition $R = L$, which makes confocal resonators only marginally stable. In a second step, the science cavity support was aligned on top of it to ensure that the $\text{TEM}_{0,0}$ of each buil-up cavity is $500 \pm 50\text{ }\mu\text{m}$ away from the science cavity waist, see figure 2.8. The high-intensity beam is thus injected in a bow-tie mode and overlap with the cloud on its lower arm. Below this $500\text{ }\mu\text{m}$ separation and depending on the injected mode, interferences in running-wave modes can become non-negligible and can induce significant inhomogeneities on the atomic ensemble.

The lengths of the cavities are stabilized like the science cavity, see subsection 2.1.1. A ring piezo-actuator is placed behind the high-reflectivity mirror of each cavity for this locking. The mirrors coatings are optimized at 474 nm and 480 nm only, so the $\text{TEM}_{0,0}$ mode is used to lock the cavity. The locking beam is separated from the high-intensity beam by $500\text{ MHz}=\text{FSR}/2$ for the cavity to be resonant for both beams when it is stabilized on the locking beam. By doing so, the locking light is not resonant with the addressed Rydberg state and it does not overlap with the cloud.

To align our power beam onto the cloud, the build-up beam is first injected in the $\text{TEM}_{0,0}$. It is easily identifiable because modes are separated by $\frac{c}{2R}$ and not $\frac{c}{4R}$. Then, the position of the high-power beam is adjusted by a mirror attached to a translation stage. The translation is not perpendicular to the optical axis of the cavity so the beam angle must be corrected to match the desired configuration. We adjust the inclination to have the two outgoing beams separated by an angle of $\theta_1 = \frac{2l}{R}n$ and $\theta_2 = \frac{2l}{R}$ with respect to the input beam corresponding to a perfectly aligned bow-tie mode. In this case, $l = 0.5\text{ mm}$ is the displacement, $n = 1.52$ is

the refractive index of *BK7* at 475 nm giving a ratio of 3/2. During this kind of adjustment, we optimize the electromagnetically-induced transparency on the atoms-cavity spectrum.

Build-up factors

In theory, the running-wave mode of the power beam undergoes twice as much losses as the TEM_{00} mode. This is due to the fact that the light is reflected twice on the I/O mirror before ending its roundtrip. In reality, mirrors are always better in their center and it depends also on the quality of the length alignment to reach confocality. For the left resonator, the finesse in the bow-tie mode is estimated⁽¹⁸⁾ to be 40% of the $\text{TEM}_{0,0}$ finesse. It is worse for the left cavity with only 26%. We attribute this difference to an imperfect adjustment of the length of the second resonator. The amplification of a cavity A is defined as the ratio between the intensity inside the cavity and the input intensity and for a single-ended resonator:

$$A = \frac{I_{cav}}{I_{input}} \simeq \frac{F_m}{\pi} \quad (2.13)$$

where F_m is the effective finesse.

We observe an amplification of 45 (64 in theory) for the best cavity and 20 (41) for the second one with a waist of 200 μm . This value is estimated from the control Rabi frequency measured on the EIT spectra. When we reduce the waist by a factor 3 the build-up is changed to 30 for the best cavity and 12 for the other one. Going further only makes this effect worse, so we are currently working with a waist of 60 μm ⁽¹⁹⁾. These observations are quantitatively consistent with a defect of the confocality, which mainly stems from finite tolerances on mirror radii ($\pm 0.5\%$) and from spherical aberrations. In a perfectly confocal cavity every second mode (labeled along one Cartesian dimension) is co-resonant. Driving the cavity off-axis and/or with a beam size different of the fundamental mode amounts to exciting many of these modes. When the confocality is imperfect their spectral degeneracy is lifted and the corresponding finesse drops.

⁽¹⁸⁾Estimation from the linewidth of the mode.

⁽¹⁹⁾We are here referring to the injected waist, we do not have access to the waist inside the resonator.

2.2 Laser bench



2.2.1 Lasers

In our experimental platform at the crossing between ultracold atoms and quantum optics, lasers have to play several roles. The first one is to address rubidium transitions at the hyperfine level. This requires a monochromatic source with a narrow spectral linewidth so that we can manipulate a cloud of atoms: cooling, trapping... Laser light is also used to probe our system to study the coupling between our cavity and the atomic ensemble. From a technical point of view, we also need to stabilize the length of several resonators (science cavity, build-up cavities...) and this is also done with lasers.

DL pro and TA pro

The DL pro laser is an External Cavity Diode Laser (ECDL) built by Toptica. The system consists of a diode with an anti-reflective coating at one end, followed by a diffraction grating. Adjusting its angle allows one to send the first diffracted order at a given frequency back to the diode, forming a frequency-selective external cavity, while the fundamental order is sent to the output of the laser. A DL pro produces about a few tens of milliwatts of a narrow linewidth light with a tunable central wavelength that is perfectly adapted to our needs. Fast feedback can be sent to the current of the internal diode and slow feedback to piezoelectric actuators on the grating to stabilize the frequency.

Our first DL pro is optimized at 780 nm with an output power of 41 mW and a beam waist of 0.5 mm. This laser is dedicated to repump atoms in the 3D MOT, in the 2D MOT and during atomic manipulation within the science cavity. It can address $|5S_{1/2}, F = 2\rangle \rightarrow |5P_{3/2}, F' = 1, 2\rangle$ transition depending on the context. The second one is used at 795 nm with 36 mW and it is used to address the D_1 line of rubidium 87 as a probe during experiments with Rydberg atoms (rubidium lines are shown in figure 2.9). The last DL pro is optimized at 780 nm with 60 mW for degenerate Raman sideband cooling and its frequency is 10 GHz above the Repumper laser.

As it can be seen the output power of a DL pro does not exceed 60 mW which is not enough for some trapping applications, for instance our 3DMOT alone requires about 200 mW⁽²⁰⁾.

⁽²⁰⁾ 10 mW in each arm with a splitter efficiency of 50% and double-pass acousto-optics modulator with 50% efficiency.

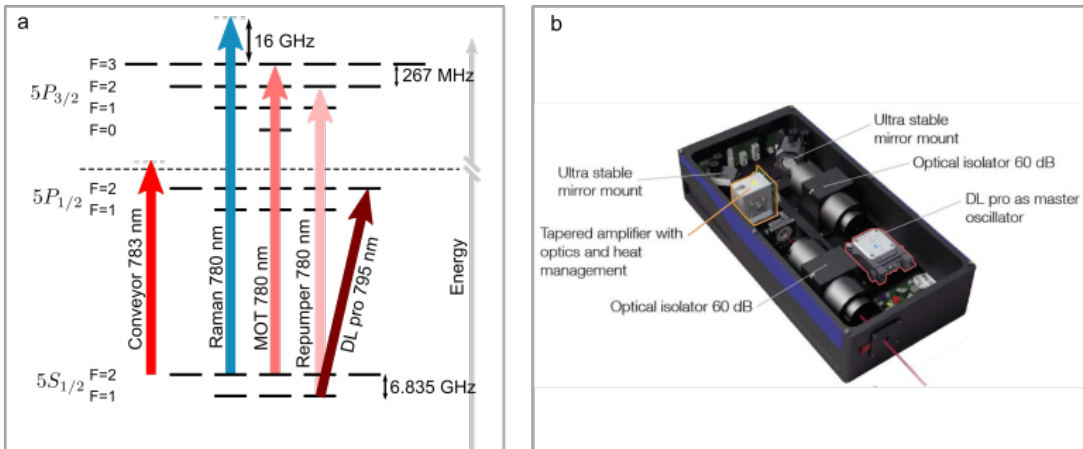


Figure 2.9: Rubidium Lines and TA pro. a- Rubidium D_1 ($5S_{1/2} \rightarrow 5P_{1/2}$) and D_2 ($5S_{1/2} \rightarrow 5P_{3/2}$) lines with the hyperfine structure and the lasers (in red). b- TA pro with the tapered amplifier (in orange) and the DL pro (in red), image from toptica.com.

To gain power we use a Tapered Amplifier laser system (TA pro), also marketed by Toptica, that produces about 1 W of laser light. The first one was optimized at 780 nm to be resonant with the D_2 line of rubidium 87, mostly applied on $|5S_{1/2}, F = 2\rangle \rightarrow |5P_{3/2}, F' = 3\rangle$. It is used in the 3D MOT and 2D MOT to trap and cool down atoms, for absorption imaging but also as a hyperfine pump for Raman degenerate sideband cooling. In this laser system, a DL pro is used as a master oscillator. It is followed by an optical isolator to prevent the intensity from returning back inside the laser diode. The light is then focused and led to a tapered amplifier where the geometry allows to both amplify and spatially filter the beams. The resulting output beam has a good quality factor⁽²¹⁾ with M^2 below 2. The output beam waist is 0.5 mm with an output power of 800 mW, which can exceed 2 W when the amplifier is driven with its maximal current. Finally, a second optical isolator is put on the exit of the amplifier to further protect the optical system. We also have an older version of this laser, that is used to transport atoms from the 3D MOT to the optical cavity (the conveyor belt). The frequency of the laser is tuned at 783 nm with an output power of 1.1 W and a 500 μm waist.

Titanium-Sapphire Laser and External Cavity Doubler

We also need a control laser to address the Rydberg levels between 474 nm and 480 nm. One of the first constraint is to have a tunable laser on this frequency range. Furthermore, Rydberg states have a small overlap with the low excited states, so a high laser power is required to address them. Finally, the spectral width of the laser must be small enough not to broaden the targeted Rydberg state too much.

The best option on the market to meet our expectation is to use a frequency doubling crystal in cavity fed by a Titanium-Sapphire laser. Our two SOLTIS lasers from Msquared focus on this demanding task and can deliver about 1 W between 460 nm and 490 nm. First, 18 W of 1064 nm is produced by a Lighthouse Photonics SPROUT pump and it is then frequency-doubled at 500 nm. This beam is sent to a standard Titanium-Sapphire laser (Msquared SolsTiS) with a tunable frequency from 680 nm to 1100 nm. The output beam is finally injected in a bow-tie cavity dedicated to Second Harmonic Generation and amplification (Msquared SolsTiS ECD). The non-linear crystal inside the cavity can be adjusted

⁽²¹⁾The parameter M^2 characterizes the deviation from a Gaussian beam, it is defined as $M^2 = \theta_{div} w_0 \pi / \lambda = \theta_{div} / \theta_{Gauss}$. θ_{div} is the output divergence angle and θ_{Gauss} the divergence angle for an ideal Gaussian beam of waist w_0

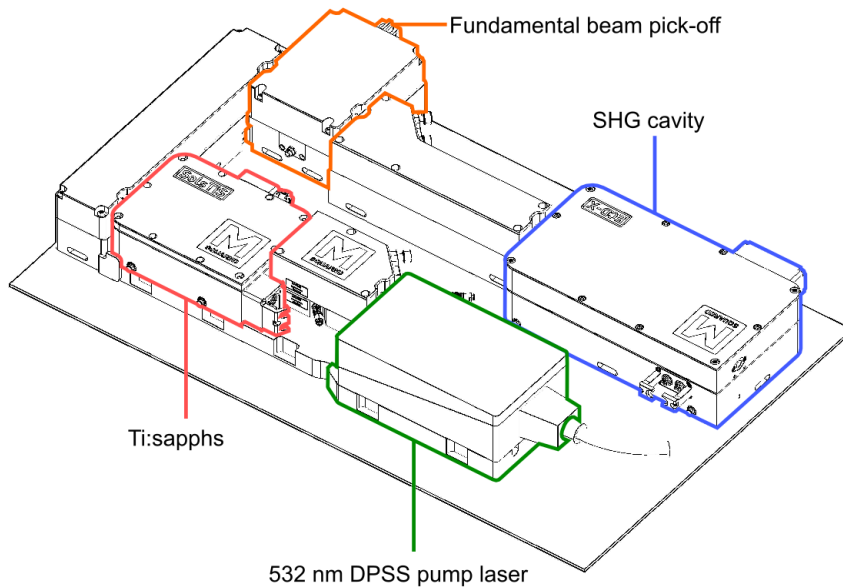


Figure 2.10: SOLSTIS laser. The titanium-Sapphire laser (in red) is pumped by a 532 nm laser diode (DPSS in green), itself pumped by a SPROUT laser at 1064 nm (18 W). A small amount of the Ti:sapph light is picked off (orange) to lock the laser while most of the power goes to the SHG cavity (in blue) to produce up to 1 W of blue light at 475-480 nm. The gain profile of a TiSa crystal is very broad, so an etalon and filters are put inside the resonator to select a single mode of emission.

for mode-matching to cover the full range of frequencies from the TiSa. This laser can be stabilized by acting on two piezo actuators with two different ranges, one around ± 15 GHz for slow drifts and another one with ± 40 MHz for high frequency noise.

High Power 1064 nm fiber laser

The 1064 nm laser from Azur Light System (ALS) is a high-power laser with up to 8 W of output light. This laser is only used to trap atoms inside a crossed dipole trap. A seed laser is amplified by a high-power amplifier chain and goes to a fibered head. This makes the output beam quality factor very high, with $M^2 < 1.1$. We initially used this laser to lock the science cavity but we had numerous issues with it: mode jumps of about 1 GHz, often multimode around the setpoint frequency...

2.2.2 Frequency locking chain

As discussed in the previous sections of this chapter, the experimental platform was designed to minimize inhomogeneous broadening of Rydberg states caused by stray electric fields or control fields inhomogeneities. To continue in this direction, it is therefore necessary to precisely control the spectral linewidth of our lasers. This includes our two TiSa, the TA pro at 780 nm and the DL pro at 795 nm with the aim to reach spectral linewidths below 10 kHz. The other lasers also need to be frequency stabilized since they are all used to address the rubidium lines at the hyperfine level and some of them are needed for the length locking of our optical cavities. This allows us to compensate slow drifts and to adjust the cavity resonance to a specific rubidium transition. In the end, seven of our lasers, out of eight in total, require frequency control.

Methods

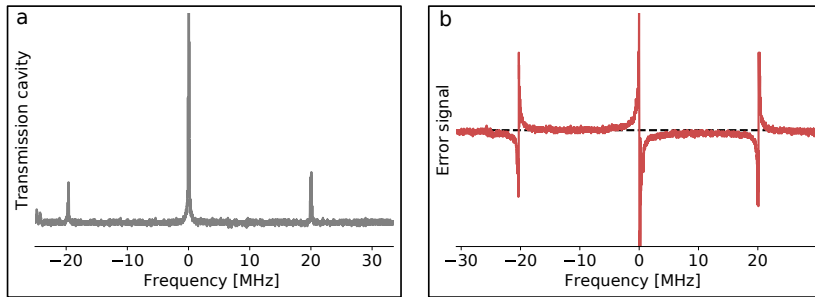


Figure 2.11: Pound-Drever-Hall. a- The laser intensity is modulated at a frequency of $\Omega=2\pi \times 20$ MHz by an EOM and the zero frequency in this plot corresponds to the carrier. b- The Pound-Drever-Hall error signal is in red while the zero is represented by the horizontal dashed line.

Two techniques are used in our experiment for this locking, the first one is the Pound-Drever-Hall (PDH) method [127] that can be implemented to lock a cavity on a laser and vice versa. The second method is a phase lock but it is only possible between two lasers. The idea, in both cases, is to have a signal to distinguish whether the frequency of the system is above or below a setpoint frequency. Then a PID controller⁽²²⁾ (via piezo actuators, current, etc.) tends to minimize this error signal to reach the setpoint. Other methods exist, for instance with saturated absorption on a vapor-cell [128], or with the Hansch-Couillaud method [129] but they are less stable than the PDH technique.

Regarding the Pound-Drever-Hall (PDH) technique, the general idea is to look at the light reflected off a cavity. For a light beam crossing a cavity resonance, the phase of the field goes from $-\pi$ to $+\pi$. This phenomenon is perfectly suited for a servo loop: one of the field quadratures is negative before a resonance and positive afterwards. The aim of the method is to obtain a signal proportional to this quantity. For this purpose, the laser intensity is modulated at a frequency Ω by an electro-optic modulator (subsection 2.2.3) to produce two sidebands to the carrier. The resulting signal is reflected by a cavity, then acquired on a photodiode and demodulated at the same frequency Ω . The resulting signal is given by:

$$S \propto \text{Im}[R(\omega)R(\omega + \Omega)^* - R(\omega)^*R(\omega - \Omega)] \quad (2.14)$$

where $R(\omega) = E_r/E_{\text{input}}$ is the cavity reflection at angular frequency ω .

Close to resonance and if the cavity linewidth is much smaller than Ω , we simply have $R(\omega \pm \Omega) \approx -1$. In this limit, the measured signal is proportional to a quadrature of the carrier:

$$S \propto \text{Im}(R(\omega)) \quad (2.15)$$

This defines the error signal of the PDH method and it is illustrated in the figure 2.11. The sign of the error signal is constant all along the range $]-\Omega, 0[$ and flips for $]0, \Omega[$ as shown in the figure. This gives a wide stability band for the PDH approach and the error signal is proportional to the offset from resonance within the linewidth of the resonator, thus providing an efficient PID locking.

The phase-lock method is even simpler: two laser fields are mixed on a beam splitter and their oscillations are recorded on a fast photodiode. This signal is demodulated at a given frequency f to obtain the error signal. The slave laser is then locked on the master laser with a frequency shift equal to $\pm f$. Even if this method is simple, it is less attractive than the

⁽²²⁾The output signal is the sum of the proportional, integral and derivative terms of the error signal.

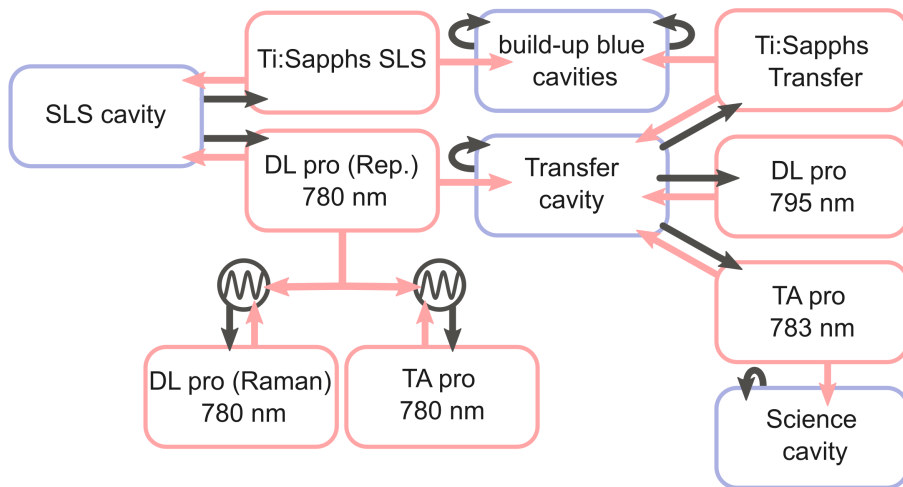


Figure 2.12: Locking chain. Cavities are circled in blue and lasers in red. Black arrows represent the electronic signal sent to stabilize a given component of the chain while red arrows symbolize the laser beams. Two lasers are phase locked on the DL pro 780 nm indicated by the black sinusoidal symbol.

PDH approach since it is hard and expensive to demodulate faster than 10 GHz while some of our lasers are separated by hundreds of terahertz.

These two methods enslave one component to another but they do not provide any frequency reference. In our case, the absolute reference is provided by an ultra-stable high-finesse cavity on which two lasers are locked. One of them is then used as a reference to stabilize a medium finesse cavity called transfer cavity. This cavity is in turn a reference for three lasers. A summary of the frequency stabilization of the lasers is shown in the figure 2.12.

Ultra-stable cavity and Transfer cavity

The absolute frequency reference of our experiment is an ultra-stable and high-finesse cavity made by Stable Laser System (SLS). The system is put under high-vacuum with a 10^{-6} mbar pressure to reduce thermal fluctuations of the optical index. The pressure inside the vacuum chamber is maintained by a ion pump (Agilent VacIon 2 L/s pump), this cavity is surrounded by an Ultra-Low Expansion glass (ULE) block and its temperature is stabilized at a value of 28 °C where the expansion coefficient of ULE is zero. We observed small drifts over months (< 1 MHz) that are easily compensated by looking at a saturated absorption spectrum on a rubidium cell. The distance between the two mirrors is $L = 10$ cm with a measured finesse of 26400 at 780 nm corresponding to a free spectral range of 1.5 GHz and a full width at half maximum of 59 kHz. The coating of the two mirrors were optimized for wavelengths at 780 and 980 nm so that our DL pro laser (Repumper) at 780 nm and one of the Ti:Sapphs are locked on that cavity. It was impossible to obtain a coating covering the whole set of laser frequencies while keeping the finesse of the resonator at this magnitude. For that reason, we have a second resonator: the transfer cavity with a medium finesse to lock three other lasers.

The transfer cavity is a homemade cavity stabilized by the DL pro (Repumper). The cavity full width at half maximum is 100 kHz, close to the SLS cavity linewidth. The free spectral range is much shorter with 200 MHz (instead of 1.5 GHz for the SLS cavity) to make the stabilization of others lasers easier. Thereby, the frequency of a laser can be adjusted over 200 MHz with a double-pass AOM to be resonant with the cavity. This constrains the

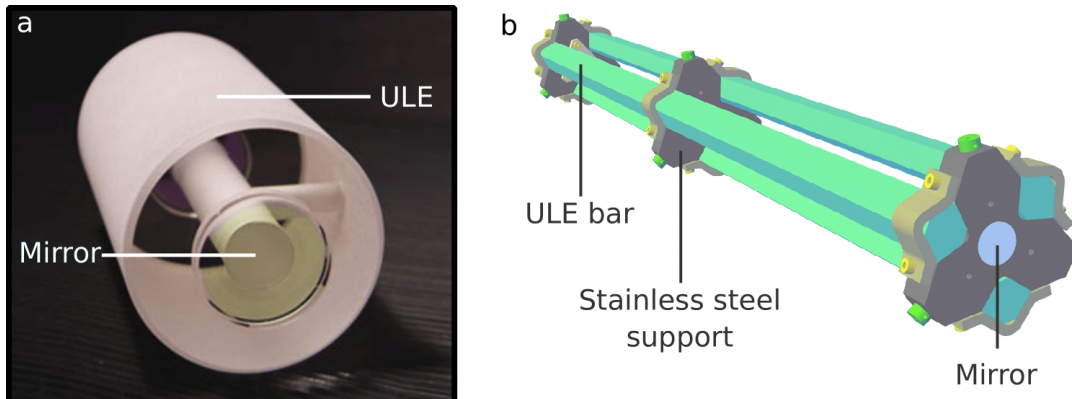


Figure 2.13: Stable Laser System cavity and transfer cavity. a- SLS cavity surrounded by a coat of ULE glass. The assembly is put inside a vacuum chamber not visible in this picture, from stablelasers.com. b- The transfer cavity with three Invar steel supports each resting on two Viton cylinders for thermal and vibrational isolation. Three ULE bars maintain the whole system inside the vacuum chamber, mirrors stand on each end.

length of the cavity to $L = 75$ cm. This resonator was designed to be stabilized by one laser and to lock three others. This requires mirrors coating optimized at 960 nm, 780 nm, 795 nm and 1064 nm. This is of course only possible at the cost of a lower finesse (1800 at 795 nm). This cavity is also put under vacuum $P = 1.10^{-7}$ mbar for the same reason as the SLS cavity and its pressure is also preserved by an ion pump (Agilent VacIon Plus 20 pumps) with a 20 L/s flow. Mirrors are sustained by three ULE glass bars hooked to the mirrors supports and these supports are resting on Viton seals to further reduce mechanical vibrations (shown in figure 2.13). The DL pro at 795 nm, the 2nd Ti:Sapphs and the 783 nm laser are all locked on this cavity with the Pound-Drever-Hall technique. Each wavelength is separated by a grating after reflection and each beam is acquired on a dedicated photodiode for locking.

The beatnote noise⁽²³⁾ of our two Ti:sapphs lasers locked with the PDH method is estimated to 3 kHz. We also measured the noise of one of the infrared probe, the DL pro 795 nm with a half width at $e^{-1/2}$ of 2.5 kHz. This width is obtained by comparing the amplitude of the error signal with the rms noise of the signal during the lock.

2.2.3 Optical modulator: frequency control and switch

There are still two important elements to introduce for our experimental platform: the acousto-optic modulators (AOM) to shift the frequency and turn on and off our beams and the electro-optics modulators (EOM) to modulate beams for the Pound-Drever-Hall technique.

In the case of an AOM, a radio-frequency signal is sent to a crystal to induce an acoustic standing-wave producing a Bragg grating. Hence, the light is deflected and its frequency shifted in proportion to the radio-frequency and the diffraction order. In practice, the first order is preferred since it has the most efficient conversion ratio (efficiency up to $\sim 90\%$). The problem here is that the output beam is almost always coupled to a single mode fiber and thus single-pass configurations can only be used at a constant frequency to not lose the coupling with the fiber mode. Most of the time, a double-pass setup is preferred: light is deflected once, then reflected by a curved mirror back to the AOM to be finally deflected a second time. The input and output modes are then superimposed and we use a quarter-wave plate on the optical path to separate them. The frequency of the beam is shifted by twice the radio-frequency and the beam does not depend on the deflection angle anymore. Our

⁽²³⁾Half width at half maximum, acquisition duration of 15 ns.

AOMs⁽²⁴⁾ are designed to work around a resonant frequency either at 110 MHz or 80 MHz but in practice we can adjust this frequency up to ± 40 MHz around the carrier at the cost of a significant drop in the diffraction efficiency on the edges. This configuration is therefore well suited for frequency sweeps.

We also have EOM, where an electrical field induces a modulation of the optical index. This results in symmetric sidebands around the carrier frequency that are used for our locking chain. We have resonant bulk EOMs working at 20 MHz and fibered EOMs⁽²⁵⁾ with a bandwidth at a few GHz depending on the precise model. These elements are thus also helpful for the adjustment of the laser frequencies in the GHz range that is impossible to cover with our AOMs. This is for instance the case with the lasers to be locked on the SLS cavity where the free spectral range has a value of 1.5 GHz.



⁽²⁴⁾ AA opto-electronic, MT-110 or MT-80

⁽²⁵⁾ Photline, iXblue

2.3 Control setup

This kind of experimental platform lies between cold atoms physics and quantum optics experiments. Therefore, there is an important difference in time scale between our needs for the atomic preparation and the optical part. For atomic manipulation, we need control from the microsecond range to a few seconds while the duration of our light pulses or the lifetime of our polaritons is about 100 ns. This particularity of our experiment has several consequences on the control and acquisition for both hardware and software means.

2.3.1 Hardware

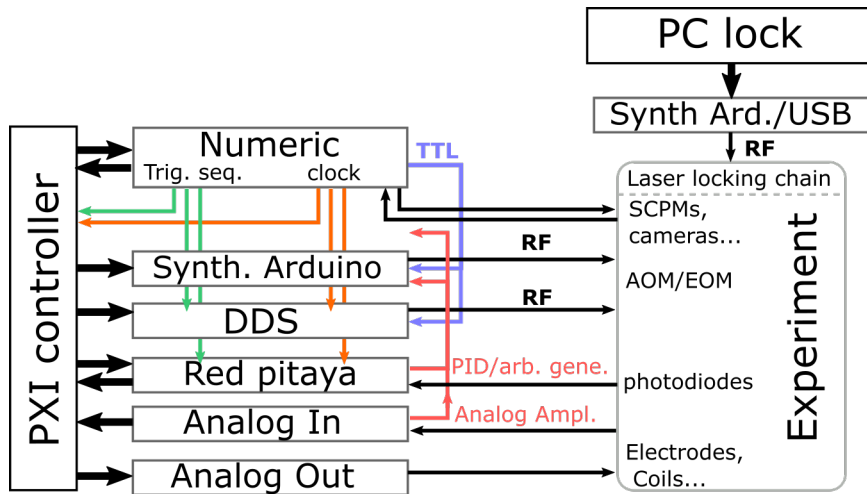


Figure 2.14: Control of the experiment. The PXI system sends instructions to the different cards. The instruments are synchronized by a trigger signal generated by the numeric card. DDS and Arduino channels produce RF signals for AOMs and EOMs on the experiment to adjust the frequency of our lasers beams or to simply switch light on/off. Digital channels can be used as on/off controls for RF channels, for our cameras... Some of these channels are configured to acquire data from our SPCMs, either timestamps or with adjustable time bins. Output Analog cards are devoted to the analog control of our RF signals, the voltage of our 8 electrodes, etc. Input Analog cards records photodiodes signals from 100 kHz to 250 MHz. Red Pitaya boards are programmed as a PID to lock the intensity of a laser beam during the sequence or can be used as arbitrary function generators. A second controller is dedicated to the laser locking chain to adjust the frequency of each laser by driving AOMs and EOMs through Arduino and USB synthesizers.

The run of a single experimental cycle takes about 100 ms, from the 2D MOT loading to a measurement with the science cavity. In this short period of time, we must be able to switch off and on beams, sweep frequencies and acquire data. This whole process is managed by a PXI controller from National Instrument with several specialized electronic cards. The control of the experiment is sketched in figure 2.14 and we now describe each task separately.

First of all, we need RF generators to drive AOMs in order to adjust the frequency of our beams. RF frequencies up to 300 MHz are generated by DDS (Direct Digital Synthesizer). These RF generators are controlled by a FPGA (Field Programmable Gate Array) with the aim of modifying or sweeping the frequency, amplitude and phase of the signal during an experimental cycle. We also have home-made generators built from Arduino boards where the same parameters can be adjusted but constant for each cycle. For gigahertz waves, we make use of commercial USB generators built by Winfreaktech. Each DDS and Arduino channel can be switched off/on by an external on/off controls and the amplitude can be adjusted by an external analog signal. This is for instance useful when we want to lock the intensity of a laser beam.

Our digital cards generate on/off LVTTL signals and are used to acquire data with SPCMs (Single Photon Counting Modules). Two modes are possible, either with digital input channels where we record timestamps with a resolution of 10 ns or digital analog input channels with an adjustable time bins adapted to a high photon rate. The standard signal acquisitions is carried out by analog cards in input mode with sampling rate up to 250 MHz for our two fast cards and at a rate of 100 kHz with slow cards. We also have analog cards in output mode for the analog control of RF generators, electrodes driving...

Finally, we have Red Pitaya boards with an integrated FPGA for arbitrary function generation. It is for instance used to shape short Gaussian pulse (50 ns intensity rms⁽²⁶⁾). They are programmed to work as an analog control and/or as a servo loop with the capability to adjust or sweep the setpoint during a cycle with a 125 MHz logic clock.

The synchronization between instruments is ensured by a reference clock at a frequency of 25 MHz and a sequence TTL defines the beginning of the sequence for the whole system.

2.3.2 Software

The control of the platform is done through a home-made LabView program (VITO) on our PXI system. The user interface is separated in four main panels:

- **Select Channels:** The first interface is where the user picks channels to control from the list of instruments discussed in the previous subsection. Only these instruments take part to the sequence.
- **Config Sequence:** This one is dedicated to the global structure of the sequence. This is where we define the steps with adjustable durations. Each step is executed one after the other with the option to make loops. This succession of steps defines what is called the experimental cycle. In this window, one can also define variables that are used to scan parameters between experimental cycles.
- **Config Channels:** The third panel is where the user programs each channel. For instance, a DDS channel can be configured for each step and each step can be split in substeps. One can also use previously defined variables to scan a parameter between experimental cycles.
- **Run Sequence :** In the last interface, the user defines the number of cycles and starts sequences. This panel can display the data and handles its storage. The complete sequence can be saved in a SQL database and previously saved sequences can be loaded. Data are stored in a TDMS files while the associated sequence is automatically uploaded to the database. They both share a unique ID key to ensure unambiguous identification.

An example is shown in figure 2.15 and figure 2.16, with two of the four panels. We have a second software programmed in Python (RubImaPy) for imaging. This program collects images from our cameras and is thus used in parallel of the VITO program.

⁽²⁶⁾Half width at $e^{-1/2}$ of the intensity.

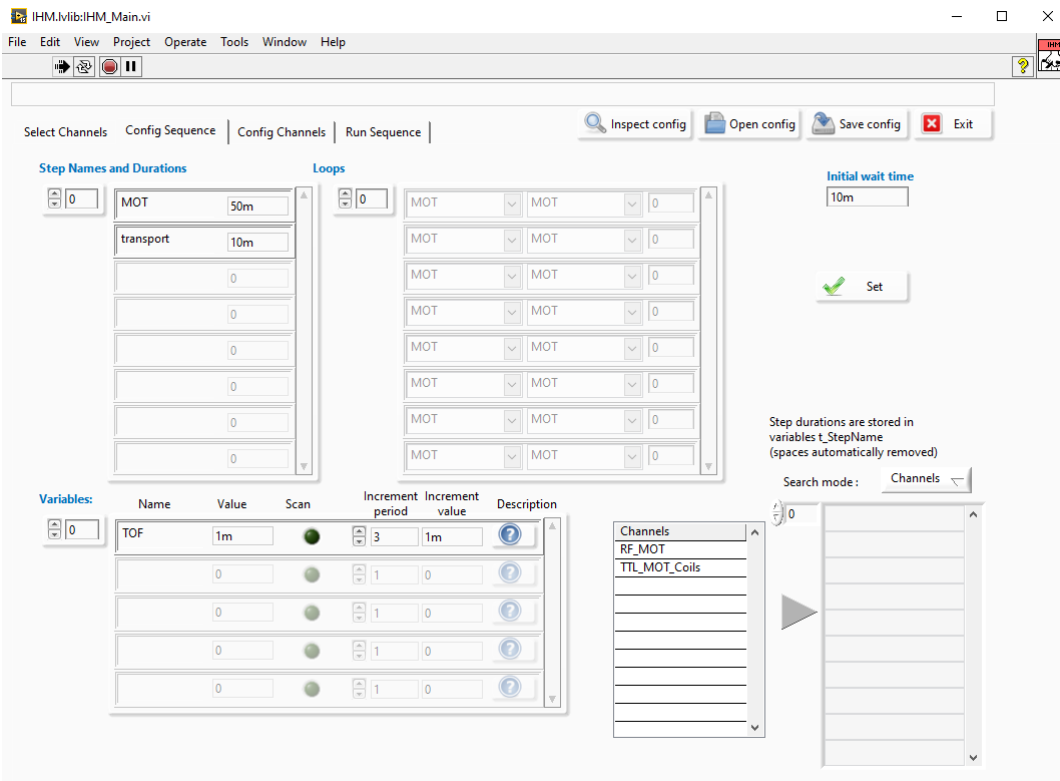


Figure 2.15: Vito, Config Sequence.

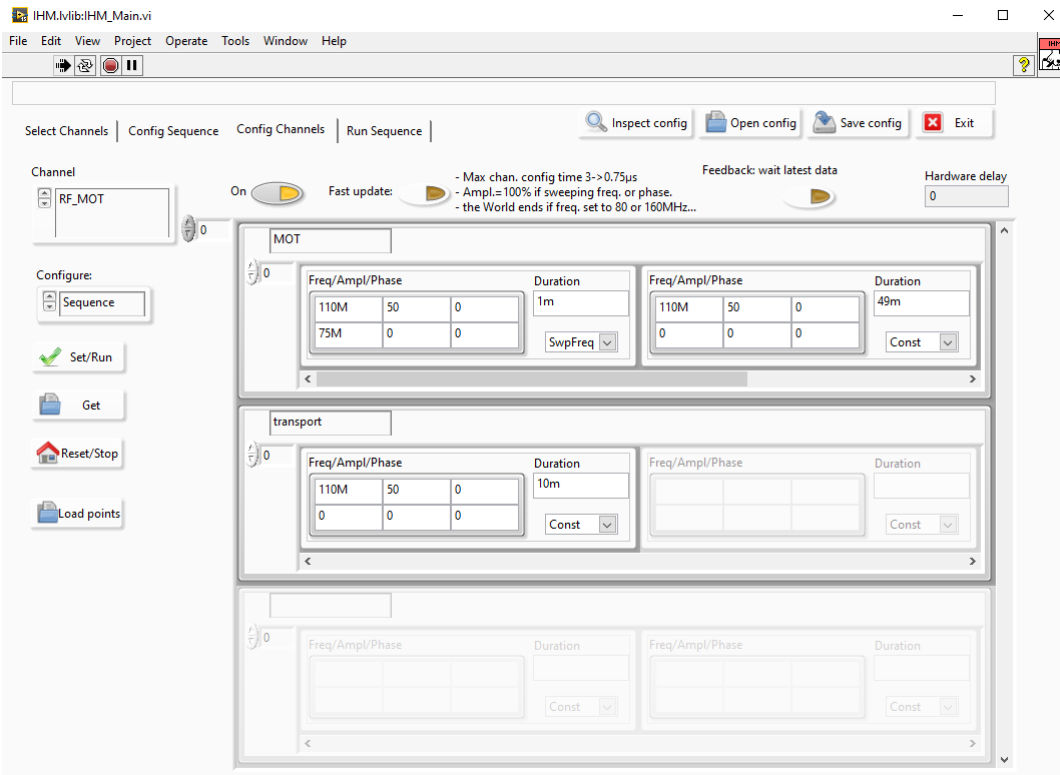


Figure 2.16: Vito, Config Channels.

Chapter 3

Preparation of an atomic ensemble inside the science cavity

Contents

3.1 Magneto-optical traps	57
3.1.1 Atomic beam: 2D MOT	58
3.1.2 3D Magneto-optical trap	59
Absorption imaging	60
Compression and optical molasses	61
Magnetic field compensation	62
3.2 Optical dipole traps	64
3.2.1 Conveyor belt	65
Transport	66
Longitudinal trapping frequencies	67
3.2.2 Crossed-dipole trap	67
3.3 Degenerate Raman sideband cooling	69
3D optical lattice	69
Raman transitions	70
Experimental result	71

This new chapter focuses on the preparation of a small cold and dense atomic cloud in our science cavity. We want to work in a regime where the number of Rydberg polaritons through the resonator is limited to one. For this purpose, we use an atomic ensemble smaller than the Rydberg blockade radius. The size of the blockade sphere depends on several parameters but the order of magnitude is $R \simeq 20 \mu\text{m}$ for the 100S Rydberg state⁽¹⁾. Once this size is fixed, the atomic density directly sets the coupling between the cavity and the atomic sample. We are thus free to explore the response of our system in several coupling regimes with density values up to $4 \times 10^{11} \text{ cm}^{-3}$ ⁽²⁾. The last parameter of interest is the temperature of the cloud that we managed to decrease to $\simeq 2 \mu\text{K}$. At this temperature, the Doppler contribution and the inhomogeneous lightshift of the trap are small enough to not broaden too much the Rydberg linewidth.

⁽¹⁾ $C_6 = 56 \text{ THz } \mu\text{m}^6$ for a linewidth of $\Gamma_{EIT} = 2\pi \times 1 \text{ MHz}$, $R = (C_6/\Gamma_{EIT})^{1/6}$.

⁽²⁾ A too important atomic density results in collisions between Rydberg excitations and ground-state atoms, as mentioned in chapter 1, see [108].

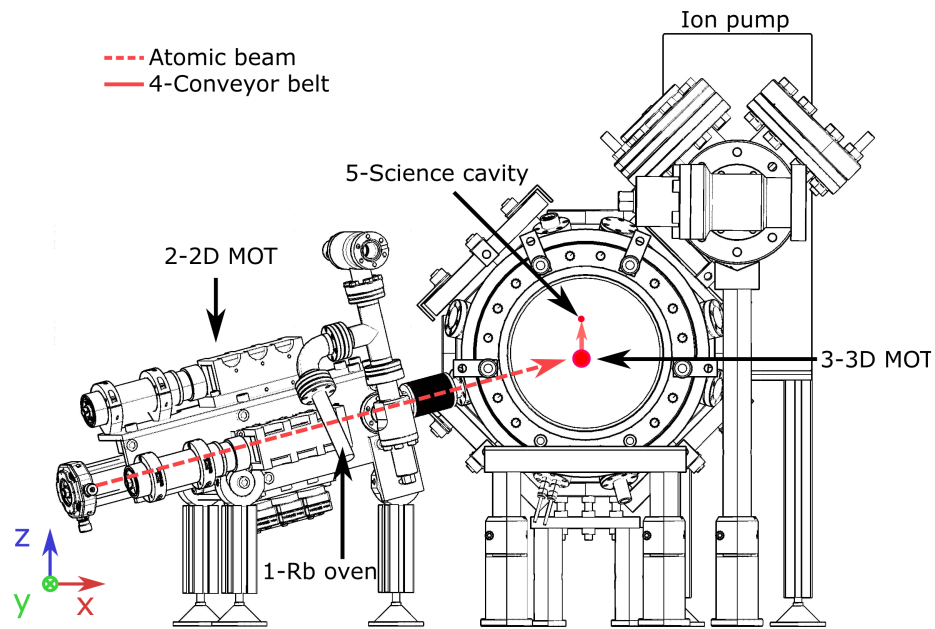


Figure 3.1: Vacuum chamber. 1- A solid sample of rubidium is heated at a temperature of 37 °C in the oven. 2- Atoms are trapped and cooled down in two directions and pushed along the third one in the 2D MOT cell. 3- Our 3D MOT is loaded by the atomic beam in the main vacuum chamber. 4-Cold atoms are transported over 33 mm in a conveyor belt. 5- Once inside our optical cavity, the cloud is cooled down using degenerate Raman sideband cooling and loaded in a crossed dipole trap.

Initially, the hot rubidium vapor is not located in the main chamber to keep the pressure as low as possible in there. Several steps are necessary to cool, transport and trap atoms inside the science cavity, as it is depicted in figure 3.1. First of all, a solid rubidium sample is heated at 37 °C in the oven. The produced gas spreads to the 2D MOT chamber (Magneto-Optical Trap) where it is trapped and cooled down along the transversal axes by retro-reflected beams. A third beam is sent along the longitudinal direction to push atoms: they leave the 2D MOT through a differential pumping tube and enter the main vacuum chamber. The atomic beam generated by the 2D MOT is again trapped and cooled down in a three-dimensional magneto-optical trap (3D MOT) inside the main chamber. The first section of this chapter is devoted to this part of the atomic manipulation, with a review on magneto-optical traps for rubidium 87 and a presentation of the parameters of our setup.

Once atoms are trapped in the 3D MOT, the cloud is loaded into a 1D standing wave optical trap and it is transported 33 mm upwards at the level of the science cavity. This separation between the MOT and the cavity increases the duty cycle of our experiments as it is thus possible to keep atoms in the MOT while doing acquisitions with our science cavity. Finally, the cloud inside the cavity is cooled down by means of the degenerate Raman sideband cooling technique and loaded in a small crossed dipole trap. As mentioned in the beginning, this Raman cooling step reduces the inhomogeneous broadening of the Rydberg linewidth and increases the coherence time of a collective excitation in the gas. In addition, the lifetime inside the dipole trap is about few seconds and the trap induced light shift is low enough to probe several times the same cloud directly in the trap without reloading from the 3D MOT. The second section is dedicated to optical dipole traps, especially atomic transport to the science cavity and the small crossed dipole trap. In the last part of this chapter, we discuss the degenerate Raman sideband cooling protocol used to reach temperature values on the order of 1 µK at the science cavity level.

3.1 Magneto-optical traps

This standard technique in ultra-cold experiments was used for the first time in the experiment conducted by the group of Pritchard [130] and allows one to cool and trap atoms with light. In a magneto-optical trap (MOT), counter-propagating beams produce a frictional force on the atoms induced by the combination of the Doppler effect and radiation pressure. For an atom moving towards one of the beams with a velocity v , the Doppler shift reduces the detuning between the atomic transition and the frequency of this beam proportionally to the velocity. The detuning is on the contrary increased for the second beam propagating in the opposite direction. On average, the atom absorbs thus more photons from the first beam leading to a decrease of the velocity. In this one dimensional case, the force can be written as:

$$F_c(v) = -\alpha v \text{ where } \alpha = -\hbar k^2 s_0 \frac{2\Gamma\delta}{\Gamma^2/4 + \delta^2} \quad (3.1)$$

where \hbar is the reduced Planck's constant, Γ the transition linewidth, c the speed of light, I the light intensity, k the wavenumber and $\delta = \omega_L - \omega_a$ the frequency detuning of the laser ω_L , with respect to the transition ω_a , which has to be negative to ensure that $\alpha > 0$. Finally, s_0 is the saturation parameter of the transition:

$$s_0 = \frac{I/I_s}{1 + 4\delta^2/\Gamma^2} \text{ with } I_s = \frac{\hbar\omega_a^3\Gamma}{12\pi c^2} \quad (3.2)$$

This expression of the light force remains valid as long as $s_0 \ll 1$, meaning that the transition is not saturated by light. In this low saturation limit, the maximum of α is reached when $\delta = -\Gamma/2$.

In addition to this frictional force, a harmonic trap is obtained by adding a magnetic field gradient of slope b to take advantage of the Zeeman effect in the light absorption process. As the Zeeman shift is linear with the magnetic moment μ , one can choose the polarization of counter-propagating beams to be opposite in an absolute referential to address $\sigma+$ and $\sigma-$ transitions. For atoms in the zero magnetic field region, the two beams induce an equal and opposite pressure leading to a zero mean force. However, when atoms are out of this region, the magnetic field gradient breaks this force balance. The detuning is reduced for one of the beams and increased for the other one due to the circular polarization. By adjusting the gradient direction with respect to the choice of polarization between the two beams, the light kicks atoms back to the zero field region. Therefore, this mechanism leads to a harmonic trapping force. In this one dimensional case and in the low saturation limit, this force is given by:

$$F_t(x) = -Kx, \text{ with } K = -k\mu b s_0 \frac{2\Gamma\delta}{\Gamma^2/4 + \delta^2} \quad (3.3)$$

It is assumed here that the cloud width is much smaller than that of the beam, $I(r) \approx I_0$.

We work with rubidium 87, a widely used atom in ultracold atoms experiments because of its well-known atomic structure and the technology maturity of laser diodes to address these atomic resonances. ^{87}Rb fundamental fine doublet is made of the line $5S_{1/2} \rightarrow 5P_{1/2}$ at 795 nm and $5S_{1/2} \rightarrow 5P_{3/2}$ at 780 nm that are called D_1 and D_2 respectively and the population decay rates of this doublet is $\Gamma_1 = 2\pi \times 5.75 \text{ MHz}$ and $\Gamma_2 = 2\pi \times 6.07 \text{ MHz}$. See the detailed article of Daniel Adam Steck on Rubidium 87 [131] for further information about it. In the context of a magneto-optical trap, the D_2 line is preferred due to the existence of a cycling transition $|F = 2, m_F = \pm 2\rangle \rightarrow |F' = 3, m_{F'} = \pm 3\rangle$ with the strongest dipole matrix element (stretched states). Atoms fallen in $5S_{1/2} F = 1$ are repumped by a dedicated beam to $5P_{3/2} F' = 2$ state, shown in figure 3.2. The temperature in the Magneto-optical trap is limited by light diffusion such that at the optimum $\delta = -\Gamma/2$, the Doppler temperature for

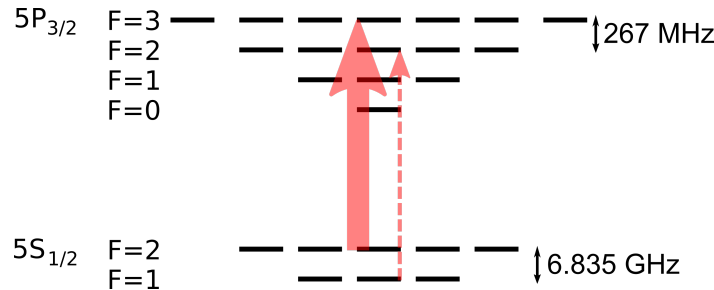


Figure 3.2: MOT beams for the D_2 line of rubidium 87. The rubidium 87 D_2 line is used for the magneto-optical trap with a repumper beam (dashed line) and the trapping/cooling beam (solid).

^{87}Rb is $T = \hbar\Gamma/(2k_B) = 146 \mu\text{K}$, where k_B is the Boltzmann constant. One can switch off the magnetic field to get past this limit by taking advantage of the temperature scaling law in an optical molasses, as we will see for the 3D MOT [132].

3.1.1 Atomic beam: 2D MOT

Our 2D MOT is a compact Low-Velocity Intense Source of atoms (LVIS) for ultracold experiments [133]. The system can be decomposed in two parts.

The first one is a standard two-dimensional magneto-optical trap for rubidium 87 and ensures trapping and cooling in the transverse plane of the setup. The repumper applied on $5^2\text{S}_{1/2}, F = 1 \rightarrow 5^2\text{P}_{1/2}, F' = 2$ is generated by an external cavity laser diode (ECDL, Toptica DL Pro) and the MOT beam is provided by a taper-amplified ECDL (Toptica TA Pro), see chapter 2 for more information about our lasers, section 2.2.1. This DL pro is locked on our ultra-stable cavity and it is used as a reference for the TA pro (phase lock 6.8 GHz below). Both the power of the MOT beam and its frequency can be adjusted by a double-pass Acousto-Optic Modulator (AOM) with a frequency shift between 150 and 250 MHz. The intensity of the repumper beams is also controlled by a single-pass AOM. Repumper (total output of 400 μW) and MOT (50 mW) beams are combined and sent through two fibers to the two transversal axes of the 2D MOT system.

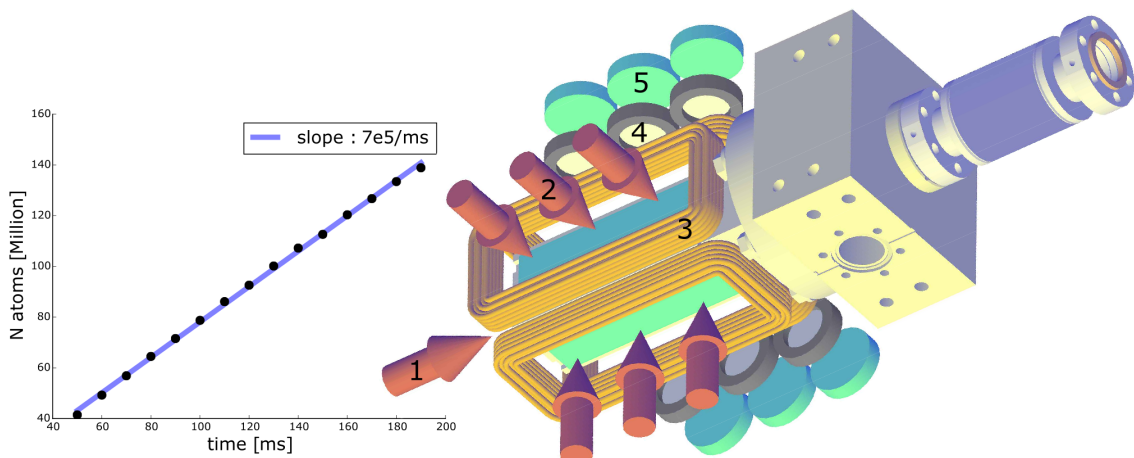


Figure 3.3: 2D MOT drawing and 3D MOT loading rate. Left- Loading rate of the 3D MOT by the atomic beam in the linear regime. Right- Simplified drawing of the 2D MOT: pusher laser (1), transverse cooling beams (2), anti-Helmholtz coils (3), quarter-wave plates (4) and mirrors (5).

Along each of these two axes the output light is split in three parts by unpolarizing beam splitters to enlarge the trapping area ($\simeq 13$ mm waist) all along the vacuum cell where rubidium vapor is located. This light is then retro-reflected and its polarization is controlled by quarter wave-plates. A simplified drawing of the 2D MOT is shown in figure 3.3. Finally, two pairs of coils in anti-Helmholtz configuration generate a magnetic field gradient of 8.3 G cm $^{-1}$ with a current of 2.5 A.

The glass cell itself is made of BK7 antireflection-coated windows and was glued on a titanium frame (same expansion coefficient). It is connected to the rubidium oven where the solid sample is heated at 37°C to produce a hot vapor. Finally, the pressure inside the 2D MOT is $\sim 10^{-7}$ mbar and is maintained by the differential pressure existing within the main chamber.

Along the third axis, a collimated beam crosses the glass cell to arrive at the level of a mirror with a 1 mm-diameter hole in its center. This resonant light exerts radiation pressure on the atoms by momentum transfer. In a retro-reflected configuration, atoms are equally kicked in the two opposite directions resulting in a zero mean force. Here, the part of the beam going through the hole breaks this balance and induces a force accelerating the atoms:

$$F_p = \frac{\Gamma}{2} \hbar k \frac{s_0}{1 + s_0} \text{ at } \delta = -3\Gamma \quad (3.4)$$

This acceleration is maintained by the repumper beams and stops as soon as atoms leave the 2D MOT, with a velocity of 6 m s^{-1} . The atomic source is connected to the chamber by a flexible port aligner and rests on adjustable feet to align the atomic jet with respect to the main chamber. The power and detuning of repumper and MOT beams were optimized via the loading rate of the 3D magneto-optical trap inside the main chamber, $\approx 7.10^8\text{ s}^{-1}$ (see left panel in figure 3.3).

3.1.2 3D Magneto-optical trap

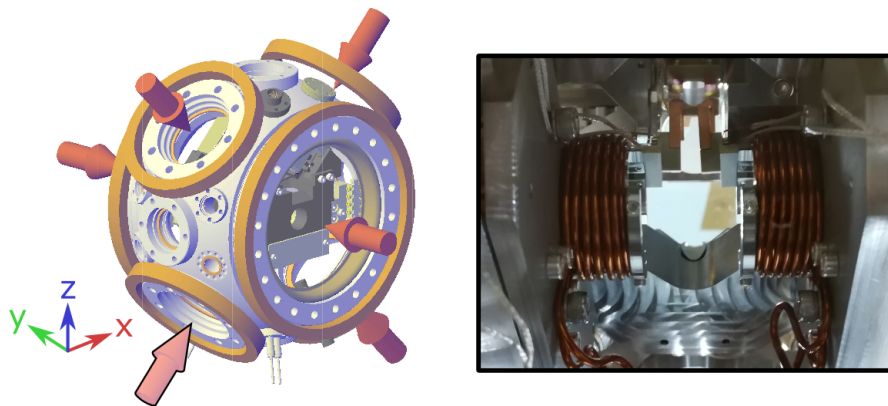


Figure 3.4: Magneto-optical trap setup. Left- The vacuum chamber with the six MOT beams (red arrow) and the six compensation coils (orange). Right- MOT coils inside the vacuum chamber, image taken from the arrow circled in black on the left drawing.

The first trap in the main vacuum chamber is a three-dimensional magneto-optical trap. Its role is to act as a reservoir of cold atoms to rapidly reload atoms inside the science cavity. The MOT and repumper beams come from the same lasers as those of the 2DMOT. The frequency and the power of the MOT beams are adjusted by a double-pass AOM while the repumper is only controlled in intensity by a single-pass AOM. Repumper and MOT beams

are combined by a Schäfter-Kirchhoff variable fibered splitter (2 inputs-6 outputs). Each output beam contains approximately 12 mW of TA pro and 200 μW of repumper and has a 7.5 mm radius after collimation. The beams are distributed along three orthogonal axes. This splitter has two photodiodes for each input beam, that are used to lock the intensity via a PID loop feeding back the associated AOM. The magnetic field gradient is generated by a pair of coils placed inside the vacuum chamber to reduce the value of the current, especially to avoid water/air cooling. These two coils are in anti-Helmholtz configuration, each made of 12 turns of copper wire and powered via a feedthrough by a DC Power supply from Delta Elektronika (SM 15-100) with a homemade analog electronic circuit for current control. The ground of this supply is isolated from others electrical devices by an opto-isolator to protect them from voltage or current spikes. The typical current sent through the MOT coils during a sequence is around 7 A resulting in a magnetic gradient of 8 G cm^{-1} with a 25 μs switch time. The magnetic field zero is obtained by three pairs of coils in Helmholtz configuration, placed outside the chamber. The method used to properly compensate stray magnetic fields is detailed in a following subsection. MOT beams, MOT coils and compensations coils are all shown in figure 3.4.

Absorption imaging

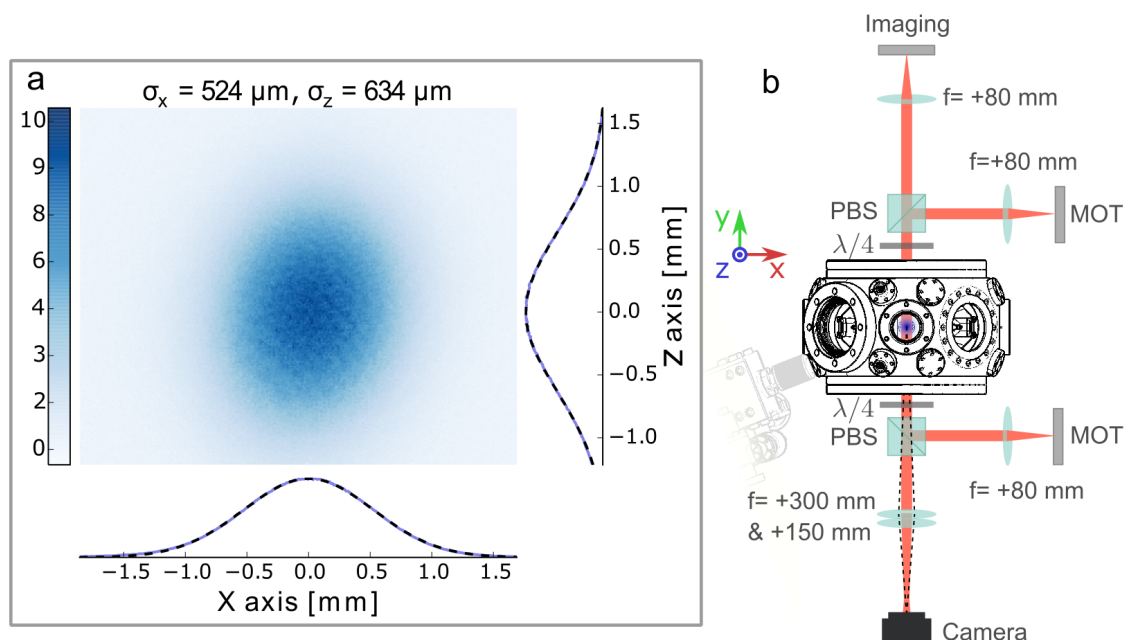


Figure 3.5: Absorption imaging. Left- Absorption imaging after a 10 ms time of flight. The color bar represents the integrated atomic density in μm^{-2} . The Gaussian rms width σ_x is obtained by a Gaussian fit of the integrated image along the z axis and vice versa for σ_z . Right- Imaging setup: PBS for Polarizing beam splitter and $\lambda/4$ for quarter-wave plate. The imaging light is combined to the MOT beam with a PBS. Then it crosses the cloud and is acquired on the Point Grey camera.

A Point Grey camera (CM3-U3-13Y3) is aligned with one of the 3D MOT beams to access some parameters of the cloud by absorption imaging [134]. A resonant light is combined with the horizontal arm of our MOT via a polarizing beam splitter. Light is partially absorbed by the atomic sample which locally reduces its intensity. On the other side of the chamber, the beam is then collected by two thin lenses in contact and measured by the camera (1/2 magnification). This contact configuration is preferred to reduce optical aberrations in the

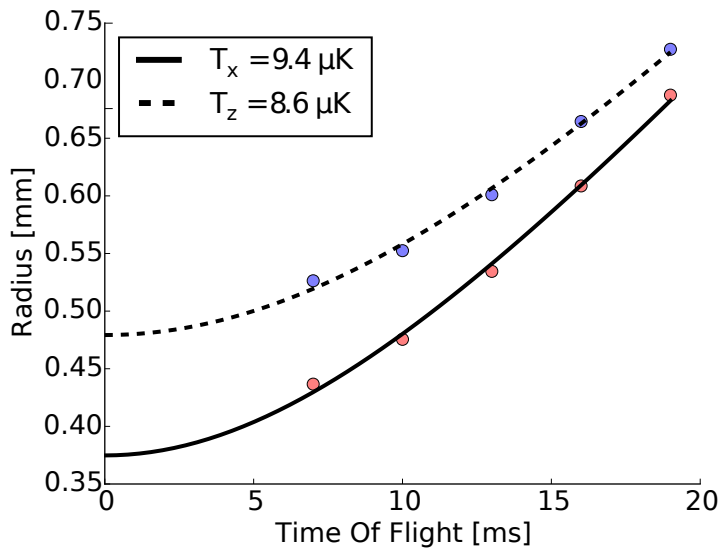


Figure 3.6: Time of flight. Estimation of the temperature along the two axes perpendicular to the imaging beam. The fitting function is defined by equation 3.6 and only depends on two parameters: the temperature and the initial size of the atomic cloud. We performed this measurement after the optimization of the compression and molasses steps with a fine magnetic field compensation, see following subsections.

imaging. Finally, this image is compared to a reference image without any atom taken 100 ms later. The ratio pixel by pixel between these two images gives access to the optical depth (OD) of the cloud:

$$\frac{I(x, y)}{I_0(x, y)} = e^{-OD}, \text{ with } OD = -\sigma_0 \int_l dz n(x, y, z) \quad (3.5)$$

where n is the atomic density, $\sigma_0 = 2.907 \times 10^{-9} / \text{cm}^2$ is the resonant cross section. It is possible to infer the total number of atoms, the integrated density $n(x, y)$ and the transverse Gaussian size of the cloud, as shown in figure 3.5.

On top of that, we can estimate the temperature of the cloud by a time of flight technique: the size of the cloud is measured for different delays between the end of the MOT step and the imaging step. The expansion of the cloud is then given by:

$$\sigma_{rms}(t) = \sqrt{\frac{k_B T}{m} t^2 + \sigma_{rms}(0)^2} \quad (3.6)$$

where $m = 1.44 \cdot 10^{-25} \text{ kg}$ is the atomic mass of rubidium 87 and σ_{rms} is the rms width of the atomic density distribution. This method is illustrated in figure 3.6 to estimate the temperature after a molasses step.

Compression and optical molasses

In order to transport as many atoms as possible to the cavity, the MOT undergoes a compression phase followed by a molasses step to get past the Doppler temperature. The loading of the 3D MOT by the 2D MOT is done in 50 ms. The MOT beams are 3Γ red-detuned from $5S_{1/2}, F = 2 \rightarrow 5P_{3/2}, F' = 3$ line while 2D MOT beams are 10 MHz red-detuned to reduce heating. The repumper intensity is kept above saturation with 6 mW cm^{-2} and 2 mW cm^{-2} respectively for the 2D MOT and our 3D MOT, but the cloud is essentially insensitive to

that parameter. During this loading, the magnetic field gradient is 8 G cm^{-1} for both the 2D MOT and the 3D MOT. The second step is the compression: during one millisecond, the magnetic field gradient is swept from 8 to 21 G cm^{-1} with the aim to increase the atomic density in the trap, while others parameters are kept constant. In the last step, the magnetic field is adiabatically switched off in two milliseconds to produce a molasses to get past the Doppler limit ($T=146 \mu\text{K}$). As explained in the article of Jean Dalibard [135], the reachable temperature in the molasses scales as $T \propto I/\Delta$ where I is the intensity of the MOT beam and Δ is the detuning. In the first millisecond, the frequency of the MOT beam is swept from -3Γ to -12Γ (red-detuned). Its intensity is linearly decreased by a factor 30 during two milliseconds and at the same time, the repumper intensity is also decreased close to zero. After this sequence, the cloud temperature is $9 \mu\text{K}$, the number of atoms reaches $N \simeq 30.10^6$ with a Gaussian rms width of 0.5 mm. A table summarizes the range of the main parameters of our magneto optical trap.

Number of atoms	30.10^6
Gaussian rms width	0.5 mm
Density	10^{10} cm^{-3}
Temperature with molasses	$9 \mu\text{K}$
Magnetic field gradient	$8\text{-}21 \text{ G cm}^{-1}$
MOT beam detuning	$3\Gamma\text{-}12\Gamma$
MOT beam intensity	17 mW cm^{-2}

Table 3.1: Main numbers for the 3DMOT after a 50 ms loading.

Magnetic field compensation

One important step for the optimization of the MOT is to cancel residual magnetic fields at the cloud center. Any offset in the magnetic field will move the center of the magnetic trap resulting in a heating of the cloud.

Three pairs of coils in Helmholtz configuration were attached around the viewports of the chamber, the two DN 160 and the four DN 60 in diagonal (figure 3.4) to produce a constant compensation field in the three dimensions. Each pair is driven by a High Finesse bipolar current power supply controlled by an analog voltage ($1\text{A}\Leftrightarrow5.5\text{V}$). In order to obtain the value of the magnetic field at the cloud position, we looked at the Zeeman splitting of the transitions between $5S_{1/2}$ hyperfine sub-levels ($6.834\,683 \text{ GHz}$, $F = 1 \rightarrow F = 2$). The Zeeman splitting between states $|L = 0, F = 1, m\rangle$ and $|L = 0, F = 2, m'\rangle$ is given by:

$$\delta f_{m,m'} = f_{m'} - f_m = \frac{\mu_B}{\hbar} g(m' + m) |\mathbf{B}| = \delta f_{0,1}(m + m') \quad (3.7)$$

where $|\mathbf{B}|$ is the norm of the magnetic field, μ_B is the Bohr magneton and g is the Landé factor⁽³⁾ of the hyperfine state $5S_{1/2}$, $F = 2$ in Eq. 3.7.

The sequence starts by a simple MOT loading by the 2D MOT in 50 ms. Then, the magnetic field gradient and all beams are switched off except for the repumper to bring the cloud in $5S_{1/2}$, $F = 2$ state ($\sim 100 \mu\text{s}$). Next, the repumper is switched off while the microwave field is emitted from an antenna close to the vacuum chamber during $\sim 1 \text{ ms}$. The 6.834 GHz microwave signal is generated by a Windfreaktech Synth HD, mixed with an intermediate frequency signal (IF range: 1 kHz to $\sim 100 \text{ MHz}$) to adjust the frequency. The overall signal is amplified (KUHNE electronic RF power amplifier⁽⁴⁾, gain: + 40 dBm) before

⁽³⁾here we have $g \equiv g_{F=2} \approx -g_{F=1} \approx \frac{1}{2}$.

⁽⁴⁾ref KUPA640720-10A

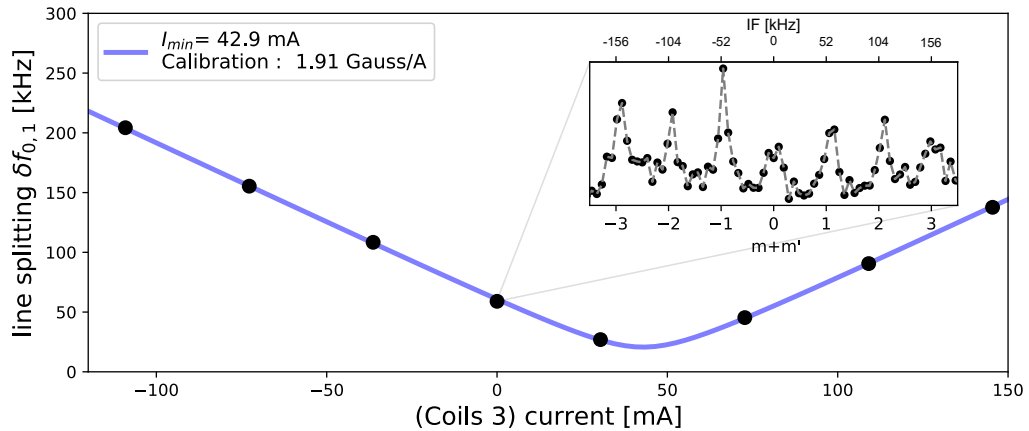


Figure 3.7: Magnetic field compensation. Radio-frequency measurement of the hyperfine splitting. Main plot- The splitting frequency of ${}^5S_{1/2}$ hyperfine levels $\delta f_{0,1}$ as a function of the current in the Y compensation coils (data in black, fit in blue). The fitting function is $f(I) = \mu_b g / h \sqrt{p_{cali}^2 (I - I_{min})^2 + B_{off}^2}$, with three free parameters : p_{cali} , I_{min} and B_{off} . Top right corner - Illustration of the splitting between the seven hyperfine lines as expected from equation 3.7.

emission. Provided that the microwave signal is resonant with one hyperfine transition, a part of the cloud is pumped in $F = 1$. A resonant beam removes atoms in $F = 2$, then atoms in $F = 1$ are repumped in $F = 2$ and the number of atoms in $F = 2$ is measured by imaging. We obtain the hyperfine spectrum of the ${}^5S_{1/2}$ state by repeating this procedure for several values of the microwave frequency, see top right corner plot in figure 3.7. This measurement is performed for different current values for each pair of compensation coils to extract the optimal value of the current in the three directions. An example is shown in figure 3.7, for one pair of coils.

Once the optimization is done, the full width at half maximum of the transition is ~ 50 kHz and the frequency splitting (~ 12 kHz) gives a residual magnetic field of ~ 17 mG.

3.2 Optical dipole traps

The previous section discussed the role played by radiation pressure in magneto-optical trap mechanisms. There is in fact a second light force, coming from the interaction between light and the induced atomic dipole. In 1970, Arthur Ashkin proposed to make use of this force to trap small dielectric objects with the so-called optical tweezers [136]. This method is nowadays massively employed in chemistry, physics and biology to manipulate atoms [137], cells [138], etc.

We take advantage of this force to first transport atoms from the 3D MOT to the science cavity and then to create a conservative potential for our atomic sample inside the resonator. The potential describing this effect takes a simple form for rubidium atoms when the detuning between the laser frequency and the optical transition is big compared to the hyperfine splitting [139]. It is then simply given by:

$$U(\vec{r}) = \frac{\pi c^2 \Gamma}{2\omega_0^3} \left(\frac{2}{\Delta_2} + \frac{1}{\Delta_1} \right) I(\vec{r}) \quad (3.8)$$

where \vec{r} is the position vector, $\Delta_{1,2} = \omega_L - \omega_{1,2}$ is the detuning between the laser of angular frequency ω_L , and the $D_{1,2}$ line with angular frequency $\omega_{1,2}$. Here, $\omega_0 \approx \omega_{1,2}$ because $\delta = \omega_1 - \omega_2 \ll \omega_{1,2}$ and we assume that light is linearly polarized. From equation 3.8, we see that atoms are attracted towards increasing intensity for a red-detuned potential, $(2/\Delta_2 + 1/\Delta_1) < 0$, and repelled from high intensity regions in the case of a blue-detuned potential, $(2/\Delta_2 + 1/\Delta_1) > 0$. From now, we will only consider red-detuned optical dipole traps.

The propagation of a beam in the small-angle approximation obeys the paraxial wave equation discussed in more details in chapter 2, see equation 2.2. One of the solutions to this equation is the Gaussian beam corresponding to the profile of our laser beams and to the output mode of our single-mode optical fibers, see figure 3.8. For a light beam with a wavelength λ , we recall that the intensity profile is:

$$I_1(z, r) = I_0 \left(\frac{w_0}{w(z)} \right)^2 e^{-2r^2/w(z)^2} \quad (3.9)$$

where $r = \sqrt{x^2 + y^2}$ is the radial coordinate, $w(z) = w_0 \sqrt{1 + (z/z_r)^2}$ is the spot size parameter and z_r is the Rayleigh range.

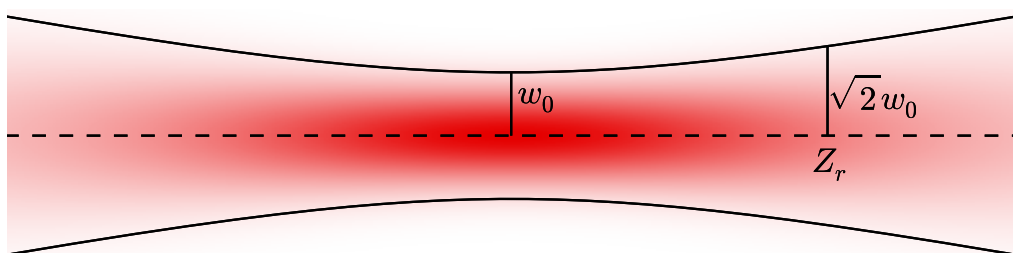


Figure 3.8: Gaussian beam. The intensity profile for a Gaussian beam of waist w_0 is in red while $w(z)$ is plotted in black as a function of z . For a red-detuned beam, a dielectric object is attracted towards the maximum of the intensity, here at the waist position.

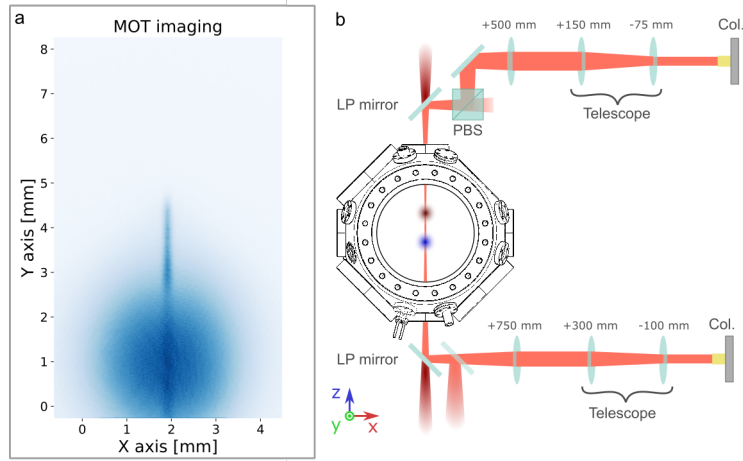


Figure 3.9: Conveyor belt. a- Our conveyor belt leaving the Magneto optical trap (imaging of the MOT). b- Optical setup, Col.: collimator. PBS: polarizing beam splitter. LP: 900 nm low-pass mirror. The conveyor beams are sent to the chamber table through two fibers and are collimated by two Schäfter and Kirchhoff collimators with an output waist of 1 mm. For each arm, a telescope adjusts the size of the beam and a third lens focuses the light in between the resonator and the 3D MOT with a 70 μm waist.

For instance, in the case of a single beam and in the limit where $z/z_r \ll 1$ and $r/w_0 \ll 1$, one recovers a harmonic trap in the three directions:

$$U(r, z) \approx -U_0 + \frac{1}{2}m(\omega_z^2 z^2 + \omega_r^2 r^2) \text{ with } \omega_r = \sqrt{\frac{4U_0}{mw_0^2}}, \omega_z = \sqrt{\frac{2U_0}{mz_r^2}} \quad (3.10)$$

where ω_r and ω_z are the radial and longitudinal angular frequencies associated to the trap and U_0 is the absolute value of the potential in its center $U(0, 0)$. This elementary solution corresponds to an optical tweezer.

This process originates from the refraction of light induced by the small dielectric medium, causing a change in the momentum of the light. The law of action and reaction implies that the small particle is also subjected to an equal and opposite force. As it is, there is so far no absorption of light in the process. However, the frequency detuning has a large but finite value which results in a low but non-zero probability of absorption. This phenomenon increases the velocity of our atoms and eventually induces losses. We can define a spontaneous emission rate, equivalent to a heating rate, to take this effect into account. For Alkali atoms its expression is:

$$\Gamma_{sc}(\vec{r}) = \frac{\pi c^2 \Gamma^2}{2\hbar\omega_0^3} \left(\frac{2}{\Delta_2^2} + \frac{1}{\Delta_1^2} \right) I(\vec{r}) \quad (3.11)$$

This rate has to be as small as possible if we want to trap atoms with an optical tweezer and this is even more true if we want to keep them in a specific atomic state. For high detuning values, where $\Delta_1 \approx \Delta_2$, there is a simple scaling factor between this quantity and the trap depth: $\hbar\Gamma_{sc} = GU/\Delta$ where $U \propto 1/\Delta$. There is an obvious advantage to go as far as possible to bring this rate as close to zero as possible. However, the finite amount of available power for our dipole traps imposes a trade-off depending on the context and needs.

3.2.1 Conveyor belt

33 mm separate the atoms inside our 3D MOT from the optical cavity. Two counter-propagating beams along the vertical axis are used as a dipole trap to transport atoms

over this distance. We will now call it conveyor belt and the intensity profile is:

$$I_{conv}(r, z) = 4I_0(r, z) \cos(kz - \delta\omega t/2 + \phi)^2 \quad (3.12)$$

Here, we assume that the two beams have the same intensity I_0 , k is the modulus of the wave vector, ϕ is a phase, and $\delta\omega = \omega_1 - \omega_2$ is the frequency detuning between the two beams. The taper-amplified Toptica laser used to produce this dipole trap is tuned between the D_1 and D_2 line at $\lambda = 782.9$ nm, in the red-detuned regime. This configuration corresponds to a 1D lattice of trapping along the z axis. The maximum available power in one arm is 250 mW with a 70 μm waist leading to $z_r = 19$ mm. To obtain a good overlap of the conveyor with the MOT but also between the two arms, we first align the lower arm of the conveyor on the MOT with a camera placed on the upper arm. Once this is done, the upper part is adjusted to maximize the coupling of light in the lower collimator, see figure 3.9.

Transport

If we consider the situation where $\delta\omega \neq 0$, the intensity maxima move at a velocity $v = \delta\omega/(2k)$ and take away the cloud just as a conveyor belt would do. This method ensures fast transport of a high amount of atoms, $\sim 10^6$, with a high density $\sim 1 \times 10^{11} \text{ cm}^{-3}$ and a reasonable temperature $T \approx 50 \mu\text{K}$ for a symmetric configuration (i.e. when the waist is placed halfway, see next subsection). During transport over a distance d , atoms are first accelerated with a frequency sweep $\delta\omega = Rt$ during a time t_0 and then decelerated with the same slope R during t_0 . In these conditions, atoms undergo an acceleration $a = d/t_0^2$. Of course, we want the transport step to be as short as possible but diminishing the step duration increases the acceleration. In the reference frame of an atom, the acceleration shifts the potential by a linear term in z and thus reduces the depth of the trap in one direction [140]. We measured the number of transported atoms versus the total duration of the step $t_{tot} = 2t_0$ and found a good compromise at $t_{tot} = 10$ ms, shown in figure 3.10.

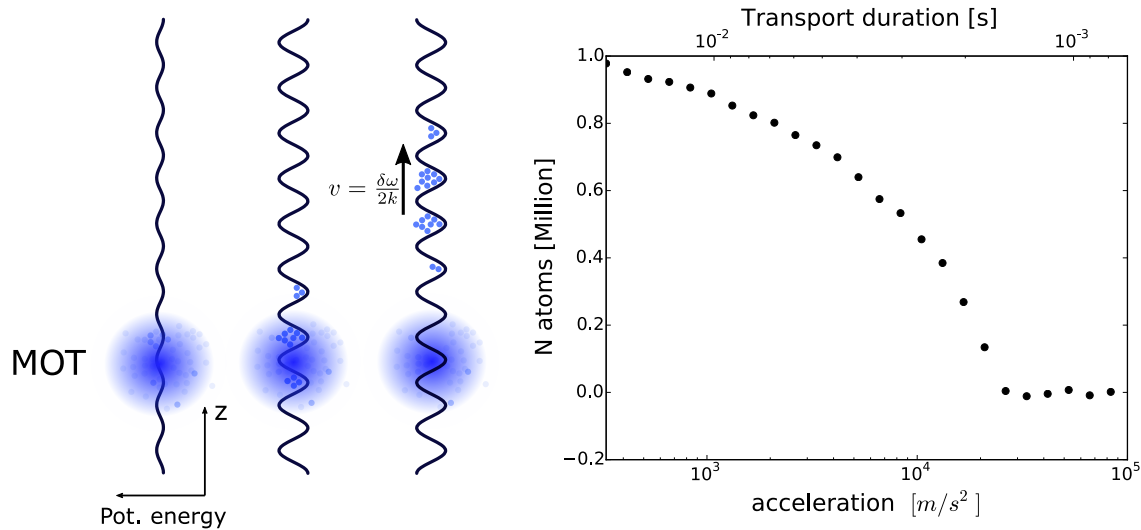


Figure 3.10: Transport with the conveyor belt. Left- Main steps for the transport. First, the conveyor belt amplitude is ramped up to trap atoms at the MOT position. We then shift the frequency of the lower arm, $\delta\omega$, to induce a displacement at a velocity $v = \delta\omega/(2k)$. Right- the number of atoms at the resonator level as a function of the acceleration, or equivalently the transport duration.

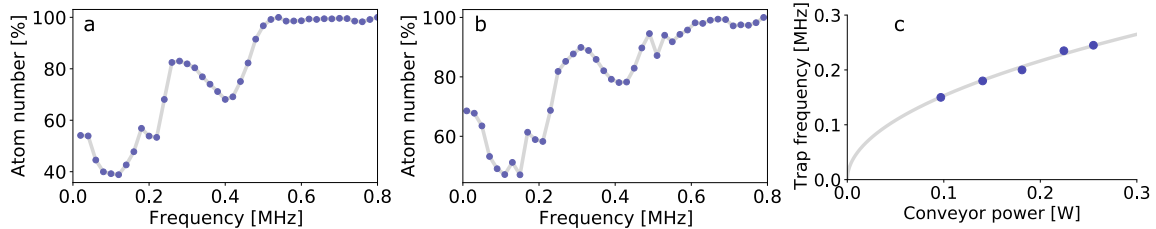


Figure 3.11: Longitudinal frequencies . a- Amplitude modulation of the lower arm at full power with atoms close to the 3D MOT. The atom number is recorded by the MOT camera for several values of the modulation frequency. A resonance is visible for a modulation frequency of 420 kHz corresponding to twice the trapping frequency. b- The same plot but at the cavity level. We observe the same resonance, as expected for a waist located halfway between the MOT and the resonator. c- Trap frequency as a function of the power in the conveyor arms at the MOT position P . Here, the fitting function is $C\sqrt{P}$. Note: we took the last measurements before adjusting the position of the waist, the maximum frequency is now about 210 kHz.

Longitudinal trapping frequencies

Let us now look at $\delta\omega = 0$, where the two beams form a standing wave. We want to check that the focus of our conveyor belt is halfway between the 3D MOT and the science cavity to reduce the compression-induced heating while transporting enough atoms. In this case, the longitudinal trapping frequencies should be identical at the MOT and cavity positions. This information is also important for the Raman cooling step described in section 3.3.

One can expand the cosine function around a maximum at a distance z of the waist position. The longitudinal frequency is then:

$$\omega_z = k\sqrt{\frac{2U_z}{m}} \text{ with } U_z = \frac{U_0}{1 + (z/z_r)^2} \quad (3.13)$$

where U_z is the trap depth at position z ⁽⁵⁾, constant over the typical length of the trap since $z_r \gg \lambda$. The radial frequency at a distance z is obtained from equation 3.10 by substituting U_0 with U_z and the waist w_0 by the spot parameter $w(z)$: $\omega_r = \sqrt{4U_z/(mw(z)^2)}$.

The longitudinal frequency can be measured by mean of parametric heating. The intensity is modulated at a given frequency which induces losses when this frequency corresponds to twice the trapping frequency [141]. It is shown in figure 3.11 where we measured the frequency both in the MOT and inside the science cavity. At full power, the longitudinal trapping frequency has a value of 210 kHz in the MOT and at the science cavity level. This indicates that the waist of the beam is indeed standing in between the 3D MOT and the science cavity. We do not have access to the radial frequency with this method because of its low value ($\omega_r/\omega_z = \sqrt{2}/(kw(z)) \ll 1$).

3.2.2 Crossed-dipole trap

Once atoms are transported inside the cavity, we want to confine them within a unique blockade volume. For the 100 Rydberg state, the interaction coefficient is $C_6 = 56 \text{ THz } \mu\text{m}^6$ corresponding to a e^{-2} radius⁽⁶⁾ of 20 μm for a 1 MHz linewidth. For this purpose, we thus employ two crossing beams at 1064 nm with opposite polarizations to avoid interference. This is equivalent to two superimposed optical tweezers, that we mentioned in the introduction of this section. The trap is loaded after a step of degenerate Raman sideband cooling to

⁽⁵⁾Here $z = 0$ is the position of the waist.

⁽⁶⁾the distance at which the atomic density distribution falls to $1/e^2$ of its maximum.

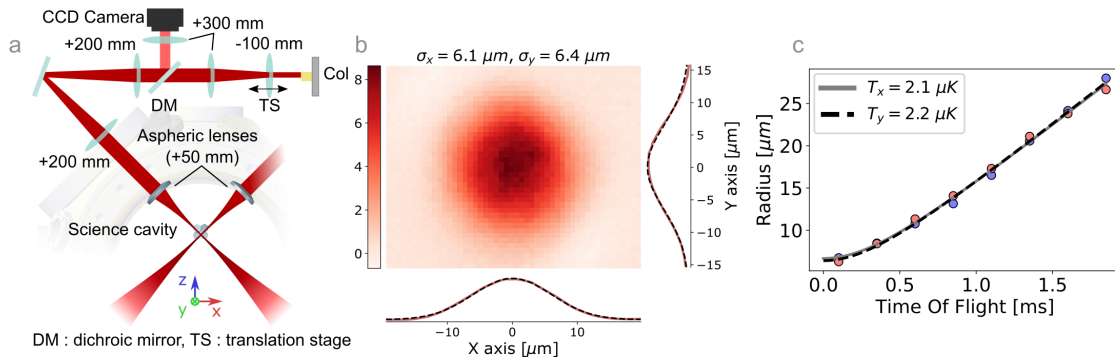


Figure 3.12: 1064 nm crossed-dipole trap . a- Optical setup: two beams are focused at the science cavity position by two aspheric lenses placed inside the main vacuum chamber. The first lens after the collimator stands on a translation stage to adjust the size of the beam at the crossing point. These two in-vacuum lenses are also used for a high-resolution imaging of the small cloud. b- High resolution imaging: imaging after a $100 \mu\text{s}$ time-of-flight. The color bar on the left gives the atomic density integrated along the optical path in μm^{-2} . c- Temperature: estimation of the temperature after a sequence of degenerate Raman sideband cooling followed by a 50 ms waiting time inside the dipole trap.

reduce the temperature of the cloud to $\simeq 2 \mu\text{K}$ (see the next section). We are thus able to reduce the depth of the trap to $25 \mu\text{K} = U_0/k_b$ and we can directly probe the atomic sample inside the trap since the differential light shift is about 50 kHz for atoms at a temperature of $2 \mu\text{K}$. Another advantage of the Raman cooling step is to increase the density by alternatively cooling and compressing. In our case we managed to reach an atomic density of $4 \times 10^{11} \mu\text{m}^{-3}$ in the small 1064 trap. In practice, each beam is made of 50 mW focused on a $\sim 20 \mu\text{m}$ waist resulting in a $7 \mu\text{m}$ Gaussian rms width for the atomic density distribution, as shown in figure 3.12. Notice that we are able to adjust the size of the cloud from $7 \mu\text{m}$ down to $5 \mu\text{m}$ by tuning the position of a lens attached to a translation stage in each arm⁽⁷⁾.

⁽⁷⁾We are here limited by the density and the need to keep a thousand atoms within the trap to maintain a sufficient atom-cavity coupling ($\approx 2\pi \times 10 \text{ MHz}$).

3.3 Degenerate Raman sideband cooling

The degenerate Raman sideband cooling (DRSC) technique consists in the accumulation of atoms in the vibrational ground state of an isotropic three-dimensional trap [142]. An all optical cooling protocol reaching quantum degeneracy has recently been implemented with this method [143]. This cooling approach is indeed very efficient to get past the temperature lower bound set by light diffusion in dense atomic gases. With a few micro Kelvin cloud in our case, the contribution of the Doppler effect to the inhomogeneous broadening of the Rydberg linewidth is limited to a few tens of kilohertz. The latter is a crucial parameter that sets the level of electromagnetically-induced transparency, the dynamics of our polaritons and the blockade volume. It also enables us to probe the cloud directly in the small crossed dipole trap at 1064 nm as the trap depth can be reduced to 25 μK and thus reach a satisfying differential light shift value ($\lesssim 50 \text{ kHz}$).

3D optical lattice

As mentioned in the introduction, atoms have to be trapped in a 3D optical lattice. More precisely, atoms must be in the Lamb-Dicke regime where the recoil energy, induced by light, is much smaller than the energy spacing of the trap $\hbar\omega_t$. In this limit, the energy transferred by one absorption process is negligible compared to the trapping strength. It is concretely expressed by the condition:

$$\eta^2 = \frac{E_R}{\hbar\omega_t} \ll 1 \quad (3.14)$$

where the recoil energy is simply $E_R = \frac{\hbar^2 k^2}{2m}$ and k is the wave vector modulus of the electromagnetic field transferred to an atom. In other words, the coupling of the electromagnetic field with the motion of an atom can be treated as a perturbation of the trapping Hamiltonian. The ordering is given by the η parameter and consequently the first non-trivial term of this perturbation involves a change of one motional quantum only.

In our case the 3D lattice is made of the conveyor belt light for the confinement along the z axis, in addition to four others beams with a 150 μm waist to ensure confinement within the (x, y) plane. The first pair of beams comes along the diagonal MOT beams with a polarization parallel to y to trap atoms in the x direction and $\sim 3 \text{ mW}$ in each arm. On top of that, the second pair propagates in the (x, y) plane with a polarization along z with $\sim 10 \text{ mW}$ per beam. One of its arms makes an angle $\theta = 21^\circ$ with the y axis, while the other arm is tilted by the same amount but in the other direction. The full configuration is depicted on figure 3.13.

The set of beams for the horizontal lattice comes from a DL pro, phase locked 16 GHz above the $F = 2 \rightarrow F' = 3$ hyperfine transition of the D_2 line, on the Repumper DL pro at 780 nm. The two pairs are spectrally separated: each goes through a 110 MHz double-pass AOM but aligned on opposite orders, leading to a 440 MHz shift. On one hand, the relatively small detuning on both the D_1 and D_2 lines reduces the amount of necessary trapping power. On the other, it induces an important spontaneous scattering that limits the lifetime within the trap. We work with a blue-detuned lattice where atoms are attracted towards minima of the electromagnetic field to reduce this effect. Since the 3D lattice is also responsible for the Raman process, one could think that it also reduces the Raman rate, but we will see that it is not true. Despite the blue detuning, the trapping lifetime is still short (about 3 ms). Atoms are thus only loaded in this 3D lattice during a cooling process where the Raman cooling rate overcomes the heating. Finally, the power in each beam is adjusted such that the trap is isotropic. The trapping frequency in each direction is estimated by the parametric heating method introduced in the previous section. We set its value to 180 kHz to ensure

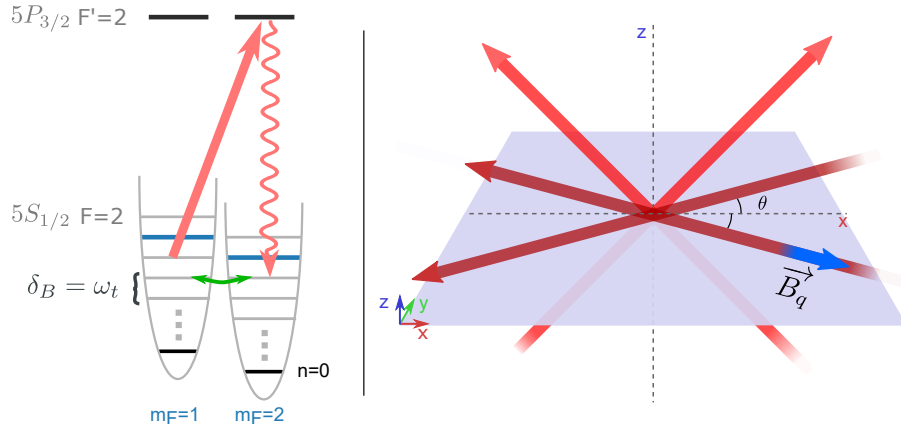


Figure 3.13: Degenerate Raman Sideband Cooling. Left- A magnetic field is adjusted to induce a Zeeman splitting in $5S_{1/2}, F = 2$ equal to the trapping frequency of our isotropic 3D trap. Hence, Raman transitions (in green) can transfer an atom between $|F = 2, m_F - 1, n - 1\rangle$ and $|F = 2, m_F, n\rangle$. A $\sigma +$ polarized beam (red arrow) ensures optical pumping in the stretched state $5S_{1/2}, |F = 2, m_F = 2\rangle$ without affecting the vibrational state of the atom. The combination of the two is equivalent to optical pumping with a dark state corresponding to the stretched state in the lower vibrational state of the trap, $|F = 2, m_F = 2, n = 0\rangle$ (black line). Right- A sketch of the four blue-detuned beams that ensure trapping in the (x,y) plane. The first pair in light red extends in the (z,x) plane with a polarization along y. The second pair is contained in the (x,y) plane with a polarization towards z.

that atoms stand in the Lamb-Dicke regime, the typical recoil energy being of the order of $E_R/h = 10\text{ kHz}$.

Raman transitions

The second ingredient for DRSC is the magnetic field. It has to be tuned to induce a Zeeman splitting matching the trapping frequency for atoms pumped in $5S_{1/2} F=2$. The magnetic field magnitude, around 150 mG, makes it necessary to properly compensate residual magnetic field at the cavity level. We employed the same technique as in the 3D MOT (more details in subsection 3.1.2). When this condition is fulfilled, trapping light can also induce Raman transitions from $|F = 2, m_F, n\rangle$ to $|F = 2, m_F - 1, n - 1\rangle$, n being the quantum number associated to the trap. The Hamiltonian describing this phenomenon, in the far-detuned regime ($\Delta_{1,2} \gg \Delta_{HF}$ ⁽⁸⁾), for rubidium and Alkali atoms is [144, 145]:

$$\hat{H}_R = \frac{id_1^2}{12\hbar} \left(\frac{1}{\Delta_1} - \frac{1}{\Delta_2} \right) \frac{\hat{\mathbf{C}} \cdot \hat{\mathbf{F}}}{\hbar F} \quad (3.15)$$

with $\hat{\mathbf{C}} = \mathbf{E}^*(\hat{r}) \times \mathbf{E}(\hat{r}) = i \operatorname{Im}(\mathbf{E}^*(\hat{r}) \times \mathbf{E}(\hat{r}))$ where \mathbf{E} is the complex electric field.

One sees that it is possible to couple different sublevels m_F with operators \hat{F}_+ and \hat{F}_- by a careful adjustment of the vector $\hat{\mathbf{C}}$. Thus, the Raman light induces transition with $\Delta m_F = \pm 1$ as one can expect in the far-detuned regime where the relevant spin coupled to light is a spin $1/2$ ⁽⁹⁾. Here, the scaling of this energy with respect to the frequency detuning is different from the dipole trap potential and goes to zero more rapidly. This is another motivation to keep our Lattice beams close to one resonance as they also aim to produce Raman transitions.

⁽⁸⁾ Δ_{HF} refers to the hyperfine coupling of the two excited states $5P_{1/2}$ and $5P_{3/2}$.

⁽⁹⁾ J is the good quantum number and $J = 1/2$ in the ground state. A Raman transition can be written $|J, m_j^{(i)}\rangle \rightarrow |J', m_j'\rangle \rightarrow |J, m_j^{(f)}\rangle$ and thus $\Delta m_F = \Delta m_J = 0, \pm 1$.

Let us take the example of a pair of plane waves with linear polarizations and the same intensity for simplicity. In this case, the complex electric field can be written as:

$$\mathbf{E}(r) = \mathcal{E}e^{i\phi_1(r)}\mathbf{u}_1 + \mathcal{E}e^{i\phi_2(r)}\mathbf{u}_2 \quad (3.16)$$

where \mathcal{E} is the amplitude, $\phi_j(r) = \mathbf{k}_j \cdot \mathbf{r}$ and \mathbf{u}_j is a unitary vector along the j^{th} electric field. Consequently, the vector \mathbf{C} is simply:

$$\mathbf{C} = 2i \sin \theta |\mathcal{E}|^2 \sin \delta_\phi(r) \mathbf{u}_\perp \quad (3.17)$$

where θ is the angle between \mathbf{u}_1 and \mathbf{u}_2 , $\mathbf{u}_\perp = (\mathbf{u}_1 \times \mathbf{u}_2) / \|\mathbf{u}_1 \times \mathbf{u}_2\|$ and $\delta_\phi(r) = \phi_1(r) - \phi_2(r) = \|\mathbf{k}_1 - \mathbf{k}_2\| r_\parallel$ is the phase difference between the two optical beams.

If we expand the spatial contribution at the bottom of a blue-detuned trap and re-express the operator position with creation/annihilation operators $\hat{r}_\parallel = \sqrt{\hbar/(2m\omega)}(a + a^\dagger)$, we get the following expression for the Raman Hamiltonian at lowest order:

$$H_{Raman} = \Omega_R a^\dagger \hat{F}_+ + \Omega_R^* a \hat{F}_-, \quad \Omega_R = \frac{\eta d_1^2 |\mathcal{E}^2|}{6\hbar^2 F} \left(\frac{1}{\Delta_1} - \frac{1}{\Delta_2} \right) \sin \theta (u_x - i u_y) \quad (3.18)$$

where $\hat{F}_\pm = \hat{F}_x \pm i \hat{F}_y$ are the ladder operators of the angular momentum and $\eta = \|\mathbf{k}_2 - \mathbf{k}_1\| \sqrt{\hbar/(2m\omega)}$ is the Lamb-Dicke parameter. Here, we also ignore the term proportional to \hat{F}_z because it is off resonant as it only changes the quantum number associated to the trap. Notice that this expression is identical for a red-detuned trap, while we might naively expect that Raman transitions are much more important at an intensity maximum. The optimal angle θ is a trade-off between the need to have interferences to produce a trapping lattice $\propto \cos \theta$ and the associated Raman rate directly proportional to $\sin \theta$. In practice, we use a small angle to ensure that the trapping dominates and the angle θ is optimized experimentally. This is performed experimentally thanks to a 10° tilted half-wave plates on three of our trapping beams to independently optimize the Raman rate along the three directions. Each pair of beams of the optical lattice contributes independently to the cooling process as they are all spectrally separated by at least 400 MHz: crossed contributions are rapidly oscillating and averaged to zero in front of the trapping frequency.

Simultaneously, a $\sigma+$ polarized pump drives the D_2 transitions from $|F = 2, m_F = 1, n - 1\rangle$ to $|F' = 2, m_F, n - 1\rangle$. Atoms can be transferred by spontaneous decay back to states in $5S_{1/2}$: $|F = 2, m_F, n - 1\rangle$ or $|F = 2, m_F \pm 1, n - 1\rangle$ while a repumper beam maintains atoms in $F = 2$ to avoid losses in $F = 1$ states. The overall technique decreases the quantum number n and eventually leads to the dark state $|F = 2, m_F = 2, n = 0\rangle$ where no Raman transition is possible.

Experimental result

The experimental sequence is an alternation of Raman cooling and compression to both decrease the temperature and gain in density. The typical duration of a Raman step to significantly decrease the temperature is 1.5 ms, as shown on the figure 3.14, right panel. The magnetic field is set to 0.15 mG but the resonance is broad making this setting not critical. On the contrary, the polarization of the pump is a sensitive parameter in order to properly define the dark state. It is adjusted by a zero-order quarter-wave plate placed right before the beam passes through the atomic ensemble. The power of the pump has a value of $\sim 2 \mu\text{W}$ and the beam is collimated with a 1 mm waist.

After this Raman cooling step, we can compress the cloud by rising the depth of our conveyor belt. Once atoms are down in the trap, a new sequence of Raman cooling is

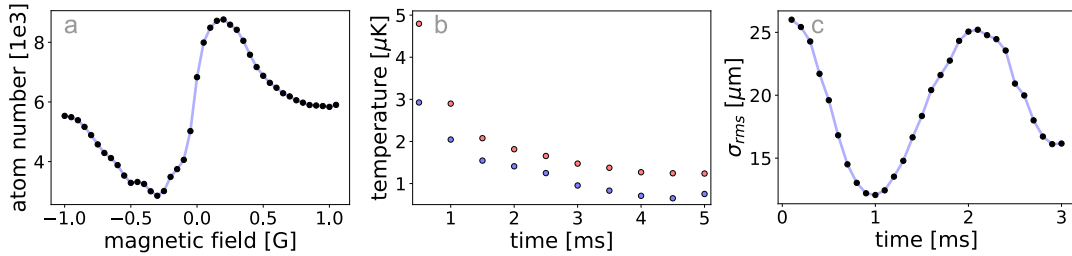


Figure 3.14: Optimization of the cooling and compression. a- We measure the number of remaining atoms as a function of the magnetic field applied in a 5 ms Raman cooling step. A broad resonance is visible for a positive magnetic field (0.05-0.3 mG) resulting in an efficient Raman cooling while we observe an anti-resonance for negative values corresponding to an anti-Stokes configuration that heats the atoms. b- Temperature vs. cooling time. The temperature is measured along the two transverses axes of one of the high-resolution imaging (vertical in blue and horizontal in red). The value saturates around 1.2 μK . c- After 5 ms of Raman cooling, we turn off the blue-detuned lattice to observe the compression in the conveyor belt. The best compression is obtained after 1 ms in the trap.

run. This compression timing is adjusted by looking at the evolution of the size of the sample, shown on figure 3.14. Between these compression and cooling steps, the Raman lattice is adiabatically raised up and down in 100 μs . By using the conveyor belt, we were able to compress the atomic sample within the (x,y) plane without affecting much the last direction. We were not able to compress with our blue-detuned Raman lattices because, as mentioned earlier, the heating in absence of cooling induces important losses. Instead, we put a compression beam within the (x,y) plane at 783 nm to obtain a compression along the third axis. The beam is loaded after a sequence including a step of cooling, compression in the conveyor and a second step of cooling. This second compression is again followed by a 5 ms Raman cooling step to further decrease the temperature down to 2 μK with our small crossed dipole trap on⁽¹⁰⁾.

⁽¹⁰⁾We also tested this step with the trap off but we did not observe a significant difference on the loading.

Conclusion

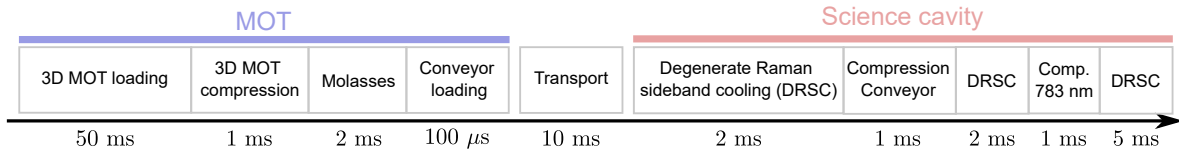


Figure 3.15: Sequence for the preparation of the atomic cloud. The sequence starts by the loading of the 3D MOT by the 2D MOT. It is then compressed and finally cool down to $9 \mu\text{K}$ in the molasses step. The conveyor belt is loaded to transport $\sim 10^6$ atoms to the science cavity. Once at the resonator level, the cloud is cool down to $\sim 2 \mu\text{K}$ and compressed to reach a peak atomic density of $4 \times 10^{11} \text{ cm}^{-3}$ inside the crossed dipole trap.

In this chapter we detailed the numerous steps and techniques used for the preparation of the atomic ensemble. It starts by the loading of the 3D MOT by the 2D MOT in ~ 50 ms followed by a compression (1 ms) and an optical molasses (2 ms) to gain in density and reduce the temperature. These two steps help to maximize the number of atoms loaded in the conveyor belt. After 10 ms of transport, the atomic sample is quite hot $\sim 50 \mu\text{K}$ and we use the degenerate Raman sideband cooling technique to decrease the temperature close to $2 \mu\text{K}$. This step is interspersed with compressions to gain in density. Finally, we load the crossed dipole trap at 1064 nm resulting in a peak density of $4 \times 10^{11} \text{ cm}^{-3}$ and a small cloud width at e^{-2} : $\simeq 10 \mu\text{m}$.

With these parameters, we have an atomic ensemble smaller than the blockade radius for the targeted Rydberg state ($\sim 100S$) without too much broadening from the Doppler shift (~ 40 kHz) or from the light shift induced by the crossed dipole trap (~ 50 kHz). In conclusion, the control of these critical parameters should allow us to obtain high electromagnetically-induced transparency as well as strong nonlinearities in our system.

Chapter 4

Detection of the atom-cavity coupling

Contents

4.1	Detection setup	76
4.1.1	Intensity measurements	76
Avalanche photodiodes and single-photon avalanche diodes		76
Correlation measurements		77
4.1.2	Balanced homodyne detection	79
Wigner function reconstruction via maximum likelihood algorithm		80
Noise characterization		82
Phase lock		83
4.1.3	Optical setup	84
4.2	Collective strong coupling regime	86
4.2.1	Optical pumping	86
Alignment		86
Optical pumping: population in $5S_{1/2}, F = 1$		87
4.2.2	Coupling to $ 5S_{1/2}, F = 1, m_F = 1\rangle \rightarrow 5P_{1/2}, F' = 2, m_{F'} = 2\rangle$	89
Experimental sequence		89
Transmission and reflection		90
Quadrature measurements		91

In chapter 2 we presented the experimental platform and especially the optical resonator with the aim to achieve strong and efficient interactions between photons. In chapter 3, we detailed the numerous steps to prepare a small atomic ensemble inside the resonator. This chapter focuses now on the coupling between our science cavity and the small atomic ensemble, as presented theoretically in chapter 1.

In the first section of this chapter we introduce the detection part of our experimental platform with particular emphasis on two methods: photon counting and homodyne measurements. We discuss the two techniques together with their specific technical characteristics.

The second section is devoted to the characterization of the collective strong coupling regime. For this, we need to isolate one ground state out of the many hyperfine and Zeeman ground states of rubidium 87. To this end, we discuss the optical pumping step to accumulate atoms in a single ground state. This step makes our cold atomic ensemble close to a perfect collection of two-level systems as described in chapter 1. We conclude on this point by an estimation of the purity of our atomic ensemble after this step. In the last part of this section, we discuss the alignment of the atomic ensemble on the mode of the science cavity to finally characterize the collective coupling by measuring the intensity of the light transmitted through and reflected from the cavity, and by measuring the phase of the light field reflected from it.

4.1 Detection setup

Light is at the heart of our experimental platform, we use it for instance to study the coupling of the cavity with the atoms. The detection of light and the associated techniques are therefore a crucial aspect of our experiments. This section addresses the presentation of this part of the platform.

In quantum mechanics there are two complementary approaches to describe the electromagnetic field. On one hand, a quantum state of light in a given mode can be described by discrete ladder annihilation/creation operators: \hat{a}, \hat{a}^\dagger . On the other, one can consider continuous variable with quadrature operators: $\hat{X} = \sqrt{1/2}(\hat{a} + \hat{a}^\dagger)$, $\hat{P} = i\sqrt{1/2}(\hat{a}^\dagger - \hat{a})$.

In our experimental platform we take advantage of the two approaches: we have detectors to counts photons, the measurement in this case is related to the particle-like behavior, or we can use a homodyne detection to measure the quadratures of the field.

4.1.1 Intensity measurements

The easiest way to extract information about our atom-cavity system is to measure the intensity of the electromagnetic field. It is however not an easy task because the field that escapes from the cavity is usually very weak. For instance, we will see in the next chapter that the Rydberg blockade induces a saturation of the transmission flux at a few megahertz since at most one photon can propagate through the resonator per polariton lifetime. As an order of magnitude, a 10 MHz photon flux at 780 nm is only equal to $\simeq 2.5 \text{ pW}$ which makes standard photodiodes inadequate. Instead, we make use of single-photon avalanche diodes (SPAD) and avalanche photodiodes (APD) depending on the context.

Avalanche photodiodes and single-photon avalanche diodes

Single-photon avalanche diodes (SPAD), also called single-photon counting modules (SPCM), is one of the most standard devices to record weak photon flux. Other approaches exist, for instance with superconductor nanowires (SSPD) [146] or photomultipliers [147]. This kind of detector is based on a nonlinear response of the system to produce a pulse for each incident photon, in the limit of the device bandwidth. The output signal of the device is then binary and can be used for photon flux measurements, with access to the arrival time of photons (rising edge). In the case of SPAD, the nonlinearity comes from a silicon avalanche diode with a bias voltage far above the voltage breakdown to produce a strong current out of a single photon, as illustrated in figure 4.1. As a result, this detection is very fragile: the system is thermoelectrically cooled and its temperature is controlled to ensure a good stability.

Our modules (Excelitas SPCM NIR 780 24) have a detection efficiency of 70% at 780 nm with a maximum count rate of $\sim 40 \text{ MHz}$. The deadtime of our detectors is $\sim 25 \text{ ns}$ for

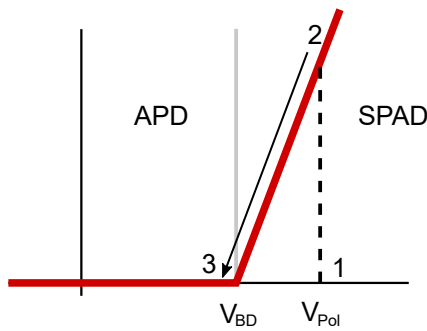


Figure 4.1: SPAD vs APD. Current-voltage characteristic of a diode. Below $V=V_{bd}$ (breakdown voltage) the system responds linearly with the input intensity. Avalanche photodiodes operate in this regime. On the contrary, a SPAD is used well above the breakdown point to produce a strong current out of a single photon. After the detection of a photon, a fast electronic circuit decreases the bias voltage to stop the amplification.

an input rate below 1 MHz and the typical pulse width is ~ 20 ns. One key characteristic of such a detector is the darkcount rate: the excitation of an electron by the background noise induces a cascade effect and leads to a false positive click on the avalanche photodiode. For our detectors, the darkcount rate is announced at less than 100 Hz. However, some of them have increased to ~ 300 Hz. Another artifact comes from the probability to observe a fictitious photon right after the detection of a real photon. Again, it depends on the quality of the device and our detectors have an afterpulse probability of 0.1%.

Two recording modes are possible with the control system of our platform, see chapter 2. It is either done with timestamps at a 10 ns resolution or with an adjustable binning suitable for high-photon rates⁽¹⁾. The first method is interesting for correlation measurements where the crucial information is precisely the arrival time of photons, see next subsection. The second approach is preferred when we record the spectrum of our resonator, the steady state of the system⁽²⁾, etc.

There is currently one Laser Components avalanche photodiode (LCSA500-01) in our experiment. In this case, the bias voltage is maintained below the voltage breakdown to ensure the linearity with respect to the input flux. This avalanche photodiode is not often used but it is helpful to align and optimize the coupling between the cavity and our atomic sample. The optimal photon flux for this procedure, high enough to make it fast but low enough to leave the atoms undisturbed, exceeds the ≈ 40 MHz limit of a SPAD but remains too low to be detected by a conventional Si PIN photodiode, making the APD the most convenient choice.

Correlation measurements

Counting photons is a technical achievement on its own but more information on the nature of light can be obtained with this kind of devices. In particular, a SPCM returns a click each time at least a photon is present in front of the detector but it is unable to make a distinction between different photon numbers. Instead, it is possible to obtain the light's statistics by looking at correlations between the arrival time of photons on two SPCM detectors. The idea is to split the signal of interest in two on a beam splitter and to record coincidences between the two detectors. This corresponds to a measurement of the second-order autocorrelation

⁽¹⁾It reduces the total amount of data.

⁽²⁾See next chapter, for instance with saturation measurements induced by Rydberg blockade.

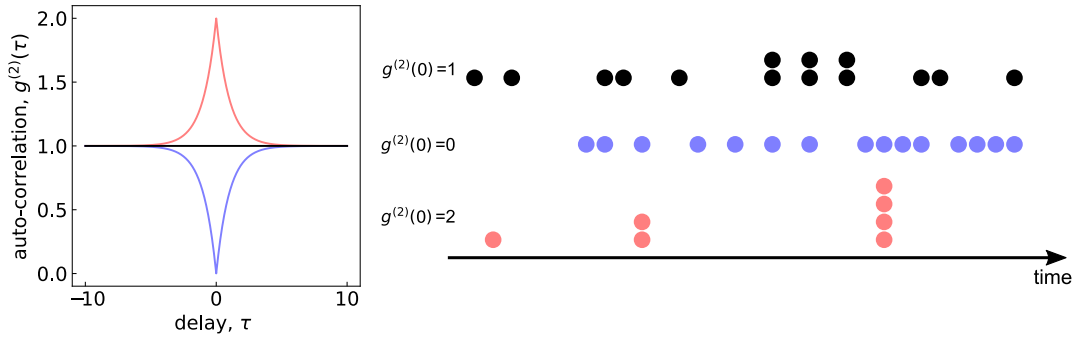


Figure 4.2: Photon statistics. Left- Second-order autocorrelation function ($g^{(2)}$) as a function of time. The correlations for thermal light (red curve) feature a maximum at zero delay ($g^{(2)}(0) = 2$) while single-photon correlations show a minimum at $g^{(2)}(0) = 0$ (blue). A standard laser beam (black) has a flat autocorrelation function. Right- The three configurations (same colors) randomly generated as a function of time.

function:

$$g^{(2)}(t, t') = \frac{\langle \hat{a}_1^\dagger(t)\hat{a}_2^\dagger(t')\hat{a}_2(t')\hat{a}_1(t) \rangle}{\langle \hat{a}_1^\dagger(t)\hat{a}_1^\dagger(t) \rangle \langle \hat{a}_2(t')\hat{a}_2(t') \rangle} \quad (4.1)$$

where \hat{a} is the annihilation operator of the field while the subset 1, 2 refers to the detector. The measurement is performed at time t on the first detector, t' on the second one and the function is normalized by the mean photon number of both channels to have $g(-\infty, +\infty)=1$ in the continuous regime.

The second-order autocorrelation is plotted in figure 4.2 for three different statistics. If we consider a single mode coherent state, we see that the correlation function is just equal to 1 (black line). Instead it vanishes for a single-photon state at zero delay, this corresponds to the so-called photon antibunching (blue). The explanation for this is quite straightforward: a single photon arriving on the beam splitter can either go to the first output channel or to the second one but it is not possible to split it in two. As a result, there is never a click on both detectors at the same time. For a continuous stream of single photons, coincidences are however possible for a delay between the two paths corresponding to the separation between consecutive photons.

This kind of measurements was performed for the first time by Hanbury Brown and Twiss to measure the angular size of stars [148]. In their measurements, the two detectors were separated by an adjustable distance d to record light from a very distant source. They observed the decrease of the second-order autocorrelation as a function of the distance between the two detectors to estimate the coherence time of the source. This can be explained classically with a thermal state, i.e. the superposition of several coherent states with random phases (red curve in figure 4.2). In this case, the correlation function can be rewritten as:

$$g^{(2)}(\tau) = \frac{\langle I_1(t)I_2(t+\tau) \rangle}{\langle I_1(t) \rangle \langle I_2(t+\tau) \rangle} \quad (4.2)$$

where we assume time invariance such that the autocorrelation only depends on the delay between the two detectors $t' - t = \tau$. Here, the statistics are purely classical and since $\langle (I(t) - \langle I(t+\tau) \rangle)^2 \rangle \geq 0$ one sees that $g^2(0) \geq 1$ and $g^2(0) \geq g^2(\tau)$. For a thermal light, the autocorrelation rises to $g^{(2)}(0) = 2$ [149] while one must recover $g^{(2)}(\tau) = 1$ when the delay exceeds the coherence time of the source. In their experiments, they only observed a

few percent increase of the autocorrelation at zero delay because of the limited bandwidth of their detectors.

This approach can be generalized to n detectors to measure the n^{th} autocorrelation function of the electric field. A drop at zero delay would indicate a decrease of the probability to measure at least n photons at the same time, while a coherent state would always exhibit a flat response.

4.1.2 Balanced homodyne detection

The basic idea of the Homodyne Detection (HD) is to obtain a measurement sensitive to the electromagnetic field of a weak probe and not its intensity. In optics, balanced homodyne detection was proposed by Yen and Chan in 1983 [150] and later demonstrated by Abbas, Chan and Yee [151] during the same year.

Measuring the electromagnetic field in optics is an entire field of investigation. It is for instance used for imaging applications to reconstruct the wavefront scattered by a diffuser via holography techniques [152]. Here, the method focuses on the phase of a single optical mode. The signal of interest is combined with a reference laser beam at the same frequency to produce an interference term between them. This reference laser is called the local oscillator (LO). In our case, the probe is combined with the LO on a balanced unpolarizing beam splitter and the two output channels are recorded on photodiodes as depicted in figure 4.3. The difference of the two photocurrents gives access to the interference term between the LO and the probe:

$$\hat{I}_1 - \hat{I}_2 \propto \|E_{LO}\| \hat{X}_\theta \quad (4.3)$$

where $\hat{I}_{1,2}$ is the photocurrent of detector 1 and 2, $\|E_{LO}\|$ is the modulus of the LO field used at high intensity and thus treated classically. $\hat{X}_\theta = \cos(\theta)\hat{X} + \sin(\theta)\hat{P}$ is a quadrature of the probe and θ is the phase difference between the LO and the probe.

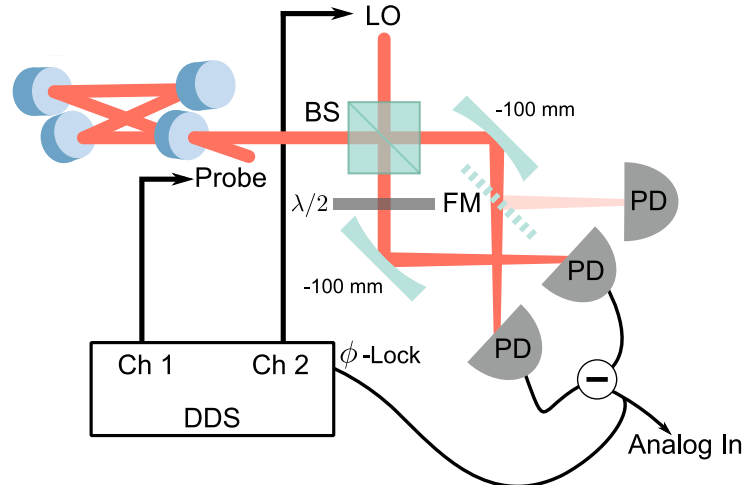


Figure 4.3: Homodyne detection. The local oscillator (LO) and the probe are combined on a 50:50 beam splitter (BS) and the output beams are focused by two curved mirrors ($f = -100 \text{ mm}$) before being recorded by two photodiodes. The output signal of the homodyne detection is the difference between the two photocurrents, leaving only the interference term. A half-wave plate ($\lambda/2$) is there to make a fine balance between the two output channels to cancel terms proportional to the LO intensity. A flip mirror (FM) can be switched to optimize the spatial overlap between the LO and the probe on a dedicated photodiode. The phase is also locked by sending the homodyne signal to the Direct Digital Synthesizer (DDS) that controls our two beams (see text for more details).

The quantum state to be characterized is usually very weak, on the order of a few photons, and this method allows to amplify the interference term, via the LO power, to extract the quantum signal out of the background noise. This also shows that it is important to have a good mode overlap between the two beams in order to maximize this interference term. All of this makes homodyne detection very sensitive to changes of alignment and path lengths of the interferometer and consequently this method requires the control of several parameters to ensure stability during measurements.

First, the two output channels must be balanced to cancel out the terms proportional to the intensity of the LO. Any residual offset would induce extra fluctuations over the weak signal. Another important quantity is the relative phase between the two beams. This phase must be controlled or at least measured. This issue is addressed in one of the following subsections.

Assuming these conditions are met, the probability distribution of a given quadrature is estimated from the accumulation of measurements. The acquired data are only proportional to the quadrature and a conventional way to normalize it is to fix the vacuum variance $\langle 0 | \Delta \hat{q}_\theta | 0 \rangle$ to 1/2. In practice, this kind of measurements are performed with short pulses (from ~ 40 ns rms Gaussian pulses to ~ 100 μ s square pulses) while the LO beam is used in continuous mode to avoid drifts in the photocurrent. In this case, the quadrature of a pulse is given by:

$$\hat{X}_\theta = X_0 \int v(t)[\hat{I}_1(t) - \hat{I}_2(t)]dt \quad (4.4)$$

where X_0 is a normalization factor and v the temporal envelope of the mode. The choice of the function v depends on the measurement, in this chapter we will only consider square pulses but more sophisticated examples will be given in chapter 6.

This method allows for a measurement of the probability distribution along any quadratures, especially \hat{X} and \hat{P} . This makes the homodyne detection well suited for phase space reconstructions. It is however more subtle than in classical physics because of the Heisenberg's uncertainty principle.

Wigner function reconstruction via maximum likelihood algorithm

We present the Wigner function which allows to describe a quantum state in the phase space as well as the method to reconstruct this function from the quadratures.

The Wigner function contains all the information about a quantum state and it exists an univocal relation between this function (W) and the density matrix $\hat{\rho}$:

$$W(X, P) = \frac{1}{\pi} \int_{-\infty}^{+\infty} \langle X + Y | \hat{\rho} | X - Y \rangle e^{-2iPY} dY \quad (4.5)$$

This Wigner function is the equivalent of a probability density in phase space with the difference that it can take negative values for nonclassical states. It is therefore used in many experiments to emphasize the quantumness of a system [153–156]. Measuring the negativity of this function is however a challenging task for experimentalists because losses reduce the negativity and it eventually disappears beyond 50% losses [157].

Some standard examples of Wigner functions are shown in figure 4.4. For instance, a single photon $|1\rangle$ takes negative values around $(0, 0)$ and shows no angular dependence. On the contrary, a coherent state $|\alpha\rangle$ describes a classical state (for instance a laser beam) and features no negativity in its Wigner function: it is simply a Gaussian with $\langle \hat{X} \rangle = \sqrt{2} \operatorname{Re}(\alpha)$, $\langle \hat{P} \rangle = \sqrt{2} \operatorname{Im}(\alpha)$.

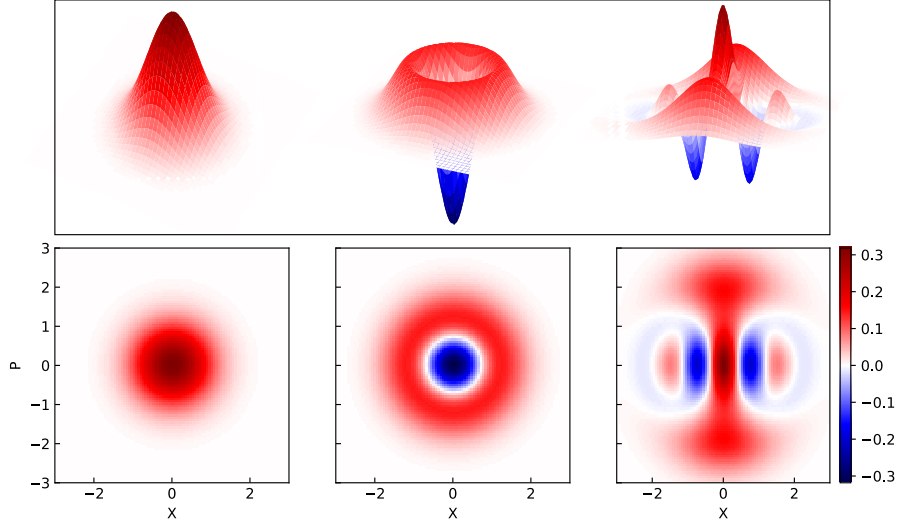


Figure 4.4: Wigner functions. Some examples of Wigner functions, from left to right: vacuum state $|0\rangle$, single-photon state $|1\rangle$ and even “Schrödinger’s kitten” state $(|\alpha\rangle + |-\alpha\rangle)/\sqrt{2}$ with $\alpha = \sqrt{2}i$. The vacuum state is a coherent state and thus does not exhibit any negativity (only red). The Wigner function of a single-photon state has negative values in the center (blue). A coherent-state superposition has a more elaborate Wigner function: it displays interference fringes that oscillate between negative and positive values. The variance of the vacuum state is normalized to $1/2$.

There is in fact a simple relation between the quadratures and the Wigner function: a quadrature distribution at angle θ is simply the integration of the Wigner function along the orthogonal quadrature $\hat{X}_{\theta+\pi/2}$. It is then possible to extract the Wigner function from its projection along several axes. This procedure is called quantum homodyne tomography.

The standard method employed to reconstruct the Wigner function from HD measurements is an algorithm called maximum likelihood [158, 159]. This approach is based on the convergence towards the most likely density matrix $\hat{\rho}$ given the set of measured distributions [160]. As a first step, the set of measurements obtained for a phase θ_k is discretized and organized into a histogram. The occurrence for a given bin x_j at phase θ_k is noted $m_{j,k}$. This quantity can be compared to the outcome of a given density matrix ρ : the probability to measure the bin x_j with the phase θ_k is $p_{j,k} = \text{Tr}[\hat{M}_{j,k}\hat{\rho}]$ where $\hat{M}_{j,k}$ is the associated projector. We can then compute the probability of measuring this data set if we assume that the system was in the state $\hat{\rho}$. This quantity is called likelihood and is given by:

$$\mathcal{L}(\hat{\rho}) = \prod_{j,k} p_{j,k}^{m_{j,k}} \quad (4.6)$$

We further assume here that the set of projectors form a complete basis for simplicity (we will go back on this assumption later). The algorithm aims at maximizing this function with respect to the density matrix to find the most likely density matrix. To this end, a new density matrix is defined iteratively from the previous one by the operation:

$$\hat{\rho}_{i+1} \propto \hat{R}(\hat{\rho}_i)\hat{\rho}_i\hat{R}(\hat{\rho}_i), \text{ where } \hat{R}(\hat{\rho}) = \sum_j \frac{m_{j,k}}{p_{j,k}} \hat{M}_{j,k} \quad (4.7)$$

and ρ is normalized after each step.

The initial density matrix is not very important, for example one can take a thermal distribution as a starting point. The essential point in this algorithm is that the most likely

distribution should exhibit a proportionality between the probability and the data occurrences, in other words $\hat{R} \propto \hat{1}$. The sought-after density matrix therefore corresponds to a stationary point for the iterative step and it is possible to show that this operation converges towards this point [161].

For a concrete implementation, one needs to restrict the size of the Hilbert space. An effective way to do this is to express all the operators in the Fock states basis and to fix a maximum value to the number of photons. One of the assumption in this derivation is to have a complete set projector which seems impossible since we need to truncate an infinite Hilbert space. In practice, this approximation remains valid as long as the investigation window of this algorithm is wider than the photon distribution in the state to be reconstructed. This is not a big issue as we are studying states with very few photons, at most 2, while the Hilbert space for our reconstructions is at least fixed to 5 photons and can be extended if necessary.

As we mentioned earlier, losses in the platform deteriorate the Wigner reconstruction. Detection losses can be taken into account in the algorithm and corrected to obtain the Wigner function at the output of our system. However, it remains crucial to minimize all sources of losses and we now turn our attention to the noise of our homodyne detector.

Noise characterization

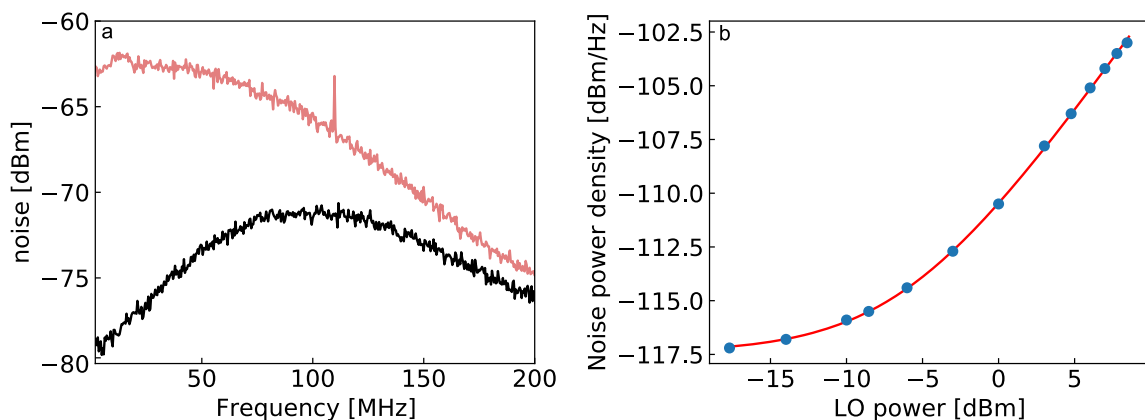


Figure 4.5: Noise of the homodyne detector. a- Noise spectrum for the homodyne detection alone (in black) and with the LO at a power of 7 mW (red). The spectrum with 7 mW of LO is ~ 15 dB above the electronic noise over the detector bandwidth (100 MHz). b- Noise power density as a function of the LO power, measured at 20 MHz. The data set (blue dots) is fitted by the function: $10 \log_{10}(\sigma_P^0 + A \times P_{LO})$ (red curve) with A and σ_P^0 two free parameters and P_{LO} the LO power. The intrinsic noise is $\sigma_P^0 = 1.8 \times 10^{-12} \text{ mW Hz}^{-1}$ and corresponds to a noise-equivalent power of $10 \text{ pW}/\sqrt{\text{Hz}}$ (at 840 nm, datasheet : $6 \text{ pW}/\sqrt{\text{Hz}}$ at 10 MHz).

The detection signal has to be shot-noise limited to faithfully capture a quantum state because extra-noise can be seen as additional losses [162]. Our homodyne detector is a HCA-S model from Femto with S3883 photodiodes and a quantum efficiency of 91% (795 nm).

The first source of noise comes from the electronics of the detector itself and the only way to reduce its impact is to increase the intensity of our LO. We are currently using the LO with about 7 mW (3.5 mW per arm) to obtain a quasi white-noise spectrum in the 100 MHz bandwidth of the detector: $\Delta S \sim 15$ dB above the electronic noise as shown in figure 4.5. This ratio translates into an effective efficiency given by $\eta_e = 1 - 10^{-\Delta S/10} \simeq 97\%$ [162]. As a check, we measured the noise power spectrum at 20 MHz as a function of LO power to verify the linearity at high intensity, right plot. The intrinsic noise is estimated to $10 \text{ pW}/\sqrt{\text{Hz}}$ close to the value on the datasheet: $6 \text{ pW}/\sqrt{\text{Hz}}$.

The second main issue is the balance between the two output channels. A half-wave plate is placed in one arm to make this compensation. The slight rotation of polarization induces a change of transmission through the glass plate in front of the sensor. This is possible because light is injected with a 20° angle⁽³⁾ on our photodiodes. Despite this fine tuning, we observed slow drifts throughout our experimental cycles that result in a low frequency noise (order of magnitude: $< 1 \text{ kHz}$). This can be attributed to fluctuations of the intensity due to polarization or temperature drifts. A long reference signal is acquired after each experimental cycle to properly define the zero to eliminate this additional noise. This sample must be long (t_0) compared to the duration of the signal of interest (t_s) because the variances add up. The effective variance after this compensation (σ_{cor}^2) for the signal integrated over a duration t_s is:

$$\sigma_{cor}^2 = \sigma_h^2 \left(1 + \frac{t_s}{t_0} \right) \quad (4.8)$$

where σ_h^2 is the variance of the homodyne signal without slow drifts. In practice, the ratio between t_0 and t_s is $\leq 1\%$. There is a third source of additional noise in our homodyne setup coming from the phase lock stability.

Phase lock

The relative phase between the local oscillator and the probe defines the rotation angle of the quadrature. In some experiments, this phase is randomly fluctuating but slowly enough to be constant over each experimental cycle. The quadrature at a given phase can be reconstructed by measuring the phase for each measurement and post-selecting the data accordingly [38]. In our case, these phase variations are due to mechanical and thermal fluctuations on the arms of our interferometer (few meters long, partially fibered). We opted for an active control to stabilize this parameter throughout the measurements in order to increase the duty cycle of our experiment.

This control is achieved by a homemade lock-and-hold phase lock, where a measurement of the relative phase is performed for each experimental cycle. Before a homodyne measurement, the small residual offset X_0 of the HD is measured in the absence of any probe signal. The probe beam is then switched on to acquire the mean value $\langle \hat{X}_\theta \rangle$ of a quadrature \hat{X}_θ where θ is the relative phase to be determined. Afterwards, the phase of the probe is $\pi/2$ shifted by changing the phase of the signal driving the corresponding acousto-optical modulator, and the orthogonal quadrature \hat{P}_θ is measured. Finally, the offset is subtracted for both quadratures to estimate the relative phase $\theta = \arctan((\langle P_\theta \rangle - X_0)/(\langle X_\theta \rangle - X_0))$. These operations are performed in 400 μs by a FPGA and the feedback signal is then sent to the DDS driving the probe and the local oscillator to zero the relative phase. This measurement is performed with the laser beams 40 MHz away from the cavity resonance (locked on the atomic transition) to avoid disturbing our atoms. The optical path difference between the local oscillator and the probe causes a phase shift when we change the frequency to study our platform close to resonance after the phase-lock step. This shift is calibrated by looking at the frequency shift needed to observe a 2π phase shift and it is automatically subtracted. After this procedure, we are free to adjust this relative phase θ between the LO and the probe for measurements of the quadrature \hat{X}_θ .

We measured the stability of the phase lock to be about $\sigma_{ph} = 6.1^\circ$. As shown in figure 4.6, this estimation is obtained by measuring the noise for several values of the phase θ with a coherent state of amplitude α . The variance of the vacuum state is normalized to 1/2 as previously mentioned and the quadrature distribution is then described by a Gaussian with a

⁽³⁾The reflectivity depends on the incident angle and polarization according to Fresnel equations.

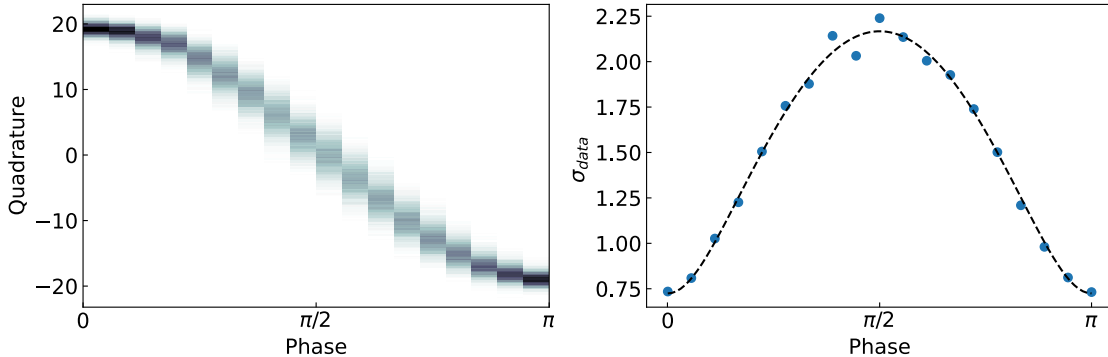


Figure 4.6: Phase stability. Left- Quadrature distribution as a function of the phase between the LO and a coherent state for $n \simeq 200$ photons. The occurrences are represented from white (zero) to black (maximum). Right- Width of the quadrature distribution as a function of the input phase. We observe an increase of the noise at $\theta = \pi/2$. This additional noise is due to an imperfect lock of the phase. We infer the phase fluctuations from a fit (dashed line): $f(\theta) = \sqrt{\sigma_0^2 + 2n\sigma_{ph}^2 \sin(\theta)^2}$ where σ_0 is the vacuum rms width and $\sigma_{ph} = 6.1^\circ$ is the phase noise, the only fitted parameter. This fit yields a phase stability of $\simeq 6^\circ$.

mean value $\langle \hat{X}_\theta \rangle = \sqrt{2}|\alpha| \cos \theta$ and a variance $\langle \Delta \hat{X}_\theta \rangle = 1/2 = \sigma_0^2$. The additional noise due to phase fluctuations is then $\sigma_{add} = \sigma_{ph} \sqrt{2n} \sin \theta$, where $n = |\alpha|^2$ in the mean photon number of the coherent state. These phase fluctuations of our phase-lock constraint the photon number in order to keep the quadrature variance close to the shot-noise, $n \ll \frac{1}{4\sigma_{ph}^2} = 23$. For instance, at $n = 1$ the additional rms noise (σ_{add}) is about 5% of the vacuum fluctuations (σ_0).

4.1.3 Optical setup

After this introduction on the two detection methods we now present the optical setup for concrete measurements with the science cavity. This optical setup surrounding the resonator is separated into three tasks.

First, we have two technical beams. One of them is used for the stabilization of the cavity length. The second laser beam is dedicated to the optical pumping step to prepare our atoms in one ground state. These two beams are sent in the opposite direction of the detection path to reduce the injection of parasitic light in our detection devices. The locking beam is at 783 nm with ~ 1 nW mode-matched to the fundamental cavity mode and is detected in reflection on a dedicated APD. A dichroic mirror (Semrock LL01-785, a few nanometers bandwidth) is placed in front of the APD to filter out the other beams, the locking technique and laser sources were introduced in the chapter 2.

The second part of the setup is related to the probes on the D_1 and D_2 lines. Two D_1 probes (795 nm) can be sent in reflection or in transmission to characterize the atom-cavity system, or perform experiments. The probe in transmission is thus injected from a high-reflectivity (HR) mirror. The intensity lock of this probe is depicted in figure 4.7, with a photodiode monitoring the intensity before its injection through the HR mirror. Note that we also stabilize the intensity of the other probes, the associated optical setup is simply not located around the experiment but before the injection fibers. The beam in reflection is collimated by a telescope to optimize the mode matching with the science cavity $TEM_{0,0}$ (translation stage on one lens). The third beam is the D_2 probe (780 nm) and is only used to

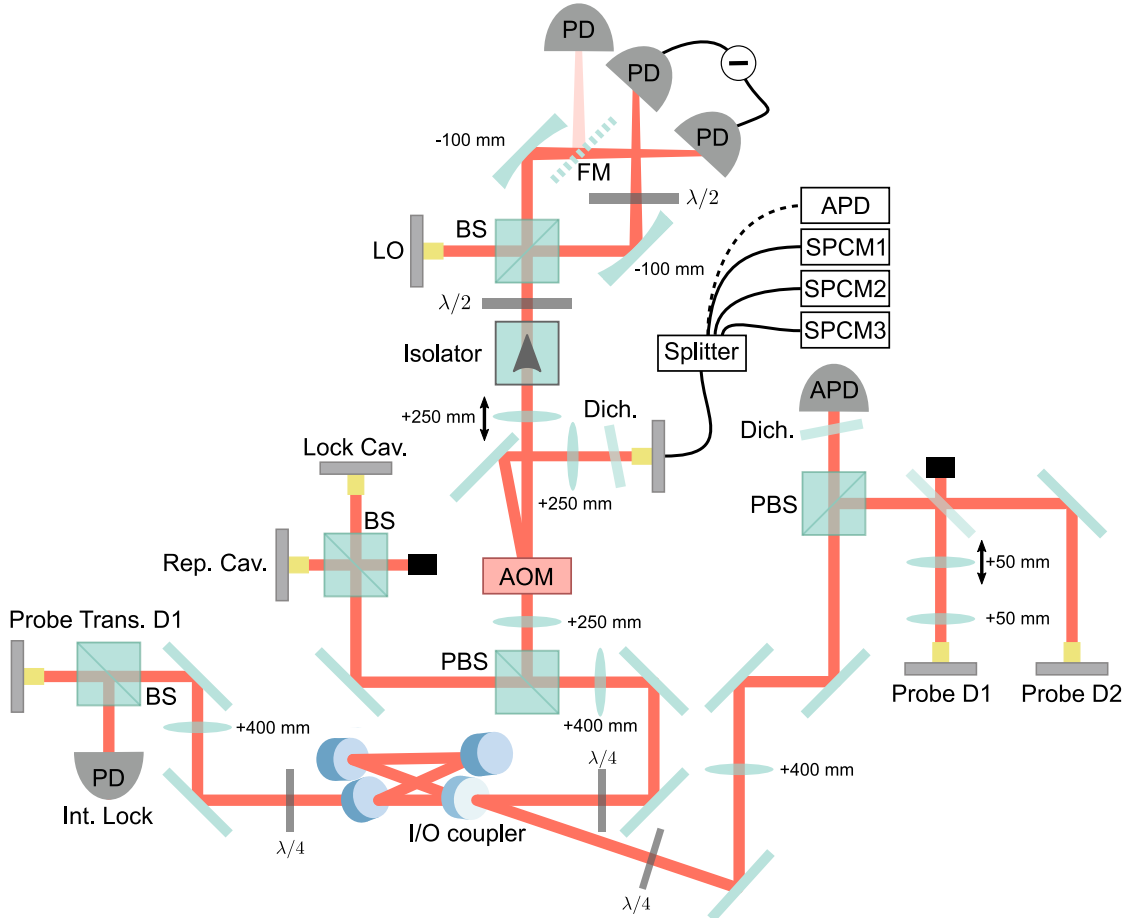


Figure 4.7: Optical setup. Optical setup for the science cavity. The optical path of the detection can be switched with an AOM to either use the homodyne setup or a SPCM. The 795 nm beam (D_1) is injected in transmission through a high-reflectivity mirror. Half of the signal is sent to a photodiode for an intensity locking. Two probes are injected in reflection at 795 nm and 780 nm (D_2). The LO is currently at 795 nm and the probe D_2 is only used to prepare a Rydberg excitation inside the cavity and is thus not detected. A dichroic mirror is placed in front of the SPCM fiber coupler, and is optimized at 795 nm with a bandwidth of a few nanometers (Semrock LL01-808). A repumper beam (Rep. Cav.) and the locking beam (Lock Cav.) propagate in the opposite direction to the probes.

coherently control a Rydberg excitation inside the resonator. This is a separate topic, which will be discussed in chapter 7.

The last part is the detection path. The output light is sent through an AOM to switch between the detections methods introduced previously. The light can be oriented towards our SPCMs or APD and is filtered at 795 nm (Semrock LL01-808). It can then be distributed by a homemade splitter, for instance for correlations measurements between two SPCMs. The other option is to measure the output field via the homodyne setup with a LO resonant with D_1 probes. The lens before the detection can be translated to optimize the mode matching with the LO beam. This optimisation is made with the probe in transmission to directly optimize the mode matching with the science cavity mode. At last, a Faraday isolator is placed right before the homodyne detection to reduce the diffusion of LO's light (~ 7 mW) back in the cavity mode (20 dB decrease⁽⁴⁾). Notice that the D_2 probe is thus never detected.

⁽⁴⁾Initially, we observed a ~ 6 MHz photon flux coupled back to the cavity mode and it now at 40 kHz. We also removed the input and output cubes of the isolator to reduce optical losses.

4.2 Collective strong coupling regime

Now that the detection paths and related detection techniques have been presented, we turn our attention to the coupling between our small atomic cloud and the optical cavity. We first discuss how to optimize the coupling of the ultracold ensemble with the cavity and then we address the pumping step to prepare all the atoms in one ground state. We will give an estimation of the purity of the atomic cloud after a pumping step. This parameter is critical to achieve a high electromagnetically-induced transparency of the atomic cloud since atoms prepared in the wrong Zeeman states can induce absorption. Finally, we briefly present some measurements of the collective strong coupling regime in several configurations.

4.2.1 Optical pumping

Alignment

In chapter 3, we presented the preparation of a small atomic ensemble inside our resonator but we did not discuss the alignment between the atomic cloud and the resonator.

The first step to obtain this coupling is to align the conveyor belt with the 20 μm waist of the science cavity. To this end, the cavity length is locked on one of the rubidium transitions in order to monitor losses induced by the presence of atoms inside the resonator. This can be done by looking at the reflection or transmission of the cavity. The probe must be weak in order not to kick the cloud out of the cavity mode. Below this limit, the beam should be as powerful as possible to make the alignment easier. This signal is thus acquired on the Laser Component APD introduced in the previous section.

The cloud is released from the trap for a few milliseconds and expands close to the cavity mode. The optimal position of the trap is then obtained when optical losses (due to absorption) are maximum at zero delay, as shown in figure 4.8. It corresponds to a coarse alignment that can be improved by directly looking at the Rabi splitting once there is enough coupling. In general, this measurement of the coupling is done in transmission. Since it only

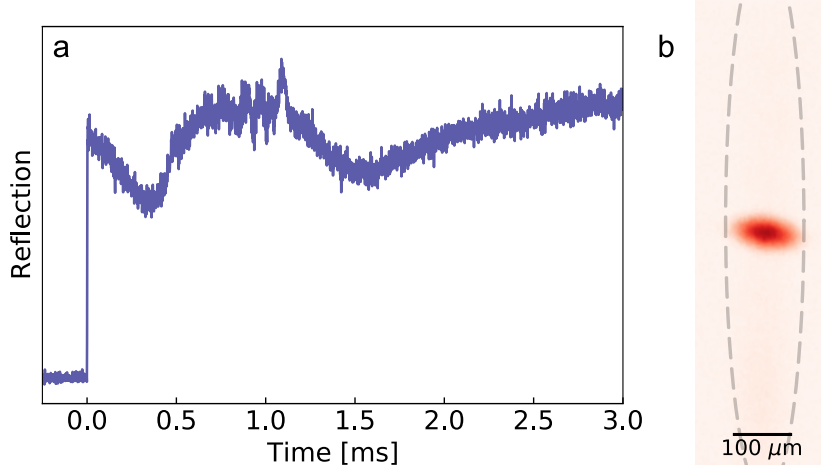


Figure 4.8: Atom-cavity alignment. a- A measurement of the cavity reflection to align the cloud with the mode of the cavity. At $t = 0$ the trap is switched off and light is sent through the cavity. Since the cloud is not yet aligned, we observe a decrease followed by an increase characteristic of the switch between Losses<Transmission regime to Losses>Transmission. b- We first pump atoms inside the conveyor belt in $F = 1$, we then sent light through the cavity to pump back atoms in $F = 2$ before imaging on $F = 2$ to observe the position of the science cavity mode.

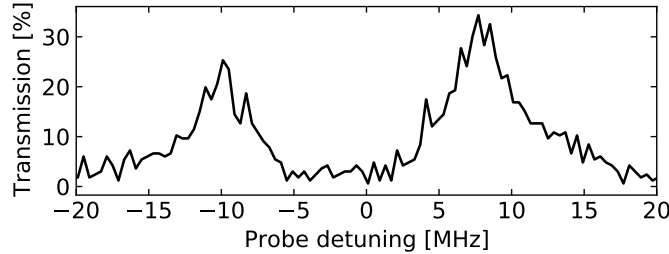


Figure 4.9: Vacuum Rabi splitting. Transmission spectrum of the resonator coupled with the small atomic ensemble. The zero detuning corresponds to the cavity resonance.

requires a small amount of power, light is injected from a high-reflectivity mirror and collected from the input/output mirror as discussed in the previous section. The transmission spectrum of the resonator is measured by scanning the laser frequency around the cavity resonance (and the cavity is locked on a rubidium transition). After this step, the vertical alignment is not at all precise because the cloud has a cigar shape inside the conveyor belt ($\sigma_z = 0.5$ mm, $\sigma_r = 35$ μ m), see chapter 3.

The idea is then to inject a large amount of light through the resonator to kick or pump atoms overlapping with the mode of the cavity to estimate accurately the position of the cavity field with respect to the cigar shaped cloud. This hole, or the remaining atoms, are then observed with a beam addressing $5S_{1/2}, F = 2 \rightarrow 5P_{3/2}, F' = 3$ along the high-resolution imaging axes, as shown in figure 4.8. It is thus possible to align our Raman beams and the 1064-nm crossed dipole trap on it. The final step consists in a slight adjustment of the two arms of the small crossed dipole trap to maximize the coupling of our small ensemble with the resonator. The vacuum-Rabi splitting is illustrated in figure 4.9 after this optimization.

This measurement is a significant step for this experimental platform as it demonstrates our ability to reach the collective strong coupling between our small atomic ensemble and the resonator. We will now focus on the optical pumping step to properly isolate two levels among the numerous states of rubidium 87 before further discussing the coupling between our atoms and the resonator.

Optical pumping: population in $5S_{1/2}, F = 1$

Let us start by a presentation of the setup and the experimental sequence for optical pumping. We work with the probe on the D_1 line (795 nm) to easily filter it from Raman, conveyor and MOT beams at 780 nm. A 3 G magnetic field quantization axis is switched on along the science cavity axis in order to address σ transitions with the circularly polarized modes of the resonator. This imposes to work with linearly polarized light for our control beams to address a single Rydberg state because of the geometry of our experimental platform, see chapter 2. The choice of the hyperfine and Zeeman state for our three-levels ladder scheme (discussed in chapter 1) depends on the precise targeted Rydberg state and on our ability to optically pump our atoms. For these reasons, we are currently working with $|g\rangle = |5S_{1/2}, F = 1, m_F = +1\rangle$, an intermediate state $|e\rangle = |5P_{1/2}, F' = 2, m_{F'} = +2\rangle$ and the Rydberg state $|r\rangle = |nS, m_J = +1/2\rangle$. The optical pumping is done with a circularly polarized beam driving $5S_{1/2}, F = 1 \rightarrow 5P_{3/2}, F' = 1$. This beam is sent through the science cavity (200 MHz out of resonance) together with a repumping beam on $5S_{1/2}, F = 2 \rightarrow 5P_{3/2}, F' = 2$ (our Zeeman pumping beam for the Raman) in free space. As a result, the atoms are brought into the dark state $|5S_{1/2}, F = 1, m_F = +1\rangle$. The step lasts 100 μ s but the repumper beam is only on in the first 20 μ s to ensure that atoms in $F = 1, m_F \neq +1$ fall in $F = 2$ or end up in

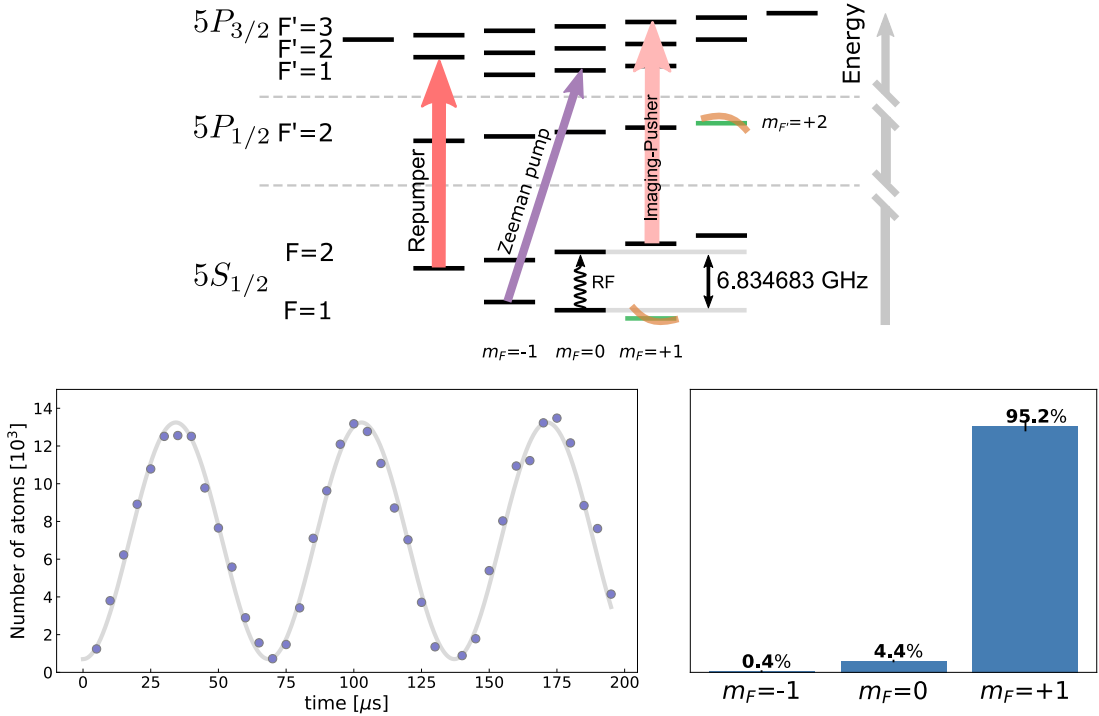


Figure 4.10: Optical pumping. Top- Schematic of ^{87}Rb transitions. The Radio-frequency probe is in black ($5S_{1/2}, F = 1 \rightarrow F = 2$), the imaging/pusher beam is in light red ($5S_{1/2}, F = 2 \rightarrow 5P_{3/2}, F' = 3$), the repumper beam is in red ($5S_{1/2}, F = 1 \rightarrow 5P_{3/2}, F' = 2$) and the Zeeman pump is in purple ($5S_{1/2}, F = 1 \rightarrow 5P_{3/2}, F' = 1$). Hyperfine lines are split by a 3G magnetic field ($\simeq 2 \text{ MHz}$) and the cavity is in orange and resonant with $5S_{1/2}, F = 1 \rightarrow 5P_{1/2}, F' = 2$ (green). Bottom left- Rabi oscillations between hyperfine states $|5S_{1/2}, F = 1, m_F = 0\rangle$ and $|5S_{1/2}, F = 2, m_F = 0\rangle$ by driving atoms with the RF antenna at a frequency of $6.834\,683 \text{ GHz}$. We observe the number of atoms transferred to $|5S_{1/2}, F = 2, m_F = 0\rangle$ with our high-resolution imaging on $5S_{1/2}, F = 2 \rightarrow 5P_{3/2}, F' = 3$. This is done for the three Zeeman ground states of $5S_{1/2}, F = 1$ to estimate the population distribution. Bottom right- Population in each Zeeman state of $5S_{1/2}, F = 1$. We found that $95 \pm 2\%$ of the population is in $m_F = +1$ after our pumping sequence.

the dark state. Atoms in $F = 2$ do not participate to absorption and are used as a reservoir to increase the duty cycle.

The pumping purity directly impacts the transparency of our atomic sample in EIT configuration, the consequence of a bad optical pumping is discussed in more details in chapter 5.

We now briefly describe the method employed to estimate the population in $5S_{1/2}, F = 1$ after pumping. We first apply a standard optical pumping sequence as described previously, then we send a strong resonant beam on $5S_{1/2}, F = 2 \rightarrow 5P_{3/2}, F' = 3$ to remove atoms in $F = 2$. The population in a given hyperfine ground state $|5S_{1/2}, F = 1, m_F = 0, \pm 1\rangle$ can be coherently transferred to $|5S_{1/2}, F = 2, m_F\rangle$ by applying a π -pulse of radio frequency from the antenna used for magnetic field calibrations, see chapter 3. This is possible because each π -transition is well separated from others hyperfine lines by at least $\sim 2 \text{ MHz}$ thanks to the quantization magnetic field (3 G). The pulse duration is initially calibrated for each transition by measuring the atom number but without the optical pumping step to keep a good visibility for $m_F = -1, 0$; one calibration of the duration is shown in figure 4.10 for $m_F = 0$. After this coherent transfer, the magnetic field is switched off to allow a homogeneous distribution of the population in the Zeeman states of $F = 2$. The number of atoms, for each Zeeman

state of $F = 1$, is then measured via absorption imaging on $5S_{1/2}, F = 2 \rightarrow 5P_{3/2}, F' = 3$ and averaged over 50 experimental cycles.

After such a pumping step, we have $95(\pm 2)\%^{(5)}$ of the atomic ensemble pumped in $m_F = +1$ as shown in figure 4.10. The majority of atoms that are not in the dark state occupy $m_F = 0$, with approximately ten times the population of $m_F = -1$. If, for some reason, this value is not high enough, it is still possible to add a step of radio frequency to coherently transfer atoms in the wrong Zeeman states to $F = 2$. The only concern is to initially remove atoms in $F = 2$, which may heat our atoms or induces losses.

4.2.2 Coupling to $|5S_{1/2}, F = 1, m_F = 1\rangle \rightarrow |5P_{1/2}, F' = 2, m_{F'} = 2\rangle$

In chapter 1 we discussed the coupling of an atomic ensemble with the electromagnetic field of a cavity. At that moment, we did not provide any specific mode for the light field. In chapter 2, we presented the modes of our cavity and showed that the fundamental mode ($\text{TEM}_{0,0}$) is a Gaussian. The two main properties of our resonator are thus its roundtrip length $\ell \simeq 94 \text{ mm}^{(6)}$ and the waist of the fundamental mode $w = 21 \mu\text{m}$. We are now able to estimate the coupling strength in this configuration. The field operator, at the waist, is given by (equation 1.11):

$$\hat{E} = \mathcal{E}_0 e^{-r^2/w^2} (\hat{a} + \hat{a}^\dagger), \text{ where } \mathcal{E}_0 = \sqrt{\frac{2\hbar c}{\epsilon_0 \lambda \ell w^2}} \quad (4.9)$$

where the value of \mathcal{E}_0 is obtained by computing the mean value of the power.

The coupling strength of a single atom at the waist of the mode is then $g_0 = d\mathcal{E}_0/\hbar \simeq 2\pi \times 400 \text{ kHz}$ for a probe addressing $|5S_{1/2}, F = 1\rangle \rightarrow |5P_{1/2}, F' = 2\rangle$. We clearly see that the coupling strength of a single atom is well below the atomic decay rate, $\gamma \simeq 2\pi \times 3 \text{ MHz}$, and the cavity damping rate, $\kappa \simeq 2\pi \times 3 \text{ MHz}$. Therefore, our cavity is not strongly coupled to single atoms, $C_0 \approx 1\%$. On the contrary, with a $4 \times 10^{11} \text{ cm}^{-3}$ peak density and a $5 \mu\text{m}$ rms width⁽⁷⁾ for our atomic ensemble, we expect about ~ 800 atoms coupled to the cavity with a collective coupling strength of $2\pi \times 10 \text{ MHz}$. We now briefly present some measurements of the atom-cavity coupling.

Experimental sequence

We start our discussion by transmission measurements to characterize the collective coupling strength. We do not consider here the coupling to Rydberg states as it will be addressed in the next chapter.

The probe is sent through a double-pass AOM to scan its frequency over 80 MHz around the cavity resonance while the APD or a SPCM records the transmitted signal. The response of the AOM is not flat over this frequency range and we use an intensity lock to compensate these drifts, as shown in figure 4.7. The sequence begins with the preparation of a small atomic sample (about 100 ms, see chapter 3 for a complete description) followed by the optical pumping step (100 μs , see previous subsection). The scan lasts 200 μs and we are able to repeat this measurement about ~ 20 times⁽⁸⁾ with the same atomic ensemble. These measurements are interspersed with short repumping steps (10 μs) to keep the coupling stable ($\simeq 2\%$ of rms fluctuations), as shown in figure 4.11, right plot. In practice we can vary the coupling strength

⁽⁵⁾Error at 1σ (Gaussian half width at $e^{-1/2}$).

⁽⁶⁾This length can be tuned by the two translation stages, see chapter 2.

⁽⁷⁾Gaussian half-width at $e^{-1/2}$.

⁽⁸⁾This can be extended to 100 or more but in practice it is not possible to go far beyond 20 with the coupling to Rydberg states.

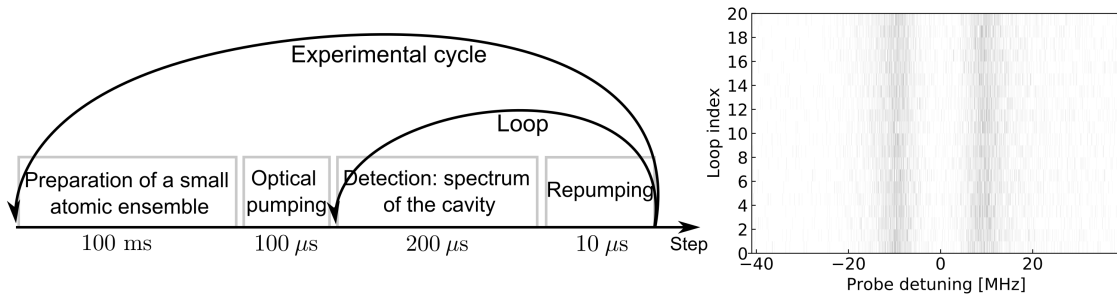


Figure 4.11: Sequence and stability. The typical experimental cycle for a spectrum measurement of the coupled system {atoms + cavity}. First, the atomic ensemble is prepared as explained in the chapter 3 (~ 100 ms). Then a $100\ \mu\text{s}$ optical pumping step is applied to put all the atoms in a unique Zeeman state. The cavity is scanned during $200\ \mu\text{s}$ with the dipole trap on. The number of atoms in $F = 1, m_F = 1$ is then readjusted with a short repumping step. The acquisition plus the repumping step are repeated ~ 20 times (loop) before restarting the full experimental cycle. Right - Check of the coupling stability throughout the loops (in transmission). Detected photons are represented in grey. Here, the atoms cavity coupling is about $g/2\pi \simeq 10\ \text{MHz}$ with $\sim 2\%$ of rms fluctuations.

g between 0 and $2\pi \times 20\ \text{MHz}$ corresponding to a cooperativity, $C = g^2/(2\kappa\gamma)$, between 0 and 22 depending on the size of the atomic ensemble. We can also adjust this value by changing the repumping duration within the pumping step.

For reflection measurements, the intensity is locked before the fiber on the detection setup. We observe residual intensity drifts that we compensate by a reference measurement. This reference signal is obtained with the cavity locked far away from the laser frequency and the atomic resonance. Otherwise, the sequence is similar to transmission measurements. We add an additional $400\ \mu\text{s}$ step to lock the phase between the local oscillator and the probe when we want to use the homodyne detection, as explained in the previous section.

Transmission and reflection

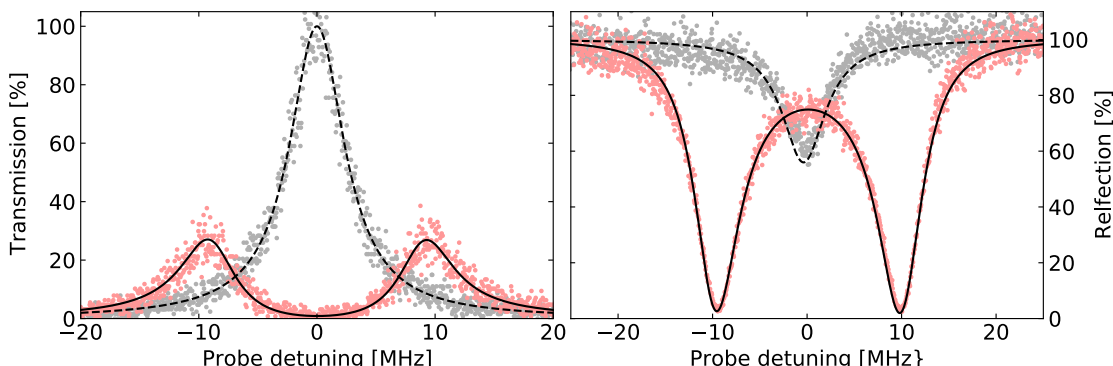


Figure 4.12: Atom-cavity coupling. Observation of the strong coupling regime between the cavity and the atomic ensemble in transmission (left) and reflection (right). The empty cavity spectrum (grey) gives access to the cavity damping rate $\kappa = 2.9\ \text{MHz}$. Two peaks are visible on the transmission when we put atoms inside the cavity, while the reflection features a drop at these two resonances $\pm g$. Data are fitted with the model from equation 1.44 and 1.55.

In the strong coupling regime ($C \gg 1$) and if the cavity is resonant with a rubidium transition, the transmission spectrum exhibits two resonances at $\pm g$. On each of these resonances, the state is a mixing between the atomic ensemble and cavity photons, corresponding to the so-called bright polaritons. Indeed, equation 1.24 from chapter 1 indicates that the

normalized expectation values of the atomic polarization \hat{P} and of the cavity field \hat{a} satisfy $\langle \hat{P} \rangle \approx \pm \langle \hat{a} \rangle$ for $\delta\omega = \pm g$ in the collective strong coupling regime. One can in fact define two bosonic operators $\hat{B}_\pm = (\hat{a} \pm \hat{P})/2$ for each polariton with a damping rate given by $\gamma_B = (\kappa + \gamma)/2$. This rate is simply the probability to be a photonic excitation, $1/2$, times its decay rate plus the probability to be an atomic excitation ($1/2$) times its damping rate. We can also find the transmission level of the two peaks with these simple arguments. When we drive one of these polaritons, the transmission is simply the squared ratio between the photonic part of the polariton decay rate over the full polariton damping rate. It gives here $\frac{\kappa^2}{(\kappa+\gamma)^2}$ and since $\gamma \simeq \kappa$ we observe a transmission of $\simeq 25\%$ on figure 4.12. The damping rate of the cavity $\kappa = 2\pi \times 2.8$ MHz is also estimated by looking at the bare resonator, as shown in figure 4.12.

The same measurement can be done in reflection. In this case, we observe that the reflectivity goes down to zero on both resonances. Again we can find simple explanations for this. When we probe the system on the resonance of one of the polaritons, we can again look at what we collect compared to what is lost. The photonic input/output rate associated to a polariton is given by $\simeq \kappa/2$ ⁽⁹⁾. On the other hand, the polariton is lost when a spontaneous emission event occurs. The loss rate of a polariton is therefore $\gamma/2$. In our platform, we are in a configuration where these two rates are almost equal. We already discussed this in chapter 1 and it corresponds to an impedance-matched system. This phenomenon is similar to the reflection of (an empty) symmetric two-mirror cavity where the two mirrors share the same transmission coefficient. The same reasoning can be extended to a non-zero detuning between the cavity and the atomic transition. The symmetry between the two polaritons is lost as one will favor its photonic nature and the other one its atomic part.

Quadrature measurements

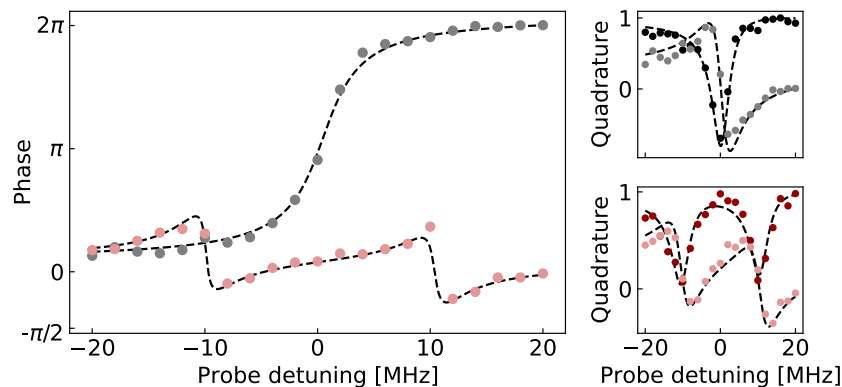


Figure 4.13: Quadratures and phase for the coupled system. Left- Phase spectrum for the empty cavity (grey) and with atoms coupled to the resonator (red). We observe a 2π -shift when the empty cavity resonance is crossed. The phase at zero detuning is π -shifted when atoms are coupled to the cavity. Right- $\hat{X} = \hat{X}_0$ (dark colors) and $\hat{P} = \hat{X}_{\pi/2}$ (light) quadratures are represented for the empty cavity (top) and for the atom-cavity coupling (bottom). Theoretical curves are only fitted to the phase curves (dashed lines). The only free parameter is the coupling strength with a value of 10 MHz.

The last information we can get from the atom-cavity coupling comes from the phase. For this purpose, we probed the atom-cavity system in the linear regime with a weak coherent

⁽⁹⁾In fact, one must take into account all the losses of the the cavity and it is therefore given by $\kappa_0/2 = T/(T + L_0)\kappa/2$ where T is the transmission of the I/O coupler and L_0 intrinsic losses of the cavity. Since we have $T \gg L_0, \kappa_0 \simeq \kappa$.

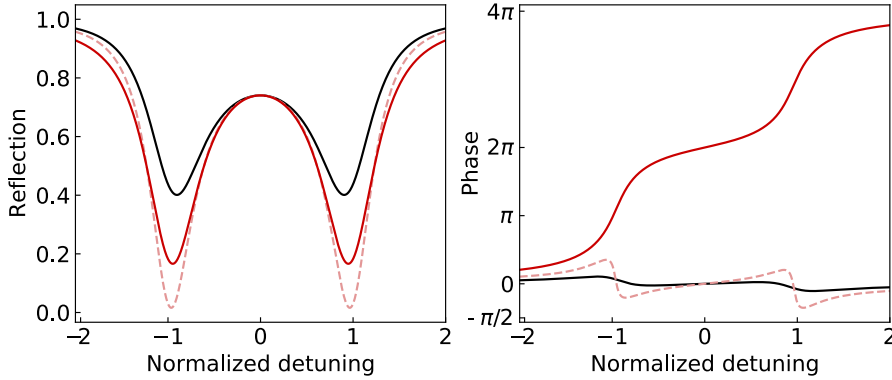


Figure 4.14: Reflection and phase vs coupling regimes. Left - Reflection of the cavity as a function of the cavity damping rate κ but at a fixed cooperativity $C = g^2/(2\kappa\gamma)$. Three configurations are considered: $g \gg \gamma \gg \kappa$ (black), $g \gg \kappa \simeq \gamma$ (dashed lines) experimental situation, $g \gg \kappa \gg \gamma$ (red). We see that the reflection minimum increases as we move away from $\kappa \simeq \gamma$. Right- Phase as a function of the frequency for the three cases (same colors). The beam is reflected on the I/O coupler when $\gamma > \kappa$ at the polariton resonances and transmitted otherwise (π -phase shift).

state. We thus measured the mean value of two quadratures $\hat{X} = \hat{X}_0$ and $\hat{P} = \hat{X}_{\pi/2}$ to infer the phase of the output electromagnetic field: $\phi = \arctan(\langle \hat{P} \rangle / \langle \hat{X} \rangle)$

First, we recover the 2π phase shift when we scan the empty cavity resonance as shown in figure 4.13. When atoms are coupled to the cavity, the phase on resonance (zero detuning) is π shifted compared to the empty cavity case. The nonlinearity we want to achieve with Rydberg interactions is precisely based on a switching of the optical response between the two configurations illustrated in figure 4.13. The coupling to a Rydberg state allows for the propagation of one photon through the cavity via a transparency window. When interactions are sufficiently strong, the propagation of a single photon is able to break the transparency window for other incoming photons. As a result, the atomic ensemble is transparent for the first excitation and equivalent to a collection of two-level systems for the additional photons. We will show this effect in chapter 7.

We also observe a phase variation near the resonance of the two bright polaritons. To understand this, it is fruitful to change the coupling regime for a constant cooperativity. For instance, let us artificially decrease the cavity decay rate, and the coupling factor accordingly, such that $g \gg \gamma \gg \kappa$. In that case, the losses due to the atomic component are much more important than the escape rate and the incident light is thus reflected so the phase spectrum is then almost flat. On the contrary if $g \gg \kappa \gg \gamma$, the atomic losses are negligible: each polariton resonance is almost like a bare cavity mode and the phase is 2π -shifted when we cross one of these resonances, as illustrated in figure 4.14.

These results highlight our ability to prepare an atomic ensemble in a well-defined ground state ($|5S_{1/2}, F=1, m_F=1\rangle$) with a 95% purity. This pumping step allows us to isolate one optical transition for the coupling to the science cavity ($|5S_{1/2}, F=1, m_F=1\rangle \rightarrow |5P_{1/2}, F'=2, m_{F'}=2\rangle$). We reached the collective strong coupling regime with a coupling factor of $2\pi \times 10$ MHz matching our theoretical expectations given the number of atoms in our crossed dipole trap. In the next chapter, we will discuss EIT in the linear regime and show strong optical nonlinearities mediated by Rydberg interactions.

Chapter 5

Rydberg EIT with polariton blockade

Contents

5.1 Rydberg EIT in the linear regime	95
5.1.1 EIT spectrum: experimental implementation	95
5.1.2 Coupling to the Rydberg state	97
Paschen-Back regime	97
Electric field compensation	98
Purity of the optical pumping	99
Estimation of the Rydberg linewidth	100
Summary of the parameters	102
5.2 Strongly interacting photons	103
5.2.1 Saturation	103
Transmission rate	103
Experimental results	105
5.2.2 Photon statistics	107
Model	107
Experimental implementation	108
Antibunching	109
Bunching of photons	111
5.3 Conclusion	114

In the previous chapter, we introduced the detection setup and obtained the collective strong coupling regime between the science cavity and our small atomic ensemble. As long as the number of excitations in the resonator remains small compared to the atom number, the system is linear and can be seen as two coupled harmonic oscillators.

In this chapter, the coupling to a Rydberg state is implemented with the aim of providing a strong anharmonicity to the system. As a first step, we will focus on the linear regime where either van der Waals interactions are small, or the probe power is very weak. The coupling to the Rydberg state then opens a window of transparency on resonance that allows a low-loss propagation of photons through the resonator. In particular, we will discuss homogeneous and inhomogeneous broadening of the Rydberg linewidth induced by several sources of noise

(stray electric fields, the optical pumping purity, etc.) in order to point out the limiting factors of this parameter, crucial for the obtained transparency.

Then, we will progressively increase the blockade volume, by addressing Rydberg states with increasing principal quantum numbers, to eventually reach polaritons interactions at the single-photon level. These strong nonlinearities result from the collective behavior of our atomic ensemble as a single Rydberg superatom, thanks to Rydberg blockade, and they demonstrate the superatom unicity. We thus achieve strong interactions between optical photons coupled to our system, an important milestone towards quantum optics applications.

We observe this nonlinearity by measuring the saturation of the transmission rate when the system is continuously driven. For a blockade radius larger than the size of the atomic cloud, the strongly coupled atom-cavity system can be seen as a two-level system with a saturation expected at half an excitation per Rydberg polariton lifetime. We will also discuss the strong photon antibunching achieved in our system by measuring the second-order autocorrelation function for the transmitted field. These results will be confronted with two different models: a numerical calculation proposed by Grankin *et al.* [115], and an analytic description for a perfect two-level system probed on resonance. We will conclude this study by looking at the system's response out of the Rydberg polariton resonance where the light is on the contrary subject to a strong bunching [114, 163] with observations in agreement with the numerical calculation.

5.1 Rydberg EIT in the linear regime

We start by discussing the coupling to a Rydberg state in the linear regime, especially the measurements of EIT spectra in direct continuation of chapter 4, where we investigated the collective strong coupling regime. The transparency induced by the mixing between photons and Rydberg excitations is a key parameter to ensure low-loss interactions between optical photons, as we pointed out in chapter 1. This quantity depends on the Rydberg linewidth γ_r and is all the closer to one as this parameter is small. We recall that the transparency level, on resonance and normalized to the empty cavity transmission, is given by (equation 1.50):

$$\mathcal{T}_0 = \left| 1 + \frac{\gamma_r}{\kappa} \tan^2 \theta \right|^{-2} \quad (5.1)$$

in the limit $\Omega^2/(4\gamma\gamma_r) \gg 1$, where $\tan \theta = -2g/\Omega$ sets the weight ratio between the photonic and atomic part in the Rydberg polariton, with g the collective coupling strength, Ω the control Rabi frequency, κ the damping field of the cavity and γ the atomic decay rate. From this equation, the role of the Rydberg linewidth at fixed g and Ω is straightforward.

We showed in chapter 1 that the natural Rydberg linewidth is expected to be small due to the poor overlap with the wave functions of the low-energy states. For instance, it is typically a few kilohertz for the 100S Rydberg state, see chapter 1. Unfortunately, this value is never reached due to several sources of inhomogeneities that broaden it [164].

One of the first issues comes from the stability of the frequency of our lasers. In order to reduce this contribution, all the important lasers are locked down to a few kilohertz linewidth via an ultra-stable narrow-linewidth reference cavity ⁽¹⁾. The second main concern is related to the extreme sensitivity of Rydberg atoms, especially to stray electric fields because of their high polarizability scaling as n^7 [165, 166]. We control the electric field with eight electrodes inside the vacuum enclosure to minimize this broadening. On top of this, the small atomic ensemble is at a temperature of a few microkelvins and loaded inside a crossed dipole trap which also slightly broadens the Rydberg linewidth, owing to differential lightshifts. We will conclude on this by considering the purity of the atomic ensemble after an optical pumping step and the consequences on the transmission spectrum to ensure that the preparation is satisfying, i.e. that it impacts only marginally our photons and the ideal three-level model presented in chapter 1.

5.1.1 EIT spectrum: experimental implementation

We make a quick recap of the experimental sequence and technical considerations to obtain EIT spectra. Following the measurements done in chapter 4 for the collective strong coupling between the cavity and the atomic ensemble, where atoms are initially prepared in the ground state $|g\rangle = |5S_{1/2}, F=1, m_F=1\rangle$, we now drive the transition between the excited state $|e\rangle = |5P_{1/2}, F'=2, m_{F'}=2\rangle$ and the Rydberg state:

$$|r\rangle = |nS_{1/2}, J=1/2, m_J=+1/2, I=3/2, m_I=+3/2\rangle \quad (5.2)$$

The excitation scheme is depicted in figure 5.1, where the control beam is shown in blue and the probe in red. The choice for the Rydberg state is imposed by the geometry of the platform: the quantization magnetic field axis is orthogonal to the optical axis of the two build-up cavities and almost aligned with the science cavity axis, tilted by 12°. In this way, the control beam is linearly polarized and addresses only a π transition while the circularly-polarized science cavity field drives a $\sigma+$ transition. We experimentally found that this

⁽¹⁾This stabilization is described in chapter 2 section 2.2.2 and is based on the Pound-Drever-Hall technique [127].

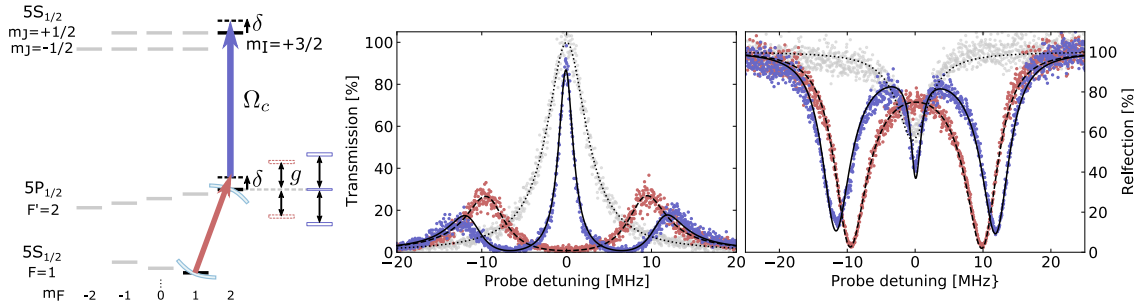


Figure 5.1: EIT spectrum. Left- Rubidium 87 levels. Atoms are pumped into the ground state $|5S, F = 1, m_F = 1\rangle$, the cavity is set on resonance with $|5S, F = 1, m_F = 1\rangle \rightarrow |5P, F = 2, m_F = 2\rangle$ and the control beam addresses the 78S Rydberg state with $m_I = 3/2, m_J = 1/2$. Atom-cavity spectrum in transmission (middle) and reflection (right) for the empty cavity (grey), the atomic ensemble strongly coupled to the cavity (red) with $g = 2\pi \times 10 \text{ MHz}$ and EIT (blue) with $\Omega = 2\pi \times 13.5 \text{ MHz}$. Each spectrum (dots) is averaged over 1000 experimental cycles and 21 loops and fitted by the model from chapter 1 (solid lines).

configuration gives better results compared to an alignment of the magnetic field with the science cavity axis. This is due to the fact that the intermediate levels are well separated in energy by the magnetic field which is not the case for the Rydberg sublevels at a given m_j . As a consequence, an approximate polarization of the control beam can lead to a coupling to other states and thus alter the EIT.

The experimental sequence is very similar to what we did in the previous chapter: 50 ms for the loading of the 3D MOT by the 2D MOT, 10 ms of transport from the MOT to the cavity mode with the conveyor belt, alternations of Raman cooling plus compressions before the loading of the 1064 nm crossed dipole trap ($\sim 10 \text{ ms}$) and a 50 ms waiting time to get rid of background atoms. Finally, the remaining small atomic ensemble is pumped in the ground state $|g\rangle$ with a 95% purity and one spectrum of the coupled system is obtained in 200 μs over a 80 MHz range around the cavity resonance. For this purpose, two D_1 probes are injected through the cavity either in transmission or in reflection. The frequency of the probe is swept by the direct digital synthesizer driving the double-pass AOM associated to this beam⁽²⁾. This step can be repeated ~ 20 times before restarting the experimental sequence since the dipole trap is kept on during these acquisitions. Between each repetition, a small repumping step is used (10 μs) to maintain the atom number constant⁽³⁾. The detection and optical paths for the probe beams were introduced in chapter 4, see section 4.1.

Regarding EIT measurements, the control beam comes from one of our TiSa laser. This beam is injected through one of the build-up cavities with a $\sim 60 \mu\text{m}$ intra-cavity waist. The driving by the control beam can reach a $2\pi \times 18 \text{ MHz}$ Rabi frequency for the 100S Rydberg state with about 0.8 W of 475 nm light in front of the build-up resonator. In this kind of measurements, we want to characterize our system in the linear regime. Therefore, the D_1 probe is used at a very small rate to avoid interactions between Rydberg polaritons and saturation effects.

The spectrum as a function of the probe detuning can either be measured in transmission or reflection, as shown in figure 5.1. In these acquisitions, the cavity frequency is resonant with the $|g\rangle - |e\rangle$ transition and the control beam frequency is resonant with the $|e\rangle - |r\rangle$ transition⁽⁴⁾. The EIT transmission spectrum and the reflection one were measured with the 78S Rydberg state. In this case, we achieve a high transmission level, $T_0 > 90\%$, while

⁽²⁾Acousto Optics Modulators and direct digital synthesizers are introduced in chapter 2.

⁽³⁾The typical variation of the collective coupling is 5%.

⁽⁴⁾ $\delta_r = \delta_e = \delta_a \equiv \delta$ in the Hamiltonian given by equation 1.40 from chapter 1.

the polariton is mostly a Rydberg excitation with a population of 70% in this state. The EIT linewidth of the transmission spectrum $\gamma_{EIT} = 2\pi \times 0.95 \text{ MHz}$ is the damping rate of the Rydberg polaritons. This rate provides an order of magnitude of the transmission saturation rate in the interaction regime $\simeq 6 \text{ MHz}$, corresponding to half a Rydberg polariton per polariton lifetime in the cavity. This saturation rate is well above the output photon rate for these measurements, at a value of 250 kHz, confirming that the system is linear in these measurements.

These experimental spectra are fitted by the model described in the first chapter (equation 1.44 and 1.55). We recall that the reflectivity on resonance is given by:

$$\mathcal{R}_0 = |1 - 2\sqrt{\mathcal{T}_0} \frac{T}{L}|^2 \quad (5.3)$$

With the parameters used for this measurement, we have $\mathcal{R}_0 = 43\%$. The value of the Rydberg linewidth is typically about 100 kHz from a direct fit of the spectrum with the two models (shown in the figure). We will discuss the origin of this value and provide a more precise estimation in what follows.

5.1.2 Coupling to the Rydberg state

We study further the coupling to the Rydberg state and how several imperfections and noise impact the spectrum of the atom-cavity system and in particular the Rydberg linewidth. We conclude by measuring the value of the Rydberg linewidth and discuss the limiting factors.

Paschen-Back regime

In chapter 1, we claimed that the hyperfine splitting was irrelevant for Rydberg atoms. This splitting originates from the coupling between the nuclear spin and the electronic angular momentum that is reduced because of the huge separation between the outer electron and the core ($\langle \hat{r} \rangle \propto n^{*2}$). Nevertheless, it remains to be determined to what extent this factor is negligible and in regard to what.

In the case of Rubidium 87, this hyperfine coupling was measured as a function of the principal quantum number, giving a hyperfine energy $h \times (33 \text{ GHz})n^{*-3}$ for nS states [88]. For instance, this energy coupling is $h \times 300 \text{ kHz}$ for $n = 50$ and $h \times 40 \text{ kHz}$ when $n = 100$. It is clearly not negligible compared to a Rydberg linewidth of a few kilohertz.

One way to get rid of this problem is to work in the Paschen-Back regime, with an important quantization magnetic field to ensure that the hyperfine energy is negligible compared to the Zeeman splitting. In this limit the contributions from the nuclear spin and the total angular momentum decouple. On top of this, the Landé factor for the nuclear spin is very small $\sim 10^{-3}$ compared to $g_S \simeq 2$ for the spin of the electron and $g_L \simeq 1$ for the angular momentum. Consequently, the energy splitting in the Paschen-Back regime is dominated by the contribution from the total angular momentum J , while the states from the nuclear spin can remain almost degenerate. In our EIT driving scheme, we use a stretched intermediate state in the hyperfine basis $|e\rangle$ to have a unique pair $\{m_J, m_I\}$. It is therefore possible to properly address a single Rydberg state at the pair $\{m_J, m_I\}$ with the linearly polarized control field (π transition).

In practice, this magnetic field is produced by one of the pairs of compensation coils along the cavity axis with a 3 G amplitude. In this thesis work, we only drive nS Rydberg states resulting in a $h \times 8.4 \text{ MHz}$ Zeeman splitting between states with $m_J = +1/2$ and $m_J = -1/2$. This makes the contribution of the hyperfine coupling completely negligible and prevents the mixing between Zeeman states of the fine structure.

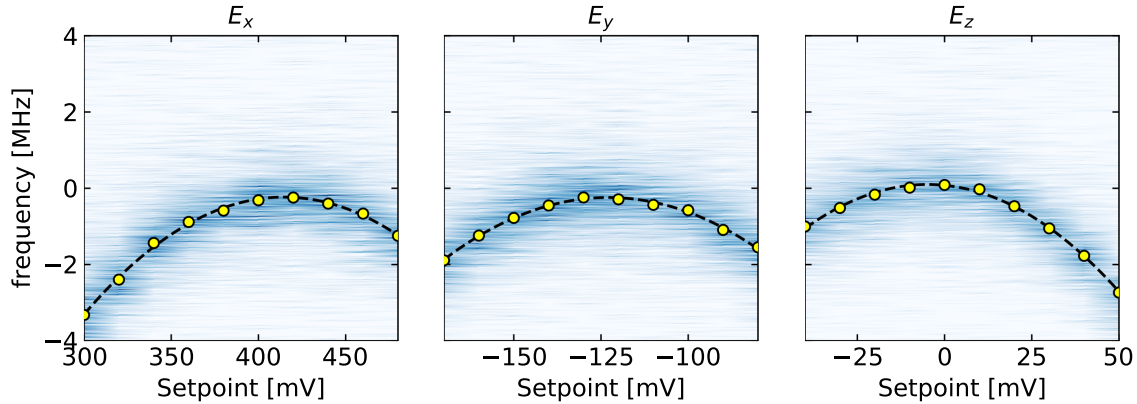


Figure 5.2: Electric field compensation. Optimization of the electric field via the EIT spectrum for the three axes (x, y, z) for a coupling strength $g = 2\pi \times 10$ MHz and a control frequency of $\Omega = 2\pi \times 10$ MHz. The colors map gives the counts on the SPCM (blue shades) for a probe frequency scanned around the EIT resonance as a function of the voltage setpoint. The position of each EIT peak (yellow) is inferred from a Lorentzian fit. Finally, a quadratic fit is performed to obtain the best setpoint voltage for the compensation (dashed line). Each spectrum is averaged over 210 realizations: 21 loops and 10 experimental cycles.

Electric field compensation

Eight electrodes were placed inside our science cavity to keep the electric field as low as possible in this region, see chapter 2 section 2.1 for technical details. We have an independent control over these electrodes in order to compensate stray electrical fields along the three orthogonal axes. For this purpose, we apply a given voltage to the electrode and then acquire the EIT spectrum. This acquisition is repeated for many values of the voltage along the three directions. The applied external electric field \mathcal{E} induces a quadratic drift of the two-photon resonance which translates into a quadratic displacement of the maximum of transparency δ_{peak} . For a small shift of the Rydberg resonance, one has (equation 1.44):

$$\delta_{peak} \simeq -\frac{g^2}{g^2 + \Omega^2/4} \delta_E \propto \mathcal{E}^2 \quad (5.4)$$

where δ_E is the dc stark shift of the Rydberg state. It is therefore convenient to keep $\Omega \lesssim g$ in order to maximize the sensitivity. Notice that on top of that, the EIT linewidth is also reduced for small Ω . This improves the accuracy but the obvious drawback is the loss of transparency (equation 5.1).

This method gives access to the minimum of the electric field and provides a calibration of our electrodes since one can estimate independently the polarizability via the ARC calculator [92]. The compensation is illustrated in figure 5.2 for the 109S Rydberg state, along the three orthogonal axes of the experiment, where y is the optical axis of the science cavity and z is the vertical axis. Each spectrum is acquired with a 20 kHz resolution while the full width at half maximum of the EIT peak is typically 1.2 MHz. A Lorentzian fit yields the center of the EIT window with a ~ 10 kHz accuracy. The positions of the EIT peaks as a function of the setpoint voltage are finally fitted by a parabola to infer the best setpoint voltage, i.e. where the electric field is minimal. The calibration from the fits is done with a 0.1 mV accuracy while the electronic card driving these electrodes⁽⁵⁾ has a 1 mV rms noise. The latter translates into a 1 kHz frequency shift close to the zero-field region for the 109S Rydberg state. This accuracy is sufficient since the linewidth of our lasers is already of a few kilohertz. On the

⁽⁵⁾NI PXIe-6738

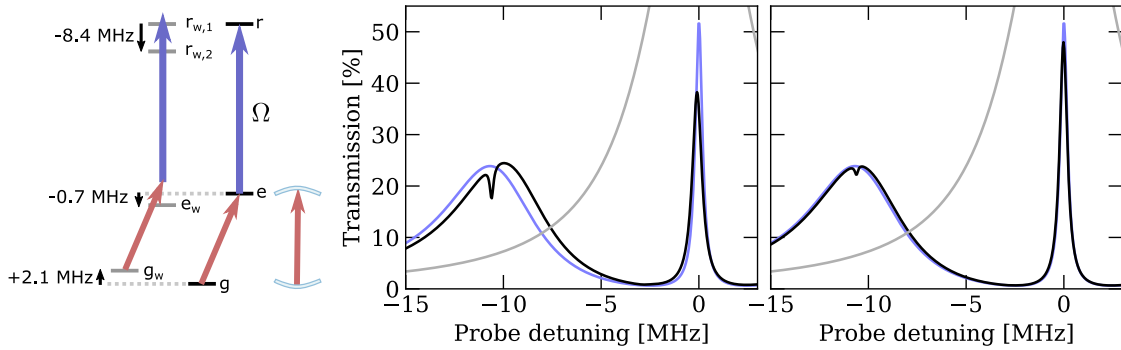


Figure 5.3: EIT spectrum for an imperfect optical pumping. Left- EIT scheme with two ground states $|g\rangle = |5S_{1/2}, F = 1, m_F = 1\rangle$ and $|g_w\rangle = |5S_{1/2}, F = 1, m_F = 0\rangle$, see text. Middle- EIT spectra. All atoms in the expected ground state $|g\rangle$ (blue) or with 20% of atoms in the ground state $|g_w\rangle$ (black) for parameters: $g = 2\pi \times 10$ MHz, $\Omega = 2\pi \times 5$ MHz and $\gamma_r = 2\pi \times 100$ kHz while the bare cavity spectrum is in grey. Right- Same plot but for a preparation efficiency of 95% corresponding to our current configuration.

figure, it is clear that the z axis compensation field is close to zero which is not the case for the two other axes. This might be due to the piezo actuators of the science cavity (y axis) and of the build-up cavities (x axis) together with the surface charges on the supports. This calibration is in general performed once in a day and the main consequence of these drifts is a displacement of the two-photon resonance, at a few hundred kilohertz, rather than a mixing between Rydberg states.

Purity of the optical pumping

In chapter 4, we discussed the pumping step to prepare all the atoms in the same ground state: $|g\rangle = |5S_{1/2}, F = 1, m_F = 1\rangle$. We also characterized the pumping step by measuring the population in each Zeeman state $m_F = -1, 0, 1$ after the optical pumping phase. We established that $\eta = 95\%$ of the atomic population is well prepared in $m_F = +1$ while almost all the other atoms lie in $m_F = 0$. We now discuss the consequences of these 5% on the transmission spectrum.

These atoms, in $|g_w\rangle = |5S_{1/2}, F = 1, m_F = 0\rangle$, are also coupled to the cavity via an intermediate state $|e_w\rangle = |5P_{1/2}, F' = 2, m_{F'} = 1\rangle$ with a dipole transition reduced by $1/\sqrt{2}$ compared to the transition that we want to address ($|g\rangle - |e\rangle$). This excited state, in $m_{F'} = +1$, is then coupled to two Rydberg states by the control beam:

$$\begin{aligned} |r_{w,1}\rangle &= |nS, J = 1/2, m_J = +1/2, I = 3/2, m_I = +1/2\rangle \\ |r_{w,2}\rangle &= |nS, J = 1/2, m_J = -1/2, I = 3/2, m_I = +3/2\rangle \end{aligned} \quad (5.5)$$

The Clebsch–Gordan coefficients for these transitions result in two control Rabi frequencies at $\Omega_{w,1} = \Omega\sqrt{3/4}$ and $\Omega_{w,2} = -\Omega/2$, where Ω is the Rabi frequency associated to $|e\rangle - |r\rangle$ transitions. For atoms prepared in $|g_w\rangle$, the steady-state equations from chapter 1 (equation

38) are slightly modified to take into account the two Rydberg states:

$$\begin{aligned}
\langle \hat{a} \rangle &= \frac{1}{\delta_a + i\kappa} \left(i\alpha\sqrt{2\kappa_0} + g_{ge}\langle \hat{P} \rangle + g_w\langle \hat{P}_w \rangle \right) \\
\langle \hat{P}_w \rangle &= \frac{1}{\delta_{e,w} + i\gamma} \left(g_w\langle \hat{a} \rangle + \frac{\Omega_{w,1}}{2}\langle \hat{S}_{w,1} \rangle + \frac{\Omega_{w,2}}{2}\langle \hat{S}_{w,2} \rangle \right) \\
\langle \hat{S}_{w,1} \rangle &= \frac{\Omega_{w,1}}{2(\delta_{r,1} + i\gamma_r)}\langle \hat{P}_w \rangle \\
\langle \hat{S}_{w,2} \rangle &= \frac{\Omega_{w,2}}{2(\delta_{r,2} + i\gamma_r)}\langle \hat{P}_w \rangle \\
\langle \hat{P} \rangle &= \frac{1}{\delta_e + i\gamma} \left(g_{ge}\langle \hat{a} \rangle + \frac{\Omega}{2}\langle \hat{S} \rangle \right) \\
\langle \hat{S} \rangle &= \frac{\Omega}{2(\delta_r + i\gamma_r)}\langle \hat{P} \rangle
\end{aligned} \tag{5.6}$$

where the collective operators indexed by w are defined on the subset of atoms pumped in $m_F = 0$ and $g_w = g\sqrt{(1-\eta)/2}$ is the effective collective coupling strength, while the coupling for atoms in $m_F = 1$ is reduced to $g_{ge} = g\sqrt{\eta}$.

Finally, we must also take into account the frequency shift induced by the quantization magnetic field. We assume that the cavity is resonant with the $|g\rangle - |e\rangle$ transition for a 3 G magnetic field. Then, the ground state $|g_w\rangle$ is shifted by +2.1 MHz with respect to the ground state $|g\rangle$, the intermediate state $|e_w\rangle$ is -0.7 MHz from $|e\rangle$ and the Rydberg state $|r_{w,2}\rangle$ is detuned by -8.4 MHz from the Rydberg state with $m_J = +1/2$, as illustrated in figure 5.3, schematic on the left.

Let us first look at the evolution of the spectrum when these defects are taken into account. This is an important information since we will compare this spectrum to the three-level model (equation 1.44) to estimate the Rydberg linewidth. For a 95% purity, this correction leads to a drop of transparency of only 2% compared to the ideal case for realistic parameters $g = \Omega = 2\pi \times 10$ MHz, $\gamma_r = 2\pi \times 100$ kHz, while this drop is close to 7% when $\eta = 80\%$. Since atoms initially in $|e_w\rangle$ are also subject to EIT, the consequences of a bad preparation are more apparent at a low control Rabi frequency, see figure 5.3 for $\Omega = 2\pi \times 5$ MHz. When the preparation efficiency has a value of 95%, the drop remains low at 3.6% (right panel) while it reaches 15% for $\eta = 80\%$ (middle). Finally, we have a small distortion at a detuning of -11 MHz caused by the coupling to the Rydberg state $|r_{w,2}\rangle$ that we can also observe on our measurements when the cloud is not correctly pumped.

Notice that these atoms in the wrong ground state may cause other troubles. The consequence depends on both the parameters and the experimental protocol at stake. Let us consider the coherent driving of the atomic ensemble between the ground state and one delocalized Rydberg excitation. The mismatch in energy between the $|g\rangle - |r\rangle$ and $|g_w\rangle - |r_{w,1}\rangle$ transitions, of a few megahertz, causes a dephasing between these two subsets. A conservative approximation is to assume that the $1 - \eta$ population in the wrong ground state are lost during the process.

As a consequence, for a purity of $\eta = 95\%$, the broadening of the Rydberg polariton or the loss of transparency caused by the imperfect preparation can be neglected and we should not be too dramatically impacted for other protocols.

Estimation of the Rydberg linewidth

In the last discussion, we shown that the EIT spectrum in our platform can be quite different from the ideal three-level model. Other phenomena, such as the inhomogeneities of the control

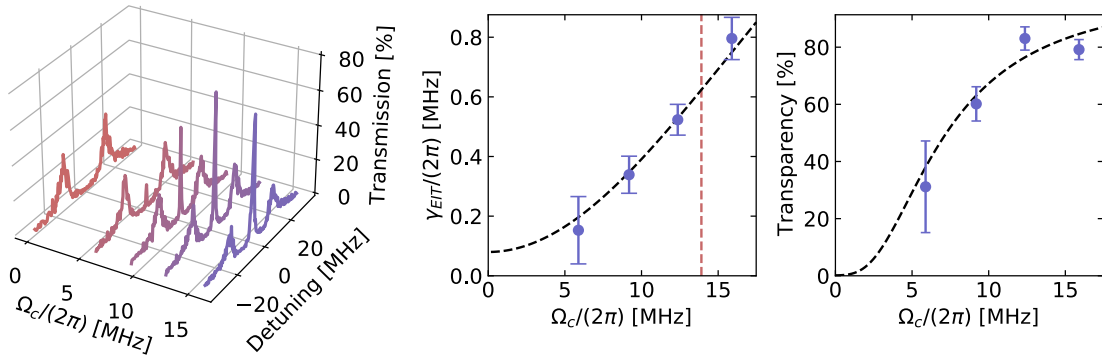


Figure 5.4: 100S Rydberg linewidth. Estimation of the Rydberg linewidth for the 100S Rydberg state by scanning both the control Rabi frequency and the probe frequency. Left- EIT spectra as a function of the probe detuning and the Rabi frequency. Middle- EIT linewidth as a function of the control Rabi frequency (blue dots). Data are fitted by the model (equation 1.49, dashed line) to infer the value of Rydberg linewidth: $\gamma_r = (80 \pm 40)$ kHz. The collective coupling factor $g = 2\pi \times 13.9$ MHz is the vertical red dashed line. Right- Transparency on resonance as a function of the control Rabi frequency. Each spectrum is averaged over 100 realizations and the output rate is at a value of 390 kHz for the empty cavity.

beam could also drastically impact our measurements. We observed experimentally that it is important to have a good overlap between the control beam and the atomic ensemble but also to keep it homogeneous. This alignment is difficult to handle and significant increases of the Rydberg linewidth are observed (more than a factor of two) during the alignment of the build-up mode.

We now discuss the estimation of the Rydberg linewidth to check that the broadening is not too important in our experimental platform. In figure 5.4, we present the method to estimate the Rydberg linewidth from the transmission spectrum in the linear regime. The spectrum is measured for several values of the control beam power at the input of the build-up cavity, left plot. The control Rabi frequency at a given input power is estimated from the light shift of the two bright polaritons detuned by $\pm\sqrt{g^2 + \Omega^2/4}$. This effect is for instance visible in figure 5.1 and allows us to estimate the build-up factors of our resonators. Then, we fit the EIT peak by a Lorentzian to infer the EIT linewidth. In the last step, the linewidth as a function of the control Rabi frequency is fitted by the theoretical EIT linewidth derived in the first chapter: $\gamma_{\text{EIT}} = \kappa \cos^2 \theta + \gamma_r \sin^2 \theta$ (equation 1.49). The only free parameter is the Rydberg linewidth (γ_r) with a fitted value of (80 ± 40) kHz. Finally, we plot the theoretical transparency (equation 5.1) as a function of the control Rabi frequency for this effective linewidth (right panel), which reproduces well the values measured with our experimental platform. Notice that a direct fitting of the EIT spectrum by the model (equation 1.44) already provides a good estimation of the Rydberg linewidth, typically 100 kHz, confirming that our platform is well captured by the homogeneous three-level model.

Beside the source of broadening discussed previously, a $2\mu\text{K}$ temperature induces a Doppler broadening of $\simeq 30$ kHz and a trap-induced broadening of $\simeq 50$ kHz for atoms in the ground state. The contribution for the Rydberg state is more difficult to compute due to the numerous transitions but is expected to have a smaller contribution since the detuning between the transitions and the trapping light is larger than for atoms in the ground state. This is somewhat confirmed by the previous estimation of the Rydberg linewidth that matches the contribution from the dipole trap plus the Doppler effect. At this magnitude, the contribution from the lasers on the Rydberg linewidth is negligible (a few kilohertz).

Summary of the parameters

With a Rydberg linewidth of 80 kHz, we already have a quite satisfactory configuration. For a Rydberg polariton in an equal superposition of a cavity photon and a Rydberg state ($\tan^2 \theta = 1$), the transparency has a value of 95% and because $\kappa \gg \gamma_r$, $\gamma_{\text{EIT}} \simeq \kappa/2$. In this case however, the interaction between polaritons is only a quarter of its maximal value ($\propto \sin^4 \theta$). If we rise the Rydberg population to $1/\sqrt{2}$ for the polaritons, the interaction is twice as important and the transparency slightly drops to 88%.

In practice, we can reach a control Rabi frequency of $2\pi \times 18$ MHz for the 100S Rydberg state and a collective coupling factor of $2\pi \times 20$ MHz with a $7 \mu\text{m}$ radius cloud, which offers a large exploration range for our experimental platform. The parameters of the atom-cavity system are summarized in table 5.1.

Parameter	Symbol	Range/value (MHz)
Control frequency (100S)	Ω	$2\pi \times (0 - 18)$
Collective coupling	g	$2\pi \times (0 - 20)$
Rydberg damping rate	γ_r	$2\pi \times 0.08$
D_1 damping rate	γ	$2\pi \times 2.873$
Cavity damping rate (795 nm)	κ	$2\pi \times 2.9$
I/O coupler driving rate (795 nm)	κ_0	$2\pi \times 2.6$

Table 5.1: Main parameters of the atom-cavity system.

5.2 Strongly interacting photons

In the previous section, we probed the system with a very low input rate to observe the linear regime for the characterization of EIT and our Rydberg polaritons. We saw that the response of our system is well captured by the linear EIT model derived in the first chapter (equation 1.44) for an effective Rydberg damping rate of $2\pi \times 80$ kHz. In particular, this parameter is low enough to achieve high transmission for the optical photons injected through the resonator.

This section now presents a completely different regime, where interactions are dominant and a mean field description of our atom-cavity system is no longer sufficient. In this regard, we discussed the preparation of a 7 μm-radius atomic ensemble in chapter 3⁽⁶⁾. For instance, the mean distance between atoms in the atomic cloud, $\simeq 14$ μm, is smaller than the 19 μm blockade radius for the 100S Rydberg state, if we assume a Rydberg polariton damping rate $\gamma_{EIT} = 2\pi \times 1$ MHz.

A first method to demonstrate strong interactions between polaritons is to look at the transmission rate of our resonator when the input intensity is increased. Since we expect to have a blockade of the transmission by only one Rydberg polariton, we should observe a strong saturation of the output rate. If this regime is reached, we expect to have only single photons transmitted by the resonator which can be characterized via coincidence measurements to infer the second-order autocorrelation function [148]. We start by presenting the study of the saturation rate as a first hint towards strong photon-photons interactions. In a second part, we discuss coincidence measurements to demonstrate that we can reach strong interactions between optical photons.

5.2.1 Saturation

In the linear regime the control beam allows for low-loss propagation of photons through the atom-cavity platform as Rydberg polaritons. This mapping remains true as long as the photon rate is much smaller than the decay rate of a Rydberg polariton to ensure that the number of excitations in the resonator is very small compared to 1. Beyond this limit, and if the distance between atoms within the dipole trap is smaller than the blockade radius, only one photon at a time can be transmitted. In this case, the strongly coupled atom-cavity system can be described as a single two-level system in the vicinity of the Rydberg polariton mode. The ground state corresponds to zero cavity photon and all atoms in the atomic ground state, while the excited state is given by a single Rydberg polariton. For a continuous driving of the atom-cavity system, we therefore expect to observe a saturation of the transmission at half an excitation, resulting in a maximal output rate given by $\sim \gamma_{EIT}$.

Transmission rate

We derive here the saturation of the transmission from the EIT model introduced in the first chapter (equation 1.57). The atomic ensemble is strongly coupled to the resonator and we assume a continuous driving of the system from one of the high-reflectivity mirror with a transmission T_{HR} . The probe is resonant with the Rydberg polariton mode and we simply ignore the two bright polaritons detuned by $\pm \sqrt{g^2 + \Omega^2/4}$. At last, we examine the response of the atom-cavity system for infinite van der Waals interactions such that the population in multiply-excited Rydberg states can be approximated to zero. We recall that the driving of the cavity is given by the operator (equation 1.12):

$$\hat{F}_{HR} = i\hbar\sqrt{2\kappa_{HR}}\alpha(\hat{a}^\dagger - \hat{a}) \quad (5.7)$$

⁽⁶⁾7 μm is the half-width at $e^{-1/2}$.

where the field damping rate of the input/output mirror κ_0 is substituted by $\kappa_{HR} = \kappa T_{HR}/L$, the field feeding rate of the high-reflectivity mirror.

For an empty cavity, the output photon flux can be computed classically:

$$f_{out}^{(0)} = \frac{4TT_{HR}}{L^2}\alpha^2 \quad (5.8)$$

where we recall that T is the transmission of the input/output coupler, L the total cavity losses such that $\kappa_0/\kappa = T/L$. The empty cavity output rate is easier to measure than the input rate and is of course proportional to it, so we will use this quantity to characterize the input driving of our polaritons.

We recall the expression of the Hamiltonian describing our atom-cavity system for an ideal blockade (equation 1.57):

$$\hat{H}_s = \frac{\Omega}{2}(|R\rangle\langle G|\hat{P} + |G\rangle\langle R|\hat{P}^\dagger) + g(\hat{P}^\dagger\hat{a} + \hat{P}\hat{a}^\dagger) \quad (5.9)$$

where \hat{P} is the collective operator between the ground state and the intermediate state, assuming that the lasers are resonant with the atomic transitions and \hat{a} the annihilation operator of the cavity mode.

The Hamiltonian from equation 5.9 preserves the number of excitations in the system, i.e $[\hat{H}_s, \hat{N}] = 0$, where \hat{N} is the excitation number operator. The one-excitation resonant (i.e. zero-energy) eigenstate of the atom-cavity system is thus the dark Rydberg polariton:

$$|\psi_d\rangle = \cos\theta|1, 0, G\rangle + \sin\theta|0, 0, R\rangle \quad (5.10)$$

where $|n, 0, i\rangle$ denotes the state of the cavity field $n = 0$ or 1 photon, the index i for the atomic part: the collective ground state $|G\rangle$ or the collective Rydberg state $|R\rangle$ (equation 1.22) and the intermediate state is of course empty.

One can for instance compute the two-excitation resonant eigenstate to understand the mechanism at stake:

$$|\psi_d^{(2)}\rangle = \frac{(1 - \epsilon^2)|2, 0, G\rangle + \epsilon\sqrt{2}|1, 0, R\rangle - |0, 2, G\rangle}{\sqrt{(1 - \epsilon^2)^2 + 2\epsilon^2 + 1}} \quad (5.11)$$

and we set $\epsilon = \Omega/g$. Here, it is interesting to consider the case where the one-excitation polariton is essentially a Rydberg atom to ensure a strong blockade, i.e. $|\tan\theta| = 2g/\Omega \gg 1$. The driving rate of the one-excitation polariton is:

$$\frac{i\Omega_p}{2} = \frac{1}{\hbar}\langle\psi_d|\hat{F}_{HR}|0, 0, G\rangle = i\sqrt{\frac{L}{2T}}\sqrt{f_{out}^{(0)}\kappa}\cos\theta \quad (5.12)$$

and this driving frequency scale as $\epsilon \ll 1$. In this limit, the driving from the one-polariton state to the two-excitation resonant state is negligible:

$$\langle\psi_d|\hat{F}_{HR}|\psi_d^{(2)}\rangle \sim \epsilon^3 \quad (5.13)$$

while this driving scales as ϵ in the absence of Rydberg interactions. This is worse for a higher number of excitations in the system and we can simply assume that our system is equivalent to a two-level system when $\epsilon = \Omega/g \ll 1$. One can rewrite the driving of the cavity in this limit:

$$\hat{F}_{HR} \simeq \frac{i\Omega_p}{2}(|\psi_d\rangle\langle 0, 0, G| - |0, 0, G\rangle\langle\psi_d|) \quad (5.14)$$

The damping rate for the coherence of the one-excitation polariton is simply given by the EIT decay rate (equation ??): $\gamma_{\text{EIT}} = \frac{1}{\sqrt{\mathcal{T}_0}} \kappa \cos^2 \theta$. We can therefore define the saturation parameter on resonance, like for any two-level system [68]:

$$s_0 = \frac{2\Omega_p^2}{(2\gamma_{\text{EIT}})^2} = \sqrt{\mathcal{T}_0} \frac{L}{T} \frac{f_{\text{out}}^{(0)}}{\gamma_{\text{EIT}}} \quad (5.15)$$

By solving the optical Bloch equations in this two-level subspace, one finds the steady-state population in the Rydberg polariton:

$$\langle \psi_d | \hat{\rho} | \psi_d \rangle^{(\text{ss})} = \rho_{dd}^{(\text{ss})} = \frac{1}{2} \frac{s_0}{1 + s_0} \quad (5.16)$$

The last step is to compute the escaping rate for the photonic part of the polariton, which corresponds to the quantity that we can actually measure. The output rate is:

$$f_{\text{out}} = 2\kappa_0 \langle \hat{a}^\dagger \hat{a} \rangle = 2\kappa \cos^2 \theta \frac{T}{L} \rho_{dd}^{(\text{ss})} = \gamma_{\text{EIT}} \sqrt{\mathcal{T}_0} \frac{T}{L} \frac{s_0}{1 + s_0} \quad (5.17)$$

In the linear regime, for $s_0 \ll 1$, we recover the linear transmission with the EIT transparency: $f_{\text{out}} = \mathcal{T}_0 f_{\text{out}}^{(0)}$. On the contrary, the output saturates at $\gamma_{\text{EIT}} \sqrt{\mathcal{T}_0} T / L$ for a very high input rate, $s_0 \gg 1$. Notice that for an ideal platform ($\gamma_r \rightarrow 0$ and $T/L = 1$) one finds a saturation rate equal to γ_{EIT} , which is half the Rydberg polariton damping rate for the population, as expected.

Experimental results

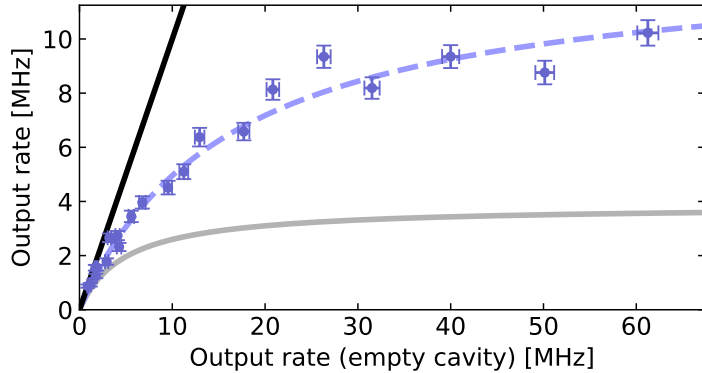


Figure 5.5: Saturation for the 77S Rydberg state. EIT transmission rate on resonance as a function of the output rate for the empty cavity, for $g = 2\pi \times 15$ MHz and $\Omega = 2\pi \times 21$ MHz. The measurement (blue dots) is detached from the linear regime (black, $\mathcal{T}_0 = 90\%$) but is well above the saturation for an ideal two-level system (grey line) with ~ 3 Rydberg polaritons at saturation.

We now discuss the concrete measurement of this saturation rate in transmission. The experimental sequence for the saturation measurements is identical to that presented for the EIT spectra except that the probe is not swept but kept on the Rydberg polariton resonance, and one acquisition lasts 100 μ s.

The output rate in transmission was acquired as a function of the input intensity for the 77S Rydberg state and the 100S Rydberg state, with a 7 μ m-rms-radius atomic ensemble. The same measurement was also performed for the empty cavity to calibrate the input driving, $f_{\text{out}}^{(0)}$. The van der Waals coefficient is $C_6^{77S} = 2.7$ THz μm^6 for the first Rydberg state and reaches $C_6^{100S} = 57$ THz μm^6 for the 100S Rydberg state. Concretely, switching from the 77S

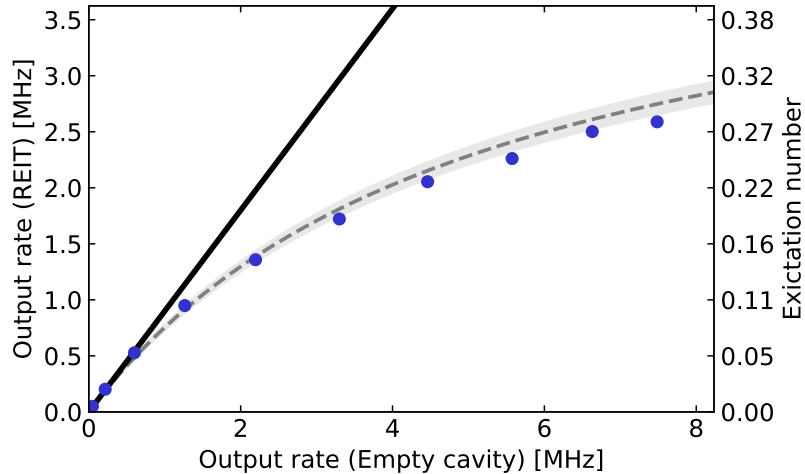


Figure 5.6: Saturation for the 100S Rydberg state. Saturation of the transmission rate for $g = 2\pi \times 11$ MHz and $\Omega = 2\pi \times 15$ MHz. The measurements from our platform (blue dots) are indeed saturating, well below the linear regime (black line) and very close to the saturation at half an excitation (grey dashed line). The theoretical saturation curve is estimated from the parameters measured on the EIT spectrum, resulting in 4% rms fluctuations (light grey).

state to the 100S represents a $\simeq 1.5$ -fold increase of the blockade radius, all other parameters being equal.

Data for the 77S Rydberg state are plotted as blue dots in figure 5.5. The polariton is characterized by the damping rate of its coherence $\gamma_{\text{EIT}} \simeq 2\pi \times 1$ MHz, a Rydberg population of 67% while the two bright polaritons are far away, detuned by ± 18 MHz, and can be forgotten. In this case, we expect to have a saturation above the single excitation for the 77S state since the blockade radius is 10 μm while atoms are, on average, separated by $\simeq 2\sigma = 14$ μm in our atomic ensemble. In practice, we clearly observe a saturation of the transmission, the linear EIT regime for a transparency of $\mathcal{T}_0 = 90\%$ is indeed well above the measurements but the saturation rate for a perfect two-level system (equation 5.17) is much smaller. We observe that the saturation is reached for about ~ 3 polaritons instead of $1/2$ by fitting the function from equation 5.17 where the population at saturation is the only free parameter.

Let us move to the measurement of the saturation rate for the 100S Rydberg excitation, shown in figure 5.6. For this data set, the Rydberg polaritons are made of 70% of a Rydberg excitation, we are therefore working with parameters similar to the 77S Rydberg state, apart for the blockade volume. Here, we expect to have strong enough interactions with this Rydberg state to reach the saturation at the single-polariton level since the blockade radius is 17 μm . Again, the transmission rate clearly saturates if we compare it to the linear regime for a $\mathcal{T}_0 = 89\%$ transparency. For this Rydberg state, however, we indeed observe a saturation of the output rate very close to the theoretical curve from the two-level model (equation 5.17). This is a solid evidence that we have reached the strongly interacting regime for optical photons in our experimental platform, which is an important achievement for this project.

Our measured transmission rates are even slightly below the theoretical curve. This decrease is due to a small but non-zero probability to have two polaritons at the same time inside the resonator. When such an event occurs, the strong interactions dephase the polariton pair out of the “symmetric” Dicke states but also induces absorption. Consequently, the photonics part ends up being decoupled to the cavity mode or is absorbed which translates into optical losses. From this data set, we obtain an effective saturation of 0.46 ± 0.02 instead of $1/2$ corresponding to $\simeq 8\%$ of losses compared to the ideal two-level model.

Since we have here the saturation at half an excitation, our atomic ensemble made of about a thousand atoms is indeed equivalent to a single Rydberg superatom. This superatom can either be in the collective ground state of the atomic ensemble, $|G\rangle$, or in the first collective Rydberg state of the system delocalized over the atomic cloud $|R\rangle$. In this regime of a single Rydberg superatom strongly coupled to the resonator, the output light statistics is drastically impacted. Since at most one polariton can propagate through the resonator per polariton lifetime, we expect to obtain a strong photon antibunching at the output of the resonator.

5.2.2 Photon statistics

We now investigate the statistics of light at the output of the science cavity. Since the transmission rate saturates at half an excitation, the atomic ensemble seems to behave as an effective two-level superatom which should enable us to observe non-classical effects on the statistics of the output photons [57].

First, we present a model to describe the second order autocorrelation assuming a perfect blockade. Then, we describe the technical details for this kind of measurements in the continuous regime. After this introduction, we discuss the results obtained with our platform, from the strong antibunching at the Rydberg polariton resonance to the observation of bunching out of this resonance.

Model

In chapter 4, we introduced the second-order autocorrelation function and motivated its use for characterizing a light stream. Here, we focus on the autocorrelation for a continuous driving of the system such that we can assume time invariance in the response of the atom-cavity system. A rather different regime will be investigated in the next chapter, for which we will measure the autocorrelation function when the system is probed with short pulses, in which case the time invariance assumption is, of course, no longer valid.

An accurate description of the atom-cavity system at a finite blockade volume is a considerable challenge because of the shape of van der Waals interactions and the size of the Hilbert space. Several approaches and approximations exist for a free space atomic ensemble [111–113] but also in a cavity [167]. Even if we assume an infinite blockade volume, the system remains strongly correlated and analytical developments are not straightforward. One option, proposed by Grankin *et al.* [114, 115], is to make a perturbative approximation of the optical Bloch equations in order to compute the second-order autocorrelation function at the lowest, non-trivial, order in the input rate. In their approach, Grankin *et al.* demonstrated that the autocorrelation function $g^{(2)}$ can be computed from the correlator $\hat{a}(t + \tau)\hat{a}(t)$ as:

$$g^{(2)}(\tau) = \frac{|\langle \hat{a}(t + \tau)\hat{a}(t) \rangle|^2}{\langle \hat{a}^\dagger \hat{a} \rangle^2} \quad (5.18)$$

This approximation involves second order corrections with respect to the input photon flux and requires to solve the set of equations between all the two-operator correlators between \hat{a} , \hat{P} and \hat{S} . This model is, as expected, greatly simplified when one assumes that the atomic ensemble behaves as a single Rydberg superatom shielded by an infinite blockade volume, meaning $\langle \hat{S}\hat{S} \rangle = 0$. The full set of equations for this numerical calculation is presented in appendix 7.2.3. The general idea is to first obtain the zero-delay expression from the steady-state solutions of optical Bloch equations and then to compute the evolution for a non-zero delay.

With the measurement of the saturation rate for the 100S Rydberg state, we showed that our atom-cavity platform can be seen as a two-level system when driven on the Rydberg

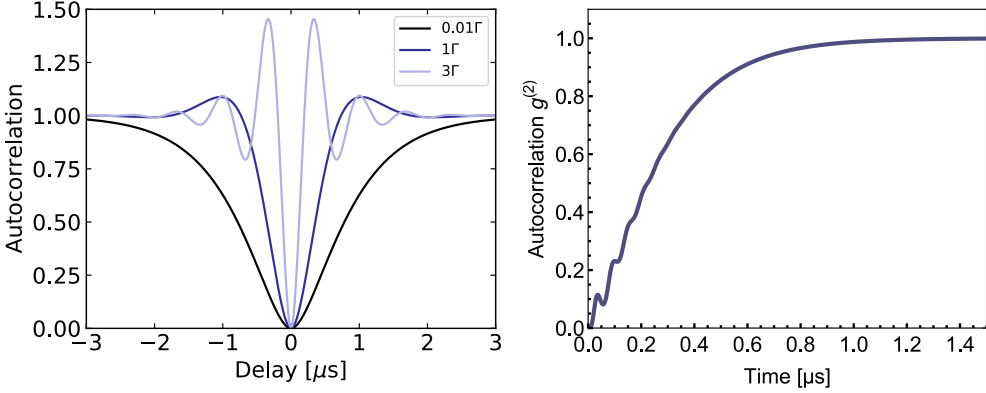


Figure 5.7: Model for the two-level antibunching. Left-Autocorrelation as a function of the delay for a two-level system with a damping rate Γ , driven at $\Omega = 0.01, 1, 3 \times \Gamma$. When $\Omega > \Gamma/4$, the autocorrelation features oscillations due to the coherent driving of the system. Right- Numerical calculation with $g = 2\pi \times 14$ MHz, $\Omega = 2\pi \times 18$ MHz and $\gamma_r = 2\pi \times 80$ kHz for a weak driving $\Omega \ll \Gamma$.

polariton resonance. This is interesting because the second-order autocorrelation function of a two-level system has a rather simple expression for a resonant driving [168]. In our case, the lower state is given by the ground state of the atomic ensemble and the empty cavity $|0, G\rangle$, while the excited state is the Rydberg polariton $|\psi_d\rangle$. In particular, this approximation requires to neglect the contributions from the two bright polaritons at $\pm\sqrt{g^2 + \Omega^2/4}$ and to have a large Rydberg population, i.e. $\Omega/g \ll 1$. It is therefore important to operate in the collective strong coupling regime for this approximation to be valid and to drive the system accordingly. In this case, the autocorrelation function is simply:

$$g^{(2)}(\tau) = 1 - e^{-3\gamma_{\text{EIT}}|\tau|/2} \left[\cosh(\beta|\tau|) + \frac{3\gamma_{\text{EIT}}}{2\beta} \sinh(\beta|\tau|) \right] \quad (5.19)$$

where $\beta = \sqrt{(\gamma_{\text{EIT}}/2)^2 - \Omega_p^2}$.

From this simple model, we expect to observe oscillations as a function of the delay on the second-order autocorrelation function when the driving frequency Ω_p exceeds the damping rate γ_{EIT} , valid as long as $\Omega_p, \gamma_{\text{EIT}} \ll \sqrt{g^2 + \Omega^2/4}$. We give an illustration of these oscillations in figure 5.7. When the point $\Omega_p = \gamma_{\text{EIT}}/2$ is crossed, the autocorrelation features both bunching and antibunching at non-zero delays due to a coherent driving of the two-level system. The first method is also depicted in figure 5.7, right panel. We recover the result from equation 5.19 for a low driving with additional oscillations due to the coupling to bright polaritons modes, but we will discuss this further during the presentation of our measurements.

Experimental implementation

In this section, we concretely implement the measurement of the autocorrelation function by counting coincidences between two detectors. The acquisition for this kind of measurements consists in the recording of timestamps from the two SPCMs, with a temporal resolution $t_d = 10$ ns, and in comparing the arrival times between the two detectors. The probability to have a coincidence during a time bin t_d for a delay τ between the two detectors is: $P_c(\tau) = N_c(\tau)t_d/t_a$ where $N_c(\tau)$ is the number of coincidences recorded during an acquisition duration t_a . Moreover, the probability to have a click on one of the two SPCM is given by $P_{1,2} = N_{1,2}t_d/t_a$, where $N_{1,2}$ is the number of clicks on the detector 1, 2 accumulated during t_a . Notice that the probabilities $P_{1,2}$ do not depend on the delay τ because we assume time

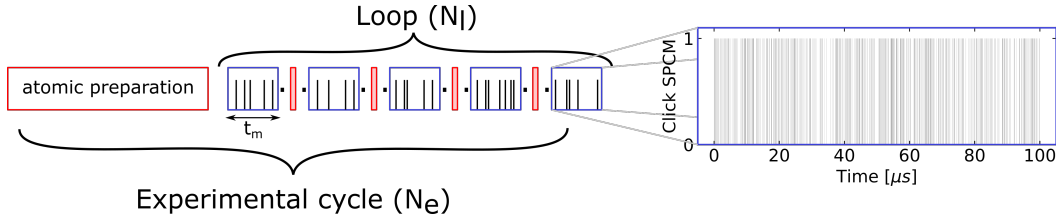


Figure 5.8: Experimental sequence for coincidence measurements. Schematic for a standard acquisition of the autocorrelation. An experimental cycle starts by the preparation of the atomic ensemble inside the resonator. A measurement is then performed during a time t_m (blue boxes) followed by a small repumping step to stabilize the atom number. This step is repeated (loop) N_l times before restarting an experimental cycle. Right- Illustration of the acquisition from one of our SPCMs with $t_m = 100 \mu\text{s}$.

invariance. In the limit where the delay τ is large compared to the polariton lifetime τ_d , the correlations are lost and the probability to measure a coincidence is just the product of the probability to have a click on one detector and a click on the second one: $P_c(|\tau| \gg \tau_d) = P_1 P_2$. As a consequence, the second-order autocorrelation function reads:

$$g^{(2)}(\tau) = \frac{P_c(\tau)}{P_1 P_2} = \frac{N_c(\tau)}{N_1 N_2} \frac{t_a}{\tau_d} \quad (5.20)$$

In our experiments the number of photons accumulated by one detector is $N_i = N_l \times N_e \times N_{m,i}$ where $N_{m,i} = t_m \phi_i$ is the number of counts on one SPCM, for a single-shot measurement that lasts a period of time t_m for a photon rate ϕ_i . Finally, N_l is the number of loops and N_e the number of experimental cycles. Therefore, the total acquisition duration is given by $t_a = N_l \times N_e \times t_m$. The experimental sequence for this acquisition is sketched in figure 5.8, and the typical duration for a single measurement is $t_m = 100 \mu\text{s}$, the right panel is a single-shot measurement from one SPCM.

On top of that, our SPCMs have a darkcount rate of $\phi_D = 300 \text{ Hz}$ that can be corrected by subtracting their contributions to the number of clicks per detector ($N_{1,2}$) but also on the number of coincidences N_c :

$$\begin{aligned} N_{m,i}^{(c)} &= N_{m,i} - \phi_D t_m \\ N_c^{(c)} &= N_c - \phi_D^2 t_a t_d - \phi_D t_d (N_1 + N_2) \end{aligned} \quad (5.21)$$

In the first case, we simply remove the number of clicks induced by darkcounts for each detector during a single measurement. For the coincidences, errors originate either from the two darkcount rates (ϕ_D^2) or from a darkcount of one detector with a real photon on the second detector. In what follows, we will not correct our data and only plot raw measurements because the contribution from these errors remains very small. For instance, the dominant error for the autocorrelation at zero delay is $2\phi_D/\phi$. As an upper bound for the number of false coincidences, we can assume that our SPCM detects at least a $\phi = 100 \text{ kHz}$ rate from the cavity that results in a minimal value of the autocorrelation of 0.6%.

Antibunching

We present now the measurement of the second-order autocorrelation for the 100S Rydberg state. As a first step, we probe the system on the Rydberg polariton resonance with a low output rate, for $\Omega_p \simeq 2\pi \times 0.2 \text{ MHz}$. The result is shown in figure 5.9, where we observe a drop of the second-order autocorrelation function with a value of 5% at zero delay, left plot. These measurements confirm that we have strong interactions between optical photons,

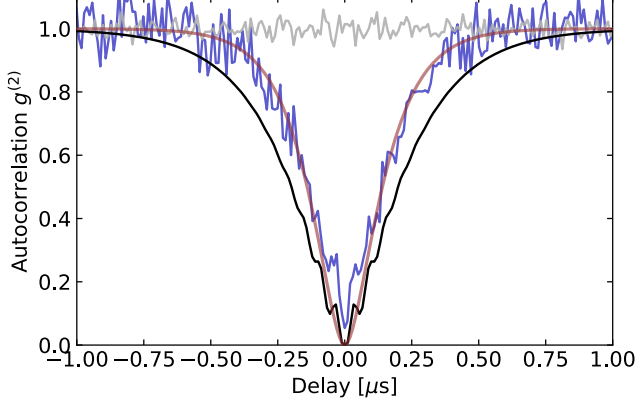


Figure 5.9: Photon antibunching. Second-order autocorrelation as a function of the delay τ between the two detectors with Rydberg polaritons (blue) and for the empty cavity (grey). The atom-cavity coupling is $g = 2\pi \times 14.5 \text{ MHz}$ while the control beam, $\Omega = 2\pi \times 18 \text{ MHz}$, drives the 100S Rydberg state, resulting in a 87% transparency in the linear regime. Data are fitted by the model from equation 5.19 (red line) assuming a driving close to zero and the perturbative calculation is also plotted as a comparison (solid black line).

and this with a high transparency ($\mathcal{T}_0 = 87\%$). For these measurements, the polaritons are characterized by a 72% Rydberg component. From a fit of the model (equation 5.19), with only the damping rate as a free parameter, we infer a polariton lifetime of $(57 \pm 2) \text{ ns}$ that does not exactly match the lifetime estimated from the EIT linewidth with a value of $(93 \pm 4) \text{ ns}$. We also used the perturbative model proposed by Grankin *et al.* [114] to compute the second-order correlation function with the same parameters and assuming a perfect blockade. The numerical calculation of the autocorrelation unsurprisingly predicts a polariton damping rate consistent with the measured EIT linewidth (solid black line). In this respect, our model with infinite interactions does not exactly fit the measurements, but we still observe similar behavior. Beside this, we observe fast oscillations on the measured autocorrelation at a frequency matching the bright polaritons detuning $\delta = \pm 2\pi \times 17 \text{ MHz}$, that are also present on the numerical calculation, and in other photon blockade experiments with a single atom strongly coupled to a cavity [163].

An easy way to increase the blockade strength is to use a smaller control Rabi frequency. We have therefore reduced this frequency by a factor 2, which has several consequences on the Rydberg polaritons, all other parameters being equal. In this configuration, the polariton is essentially a Rydberg excitation with 91% of its population in the Rydberg state. Of course the transparency drops, to $\mathcal{T}_0 = 60 \pm 7\%$, but the polariton lifetime is magnified by a factor ~ 2 since $\gamma_{\text{EIT}} = 2\pi \times 0.34 \text{ MHz}$. On top of that, the effective interaction between polaritons is increased by ~ 1.6 through the growth of the Rydberg population. All in all, the ratio blockade energy over the polariton damping rate is ~ 5 times bigger than the first measurement presented in figure 5.9. Data are shown in figure 5.10, and the fit (equation 5.19) yields a $(230 \pm 4) \text{ ns}$ lifetime consistent with the value estimated from the EIT linewidth at a value of $(230 \pm 30) \text{ ns}$ for a weak probe driving $\Omega_p = 2\pi \times 0.18 \text{ MHz}$ and a scaling factor of 1.05. It seems that in this regime, intra-cavity interactions between Rydberg polaritons are significantly suppressed. Beside this, the zero-delay autocorrelation is still very low $\simeq 4\%$.

In this configuration, it is easier to observe oscillations on the autocorrelation since the polariton has a longer lifetime. For this, we need to reach $\gamma_{\text{EIT}}/2 < \Omega_p$ but also to avoid the driving of the bright polaritons $\Omega_p \ll g_{\text{eff}}$. This is confirmed by the second plot on the figure 5.10, where we increased the input intensity to reach an output rate of 24 MHz for the empty cavity, resulting in a driving Rabi frequency of $\Omega_p \simeq 2\pi \times 1.45 \text{ MHz}$. The theoretical curve at this driving and for the previously estimated damping rate (equation 5.19) fits well

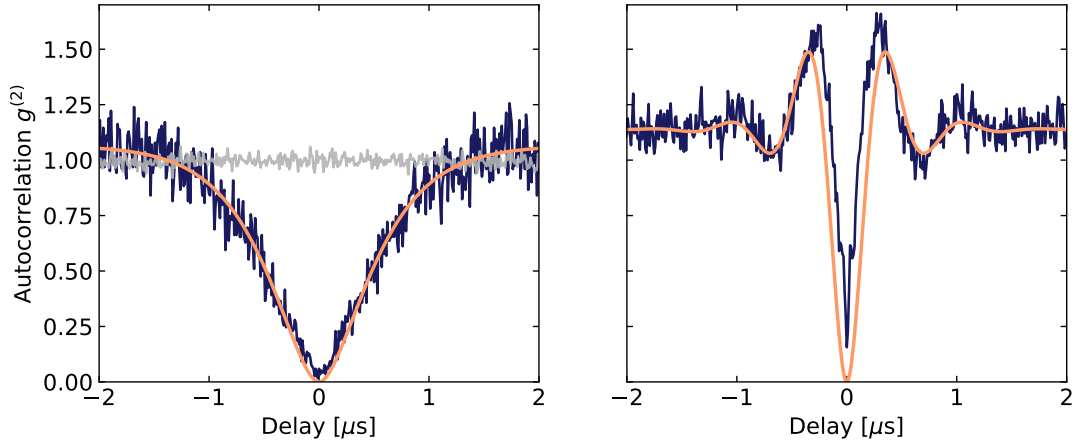


Figure 5.10: Oscillations on the autocorrelation. Second-order autocorrelation as a function of the delay τ for Rydberg polaritons (blue) and for the empty cavity (grey). These measurements are performed with $g = 2\pi \times 14.5$ MHz and $\Omega = 2\pi \times 9$ MHz in the linear regime (left plot) and for a higher input rate (right) at a frequency of $\Omega_p = 2\pi \times 1.45$ MHz. We observe oscillations for the latter case that originate from the coherent driving. The simple model for the autocorrelation (equation 5.19, orange) fits well the measurements. In the first case, we set the driving to zero and a scaling factor at a value of $g^{(2)}(|\tau| \gg \tau_c) = 1.05$ such that the only free parameter is the damping rate. On the right panel, the driving is set at its measured value with the previously estimated damping rate and a scaling factor $g^{(2)}(|\tau| \gg \tau_c) = 1.15$.

the measured autocorrelation⁽⁷⁾, even if the zero-delay level is slightly higher than expected, with a value of $\sim 10\%$. These oscillations on the autocorrelation originate from the coherent Rabi driving of the effective two-level system inside the resonator that periodically emits a photon out of the cavity. Consequently, we observe a significant photon bunching at non-zero delay on the coincidence measurements, which are damped by the finite lifetime of our polaritons.

These measurements confirm that our platform can effectively be considered as a single two-level system. For this, several criteria must be met: the atomic ensemble has to be strongly coupled to the resonator, the blockade radius associated to the targeted Rydberg state must exceed the size of our atomic cloud and of course, the system needs to be probed on the Rydberg polariton resonance. On top of this, the last observation demonstrates that we have a partially coherent evolution in the platform and that the observed antibunching is not dominated by the dephasing between polaritons inside the resonator but rather from a blockade of the transmission by one polariton.

Bunching of photons

The observation of photon antibunching with Rydberg polaritons in cavity was first obtained by the team of Jonathan Simon in 2018 [57]. In this experiment, their measurements were centered on the transmission on the Rydberg polariton resonance to hallmark interactions at the single-photon level. They also briefly mentioned the bunching of photons with one observation out of resonance. The origin of this bunching was attributed to the coupling to a Rydberg pair state shifted by the interaction energy.

There are at least three sources of bunching to be considered in our platform. The first one comes from the anharmonicity of the atomic spectrum due to Van der Waals interactions between Rydberg excitations and corresponds to the addressing of multiply-excited Rydberg

⁽⁷⁾Here, we also use a scale factor to take into account the fact that $g^{(2)}(|\tau| \gg \tau_c) = 1.15$ in this measurement.

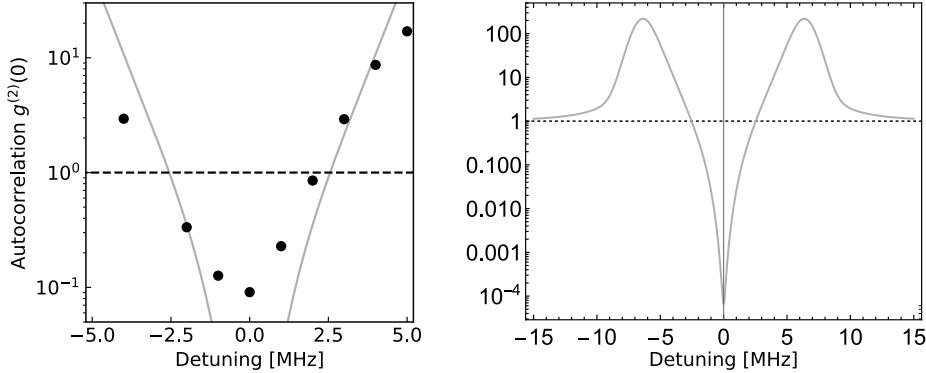


Figure 5.11: Zero-delay autocorrelation vs detuning. Left- Measurement of the zero-delay autocorrelation (dots) as a function of the probe detuning for the 100S Rydberg state, $g = 2\pi \times 16$ MHz and $\Omega = 2\pi \times 13$ MHz. We also show the numerical calculation (grey line) for the same set of parameters as a comparison. Right- Full spectrum from the numerical calculation. In both cases we observe a transition from strong antibunching at zero detuning to bunching out of resonance.

states [169]. The bunching can also result from the strong coupling between the superatom and the cavity, described by the model presented earlier. Finally, it can be observed when the size of the atomic ensemble exceeds the blockade radius, caused by a nonlinear variation of the group index [45].

We go one step further by characterizing the autocorrelation with respect to the probe detuning. Grankin *et al.* [114] predicted a strong bunching of photons out of the resonance but for an atomic ensemble hosting several blockade volumes. As introduced at the beginning of this section, we use their perturbative approach to compute the second-order autocorrelation out of resonance but assuming here that the atomic ensemble is perfectly blockaded by one Rydberg excitation.

The measurement of the zero-delay autocorrelation as a function of the probe detuning is shown in figure 5.11. These data were taken with a polariton predominantly in the 100S Rydberg state, with a 85% population, resulting in a narrow EIT linewidth $\gamma_{\text{EIT}} = 2\pi \times 0.5$ MHz, close to the last configuration where the polaritons were not affected by polariton-polariton dephasing. The left panel clearly establishes the transition from antibunching at zero detuning to a strong photon bunching out of resonance, on both sides of the Rydberg polariton resonance (zero detuning). The van der Waals interactions between the two Rydberg states are repulsive such that a bunching of photons caused by multiply-excited Rydberg states should only be observed for a positive detuning. Indeed, it seems that the bunching is more important on this side because of the Rydberg interactions while the bunching for negative detunings is very likely to be a consequence of the strong coupling between the cavity and the superatom.

The perturbative calculation for the same parameters are shown in grey and in the right plot. In this case, the bunching is of course symmetric with respect to the zero detuning because we assume infinite interactions. From this model, we expect a resonance of bunching at a detuning of $\simeq \pm 6.4$ MHz. It would be interesting to go beyond the few megahertz detuning investigated here, for instance to measure the position of this maximum. Unfortunately, the transmission drops rapidly and therefore it would require much more integration time. The strongest bunching we observed in this configuration reaches 20 at zero delay, for a probe at a detuning of +5 MHz.

The autocorrelation as a function of delay is shown in figure 5.12, for our atom-cavity system (left) and the numerical calculation (right). The perturbative calculations predict “slow”

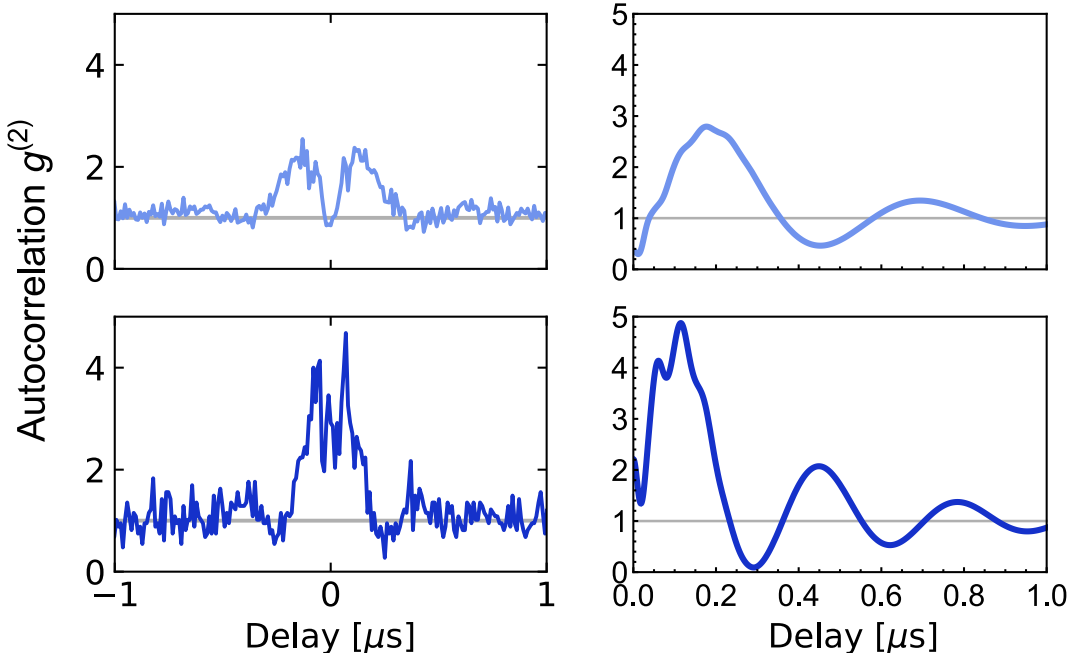


Figure 5.12: Bunching of photons. Left- Measured autocorrelation as a function of the delay at a detuning of $+2\text{ MHz}$ (top) and $+3\text{ MHz}$ (bottom). Observed with the $100S$ Rydberg state, $g = 2\pi \times 16\text{ MHz}$ and $\Omega = 2\pi \times 13\text{ MHz}$. Right- Numerical calculations for the same set of parameters. We observe a similar level of bunching and consistent oscillations that are however damped more rapidly on our data.

oscillations on the signal, that could be understood as an increase of the driving frequency for the Rydberg polariton at a frequency $\Omega_{\text{eff}} = \sqrt{\Omega_p^2 + \delta^2}$, where δ is the probe detuning. This means that for a detuning larger than $\gamma_{EIT}/2$, the autocorrelation features oscillations for all input rates. We also observe this phenomenon on the measured autocorrelations, except that the oscillations are more attenuated.

Notice that this bunching does not seem to be a two-photon blockade as it was observed for instance by Hamsen *et al.* [163] since we did not observe a drop of the third-order autocorrelation at zero delay, which would indicate that the photons are more likely to be transmitted as pairs. By lack of time, these measurements were only done with a positive detuning and could be quite different on the other side of the resonance.

These observations support that the bunching obtained for a negative detuning originates from the strong coupling between the superatom and the cavity rather than the driving of Rydberg pairs. However, the atomic density is quite high ($0.2\text{ }\mu\text{m}^{-3}$) while the Leroy radius is $3.1\text{ }\mu\text{m}$ for the $100S$ Rydberg state, meaning that on average each atom has ~ 13 atoms within this Leroy volume for which the van der Waals approximation is no longer valid. Consequently, we cannot exclude the presence of some resonances for negative detuning. In order to conclude on this, it would be interesting to measure the autocorrelation function with other principal quantum numbers but also with a lower atomic density.

5.3 Conclusion

The first section was devoted to the characterization of the linear Rydberg EIT and especially the effective linewidth of the Rydberg state. The current broadening of this parameter is dominated by the Doppler shift and the lightshift of the dipole trap resulting in a $\gamma_r = 2\pi \times 80$ kHz damping rate. It should be possible, if necessary, to decrease the temperature by a factor $\simeq 3$ and to work with the dipole trap off to further reduce the inhomogeneous broadening of this linewidth. Nevertheless, the current value of this parameter is already satisfying and close to what we wanted to obtain. In addition, we can reach a control Rabi frequency up to $2\pi \times 18$ MHz for the 100S Rydberg state. This is quite comfortable as we can vary the Rydberg population for our Rydberg polariton from 100% to almost 50% for a collective coupling strength of $2\pi \times 10$ MHz, where the atom-cavity system stands in the collective strong coupling regime. This offers a large range to explore the physics of Rydberg polaritons in cavity or to study a single superatom strongly coupled to a resonator.

Along the second part of this chapter, we observed the strongly interacting regime for optical photons. To this end, we first measured the transmission rate of the atom-cavity platform and showed a saturation at half an excitation per polariton lifetime. We then turned our attention to the statistics of light at the output of the optical resonator and demonstrated that only single photons are transmitted at the Rydberg polariton resonance. We also observed some remarkable features: the coherent oscillations on the second-order autocorrelation for strong input rates and a high photon bunching out of resonance consistent with a numerical calculation assuming a perfectly blockaded ensemble.

The achievement of these strong interactions opens plenty of interesting perspectives for this platform [38, 58, 170]. Two of them are covered in this thesis:

- The average population of the Rydberg polariton is limited to one half for a continuous driving. In the next chapter, we will show that this fifty percent threshold can be exceeded by probing and controlling the system with short pulses. For instance, it is possible to transiently convert an input photon into a Rydberg state by making a rotation of the polariton through a fast change of the control beam intensity [171, 172]. This phenomenon can be seen as a nonlinear quantum memory: only one polariton can propagate through the resonator and therefore the storage is limited to one photon. The read out of the excitation is then obtained by rapidly turning the control beam back on while the coupling of the atomic ensemble with the cavity allows for an efficient collection of the stored photon. We will show that this process constitutes an efficient and on-demand single-photon source [173]. Finally, this photon storage in an atomic ensemble preserves the phase of the input pulse. This allows us to perform a truncation of an input coherent state at one photon.
- We have just demonstrated that our atomic ensemble can be seen as a single Rydberg superatom. Another exciting possibility for this platform is to use this superatom in cavity as a mediator of interactions between optical photons through entanglement [38, 170]. For this purpose, we will present the implementation of a coherent driving of the superatom [106] and demonstrate an efficient method for the single-shot detection of its state via the blockade of the transmission. One of the important achievements in this chapter is the observation of a state-dependent optical π phase shift. All of these results constitute a toolbox for quantum engineering of light and should allow the concrete implementation of several protocols [119, 174] in the near future.

Chapter 6

Deterministic generation of nonclassical light

Contents

6.1	Nonlinear quantum memory	117
6.1.1	Presentation	117
	Nonlinear writing	118
	Storage and readout	118
6.1.2	Model for the pulsed regime	119
	Fictitious cavities	119
	Cascaded-system	120
	Optimization and choice of the output mode	120
	Simulation	121
6.2	Efficient single-photon source	123
6.2.1	Experimental setup	123
	Pulse generation	124
	Experimental sequence	125
6.2.2	Characterization	125
	Optimization of the output photon number	126
	Storage efficiency	127
	Photon unicity	128
	Overview and outlook	129
6.3	Study of the continuous variables of the field	131
6.3.1	Theoretical considerations and simulation	131
	Ideal one-photon truncated state	132
	Simulation	133
6.3.2	Output mode and homodyne signal	134
	Mode selection	134
	Phase of the output state	136
6.3.3	Experimental results	136
	Mean value and variance	136
	Tomography of the state	138
	Outlook	139

Introduction

In the previous chapter, we demonstrated that our platform can provide strong interactions between optical photons via Rydberg polaritons in the resonator. For this purpose, we investigated the response of the atom-cavity system in the continuous regime, observed the saturation of the transmission and a strong photon antibunching at the cavity exit. Unfortunately, the population of the Rydberg polariton is inevitably limited to one half with this approach: even though the system emits photons one by one, their emission times are uncontrolled.

We present a different excitation scheme in this chapter, with the idea of efficiently populating a Rydberg polariton to then generate a photon. The first step consists in rapidly driving the atom-cavity system on the Rydberg polariton resonance with a pulsed probe beam while the control field is ramped down. The probe pulse leads to a large population in the Rydberg polariton while the change of the control intensity induces a rotation of this polariton towards a Rydberg state. This constitutes the writing step of this nonlinear quantum memory. Once the control field is off, the excitation is stored in the atomic ensemble as a Rydberg spin wave. This approach again requires strong interactions between Rydberg atoms in order to suppress, or at least to significantly reduce multiple excitations in the cavity. After this storage step, it is possible to convert the excitation into a photon by turning the control beam back on, through another rotation of the Rydberg polariton. In this context, the strong coupling between the atomic ensemble and the cavity allows to efficiently collect the single excitation at the output of the resonator. We will see that this protocol provides a rather efficient and on-demand single-photon source, with up to 0.53 photon at the exit and a very low probability of having two photons in the output pulse ($< 10^{-3}$), exceeding recent observations with a similar protocol in free space [173].

When the input pulse is a coherent state hosting a few photons on average, this nonlinear process stores only one photon but preserves the phase of the input pulse. Consequently, this method can be seen as the truncation of the input coherent state at one photon [175]. This non-classical state of light is thus a superposition between a one-photon Fock state and vacuum, which features quadrature squeezing in a certain parameter range, but also a non-Gaussian Wigner function. Even more noteworthy, the reconstructed Wigner function at the output of the cavity even exhibits negativity, a hallmark of nonclassicality.

In the first section of this sixth chapter, we discuss in detail the protocol for this experiment together with a simulation inspired by the work of Kilerich *et al.* [176], based on realistic parameters that we can currently achieve with the platform. Thereafter, we present the practical implementation of this excitation scheme with our experimental system. In particular, we discuss the optimization of the storage efficiency together with the maximization of the output photon number. We then focus on the storage and readout steps, first by measuring the lifetime of the atomic excitation but also by demonstrating a strong anti-bunching for the escaping pulse. In the last part of this chapter, we focus on the quadratures of the electromagnetic field and show that the output pulse is indeed a truncated state by observing the conservation of the phase with the homodyne setup. We then compare the measurements from our platform to the ideal one-photon truncated state and the simulation. Among other things, we will show the progressive loss of the phase as the output state grows (in term of mean photon number). We conclude this section by the reconstruction of the Wigner function for several output photon numbers to emphasize the evolution from the vacuum state to an almost one-photon Fock state. Thanks to these measurements, we establish the non-Gaussian character of the output state and more importantly we observe a small negativity of the Wigner function. This protocol can therefore be seen as a method to generate nonclassical state of light in a deterministic way.

6.1 Nonlinear quantum memory

This section describes the protocol for the writing, storage and readout of a photon with our platform. Contrary to the standard DLCZ quantum memory protocol [177] for a non-interacting atomic ensemble, which relies fundamentally on the measurement of a “write” and “read” photon, the approach with Rydberg interactions allows the storage and readout of a single photon without the use of postselection. Our approach is therefore closer to the experiments performed with a single atom in cavity (QED), where the system is driven in a lambda excitation scheme to perform an adiabatic transfer of the excitation [178, 179]. It should be noted that hybrid approaches have also been carried out, for example through the use of the DLCZ protocol in a cavity, in which case the reading step is probabilistic while the emission in the cavity mode is deterministic [180].

The experiment presented here is inspired by several studies using Rydberg EIT in free space as a nonlinear quantum memory. Among the most notable results, we can mention: the control of stored Rydberg polaritons with microwaves [171] demonstrating the conservation of the coherence, the fast generation of a single excitation together with a 70 μs -long storage [181] or more recently the efficient and on-demand generation of single photons [173]. Nevertheless, the study of the output photons has so far only focused on discrete variables through the autocorrelation (Hanbury-Brown and Twiss) or indistinguishability (Hong-Ou-Mandel).

With our platform, we want to go one step further by highlighting complementary properties with the measurement of continuous variables: the quadratures of the field. Some theoretical proposals exist on this topic but the mechanism at stake involves dephasing between Rydberg excitations [182, 183] rather than our cavity blockade induced by one Rydberg polariton. This kind of measurement gives access to the phase of the output pulse, hence allows us to demonstrate the coherence of the output pulse and to study the truncation effect in detail. In this first section we start by a heuristic presentation of the protocol and describe the three important steps: writing, storage and readout. Then, we discuss a general method to simulate our atom-cavity system in the pulsed regime and present results of the simulation based on realistic parameters.

All along this chapter, we assume that the atomic ensemble is strongly coupled to the resonator, that the atomic cloud is also coupled to a highly excited Rydberg state to ensure Rydberg blockade at the single-excitation level and finally that the probe is resonant with the dark Rydberg polariton mode.

6.1.1 Presentation

In the fifth chapter, we discussed and observed the saturation of the transmission rate of the atom-cavity system on the Rydberg polariton resonance. In this context, the interactions between Rydberg atoms do not allow to excite more than one Rydberg excitation at a time and the state of the one-excitation Rydberg polariton is:

$$|\psi_d\rangle = \cos \theta |1, G\rangle + \sin \theta |0, R\rangle \quad (6.1)$$

where $\tan \theta = -2g/\Omega$, g is the collective coupling strength, Ω is the control Rabi frequency, $|1, G\rangle$ is the state with one photon in the cavity and all atoms in the ground state while $|0, R\rangle$ corresponds to zero cavity photon and one delocalized Rydberg excitation.

Here, we aim to efficiently prepare an excitation in the system and thus exceed the 50% threshold of the continuous regime. Let us discuss the response of our system in the pulsed regime.

Nonlinear writing

Along the last chapter, we also argued that the driving of our system can be simplified as (equation 5.14):

$$\hat{F} = i\hbar\sqrt{2\kappa_0}\cos(\theta(t))\alpha(t)(|\psi_d\rangle\langle 0, G| - |0, G\rangle\langle\psi_d|) \quad (6.2)$$

where this time we consider the feeding from the input/output mirror so we replace κ_{HR} by κ_0 , this expression is of course only valid in the Rydberg-dominated regime for our polaritons, meaning that the Rydberg population in the polariton is close to one ($|\tan\theta| \gg 1$) and for a strongly coupled system $g \gg \kappa, \gamma$. One last difference: here the input coherent state and the phase θ depend both on time because we want to drive our system with pulses. In the limit considered here one can make the approximation $\cos(\theta(t)) \simeq \Omega(t)/(2g)$.

Note that the variation of Ω rotates also the dark-polariton. In order to stay in the dark state along this step, the evolution has to be adiabatic: $\dot{\Omega}/\Omega, \dot{\alpha}/\alpha \ll g$.

In this excitation scheme, the control beam is initially on and the system starts in the state $|0, G\rangle$. The control beam is then decreased to zero at the arrival of the input coherent pulse. After this process, the system is rotated by an angle:

$$\beta = \int_0^{+\infty} \sqrt{2\kappa_0} \frac{\alpha(t)\Omega(t)}{g} dt \quad (6.3)$$

while the dark state ends up in the atomic excitation:

$$|\psi_d\rangle = |0, R\rangle \quad (6.4)$$

and finally the excitation stored in the ensemble is simply:

$$|A\rangle = \cos(\beta/2)|0, G\rangle + \sin(\beta/2)|0, R\rangle \quad (6.5)$$

One can then adjust the timing between the pulses and the input intensity to obtain $\beta = \pi$ in order to prepare the atomic ensemble in the Rydberg state $|R\rangle$. This mechanism consists of a nonlinear storage of one excitation from a coherent input state. Of course, this description completely omits the role of the damping terms but it would drastically complicate the discussion presented here. We will implement a simulation of our system in the next part to take into account these effects.

Storage and readout

After this nonlinear writing step, the excitation is kept in the atomic ensemble during a certain amount of time, resulting in losses. The efficiency of this storage step is taken into account with a factor η_s . Finally, the control beam is switched on in order to make a second rotation of the Rydberg polariton, the coherent part of this excitation is then:

$$|\psi\rangle = \cos(\beta/2)|0, G\rangle + \sin(\beta/2)|\psi_d\rangle \quad (6.6)$$

This polariton is eventually emitted out of the cavity and a photon is then retrieved, corresponding to the readout step. The population collected at the output of the resonator depends on two kinds of losses. The first one originates from the mirrors losses and results in a collection efficiency of $\eta_{cav} = \kappa_0/\kappa = T/L = 90\%$ for an empty cavity. The second term is due to the mixing between a photon and a Rydberg excitation, the losses in this case are given by the ratio between the photonic part of the polariton damping rate $\kappa \cos^2 \theta$ over the full damping rate γ_{EIT} , which is just the square root of the EIT transmission on resonance:

$\eta_{EIT} = \sqrt{\mathcal{T}_0}$. As a result, the collection efficiency for this readout step is given by:

$$\eta_r = \sqrt{\mathcal{T}_0} T / L \quad (6.7)$$

This is not surprising, we obtained these factors when we computed the saturation rate in chapter 5, equation 5.17. The total efficiency of the memory is finally $\eta = \eta_r \eta_s$.

6.1.2 Model for the pulsed regime

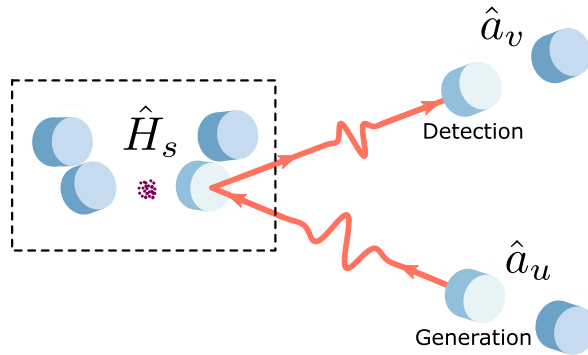


Figure 6.1: Input-output simulation with fictitious cavities. A first resonator, called “generation”, shapes the input pulse through a time-dependent coupling. The generated free space pulse impinges on the system to be described (dashed box) and an output pulse is produced by the platform. In the last step, a “detection” cavity captures a predefined mode via a change of its coupling. This approach allows to get rid of the free space modes, see text.

We present a general method for the simulation of the atom-cavity system in the pulsed regime that was proposed by Kiilerich *et al.* [176]. Leaving aside the challenges of modeling the interactions between Rydberg excitations, the main difficulty in the description of a cavity probed with short pulses comes from the infinite number of modes at the input and output of the resonator. Indeed, it seems at first sight hard to truncate the Hilbert space in order to perform a simulation for this kind of platform. For this purpose, Kiilerich *et al.* proposed to model free space input and output pulses by two fictitious resonators with time-dependent input/output couplings. One of the remarkable results is that it is possible to describe both the driving and the readout of the system with only the single optical mode of each fictitious cavity together with their couplings, thereby drastically reducing the size of the Hilbert space. This idea is depicted in figure 6.1, with our platform and the two fictitious cavities: a “generation” resonator and one for the “detection”. If defining the input pulse makes perfectly sense, since we know the shape of the incoming pulse that we want to implement on a given experiment, this is however more challenging for the output because, outside the weak-excitation regime where we can use linear response theory, we do not have a specific *a priori* form for the output pulse. One way to deal with this issue is to specify an arbitrary criterion to be maximized in order to define such a mode, this amounts to specify the detection that we want to carry out, hence the name “detection” for this cavity.

Fictitious cavities

As explained in the introduction, the general idea of this method is to consider that the quantum state of the optical pulse impinging on our system is initially contained in a single-ended cavity with a time-dependent input/output coupling that we can modulate to emit this state as a light pulse with a controlled shape. This fictitious cavity is characterized

by the driving feeding operator introduced in chapter 1 (equation 1.12), with the following expression:

$$\hat{F}_f = i \left(g^*(t) \hat{a} \hat{b}_{in}^\dagger - g(t) \hat{a}^\dagger \hat{b}_{in} \right) \quad (6.8)$$

where \hat{a} is the mode of the fictitious cavity and \hat{b}_{in} the input mode, in the vacuum state in practice. We recover the driving of our cavity (equation 1.12) if we use a constant coupling factor $g^*(t) = \sqrt{2\kappa_0}$ and drive the system with a coherent state $\hat{b}_{in} \rightarrow \alpha$.

From this time-dependent driving, we would like to generate an arbitrary mode at the output of this resonator:

$$\hat{b}_u^\dagger = \int dt u(t) \hat{b}^\dagger(t) \quad (6.9)$$

where $u(t)$ is the temporal envelop and \hat{b} the infinite basis for the free space pulses that we want to get rid of. Kiilerich *et al.* [176] showed that this mode is generated by the fictitious cavity for the following coupling factor:

$$g_u(t) = \frac{u^*(t)}{\sqrt{1 - \int_0^t dt' |u(t')|^2}} \quad (6.10)$$

This interpretation for the generation of an arbitrary mode is true the other way around because of time reversal symmetry. Assuming that the optical state emitted by our system has a temporal shape $v(t)$, one can show that in order to optimally absorb this pulse in a fictitious “detection” cavity the time-dependent input-output coupler of the latter should satisfy:

$$g_v(t) = \frac{v^*(t)}{\sqrt{\int_0^t dt' |v(t')|^2}} \quad (6.11)$$

As a consequence, one can shape and detect an arbitrary temporal mode by adjusting the coupling of a cavity.

Cascaded-system

In-between the input, or output, cavity and the system of interest, there is still an infinite Hilbert space needed for the description of the free space pulse via the operators $\hat{b}(t)$. The SLH framework [184] provides a general method for the elimination of this operator by directly describing the coupling between the input cavity mode and the atom-cavity system. The total Hamiltonian describing the driven system is then:

$$\hat{H}_{tot} = \hat{H}_s + \frac{i}{2} (\sqrt{2\kappa_0} g_u(t) \hat{a}_u^\dagger a + \sqrt{2\kappa_0} g_v^*(t) \hat{a}^\dagger \hat{a}_v + g_u(t) g_v^*(t) \hat{a}_u^\dagger \hat{a}_v - h.c.) \quad (6.12)$$

where \hat{H}_s is an arbitrary Hamiltonian describing our platform, \hat{a}_u the mode of the “generation” cavity, \hat{a}_v the “detection” cavity mode with their respective time-dependent coupling $g_u(t), g_v(t)$ and the science cavity mode \hat{a} with its coupling factor set by κ_0 . Finally, damping terms are taken into account with the following Lindblad operator:

$$\hat{L}(t) = \sqrt{2\kappa_0} \hat{a} + g_u^*(t) \hat{a}_u + g_v^*(t) \hat{a}_v \quad (6.13)$$

Optimization and choice of the output mode

In this experiment of nonlinear quantum memory, we want to retrieve as efficiently as possible the photon at the output of our resonator. The parameter to be maximized is then the photon

number in the cavity mode after release:

$$n = \int_{t_r}^{+\infty} \sqrt{2\kappa_0} \langle \hat{a}^\dagger(t) \hat{a}(t) \rangle dt \quad (6.14)$$

where t_r is the release time.

The last ingredient we need is the output mode of the photon, in other word the temporal envelope v to characterize the output photon through a fictitious cavity. The output mode is of course an arbitrary choice. Therefore, it really depends on the context of the experiment at stake. In the present case, the choice is somehow “natural” as we want to retrieve as efficiently as possible the single photon out of the resonator. This mode, $v(t)$ is given by the intensity envelop of the escaping light:

$$v(t) \propto \sqrt{\langle \hat{a}^\dagger(t) \hat{a}(t) \rangle} \quad (6.15)$$

Intuitively, the shape of this output mode is given by the rising edge of the control beam to convert the Rydberg excitation in the medium into a Rydberg polariton and then by the exponential damping of this polariton when the control Rabi frequency reaches its steady-state value.

Simulation

We present now the simulation for the specific protocol described in the introduction of this section. In this case, the driving pulse is a coherent state such that we can simply replace the operator $\hat{a}_u(t)$ by a coherent pulse $\alpha(t)$ and forget about the “generation” cavity.

We assume here infinite van der Waals interactions and consequently we model our system by the Hamiltonian from equation 5.9:

$$\hat{H}_s = \frac{\Omega}{2} (|R\rangle \langle G| \hat{P} + |G\rangle \langle R| \hat{P}^\dagger) + g(\hat{P}^\dagger \hat{a} + \hat{P} \hat{a}^\dagger) \quad (6.16)$$

where \hat{P} is the collective operator between the ground state and the intermediate state. In the same way, we use the Lindblad operators from equation 1.40 to take into account the decoherence.

We simulate the evolution with the python package QuTIP, first without selecting an output mode to reduce the computational time and look at the output photon number given by equation 6.14. The atom-cavity system is first probed with a short Gaussian pulse while the control beam is switched off, as illustrated in figure 6.2. In a second step, the readout is performed by turning the control field back on. The input pulse contains 10 photons on average and the maximal population in the Rydberg state is 83%, as shown in the middle plot. Notice that the population in the intermediate state is not zero during the rotation of the Rydberg polariton. This demonstrates that our initial model is not completely accurate in this regime because of the finite strength of the atom-cavity coupling $g = 2\pi \times 10$ MHz compared to the damping rate of both the cavity and the intermediate state $\gamma \simeq \kappa \simeq 2\pi \times 3$ MHz but also the adiabatic condition due to the use of very short pulses (44 ns for the intensity of the probe).

The Rydberg excitation is converted into a cavity photon (red curve) when the control beam is switched on (time > 0.5 μs). During the release of the excitation, almost all the Rydberg population is converted into a photon since $\kappa_0 \gg \gamma_r$ and after 400 ns of storage, about 0.5 photon is retrieved at the output of the resonator. The delay between the control and probe pulses is crucial to maximize the transfer of the excitation from the coherent

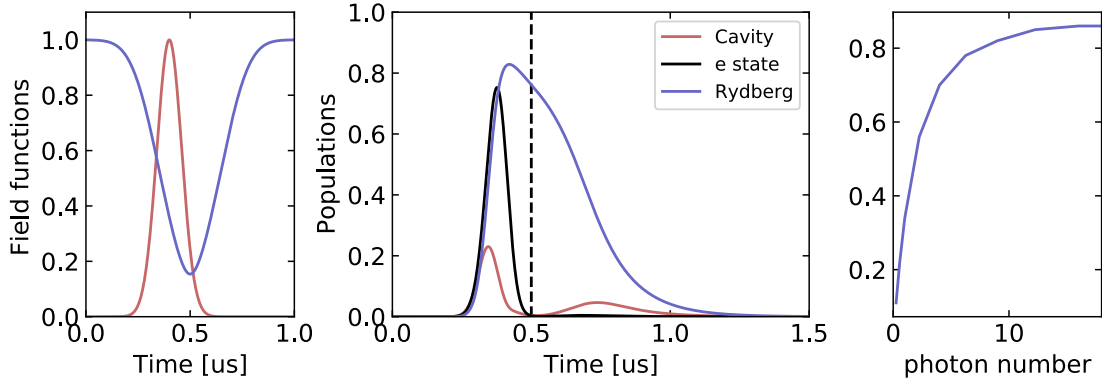


Figure 6.2: Simulation of the writing, storage and readout. Left- Pulses for the probe (red) and the control beam (blue). Middle- Population as a function of time for the Rydberg state (blue), the intermediate state (black) and the cavity mode (red). The vertical dashed line represents the minimum value of the control beam. Parameters for the simulation: $\gamma_r = 2\pi \times 80 \text{ kHz}$, $g = 2\pi \times 10 \text{ MHz}$ and $\Omega = 2\pi \times 10 \text{ MHz}$. The choice of the pulses for the control and the driving is discussed for the experimental implementation later on. Right- Maximum value of the Rydberg population, after optimization of the delay between control and probe pulses, as a function of the mean photon number in the input pulse.

pulse to the atomic ensemble and depends of course on the mean photon number of the latter. Finally, we plot the maximal Rydberg population as a function of the input mean photon number after optimization of this delay. We clearly see a saturation of the Rydberg population at high input, with value of $\simeq 86\%$.

6.2 Efficient single-photon source

Single photons have been used for only a few decades but have already allowed physicists to perform major experiments in quantum physics: the violation of the Bell inequalities [7, 8], through the measurement of correlations in polarization between entangled photons, the Hong-Ou-Mandel experiment [185] which emphasizes the bosonic nature of light, forcing the photons to exit from the same side of a beam splitter, but also the anticorrelation effect on a beam splitter for single photons, establishing the indivisible character of these particles [186].

The second experiment, for instance, was conducted with a nonlinear crystal producing pair of photons in a probabilistic way, in the sense that one does not know when the pair is emitted. This generation of photon pairs allowed the realization of numerous quantum optics experiments at the beginning of the century, to name a few: quantum teleportation [187], GHZ entanglement [188], generating optical Schrödinger kittens [189] or boson sampling [190]. This pair generation can also be turned into a single-photon source by “heralding” the presence of a photon via the measurement of its partner.

Another approach to obtain a single photon is to prepare a unique two-level system in its excited state and to use the spontaneous emission to get a photon. This kind of experiment was conducted, for instance, with single atoms [191], NV centers [192] or ions [193]. Unfortunately, the photon collection in free space is very low because of the isotropic nature of the emission. This is why many experiments couple the two-level system with a resonator in order to force the emission in the cavity mode to increase the collection efficiency. There are many investigations in this direction: it involves Josephson junctions [194], semiconductors [195], atoms [196], etc. Contrary to “heralded” sources, this approach has the benefit of controlling the timing of the emission and the current goal is to reach an efficiency of generation close to unity. Great advances have been made in recent years in the optical domain, with single atoms in a cavity [197] reaching efficiencies of about 50% but also with quantum dots, with an efficiency of up to 57% [30, 198]. However, achieving higher efficiencies with an atom relies on advanced engineering to reduce cavity losses while the fabrication process and the indistinguishability between the photons of two quantum dots remain open challenges.

We present a similar approach to these quantum dots experiments, where the emitter is replaced by our Rydberg superatom coupled to the science cavity. In our case, we of course benefit from the high indistinguishability of the photons emitted by atoms, at the cost of a heavier experimental platform. The nonlinear quantum memory that we introduced in the first part of this chapter allows us to realize the population inversion but also an efficient conversion of the atomic excitation into a cavity photon.

In this section, we discuss the concrete implementation of the storage and retrieval protocol that we introduced in the previous section. For this purpose, we address the specificities of the experimental sequence and especially the generation of pulses. We then cover the optimization of the storage step and characterize the quantum memory in term of efficiency and lifetime. In particular, we will focus on the output pulse to estimate the unicity of the single photons escaping from the atom-cavity system by means of autocorrelations measurements. The overall efficiency for the single-photon generation achieved with the platform is slightly above 50% and already exceeding the one obtained with a free space atomic ensemble [173]. We then conclude this section by suggesting realistic improvements to go further.

6.2.1 Experimental setup

We address here the technical part of this experiment, in particular the generation of pulses and the experimental sequence. For the whole chapter, the measurements were conducted

with a $5 \mu\text{m}$ -rms-radius atomic ensemble strongly coupled to the cavity, via a coupling strength $g = 2\pi \times 10 \text{ MHz}$ between the ground state $|g\rangle = |5S, F = 1, m_F = 1\rangle$ and the excited state $|e\rangle = |5P_{1/2}, F = 2, m_F = 2\rangle$. In this work, the atom-cavity system is only probed on the Rydberg polariton resonance with a D_1 beam injected through the input/output coupler in reflection. This allows us to maintain the phase between the input beam and the local oscillator for measurements with the homodyne detection. Regarding the control beam, its Rabi frequency (Ω) has a value of $2\pi \times 10 \text{ MHz}$ and couples the excited state $|e\rangle$ to the Rydberg state $|r\rangle = |109S, J = 1/2, m_J = 1/2, I = 3/2, m_I = 3/2\rangle$, motivated by the need to have large van der Waals interactions between Rydberg excitations. The transmission spectrum for this configuration is shown in figure 6.3, in the linear regime. This set of parameters allows us to reach a transparency $T_0 = 80\%$, which is an important figure to achieve an efficient readout of the stored excitation.

Pulse generation

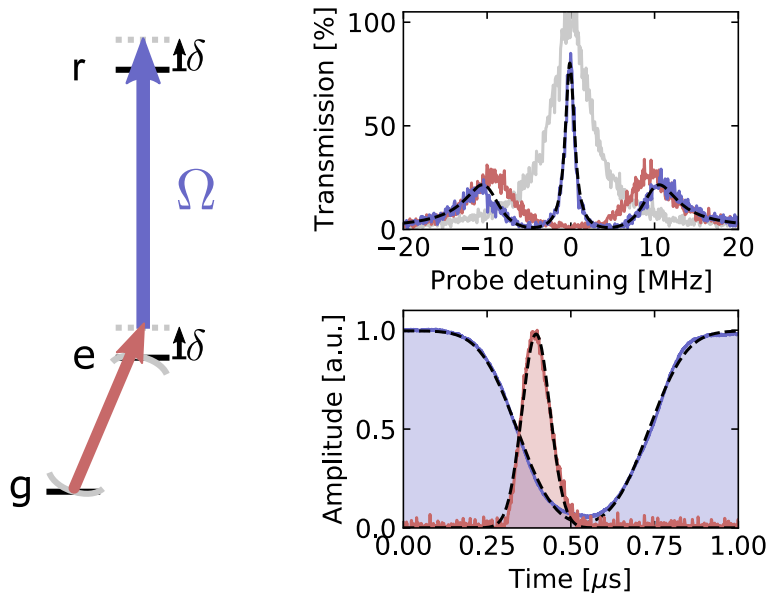


Figure 6.3: Excitation scheme and intensity envelop. Left- EIT driving scheme with the D_1 probe (in red) and the control field (in blue), see text. Top right- Transmission spectra for the empty cavity (grey), cavity + atoms (red) and cavity + atoms + control beam (blue). Bottom right- D_1 probe (red) and control intensity (blue) pulses for the storage of a single excitation and its readout.

A homemade arbitrary waveform generator⁽¹⁾ allows us to shape at will the pulses for the input coherent state. In practice, we work with a 42 ns-rms intensity Gaussian pulse but more sophisticated shapes can be implemented. This Gaussian waveform has the advantage to minimize the spectral width at a fixed duration, in order to avoid population of multiply-excited Rydberg states. This spectral width has a value of $2\pi \times 3.8 \text{ MHz}$ in this case. We also investigated this protocol with other shapes, for instance with a longer probe pulse in the hope that it would reduce the coupling to multiply-excited Rydberg states or the two bright polaritons detuned by $\pm\sqrt{g^2 + \Omega^2/4} \simeq \pm 2\pi \times 11 \text{ MHz}$ with a width of $2\pi \times 3 \text{ MHz}$ ($(\kappa + \gamma)/2$), but also with asymmetric pulses, without improving the outcome however. The mean photon number of the input coherent state is stabilized by a lock-and-hold intensity lock at the beginning of the experimental sequence, performed by the same instrument.

⁽¹⁾ A Red Pitaya board with a 125 MHz logic clock, a 250MS/s sampling rate and a 50 MHz analog bandwidth.

The control beam is directly switched off and on by the external control from our numeric card⁽²⁾. Pulses' light intensities are shown in figure 6.3, the probe pulse in red is fitted by a Gaussian with an overlap of > 99% while the control beam intensity I_c in blue is fitted by two error functions:

$$\begin{aligned} I_c(t) &\propto 1 - \frac{1}{2} \operatorname{erf}\left(\frac{t - t_d}{\sigma}\right) + \frac{1}{2} \operatorname{erf}\left(\frac{t_u - t}{\sigma}\right) \\ \operatorname{erf}(t) &= \frac{2}{\sqrt{\pi}} \int_0^t e^{-u^2} du \end{aligned} \quad (6.17)$$

where $\sigma = 126$ ns, $T_{off} = t_u - t_d = 394$ ns is the storage duration and the fit yields an overlap of > 99% with the control intensity profile. The rising, or falling, time σ is limited by the beam size through the AOM⁽³⁾ in charge of the on/off switch. The high power of the control beam (~ 1 W) does not allow for a smaller beam inside the crystal that would reduce this response time. In practice, we need the control beam to reach a value close to zero between the storage and readout which forces us to work with $T_{off} \gtrsim 4\sigma$. The minimum of the control field is equal to 24% of its maximal value for the configuration considered here.

Experimental sequence

Here is a summary of the main steps of the experimental sequence for the measurements in the pulsed regime. The sequence starts by the preparation of the small atomic ensemble inside the resonator in $\simeq 100$ ms, see chapter 3 dedicated to this task. In parallel, the intensity of the D_1 probe is measured to compensate for drifts between experimental cycles. Then, the atomic ensemble is pumped into the ground state $|G\rangle$ as described in chapter 4. If the homodyne detection is used, this pumping stage is preceded by a 400 μ s step for the phase lock of the local oscillator, that was also introduced in chapter 4. Finally, the D_1 and control beam pulses are sent to the atom-cavity system. The escaping light is either acquired by a photon counter (SPCM) or by the homodyne setup. We are free to switch from one detection to the other, chosen by acting on the detection AOM placed at the output of the resonator. The acquisition duration for one measurement is very short, of a few microseconds, which allows us to probe several times (up to 10) the system before needing to stabilize the atom number by a small repumping step⁽⁴⁾ (10 μ s). Consequently, an experimental cycle is divided into a number of pulses per loop N_p before the repumping step and to a number of loops N_l . The total number of measurements is then given by $N_a = N_p \times N_l \times N_{cy}$ where N_{cy} is the number of experimental cycles. The delay between two consecutive input pulses is also an important parameter. A too short separation is detrimental to the efficiency of this storage-retrieval process because of residual long-live Rydberg pollutants [48, 57, 173, 199]. In practice, this effect is sufficiently reduced for a $t_p \geq 80$ μ s waiting time between two runs. Options are being studied to reset the cloud between two measurements in order to reduce the time delay between two consecutive input pulses. We also observed a degradation for a “high” input intensity ($|\alpha|^2 \simeq 10$) that forced us to reduce the number of pulses per loop in this regime to maintain the output photon number constant.

6.2.2 Characterization

In this subsection, we focus on the characterization of the storage plus readout of a photon and start with its optimization. The coherence time of the atomic excitation, i.e. the accessible storage time in the memory before the loss of the photon, is an interesting figure which allows a rough estimation of the efficiency of the storage process. Another important aspect is the

⁽²⁾See chapter 2 for the presentation of the control setup in section 2.3.

⁽³⁾Acousto-optics modulators are introduced in chapter 2.

⁽⁴⁾The dipole trap is kept on during the acquisitions.

nonlinearity of the memory, to ensure that the atom-cavity system cannot store more than one excitation and as a result that the output pulse cannot contain more than one photon. To verify this, we present the measurements of the second order autocorrelation, which allows us to characterize the unicity of the single photons at the output of the cavity.

In what follows, we will only give the photon number for the output pulse corrected from the losses induced by the optical path at the output of the resonator and the detection. This figure therefore corresponds to the photon number at the exit of the cavity.

Optimization of the output photon number

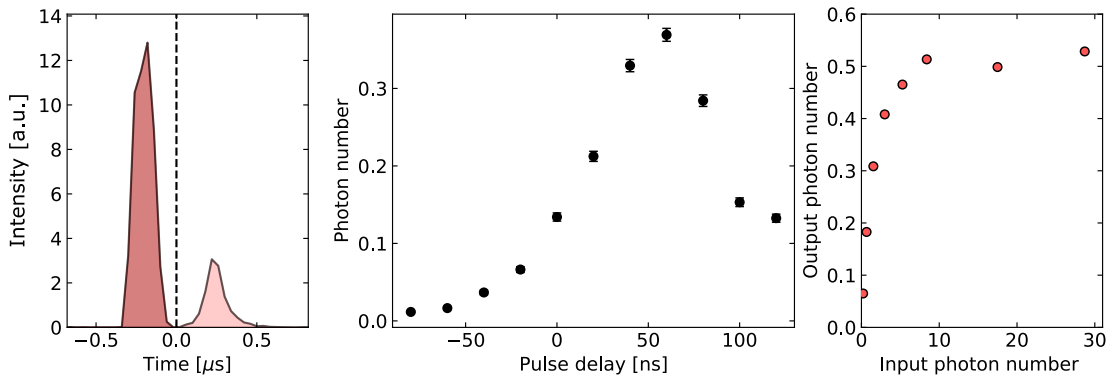


Figure 6.4: Optimization of the pulses. Left- Input pulse (dark red) and output pulse (light red) intensities as a function of time, the vertical line symbolizes the switch of the detection AOM. Middle- Output photon number as a function of the pulse delay between the probe and control pulses with up to 0.37 photon for $|\alpha|^2 \simeq 3$, averaged over $N_l = 11$, $N_p = 3$ and $N_{cy} = 400$ per point. Right- Output photon number as a function of the input photon number after optimization (red dots). We recover the saturation predicted by the simulation, figure 6.2.

We start by addressing the optimization of the pulse parameters with respect to the number of photons in the output state. These calibration measurements are therefore performed with the photon counter. The optimization of this protocol at fixed pulse shapes mostly depends on two parameters: the number of photons in the input pulse and the delay between the probe pulse and the falling edge of the control beam δt . This delay between the pulses is important to achieve an efficient storage of a photon in the atomic ensemble. This step thus consists in maximizing the efficiency of the writing step. The output pulse is isolated from the high-intensity input pulse by only switching on the detection AOM after the end of the first pulse in order to protect our detector. This separation between the input and output pulses is illustrated in figure 6.4 with a dim input state and keeping the detection AOM on during the whole acquisition. The starting time for the falling edge of the control pulse (equation 6.17) is changed for a constant storage time and the result is shown in figure 6.4, middle plot⁽⁵⁾. In that case, the input pulse contains 3 photons on average and, after optimization, we obtain 0.37 photon in the output pulse. We did this optimization of the delay δt for several input photon numbers and we show on the right panel the maximum photon number in the output pulse after this optimization. We recover the expected saturation of the output photon number as a function of the input, see figure 6.2, with at most 0.53 photon.

⁽⁵⁾This is more convenient than moving the input pulse which could appear in the detection window due to the short separation between the input and output pulses

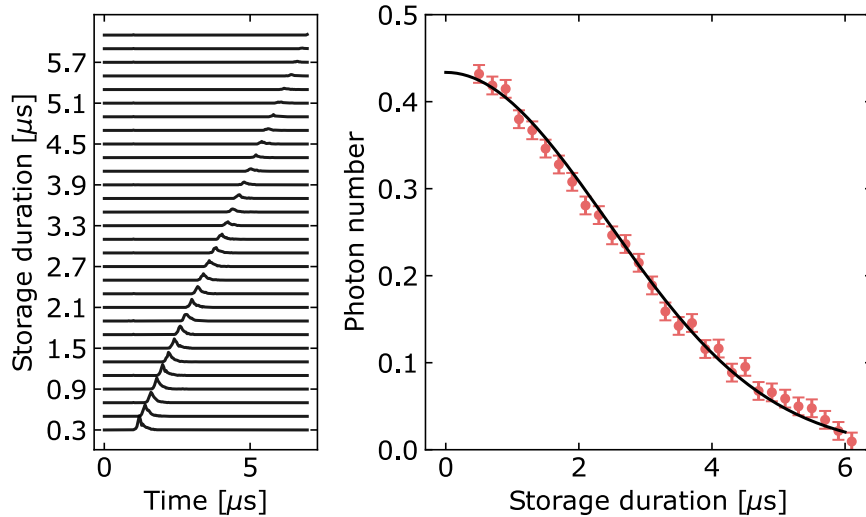


Figure 6.5: Coherence time of the atomic excitation. Left- Output pulse as a function of time and the storage duration. Data are averaged over $N_p = 1$, $N_l = 21$ loops and pulses and $N_{cy} = 400$ experimental cycles. Right- Estimation of the storage time from the photon number in the output pulse as a function of the storage duration. A fit of a Gaussian decay function yields a characteristic time $\tau = (3.52 \pm 0.03)$ μs at e^{-1} .

Storage efficiency

The coherence time of the atomic ensemble is an important parameter to estimate the losses in the storage process. Several effects are responsible for the decay of the collective atomic excitation: the temperature, the dipole trap or the interactions between Rydberg atoms. Ideally, the photon is stored in the state $|R\rangle$ corresponding to the first excited “symmetric” Dicke state. We recall its expression:

$$|R\rangle = \frac{1}{g} \sum_n g_0^{(n)} |g, \dots r_n, \dots, g\rangle \quad (6.18)$$

where $g_0^{(n)}$ is the coupling strength of the n^{th} atom.

This state consists in the superposition of a single Rydberg excitation delocalized over the whole atomic ensemble. As explained in chapter 1, this kind of excitation is very sensitive to the dephasing between the atoms via the phase of the prefactors $g_0^{(n)}$. As a consequence, this state is particularly impacted by the van der Waals potential that depends on the distance between atoms resulting in a strongly position-dependent phase. This dephasing of the collective excitation $|R\rangle$ was studied by Bariani *et al.* [200] in the case of dipole-dipole interactions. We will show in the next chapter that its contribution is negligible in a certain parameter range for the 109S in the context of Rabi oscillations. In the present case, the 3 μK temperature should result in a coherence time of $\sim 3.3 \mu\text{s}$, we will also derive this expression in the next chapter. Finally, the dipole trap is turned off during the process, it has therefore no impact on the coherence time.

We measured the photon number of the output pulse as a function of the storage duration T_{off} . Data are fitted by a Gaussian decay yielding a (3.52 ± 0.03) μs storage time at e^{-1} consistent with the temperature of our atomic sample. This measurement was done with an input pulse containing 10 photons on average. The same measurement but with a lower input, with 6 photons on average, gives a similar result suggesting that the lifetime does not depend

on the intensity of the input pulse. The fact that the population damping is well-fitted by a Gaussian decay suggests no important contribution from interactions.

From this information, we can infer the maximal coherent population in the Rydberg state right after the writing step. A conservative definition of the storage time is to consider the duration between the minimum of the control beam and the release: $T_s = T_{off}/2 = 197\text{ ns}$. The storage efficiency is then at maximum $\eta_s = 99\%$. Moreover, the EIT transmission is $\mathcal{T}_0 = 80\%$ which yields an extraction during the readout $\eta_r = \sqrt{\mathcal{T}_0}T/L = 80\%$. All in all, the population in the Rydberg excitation after the writing step is thus at least $0.5/(\eta_r\eta_s) = 63\%$. This demonstrates that we exceed the 50% population threshold for a continuous driving.

Photon unicity

We now turn to the statistics of light at the output of the resonator. We performed coincidences measurements with the output pulse to ensure that it contains at most one photon, and estimate the unicity of this single-photon source. We introduced this method in chapter 4 with the aim of characterizing a photon stream. In chapter 5, we carried out a first implementation of this method and observed strong photon antibunching with a zero-delay autocorrelation of 5% for a continuous driving of the atom-cavity system. Here we cannot assume time invariance, so we note the number of coincidences between time t and $t + \tau$: $N_c^{(0)}(t, t + \tau)$ and the total number of coincidences for a given delay is:

$$N_c^{(D)}(\tau) = \int N_c^{(0)}(t, t + \tau) \frac{dt}{t_d} \quad (6.19)$$

where t_d is the temporal resolution of our detection, here $t_d = 10\text{ ns}$.

In this work, the system is periodically probed with a waiting time $t_p = 80\text{ }\mu\text{s}$. The total number of clicks in this acquisition window on one photon counter is therefore:

$$N = \frac{1}{2}\eta_{SPCM}p_1N_a \quad (6.20)$$

where p_1 is the probability to have one photon at the output of the cavity and $\eta_{SPCM}p_1/2$ the mean photon number detected on one SPCM, with $\eta_{SPCM} = 38\%$, assuming that the splitting is well-balanced between the two detectors and N_a the total number of realizations.

We can then define the total number of coincidences per period t_p . Concretely, one has to sum the number of coincidences per delay from equation 6.19 for $-\Delta t < \tau + mt_d < \Delta t$ where Δt is the duration of the output pulses, typically one microsecond, and m an integer. Therefore, the total number of coincidences per period is:

$$N_c(m) = \int_{mt_p - \Delta t}^{mt_p + \Delta t} N_c^{(D)}(\tau) \frac{d\tau}{t_d} \quad (6.21)$$

We can then distinguish two cases. First if m is a non-zero integer, the correlations originate from the clicks between two different output pulses. The total number of coincidences in the vicinity of $\tau = mt_p$, and assuming that the pulses contain mostly zero or one photon is given by:

$$N_c(m \neq 0) = N^2 \frac{N_l N_p - m}{N_l N_p} \quad (6.22)$$

where $N_l N_p = 105$ is the total number of pulses separated by the waiting time t_d . The factor represents the number of pairs separated by a time mt_d over the total number of pulses per experimental cycle.

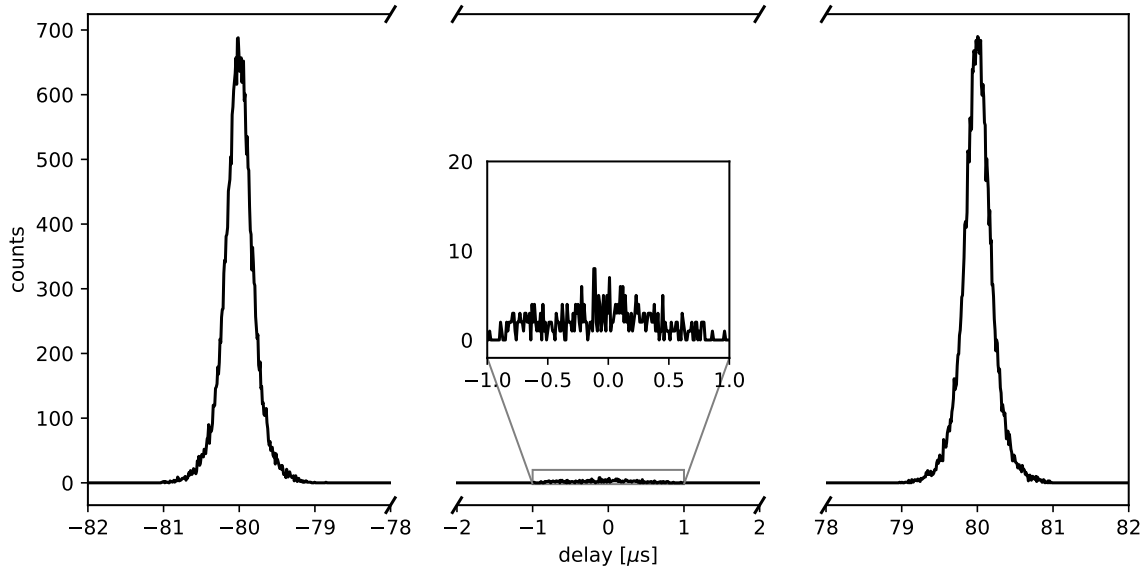


Figure 6.6: Coincidences for the output pulse. Autocorrelation for the output pulse with 0.37 photon. Pulses are separated by $t_p = 80 \mu\text{s}$ resulting in crossed correlations at $\tau \simeq mt_p$ with m non-zero integer. We observe strong photon antibunching indicating that only single photons escape from our nonlinear quantum memory. Data are averaged over $N_p = 5$, $N_l = 21$ and $N_{cy} = 70000$.

For $m = 0$, the coincidences originate from photons in the same output pulse and if we assume that it almost only contains zero or one photon, the residual correlations observed in this region can be attributed to the probability to have two photons in the pulse. If we note this probability p_2 , the coincidences are:

$$N_c(m=0) = \frac{1}{2}\eta_{SPCM}^2 p_2 N_a \quad (6.23)$$

Therefore, the probability to have two photons in the output pulse can be estimated from the ratio of coincidences:

$$p_2 = p_1^2 \frac{N_c(m=0)}{2N_c(m \pm 1)} \frac{N_l N_p}{N_l N_p - 1} \quad (6.24)$$

We carried out this measurement for an output pulse with $p_1 = 0.37$ photon. The coincidences as a function of the delay, $N_c(\tau)$, close to the zero-delay region and for $\tau \simeq \pm t_p$ are shown in figure 6.6. The ratio of coincidences between $m = 0$ and $m = \pm 1$ gives $g^{(2)}(0) = 1.2\%$ resulting in a probability to measure two photons of 0.081% (p_2), uncorrected from background noise. The output pulse is therefore a single photon with a very high unicity.

Overview and outlook

The efficiency of the storage and readout protocol in our platform is currently equal to 53% for the parameters presented here. Our platform therefore constitutes an efficient and on-demand single-photon source with a high unicity ($g^{(2)}(0) = 1.2\%$) operating however at a 13 kHz rate limited by Rydberg pollutants. This rate could ultimately reach $\simeq 2$ MHz with this apparatus once that technical problem solved. It is also possible to improve the efficiency of the protocol in two different ways. First of all, the cavity has quite important losses, see chapter 2 for a discussion about these losses, which limit the photon collection efficiency to 90% for an empty cavity. A cleaning or a replacement of the mirrors should permit to reach 99%. The other limitation is the power that we have in the control beam for the readout step. The measurements presented here were performed with the 109S to ensure a large blockade

volume but this forced us to work with Rabi frequencies of $2\pi \times 10$ MHz, and an atom-cavity coupling of $2\pi \times 10$ MHz. This allows us to recover $\sqrt{T_0} = 90\%$ of the photon from the Rydberg polariton. This value can be boosted by a finer alignment of the build-up cavity mode as well as a better alignment of the SHG cavity of the TiSa laser to gain in power. One can also reduce the effective Rydberg damping rate currently equal to $2\pi \times 80$ kHz, which is limited by the temperature and the lightshift of the crossed dipole trap. If all these factors are taken into account, the photon number at the output could reach 0.66 at maximum instead of the current 0.53 threshold.

6.3 Study of the continuous variables of the field

We present now the measurements of the quadratures of the field to complete the previous observations that were centered on the intensity of the field. We saw that the output pulse has a non-negligible population in the one-photon Fock state when prepared with a large coherent input state, around 0.5 photon per pulse and a very low probability $< 10^{-3}$ to host two photons. Moreover, the quantum memory process is expected to preserve the coherence of the excitation, so we should observe an output state with a well-defined phase and truncated at one photon. This generation of a photon in a superposition of state with the vacuum corresponds to a displacement of the vacuum in the truncated subspace [175], induced by the photon blockade which prevents having more than one excitation in our system. Similar experiments were conducted using an optical parametric amplifier and post-selection to produce single-photon-added coherent states [201]. This truncation of a coherent state, in our platform, is closely related to diffusion experiments on a two-level system, as obtained by Schulte *et al.* [202] and proposed theoretically by Carmichael [203]; it is also reminiscent of the quantum scissors device introduced by Pegg *et al.* [204], implemented by Babichev *et al.* [205] and later adapted by Ferreyrol *et al.* to achieve a noiseless amplifier [206].

Before presenting the experimental results obtained with our platform, we start by discussing the properties of the ideal one-photon truncated state (equation 6.5) in this context of continuous variables. In parallel, we use the simulation introduced in the first section, together with the mode selection via a fictitious cavity, to compute the density matrix of the output field with realistic parameters. We will then move to the concrete measurements with our homodyne setup. We address the issue of output mode selection of the local oscillator and show that the phase of the stored photon is indeed preserved by the quantum memory. In a second step, we study the evolution of the field quadratures as a function of the number of photons in the output pulse. This analysis is concluded by a homodyne tomography to reconstruct the Wigner function. These reconstructions reveal the non-Gaussian character of the output state and even negativity. We therefore demonstrate that our platform can generate nonclassical states of light in a deterministic way.

In this section, we initially optimize the photon storage by adjusting the delay between the input pulse and the control pulse for $|\alpha|^2 = 15$ photons at the input, as we did in the previous section during the optimization step. From the ideal model, the output state is then a statistical mixture between a one photon Fock state and vacuum ($\beta = \pi$, equation 6.5). When we reduce the input intensity, for the same delay δt between the pulses, we change the rotation angle β from equation 6.5. As we reduce the input intensity, we therefore expect to have some coherence between the vacuum and the one-photon Fock state.

6.3.1 Theoretical considerations and simulation

In this subsection, we want to discuss some non-classical properties of the one-photon truncated state. In the previous section, we observed the saturation of the photon number in the output pulse as we increased the input intensity and a strong photon antibunching. In direct continuation of this, we want to investigate the evolution of the two quadratures \hat{X} and \hat{P} as a function of the photon number inside the pulse. We recall that the quadratures of the field are given by:

$$\begin{aligned}\hat{X}_\theta &= \mathcal{N} \int v(t) \hat{h}_\theta(t) dt \\ \hat{h}_\theta(t) &\propto \hat{b}^\dagger(t) e^{i\theta} + \hat{b}(t) e^{-i\theta}\end{aligned}\tag{6.25}$$

where $\hat{X} = \hat{X}_0$, $\hat{P} = \hat{X}_{\pi/2}$, \mathcal{N} is a normalization factor to ensure that the vacuum state has a variance of $1/2$, $v(t)$ is the temporal envelope of the detected output mode, \hat{h}_θ is the

homodyne signal, $\hat{b}(t)$ the annihilation operator in free space and θ the phase of the local oscillator. This expression of the quadrature operator clearly illustrates the complexity of simulating quadratures measurements without the use of the fictitious cavity technique due to the infinite number of modes in free space.

Ideal one-photon truncated state

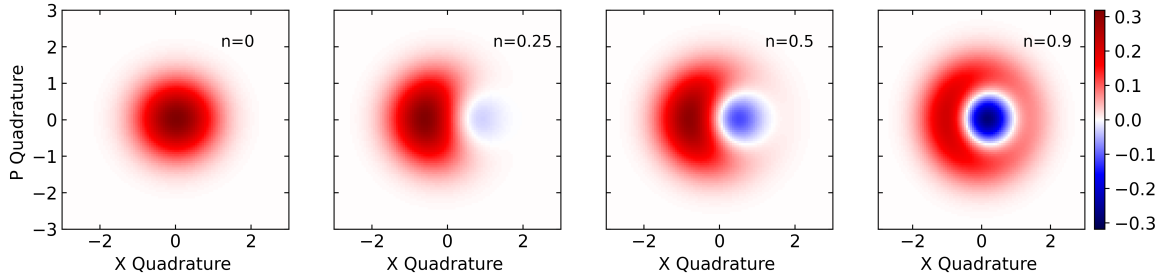


Figure 6.7: Wigner functions of the truncated state. Color map of the Wigner function for the truncated state. The photon number is progressively increased, from right to left: $n_S = 0, 0.25, 0.5, 0.9$. The maximum of squeezing is reached when $n_S = 0.25$ while the mean value is maximal for $n_S = 0.5$, see text.

We present here the ideal one-photon truncated state and its properties. The easiest quantities to study experimentally are the mean value of the quadratures and their variances. For an ideal truncated state $|S_1\rangle$, the one-photon Fock state is in a superposition with the vacuum resulting in:

$$|S_1\rangle = \sqrt{1 - n_S} |0\rangle - \sqrt{n_S} |1\rangle \quad (6.26)$$

where $n_S = \sin^2(\beta/2) \leq 1$ is the number of photons in the output pulse, and the minus sign is due to the phase convention used in this thesis. We recall that the relative phase between our local oscillator and the probe is zero when the cavity is locked out of resonance. In the case considered here, we describe a photon leaving our resonator, hence the minus sign.

The mean value of the quadratures of the field has a very simple expression for this one-photon truncated state:

$$\langle \hat{X} \rangle = -\sqrt{2n_S(1 - n_S)} \text{ and } \langle \hat{P} \rangle = 0 \quad (6.27)$$

where $\langle \hat{X} \rangle$ reaches its maximum for $n_S = 1/2$ and goes to zero as $n_S \rightarrow 1$. This is quite different from a coherent state with a mean photon number $|\alpha|^2$ for which the mean value of the \hat{X} quadrature is $\sqrt{2|\alpha|^2}$. Of course, the two states remain close as long as the photon number is small. For a coherent state with an amplitude $\alpha = -\sqrt{n_S}$, the overlap between the two states is:

$$\langle S_1 | \alpha \rangle = e^{-n_S/2} (\sqrt{1 - n_S} + n_S) \simeq 1 - \frac{n_S^2}{4} \quad (6.28)$$

In the same way, one can compute the variance of both quadratures for this truncated state, resulting in:

$$\begin{aligned} \langle \Delta \hat{X} \rangle &= \frac{1}{2} - n_S + 2n_S^2 \\ \langle \Delta \hat{P} \rangle &= \frac{1}{2} + n_S \end{aligned} \quad (6.29)$$

where we recall that the variance of the vacuum state ($n_S = 0$) is fixed at a value of $1/2$.

When $n_S = 1$, the variance of the field is maximal such that $\langle \Delta P \rangle = \langle \Delta X \rangle = 3/2$ and the distinction between X and P is no longer possible since the phase of the state is lost. At

a small photon number, the state of the escaping photon is on the contrary squeezed for the X quadrature, meaning that its noise is smaller than the vacuum variance $\langle \Delta \hat{X} \rangle < 1/2$, but of course the other quadrature is anti-squeezed to comply with the Heisenberg's uncertainty principle:

$$\sqrt{\langle \Delta \hat{X} \rangle \langle \Delta \hat{P} \rangle} = \sqrt{\frac{1}{4} + 2n_S^3} \geq \frac{1}{2} \quad (6.30)$$

The maximum of squeezing is reached for $n_S = 1/4$, is equal to $3/8$ and corresponds to three quarters of the vacuum variance (1.2 dB) which is very modest compared to the 15 dB factor obtained with the best experimental realizations of squeezed vacuum [207].

A suitable representation of this state is provided by the Wigner function that we introduced in chapter 4:

$$W(X, P) = \frac{1}{\pi} \int_{-\infty}^{+\infty} \langle X + Y | \hat{\rho} | X - Y \rangle e^{-2iPY} dY \quad (6.31)$$

where $\hat{\rho} = |S_1\rangle \langle S_1|$ is the density matrix of the state.

The Wigner function is plotted in figure 6.7 for $n_S = 0, 1/4, 1/2$ and 0.9 . We observe the squeezing of the X quadrature when $n_S = 1/4$ and the maximal displacement for $n_S = 1/2$. When the photon number is close to one, the phase is almost lost and the Wigner function features the maximum of negativity on its center, a clear nonclassical effect.

Simulation

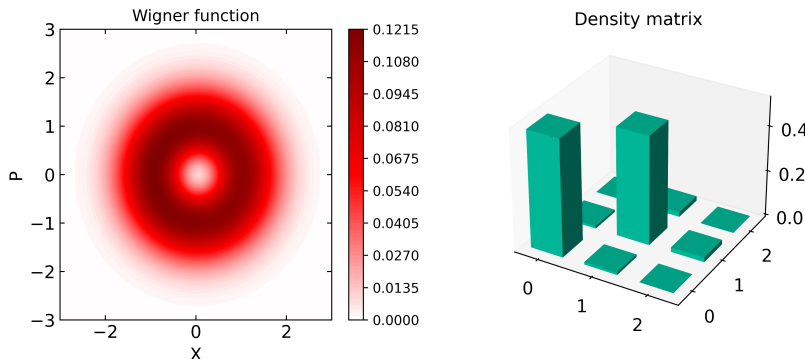


Figure 6.8: Simulation for the output density matrix. Left- Wigner function for $|\alpha|^2 = 10$, same parameters as the experiment presented in the previous section. Right- Density matrix for the output state with 0.49 photon. We show here the absolute value for the coherences. This density matrix is a statistical mixture between the one-photon Fock state and vacuum.

We now implement the simulation described in the first part of this chapter in order to obtain the density matrix of the output pulse. We want to show that we indeed reach a statistical mixture between a photon and vacuum without coherence at high-input intensity. The parameters and pulses used for this simulation are the same as those of the experiment presented in the previous section. The output mode in this case is given by the intensity profile at the exit of the cavity: $v(t) \propto \sqrt{\langle \hat{a}^\dagger(t) \hat{a}(t) \rangle}$. The result is shown in figure 6.8 for $|\alpha|^2=10$ photons in the incoming pulse. On the left, we observe a phase-invariant Wigner function with a dip in the center, comparable to the one observed in figure 6.7 for $n_S = 0.9$ without negativity however. Here the output pulse contains 0.49 photon for a waiting time of $T_{off} = 400$ ns and we set the Rydberg damping rate at a value of $2\pi \times 85$ kHz, which therefore

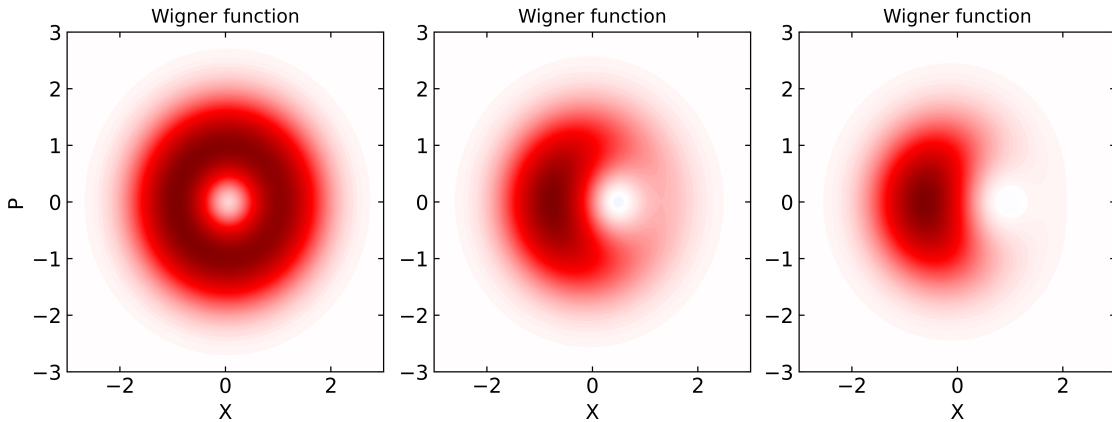


Figure 6.9: Evolution of the Wigner function. Wigner function from figure 6.8, same parameters (left), $|\alpha|^2 = 5$ (middle) and $|\alpha|^2 = 2.5$ (right) all other parameters being equal. We observe the displacement of the deep as expected when we vary β for the truncated state.

overestimates the losses during the storage. On the right, we show the density matrix. In this case, the output pulse is a statistical mixture between the vacuum state and a one-photon Fock state, as expected.

We can now look at the evolution of the Wigner function as we reduce the input intensity, see figure 6.9 where we initially optimized the delay for 10 photons on average in the incoming pulse. We give three examples, with $|\alpha|^2 = 10, 5$ and 2.5 , all other parameters being equal and we obtain at the output a population of 0.48, 0.4, 0.26. The evolution is consistent with figure 6.8: the Wigner function has initially no phase dependence (left), we recover the crescent shape for $|\alpha|^2 = 5$ and finally the squeezed state (right). Notice that due to important losses during the process the Wigner functions remain positive.

6.3.2 Output mode and homodyne signal

The storage and readout achieved with our platform is based on the coherent transfer of a photon into a Rydberg excitation. As a consequence, this translates into a preservation of the phase of light that can be measured with our homodyne detection. This measurement consists in comparing the output electromagnetic field with a reference mode provided by the local oscillator, except for the temporal envelope which remains to be defined since the local oscillator is used in continuous mode. The photon being reemitted from the cavity mode, it is therefore expected to have a well-defined polarization, spatial mode, frequency and of course phase. We start by discussing the choice of this temporal mode with our homodyne detection and the preservation of the phase at a small rotation angle β .

Mode selection

We want to characterize the quadrature of the field with the homodyne setup. Before discussing the results with our platform, we need to define the temporal mode envelope for the output field. The mode we are interested in is the one that maximizes the number of photons in the pulse, i.e. the one that corresponds to the square root of the intensity measured with the SPCM in figure 6.4. This output mode can be approximated by two mixed exponential decay functions:

$$v(t) = \frac{v_0}{e^{(t_0-t)/\sigma_0} + e^{(t-t_1)/\sigma_1}} \quad (6.32)$$

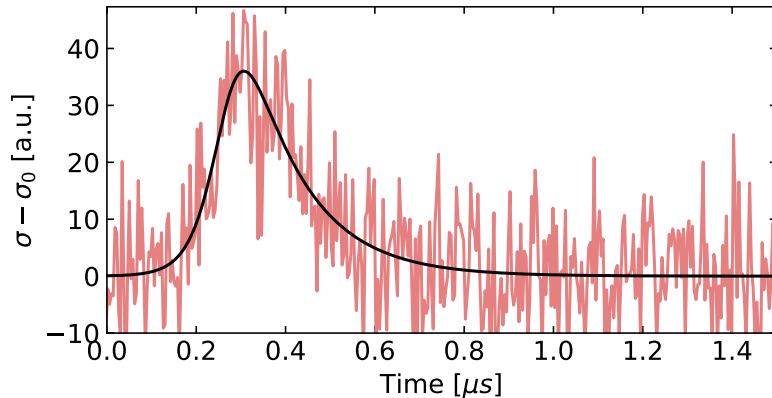


Figure 6.10: Optimization of the output mode. The noise of the in-phase homodyne signal through time reveals the temporal mode of our single photon. This signal is fitted by the function of equation 6.32, with $\sigma_0 = 39 \text{ ns}$, $\sigma_1 = 130 \text{ ns}$. This signal is estimated from 67 200 realizations ($N_p = 4$, $N_l = 21$, $N_{cy} = 800$).

where v_0 is a normalization factor, σ_0 is the rising time, σ_1 the escaping rate of the field and t_0, t_1 two delays. We could directly choose to fit this model on the measurements with the SPCM but in this case, we need to know precisely the delays between the cards and detectors to adjust the timing (t_0, t_1) for homodyne measurements. Moreover, the temporal resolution for the measurements with the SPCM is limited to 10 ns while the card recording the homodyne voltage reaches 4 ns. We therefore directly use the homodyne signal to adjust this output mode.

We can proceed by two different ways to obtain these parameters from the homodyne detection, depending on the context. If the rotation angle is small ($\beta \ll 1$), the output state is close to a coherent state, as long as the phase is preserved. In this case, the average of the in-phase homodyne signal at each instant directly provides the temporal mode of the output pulse: $\langle \alpha | \hat{h}(t) | \alpha \rangle \propto v(t)$. This is no longer possible for the optimized configuration where the rotation angle is close to $\beta \simeq \pi$. In this case we expect to have essentially a statistical mixture between a single photon and the vacuum state for which unfortunately $\langle n | \hat{h}(t) | n \rangle = 0$, because a Fock state $|n\rangle$ has no phase dependence. In the latter case, however, one can compute the variance of this signal for $\theta = \pi/2$ which is expected to be bigger than the vacuum noise, see equation 6.29. The temporal mode is then estimated by computing:

$$\sqrt{\langle \Delta \hat{h}(t) \rangle} - \sigma_0 \propto |v(t)| \quad (6.33)$$

where σ_0 is a reference without any probe or output pulse.

The rms noise of the homodyne signal is shown in figure 6.10 for 0.37 photon. We clearly observe an increase around $0.3 \mu\text{s}$ corresponding to the escaping field from the resonator. The resulting mode is very similar to the one observed with the simulation or the photon counter. Finally, the first approach based on the mean value at a small photon number gives a consistent output mode, the two approaches having a $> 99\%$ overlap for the fitted modes. This mode envelope via the mean value of the homodyne signal is shown in figure 6.11, left panel. In the following, we only use the output mode derived here from the variance of the homodyne signal.

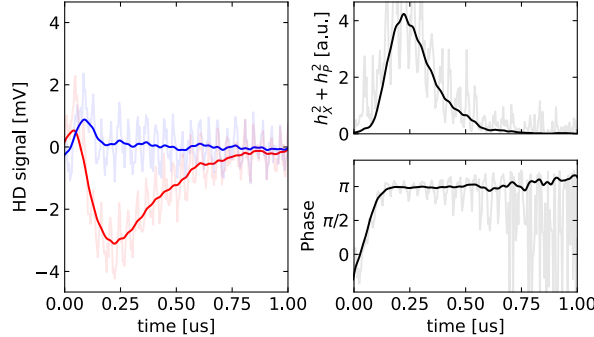


Figure 6.11: Phase of the output photon. Left- In-phase averaged homodyne signal (h_X , red) and $\pi/2$ shifted (h_P blue) as a function of time for a small angle β . A low-pass Butterworth filter is used for illustration purposes only, with a 5 MHz cut-off. Raw data are also shown in the background (light colors). Top right- The signal $h_X^2 + h_P^2$ as a function of time provides an intensity-like measurement. Bottom right- Phase as a function of time with a value of 0.99π . In the first 100 ns the signal is dominated by the input pulse with a phase of zero. Data are averaged over $N_p = 5$ pulses per loop, $N_l = 21$ loops and $N_{cy} = 800$ experimental cycles.

Phase of the output state

In the limit of a small rotation angle β , the photon state is expected to be close to a coherent state. We checked this by measuring the homodyne signal for two quadratures of the field and an output pulse containing 0.05 photons⁽⁶⁾, estimated from a measurement with the photon counter. The homodyne signal for the two quadratures of the field are plotted in figure 6.11, the in-phase signal being in red. Note that with our setup, the zero of the phase is by definition obtained for a coherent state reflected off of the input/output mirror. We clearly recognize the temporal mode $v(t)$ on the in-phase signal. The temporal envelope in intensity that we observed with the photon detector is thus recovered by computing $\langle \hat{h}_\theta \rangle^2 + \langle \hat{h}_{\theta+\pi/2} \rangle^2$, as illustrated in the plot at the top right. At last, we can derive the phase of the pulse by computing $\arctan(h_p/h_x)$ as shown in the bottom right panel. The obtained phase is 0.99π as expected for a coherent state that propagated through the cavity because our phase origin is defined by the reflection out of resonance. Notice that in the first 100 ns, the phase is not π because the input pulse has a dominant contribution.

6.3.3 Experimental results

We now study the quadratures of the field with our platform as a function of the number of photons contained in the output pulse. We first discuss the mean value and variance of the quadrature with respect to the model with losses included. Finally, we present the homodyne tomography of the electromagnetic field for several photon numbers and discuss the reconstructed density matrix.

Mean value and variance

We confront the ideal quantum truncated state that was introduced at the beginning of this section with the state obtained at the output of the cavity. It is necessary to take into account the losses caused by the storage and readout plus the detection to describe the properties of the output state. In this case, we assume linear losses only and the density matrix can then be rewritten as:

$$\hat{\rho} = \eta_t |1\rangle \langle 1| + (1 - \eta_t) |0\rangle \langle 0| \quad (6.34)$$

⁽⁶⁾The delay between the pulses was optimized for $|\alpha| = 15$ resulting in 0.53 photon. Here we work with $|\alpha|^2 = 0.2$ all other parameters being equal.

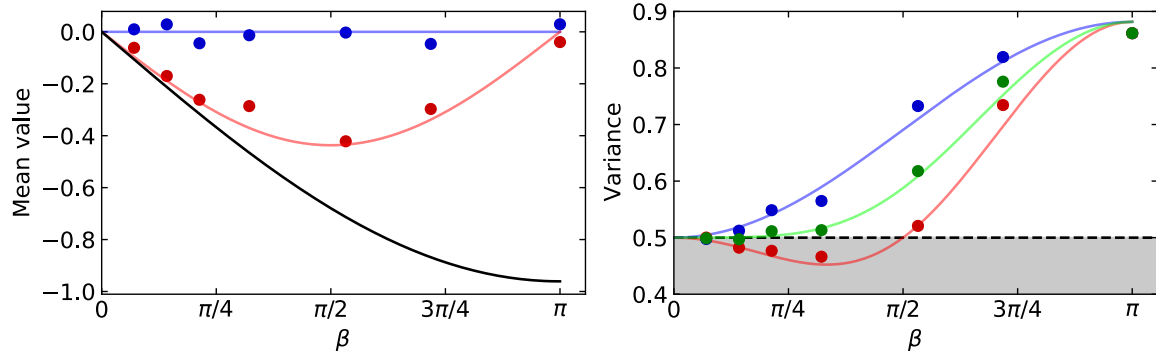


Figure 6.12: Mean value and variance of X and P quadratures. Left- Mean value of the quadratures X (red dots) and P (blue dots) as a function of the β factor. Theoretical curves (6.34) are shown in red for the X quadrature, in blue for the P quadrature and for a coherent state (black). Right- Variance as a function of the β factor for the X (red) and P (blue) quadratures. The product of the corresponding standard deviations, limited by the Heisenberg's uncertainty principle, is also plotted in green. The classical limit is delimited by the black dashed line with a value of 1/2. Data are averaged over $N_{cy} = 800$, $N_p = 1$ and $N_l=11$.

where η_t represents all the losses right after the writing step and assuming $\beta = \pi$. This expression can be derived by considering the losses as an imperfect reflection of the light (η_t) on a beamsplitter. The other fraction of the field is measured by the environment, which means that the density matrix of the whole system is traced on this non-reflected mode, resulting in equation 6.34 for the density matrix that we concretely measure. The properties obtained for the ideal truncated state, equation 6.27 and 6.29, are therefore easily transposed with losses: one has simply to average the result over the outcome for the ideal state and the vacuum state weighted respectively by η_t and $1 - \eta_t$ because of the linearity of the trace. When $\beta \neq \pi$, one has to replace the annihilation operator \hat{a} by $\sqrt{\eta_t}\hat{a} + \sqrt{1 - \eta_t}\hat{b}$ and then to trace over the mode \hat{b} . The variance is then:

$$\begin{aligned}\langle \Delta \hat{X} \rangle &= \frac{1}{2} + \eta_t(2n_S^2 - n_S) \\ \langle \Delta \hat{P} \rangle &= \frac{1}{2} + \eta_t n_S\end{aligned}\tag{6.35}$$

while the mean value is simply: $\langle \hat{X} \rangle = -\sqrt{\eta_t 2n_S(1 - n_S)}$ and we recall that $n_S = \sin^2(\theta/2)$.

The results from our atom-cavity platform are presented in figure 6.12. For these measurements, we only optimized the delay between the control pulse and an incident pulse containing 10 photons. We assume here that, in such case, the photon is a statistical mixture between the vacuum and the one-photon state ($\beta = \pi$), so we can consider that we have a storage and release efficiency given by the population in this configuration: $\eta = 53\%$ (measured with the SPCM). On top of this, we also need to take into account the detection efficiency of our homodyne step $\eta_{HD} = 72\%$, the total efficiency is thus $\eta_t = \eta_{HD}\eta$.

On the left plot, we present the mean value of the two quadratures X and P for the output state, with a temporal envelope $v(t)$, as a function of the photon number at the exit of the resonator estimated with the photon counter. The findings are very close to the theoretical model when losses are taken into account. In particular, we indeed observe a maximal value of the quadrature for $\beta = \pi/2$, where the output state corresponds to a truncated state in a balanced superposition of a one-photon Fock state and the vacuum. We also put the theoretical curve for the equivalent coherent state to highlight the truncation of the output state.

On the right plot of figure 6.12, we display the variance of the two quadratures in blue and red, while the Heisenberg's principle uncertainty (equation 6.30) is shown in green. Once again, the model with losses taken into account (equation 6.34) matches well the observations without any additional adjustment. Among other things, the maximum of squeezing is observed for an output photon number of 0.14 which indeed corresponds to a population in the Fock state $|1\rangle$ of one quarter for the truncated state ($n_S = 0.14/\eta = 26\%$), accordingly the squeezing is lost for $\beta = \pi/2$ photon as expected when $n_S = 1/2$, equation 6.29.

These observations on the quadratures show a remarkable agreement with the simple model with losses. We go one step further by performing a tomography of the state.

Tomography of the state

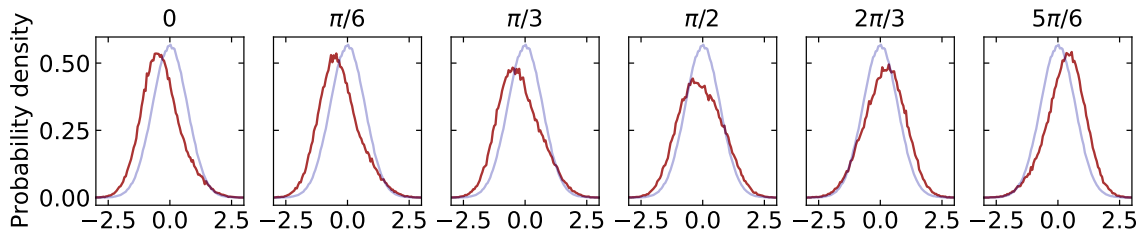


Figure 6.13: Quadratures of the field. Probability density distribution of the quadrature for an output pulse of 0.34 photon (red) and for the vacuum state (blue). Histograms are shown with a 0.06 step, 101 bins and $N = 102000$ measurements ($N_{cy} = 2000$, $N_l = 51$ and $N_p = 1$).

The reconstruction of the Wigner function is the missing element in our study as it allows us to obtain the density matrix, containing all the information about the output photonic quantum state. This reconstruction requires the measurement of the probability density distribution of the X_θ quadrature for several phases θ , which amounts to measuring different projections of the Wigner function, hence the name tomography. In order to estimate the probability density at a given phase, we repeat the measurement of the quadrature many times to obtain a histogram of the number of occurrences as a function of the value of the quadrature. In practice, we estimate this distribution for six phases:

$$\theta = \{0, \pi/6, \pi/3, \pi/2, 2\pi/3, 5\pi/6\} \quad (6.36)$$

The result is illustrated in figure 6.13 for 0.34 photon in the pulse. As a comparison, we also plotted the distribution for the vacuum state in blue. We observe a spread of the distribution around $\pi/2$ as expected from our previous measurements concerning the variance.

The reconstruction of the Wigner function then consists in finding the most probable density matrix to reproduce the measured histograms via the maximum likelihood algorithm. We do not go into the details of this method since it was introduced in chapter 4. The resulting Wigner functions for the raw measurements are shown in figure 6.14. on the left panel, while the corrected Wigner functions (detection efficiency η_{HD}) are depicted in the right plot.

Through this tomography, we recover of course the results exposed for the mean value of the quadratures as well as their variances. We observe a significant anti-squeezing for the pulse containing 0.27 photon characterized by a crescent shape. The loss-corrected Wigner function for 0.49 photon even shows a dip in the distribution and finally we obtain a small negativity for the last measurement with 0.53 photon. We find a behavior very similar to the theoretical Wigner function for a one-photon truncated state or the simulation, see figure 6.7 and figure 6.8.

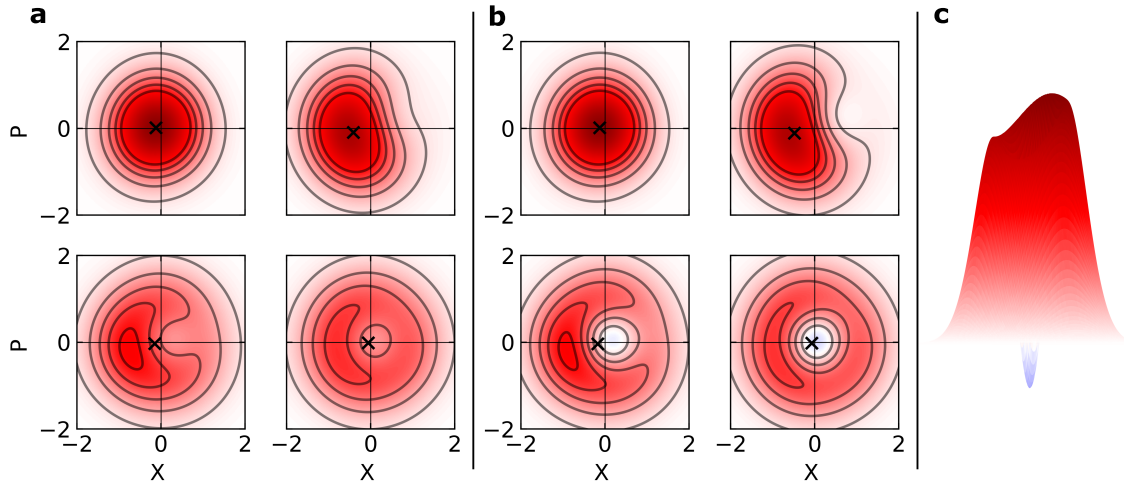


Figure 6.14: Homodyne tomography. a- Wigner functions reconstructed without any correction for 0.012 photons (top left), 0.27 (top right), 0.49 (bottom left) and 0.53 (bottom right). We observe an evolution consistent with figure 6.7. The mean value is marked with a cross. b- Wigner functions corrected for the detection efficiency $\eta_{H D} = 72\%$. For 0.53 photon, we observe some negativity (blue). c- Side view of the reconstructed Wigner function for 0.53 photon. In these reconstructions the Hilbert space is limited to 10 photons.

The Wigner function being a complete representation of a quantum state, the reconstruction of this function also gives us access to the density matrix. Let us look at the reconstructed Wigner function for 0.53 photon out of the cavity and estimated with the SPCM. We find that the output pulse has a very low population in the two-photon Fock state 0.6% while the probability to measure more than two photons is negligible with a value of 0.2%. Finally, we recover a probability of 0.53 to measure one photon when detection losses are taken into account. This experiment can thus be thought of as an on-demand generation of non classical light. On top of that, this means that the output photon is emitted in a well-defined spatio-temporal mode. This measurement is thus equivalent to Hong-Ou-Mandel tests and demonstrates a good indistinguishability.

Outlook

We demonstrated that the output pulse is indeed a truncated state and even observed a first small negativity of the Wigner function. We recovered the main properties of this state with good agreement with a simple model taking into account linear losses. Improving the memory process by means of reducing losses, as discussed at the end of the previous section, could lead to the achievement of a larger negativity which could be ultimately observed without any loss correction. It could also be interesting to look at the quadratures as a function of the delay between the pulse to highlight the coherent oscillations from zero photon to one.

We are also free to shape at will the output pulse of the photon by implementing more exotic waveforms to the control field. For an output pulse deterministically prepared in the one-photon Fock state, this could be used to make a time-bin qubit thanks to the phase preservation that we have in the platform. We focused here on the study of the output pulse but there are potentially interesting effects on the input state since it undergoes a photon subtraction during the writing step. We could investigate the evolution of the quadratures of the input pulse, for instance by injecting a squeezed state, and perform a homodyne tomography, in the same spirit as this study. However, this kind of protocol requires measuring the state of the atomic ensemble. In the next chapter, we present two detection methods that can be used for this purpose.

Conclusion

In this chapter we dealt with the nonlinear storage of a photon in our atomic cloud strongly coupled to the cavity thanks to the strong interactions between Rydberg atoms. We started our analysis by characterizing our system as a quantum memory and a single-photon source. We managed to retrieve 0.53 photon at the output of the platform for an incoming pulse containing 15 photons on average. We also showed that this single-photon source has a high unicity with a probability to measure two photons in the pulse at less than 10^{-3} . This efficiency for the generation of a single photon is already comparable to the one achieved with a state-of-the-art sources using quantum dots but can be improved to potentially reach an efficiency above 60%.

We then focused on the quadratures of the field. We demonstrated the preservation of the phase for the output pulse, indicating that the photon is in a superposition of states between the vacuum and the one-photon Fock state. In particular, we observed squeezing, anti-squeezing, and a good agreement between our measurements of the quadratures and the ideal truncated state when losses are taken into account. Finally, we reconstructed the Wigner function for several photon numbers in the output state and observed a crescent deformation consistent with the theory and a first, tiny, negativity.

We can now investigate slightly different approaches: we can study the truncation with several superatoms in the cavity [182] with the hope to make a two-photon truncated state or to use it as a source of photon pairs. This storage process can be used in the opposite way, to perform a photon subtraction as it was recently obtained in free space [208] but investigating this time the quadratures of the field.

Chapter 7

Coherent control and optical detection of a Rydberg superatom.

Contents

7.1 Collective Rabi oscillations	144
7.1.1 Rabi oscillations of a single Rydberg superatom	145
The Rabi Hamiltonian	145
Correction at finite blockade energy	146
Other sources of decoherence	148
7.1.2 Experimental implementation	150
Probes, excitation scheme and experimental sequence	150
Choice of the Rydberg pair	152
First observations	153
7.1.3 Characterization of the collective driving	154
Rydberg state	154
Scaling with the number of atoms	156
Current limitations and possible improvements	156
7.2 Detection of a Rydberg atom	158
7.2.1 Fidelity of a detector	158
7.2.2 Transmission switch	159
Model	160
Optimization	163
Single-shot fidelity	165
7.2.3 Detection via the reflected field	167
Observation of a conditional phase shift	167
Model for the detection	168
Optimization and fidelity	170
Limitation and outlook for the detections	171
Overview	173
Outlook	174

Introduction

In chapter 5, we demonstrated our ability to induce strong interactions between photons via the Rydberg blockade mechanism [57, 209]. In this regime, the coupled system reaches saturation with only one excitation propagating through the resonator. In this regard, our atomic ensemble is then equivalent to a single Rydberg superatom with properties magnified by the number of blockaded atoms. In this chapter, we take advantage of these strong optical nonlinearities to detect the state of the Rydberg superatom. In particular, we will show a high discrimination at the single-shot level with two different approaches.

The first detection method relies on the transmission saturation that we obtained in chapter 5. In this case, the EIT window of the coupled system drops close to zero in the presence of a Rydberg atom. The long lifetime of Rydberg states allows us to integrate over a long period of time ($\sim 10 - 100 \mu\text{s}$) to collect a few photons with our SPCM for a superatom in its ground state. This method is an efficient way to detect a Rydberg excitation with a single-shot fidelity of $94.7 \pm 1.1\%$.

The second method is based on the nonlinear response of the reflection coefficient. We will demonstrate that the preparation of one Rydberg atom in our system induces sufficiently high losses so that light gets reflected off of the input/output coupler. As a consequence, a single Rydberg excitation induces a π phase shift of the electromagnetic field, equivalent to a sign flip of the quadratures, that we record with our homodyne detection.

The characterization of these two detection methods supposes to deterministically create a single Rydberg excitation inside the cavity. Moreover, we want to have a coherent control of our Rydberg superatom in order to perform several quantum optics experiments in the near future [62, 170, 174]. For instance, the deterministic generation of optical “Schödinger kitten” states obtained by Gerard Rempe’s team requires the coherent control of a single atom coupled to a high-finesse cavity [38]. This protocol can be transposed to a Rydberg superatom coupled to our medium-finesse resonator. In our case, the atomic cloud is made of hundreds of atoms while we want to drive a unique transition between the ground and a single Rydberg state. Again, the strong Rydberg blockade in our atomic ensemble allows to isolate such a transition [103]. In this situation, the Rydberg excitation is delocalized all over our atomic cloud and corresponds to the W state introduced in chapter 1 [104, 210]. One striking effect of this collective driving is visible on the associated Rabi frequency which is enhanced by a factor \sqrt{N} , where N is the number of atoms inside the blockade sphere [104, 106]. This coherent manipulation is an additional feature that reinforces the parallel between our atomic ensemble and a single two-level system. Furthermore, we do not have a laser for a direct addressing between the ground and the targeted Rydberg state. In what follows, we will see how to obtain two-photon Rabi oscillations between the ground and this collective Rydberg state.

In the first section of this chapter, we describe the collective Rabi driving for an ideally blockaded ensemble before discussing some corrections to take into account excitations beyond this first excited state. These corrections at a finite interaction strength translate into a decay of the collective Rydberg state. We will take this opportunity to present the other sources of damping of the Rydberg superatom: non-zero temperature, fluctuations, etc. Next, we introduce the excitation scheme and the practical implementation of Rabi oscillations. In the last part of this section we discuss the optimization of the quality factor with respect to several parameters (Rydberg state, number of atoms...) in order to point out current limitations and to discuss possible improvements.

In the second section, we turn our attention to the detection of the superatom’s state. We start by a brief introduction on the detection fidelity and errors to obtain an unambiguous

parameter for the optimization of our detection. At first, we focus on the detection via the transmission of the resonator. We present a model that allows us to take into account the finite lifetime of the Rydberg excitation before addressing the optimization of this detection method with respect to several quantities: photon flux, integration time... In a last part, we present the limiting factors and determine the best configuration. The same analysis is performed for the phase-sensitive detection and is compared to the first approach in order to identify the limitation of both methods.

7.1 Collective Rabi oscillations

Rabi oscillations is a very standard method to coherently control the state of a two-level system. It has been employed in many quantum devices: on Josephson-Junction Qubits for quantum computing [211, 212], in quantum dots for single-photon sources [213, 214] or with ultracold atoms to emulate complex many-body Hamiltonians [81, 215]. This technique is also used for more fundamental experiments. For instance, Serge Haroche's team observed the dependence of the Rabi frequency on the number of photons in their microwave cavity, thereby demonstrating the quantization of the electromagnetic field in their system [63].

In our case, many proposals combining cavity QED and a Rydberg superatom require a coherent manipulation of the superatom's state [38, 62, 170, 174]. We do not have a laser able to directly transfer the population from the ground state to a Rydberg state. It is therefore only possible through a two-photon process with an intermediate state far from resonance [216, 217]. We will see that in the limit where our lasers are far-off resonant from the intermediate state, it is completely equivalent to a two-level situation. The other obvious issue in experiments dealing with atomic ensembles is that it is made of a huge amount of two-level systems, about a thousand in our case. However, the strong interactions existing in our experimental platform enable us to isolate a single collective Rydberg excitation out of the quasi-continuum of states [103, 104, 106].

Rabi oscillations are not the only way to achieve a population transfer. Another method is the Stimulated Raman Adiabatic Passage technique (STIRAP). This approach is also based on a two-photon transition but is less sensitive to fluctuations when performed at zero detuning on the intermediate state [218]. We showed in chapter 1 that the free space EIT Hamiltonian has a dark state, by definition uncoupled to the electromagnetic fields. This state is a superposition between the ground and the Rydberg state but has no population in the intermediate state. Moreover, the probability weight between the two components is set by the ratio between the Rabi frequency driving the first transition (Ω_1) and the control Rabi frequency (Ω_2): $|\psi\rangle = \cos\theta|g\rangle + \sin\theta|r\rangle$ where $\tan\theta = -\Omega_1/\Omega_2$. The idea behind STIRAP is to first sent a control laser pulse followed by a pulse addressing the first transition with an adjusted temporal overlap between the two in order to make an adiabatic transfer via the rotation of the dark state angle θ . After the two pulses, the dark state, initially in $|g\rangle$, is $\pi/2$ rotated to end up in the Rydberg state $|r\rangle$. This technique is therefore very reminiscent of the approach developed in the previous chapter with the rotation of the polariton but without the cavity. This method is interesting as it is less sensitive to the laser intensities or the atom number than Rabi oscillations: indeed, adiabaticity is the only requirement [219]. A method were proposed by Kis *et al.* to extend this population transfer to arbitrary rotation on the Bloch sphere but this approach, unfortunately, does not conserve the stability of the original STIRAP approach [220]. The STIRAP technique is even more complicated for a blockaded ensemble as the symmetry of the Hamiltonian makes this transfer strongly dependent on the atom number [221]. Beterov *et al.* showed that the STIRAP approach holds for a large detuning from the intermediate state as the method then becomes equivalent to the Adiabatic Rapid Passage method (ARP) for two-level systems [222]. In this case, the transfer is based on the sweep of the two-photon detuning and as a the result the accumulated phase depends on the atom number, making the technique more difficult to implement than Rabi oscillations.

In this section, the derivation of the collective Rabi oscillations is presented in the limit of a perfectly blockaded ensemble. In this regime, the interaction shift for multiply-excited state is infinite and only one collective Rydberg state remains. In a second step, we will discuss corrections to this model to take into account finite van der Waals interactions. We will then present all the sources of damping for our Rydberg superatom. In the next part, we focus on the practical implementation of Rabi oscillations in our experimental platform. A

brief presentation of the excitation scheme, the detection and the experimental sequence are provided. One last important step is the characterization of decoherence. We will therefore discuss the optimization of the Rabi oscillations with respect to several parameters (number of atoms, control Rabi frequency...) to finish by pointing out the current limitations and discuss possible improvements.

7.1.1 Rabi oscillations of a single Rydberg superatom

In chapter 1, we derived the transmission spectrum of the atomic ensemble coupled to the cavity. Here, the cavity is far-off resonant from the ground-intermediate transition and can simply be omitted. We are left with a collection of three-level atoms in free space addressed by two lasers beams.

The Rabi Hamiltonian

We present here the derivation of the Rabi Hamiltonian. We start from the three-level Hamiltonian for one atom, as introduced in chapter 1 (equation 1.37):

$$\hat{H}/\hbar = -\delta_e \hat{\sigma}_{ee} - \delta_r \hat{\sigma}_{rr} + \frac{\Omega_1}{2} (\hat{\sigma}_{eg} + \hat{\sigma}_{ge}) + \frac{\Omega_2}{2} (\hat{\sigma}_{er} + \hat{\sigma}_{re}) \quad (7.1)$$

A first beam addresses the ground-excited transition line ($|g\rangle \rightarrow |e\rangle$) with a Rabi frequency Ω_1 and a detuning δ_e while a control beam drives the excited-Rydberg transition ($|e\rangle \rightarrow |r\rangle$) at a Rabi frequency Ω_2 and a two-photon detuning δ_r .

We wish to obtain an effective driving between the ground and the Rydberg state. The issue in a three-level driving comes from the population of the intermediate state. A simple way to decrease its population is to work with an important detuning on the intermediate state: $\delta_e \gg \delta_r, \Omega_1, \Omega_2$. Then, it is possible to perform an adiabatic elimination of the state $|e\rangle$:

$$i \frac{d\alpha_e}{dt} = -\delta_e \alpha_e + \frac{\Omega_1}{2} \alpha_g + \frac{\Omega_2}{2} \alpha_r = 0 \quad (7.2)$$

where $\alpha_k = \langle k|\psi\rangle$, $|\psi\rangle$ is the state of the system and the subscript k refers to one of the atomic states g, e or r . The population in the intermediate state is then very small compared to one and reaches very rapidly its steady state. After this elimination, the effective Hamiltonian is given by:

$$\hat{H}_{\text{Rabi}}/\hbar = \frac{|\Omega_1|^2}{4\delta_e} \hat{\sigma}_{gg} + \left(\frac{|\Omega_2|^2}{4\delta_e} - \delta_r \right) \hat{\sigma}_{rr} + \frac{\Omega_2 \Omega_1}{4\delta_e} (\hat{\sigma}_{er} + \hat{\sigma}_{re}) \quad (7.3)$$

In this far-detuned regime, the ground and Rydberg states are light-shifted by a factor $|\Omega_1|^2/(4\delta_e)$ and $|\Omega_2|^2/(4\delta_e)$ respectively, as illustrated in figure 7.1. On top of this, the effective two-photon Rabi frequency is given by $\Omega_R = \Omega_2 \Omega_1 / (2\delta_e)$.

In order to generalize this result to an ensemble of N atoms, we define a collective operator between the ground and the Rydberg state by following what we did in chapter 1 (equation 1.41):

$$\hat{S}^\dagger = \frac{1}{\Omega_R} \sum_n \Omega_n \hat{\sigma}_{rg}^{(n)} \quad (7.4)$$

where the subscript n refers to the n^{th} atom and $\Omega_R^2 = \sum_n \Omega_{R,n}^2$.

In chapter 1, we emphasized the detrimental role of the inhomogeneities of the control beam on the EIT spectrum. This is also true here for these two driving beams because light shift terms broaden the two-photon resonance. We will assume that inhomogeneities are

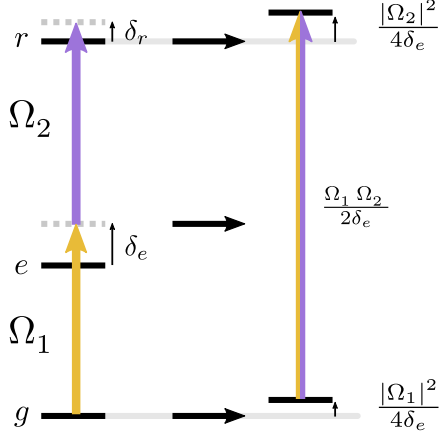


Figure 7.1: Two-photon driving. A three-level system made of a ground state g , an intermediate state e and a third state r is driven via two laser beams (Ω_1, Ω_2). The detuning from the intermediate state is δ_e and the one from the third state is δ_r . This system can be approximated by a single transition for a far-off resonant intermediate state ($\delta_e \gg \Omega_1, \Omega_2, \delta_r$). The driving is then $\Omega_R = \Omega_1 \Omega_2 / 2\delta_e$, the ground and excited states are also light-shifted as explained in the text.

negligible and that the lasers are resonant with the two-photon transition ($\delta_r = |\Omega_2|^2/(4\delta) - |\Omega_1|^2/(4\delta)$). Then, the Hamiltonian can be expressed as:

$$\hat{H}_{\text{Rabi}} = \frac{\Omega_R}{2} (\hat{S}^\dagger + \hat{S}) \quad (7.5)$$

where $\Omega_R = \sqrt{N} \frac{\Omega_2^R \Omega_1^R}{2\delta_e}$ and we assume that this frequency is a real number.

In the absence of interactions, if the number of Rydberg excitations is much smaller than the number of atoms, the collective operator \hat{S} verifies $[\hat{S}, \hat{S}^\dagger] \approx 1$: this simplified Hamiltonian is that of a driven harmonic oscillator, the equally spaced energy levels corresponding to “symmetric” Dicke states introduced in the first chapter. On the contrary, for an infinite interaction strength between Rydberg atoms, only the ground and first excited states remain. The operator \hat{S} is simply:

$$\hat{S}^\dagger = \frac{1}{\sqrt{N}} \sum_n |g_0, \dots, r_n, \dots, g_N\rangle \langle g_0, \dots, g_n, \dots, g_N| \quad (7.6)$$

where $|R\rangle = \hat{S}^\dagger |G\rangle$ is the first excited state and $|G\rangle$ is the collective ground state. Since we have $(\hat{S}^\dagger)^2 = 0$, we are unsurprisingly left with our two-level Rydberg superatom oscillating between the ground state and a delocalized Rydberg state at a Rabi frequency proportional to \sqrt{N} as observed by Dudin, Bariani and Kuzmich in 2012 [106].

Correction at finite blockade energy

In the previous derivation we did not discuss the effect of a finite interaction strength between Rydberg atoms. This is a much more difficult task: there are theoretical models and simulations to take these effects into account, as well as experimental studies, both in free space and in cavities [114, 167, 200, 223].

Naively, we expect that finite interactions will allow to off-resonantly drive the “asymmetric” Dicke states, that were defined in the first chapter. For strong enough interactions, the population in these states should be slowly growing and is expected to lightshift the “symmetric” Dicke state $|R\rangle$ (W state), corresponding to the state that we want to drive, and to

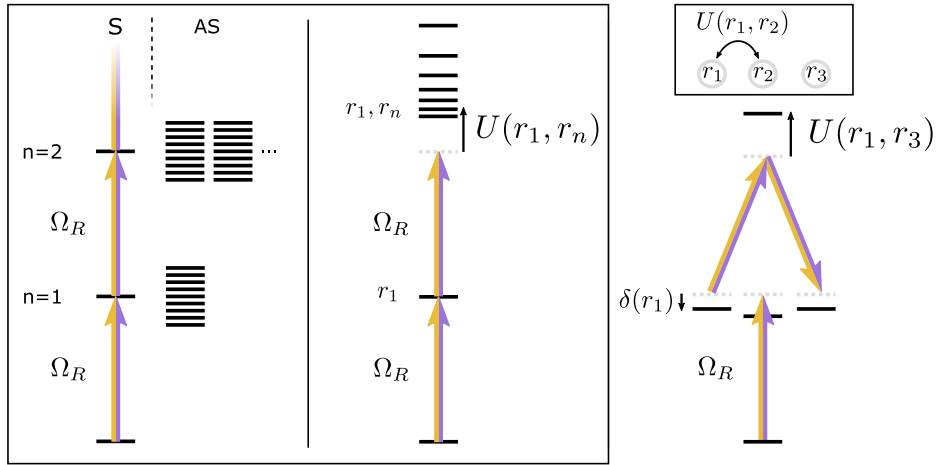


Figure 7.2: Basis for the interaction potential. Left- The “symmetric” Dicke states (S) are a natural choice for laser-driven atomic ensemble. The index n denotes the number of excited states and the “continuum” represents the “asymmetric” Dicke states (AS). Middle- The operator position is well-suited for the description of interactions. An excited state r_1 is driven on resonance while two-Rydberg states are shifted by the interactions. Right- Effective model when interactions are large $U \gg \Omega_R$. In this case, interactions can be seen as lightshift terms on first excited states $\delta(r)$ together with Raman transitions that hop the Rydberg excitation from one atom to the other.

induce decoherence via the coupling to the quasi-continuum of states formed by “asymmetric” Dicke states.

We will follow a simple approach that does not provide any exact derivation of the coherence time of the collective Rydberg state but gives a flavor of the involved processes [106]. Let us start by considering the complete Hamiltonian derived previously for a large intermediate state detuning \hat{H}_{Rabi} and complete it with van der Waals interactions:

$$\hat{H}_I = \hat{H}_{\text{Rabi}} + \sum_{n>m} U_{n,m} \sigma_{r,r}^{(n)} \sigma_{r,r}^{(m)} \quad (7.7)$$

We can perform a second adiabatic passage by assuming that this interaction term is large compared to all the others parameters. We will assume that the Rabi frequencies are homogeneous over the atomic ensemble and that our two beams are resonant with the two-photon transition in order to focus on interactions effects only. For a doubly-excited state $|r_n, r_m\rangle$, where we have a Rydberg state for atoms n and m , it leads to:

$$i\hbar \frac{d\alpha_{r_n, r_m}}{dt} = \frac{\Omega_R}{2} (\alpha_{r_n, r_m} + \alpha_{g_n, g_m}) + U_{n,m} (1 - \delta_{n,m}) \alpha_{r_n, r_m} = 0 \quad (7.8)$$

We will forget about higher excitations because the interaction term grows as s^2 for a state with s Rydberg excitations. If we inject back this expression and only keep the states with a single Rydberg excitation, we end up with the following Hamiltonian:

$$\hat{H}_I = \sum_n \frac{\Omega_R}{2} (|r_n\rangle \langle g_n| + |g_n\rangle \langle r_n|) + \delta_n^{int} |r_n\rangle \langle r_n| + \sum_{n>m} R_{n,m} (|r_n\rangle \langle r_m| + |r_m\rangle \langle r_n|) \quad (7.9)$$

where $\delta_n^{int} = \sum_{m \neq n} \Omega_R^2 / (4U_{n,m})$ and $R_{n,m} = \Omega_R^2 / (2U_{n,m})$.

When we make this correction, we obtain the transfer of the Rydberg excitation from one atom to the other via position-dependent Raman transitions. In this approximation, we have of course $R_{n,m} \ll \Omega_R$, for any n, m values. For an infinite number of atoms, this coupling

can be seen as a decay to a continuum of states. On the other hand, we have light shift terms with a strong dependence on the distance between the atoms. This is what makes this problem hard to solve: on one hand the basis that optimally respects the symmetry of the atom-light coupling is formed by the “symmetric” Dicke states, and depicted in the left panel of figure 7.2, while the natural basis for describing distance-dependent interactions pinpoints specific atomic positions, see middle schematic in figure 7.2. When the interaction strength is said infinite we are back in the symmetric subspace made of the ground state and the W state ($|G\rangle, |R\rangle$). This approach adds some corrections to this perfect blockade model in order to take into account pairs of Rydberg excitations. As a consequence, the symmetry of the first excited Dicke state is broken (shown in figure 7.2, right panel) and the interactions results in dephasing between localized Rydberg excitations. Note that this phenomenon vanishes for homogeneous interactions. This simple toy-model gives a scaling law for the interaction-induced damping:

$$\gamma_{\text{int}} \propto \frac{N\Omega_R^2}{U} = \frac{N^2(\Omega_1^R\Omega_2^R)^2}{4\delta_e^2 U} \quad (7.10)$$

Other sources of decoherence

We now present the other sources of decay associated to these collective Rabi oscillations.

The first one comes from the fluctuations of experimental parameters. For a given parameter set, several hundreds of measurements are required to accurately estimate the atomic population transfer due to Rabi oscillations. In this context, fluctuations will tend to blur the mean value of the population and it will thus reduce the quality factor of our Rabi oscillations, as illustrated in figure 7.3. The most sensitive and probably less stable parameter is the collective Rabi frequency $\Omega_R = \frac{\sqrt{N}\Omega_1\Omega_2}{2\Delta}$, with rms fluctuations σ_R . We can safely neglect the fluctuations of the detuning because our lasers are locked with a $\simeq 10$ kHz linewidth, very small compared to the 550 MHz detuning that we use. The intensity of the beam addressing the first transition line (Rabi frequency Ω_1) is locked with a rms noise of 2.5% while it is completely negligible for the control beam (Ω_2 , < 1% after a few minutes). We estimate the shot-to-shot fluctuations of the collective atoms-cavity coupling, directly proportional to \sqrt{N} , to $\sim 5\%$ for an atomic ensemble made of $\simeq 2000$ atoms. The dipole trap induces $\sim 1\%$ of Poisson fluctuations for a coupling with $N = 2000$ atoms, we are therefore limited by other effects.

When the number of realizations is large, the function describing the averaged Rabi oscillations p is given by:

$$\begin{aligned} p(t) &= \int_0^{+\infty} \frac{1}{2}(1 - \cos(\Omega t)) \frac{1}{\sqrt{2\pi}\sigma} e^{-\frac{-(\Omega-\Omega_R)^2}{2\sigma_R^2}} d\Omega \\ &= \frac{1}{2} - \frac{1}{2} \text{Re} \left\{ \int_{-\infty}^{+\infty} e^{i\Omega t} \frac{1}{\sqrt{2\pi}\sigma} e^{-\frac{-(\Omega-\Omega_R)^2}{2\sigma_R^2}} d\Omega \right\} \end{aligned} \quad (7.11)$$

where we can extend the integral because $\Omega_R \gg \sigma_R$. This is nothing else than the Fourier transform of a Gaussian and we get:

$$p(t) = \frac{1}{2} \left(1 - \cos(\Omega_0 t) e^{-\frac{-t^2}{2\sigma_F^2}} \right) \quad (7.12)$$

where $\sigma_F = 1/\sigma_R$. Fluctuations are thus equivalent to a Gaussian damping on our Rabi oscillations. This decoherence process is not directly related to the decoherence of the quantum system but rather on our ability to reproduce the same experiment throughout experimental

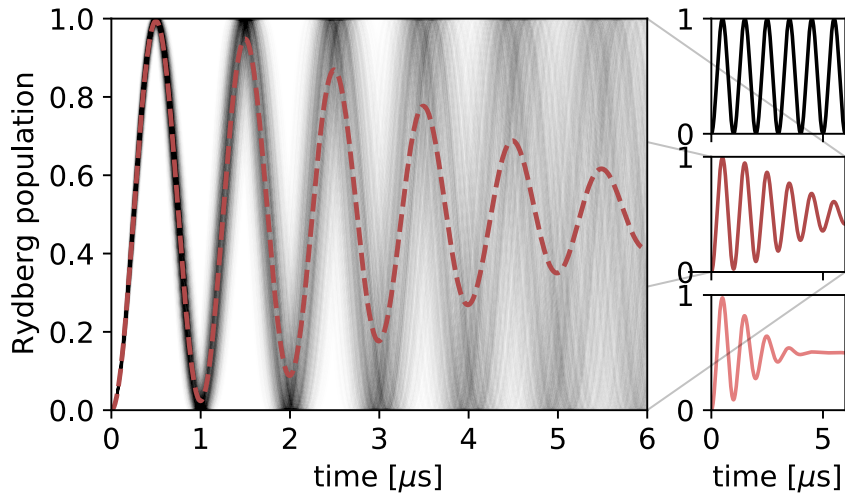


Figure 7.3: Fluctuations of the Rabi frequency. Left- Rabi oscillations with Gaussian fluctuations of the Rabi frequency and the means value (red dashed line) for a rms noise of 5%. Right- Oscillations after averaging for $\sigma = 1\%$ (top), 5% and 10% (bottom).

cycles. It is however a real issue for the control of the quantum state. The quality factor in this case is given by: $Q = \Omega_R \tau \simeq 30$, where $\tau = \sqrt{2}\sigma_F$. The second source of fluctuations originates from the phase of our lasers. This effect is quite important with laser diodes as pointed by Leseleuc *et al.* in their study of Rabi driving with a single atom [224]. In particular, the frequency lock used on our 780 nm DL pro (Ω_1^R) increases the noise in the MHz range, exactly in the frequency domain where we perform Rabi oscillations. We therefore filter our first Rabi beam (Ω_1^R) by sending it through the Transfer cavity ⁽¹⁾ with a ~ 100 kHz bandwidth before addressing the atomic ensemble. The cavity acts as a low-pass filter and reduces the extra-noise in the problematic high-frequency domain. The second beam comes from a TiSa laser much more stable than laser diodes. The beat note frequency ($\simeq 3$ kHz) between our two TiSa lasers (locked) makes the contribution of the control beam negligible.

The other main source of damping comes from the non-zero temperature of our atomic ensemble. The collective Rydberg state $|R(t)\rangle$ is a superposition of a single Rydberg excitation delocalized all over the atomic cloud. The atomic motion induces a position-dependent phase on each component of this state:

$$|g, \dots, r_n, \dots, g\rangle \rightarrow e^{i\phi_n} |g, \dots, r_n, \dots, g\rangle \quad (7.13)$$

where the phase is given by $\phi_n = \mathbf{k} \cdot \mathbf{v}_n t$, $\mathbf{k} = \mathbf{k}_1 + \mathbf{k}_2$ is the wave vector of the two-photon driving while the geometry of our excitation scheme imposes $\mathbf{k}_1 \cdot \mathbf{k}_2 \simeq 0$ and finally \mathbf{v}_n is the velocity of the n^{th} atom. The trap frequency is below the kilohertz range for atoms in the ground state, and the anti-trapping dynamics for a Rydberg atom is even smaller because of a larger detuning. As a result, the contribution from the dipole trap on the motion of an atom can be neglected. The squared overlap between the initial Rydberg collective state and the state after a time t is given by:

$$|\langle R(0)|R(t)\rangle|^2 = \left| \sqrt{\frac{m}{2\pi k_B T}} \int_{-\infty}^{+\infty} e^{ikvt} e^{\frac{-mv^2}{2k_B T}} dv \right|^2 \quad (7.14)$$

where k_B is the Boltzmann's constant, T is the temperature of the atomic ensemble and k is

⁽¹⁾See chapter 2, 2.2.2

the norm of the wave vector. Again, we recover the Fourier transform of a Gaussian function. We obtain a rms width $\sigma_T = 1/k\sqrt{m/(2k_B T)}$. At a temperature of 2 μK, the decoherence time at e^{-1} is $t_T \simeq 4.7 \text{ μs}$.

The last effect comes from the population in the intermediate state. In the derivation of the Rabi Hamiltonian we neglected its role but the steady-state population for one atom is $p_{\text{res}} = (\Omega_1^2 + \Omega_2^2/N)/(4\delta_e^2) \simeq \Omega_1^2/(4\delta_e^2) \ll 1$. For the Rabi driving of a single atom, this is also a major issue as the effective damping rate is then $\Gamma_{\text{eff}} = \Gamma_e p_{\text{res}(N=1)}$. In this case, a quantum jump from the intermediate state induces losses and the only way to reduce this effect is to make use of a large detuning. This is one of the main concerns when working on quantum simulations with Rydberg atomic arrays [224]. For the Rabi driving of an ensemble, it may seem worse as $n_e = Np_{\text{res}}$ atoms are in the excited state. However, after a typical time $1/\Gamma_e$, n_e atoms are lost and the overlap with the initial state is:

$$\left| \langle R^{(N)} | R^{(N-n_e)} \rangle \right|^2 = (N - n_e)/N = 1 - p_{\text{res}} \simeq 1 \quad (7.15)$$

This means that decoherence from the intermediate state for a single atom or a superatom atom are strictly equivalent. As a result, the overlap between the initial state and the after-jump state, for n_e atoms lost, remains close to one if $p_{\text{res}} \ll 1$. In this case, the damping rate induced by the intermediate state is Γ_{eff} rather than a naive $N\Gamma_{\text{eff}}$. In our experimental configuration we have $p_{\text{res}} = 0.01\%$ and we can safely neglect this effect compared to the temperature or the fluctuations.

7.1.2 Experimental implementation

We now discuss the practical implementation of two-photon Rabi oscillations with our platform. We already presented the detection setup in chapter 4 along with all the beams needed for the excitation and the detection. We describe here the excitation scheme used to perform Rabi oscillations on one hand and the detection of the Rydberg population on the other.

Probes, excitation scheme and experimental sequence

Two laser beams are dedicated to the Rabi driving. The first one is the D_2 probe at 780 nm with a 545 MHz detuning (δ_e) below $|5S_{1/2}, F = 1, m_F = +1\rangle \rightarrow |5P_{3/2}, F' = 2, m_{F'} = +2\rangle$. This circularly polarized light is therefore injected through the science cavity with a 3 G quantization axis and ~ 200 MHz detuned from resonance. We address the Rydberg state ($|R\rangle \equiv |n_2S, J = 1/2, m_J = +1/2, I = 3/2, m_I = +3/2\rangle$) with one of our TiSa lasers, blue-detuned by 550 MHz with respect to the $|e\rangle$ - $|r\rangle$ transition. Notice that the two-photon resonance is detuned by the light shift terms, hence the difference in detuning for the two driving beams. Both beams are switched on/off by two AOMs with a rising time inversely proportional to the beam size inside the crystal. The control beam is used at a high power (~ 1 W), it is thus not possible to focus it in the AOM as much as we do for the probe. As a consequence, the rising time is $\simeq 30$ ns for the D_2 probe and $\simeq 160$ ns for the control beam⁽²⁾ as illustrated in figure 7.4⁽³⁾. For the D_2 beam we have about 2 μW mode-matched with the science cavity resulting in a Rabi frequency $\Omega_1^R \simeq 2\pi \times 6$ MHz on the atomic ensemble. The Rabi frequency associated to the control beam depends on the Rydberg state: for $n_2 = 100$ we can go up to $\Omega_D \simeq 2\pi \times 15$ MHz.

We also need beams dedicated to the detection of the population in the Rydberg state $|R\rangle$. This is done with the D_1 probes that we use for transmission and reflection measurements, depending on the detection method. The probe in transmission is detected with a

⁽²⁾The response time of the build-up cavity is about 40 ns.

⁽³⁾The pulses are fitted with Gaussian error functions.

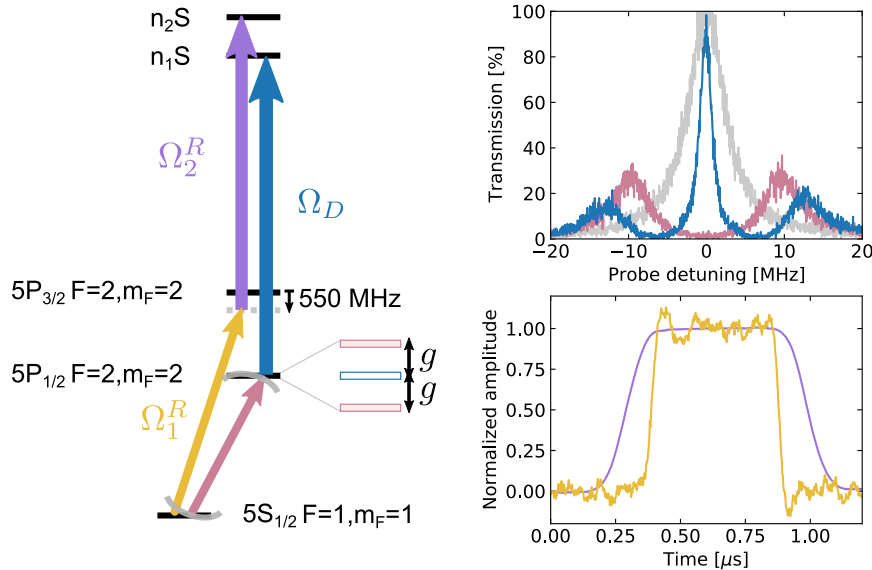


Figure 7.4: Control and detection lines. Left- Rubidium transitions and laser beams for Rabi driving and detection of Rydberg atoms. The detection is done via a D_1 probe (red arrow) resonant with the cavity and a Rubidium line. The collective atom-cavity coupling splits the spectrum in two symmetrical peaks detuned by $\pm g$ from the resonance while a control beam (blue, Ω_D) addresses a Rydberg state to induce a transparency window. This transparency is lost if a single Rydberg excitation is populated. The coherent control of the Rydberg excitation is done via two others beams. A D_1 probe (yellow, Ω_1^R) is sent 545 MHz below the intermediate state $|5P_{3/2}, F' = 2, m'_F = +2\rangle$ and detuned from the cavity resonance by $\simeq 200$ MHz. A second control beam (purple Ω_2^R) then addresses the Rydberg state. Top right- Electromagnetically induced transparency (blue) for $n_1 = 78$ with $\Omega_D \simeq 2\pi \times 14$ MHz. The collective vacuum Rabi splitting (red) is $g \simeq 2\pi \times 10$ MHz. Bottom right- Pulses synchronization for Rabi oscillations. The control beam (purple) has a 180 ns rising time while the rising time of the D_2 probe (yellow) is much shorter $\simeq 30$ ns.

SPCM (efficiency $\eta_{\text{SPCM}} = 47\%$) at the output of the cavity while the second probe is injected from the I/O coupler and its X quadrature is acquired with our homodyne detection (efficiency $\eta_{\text{HD}} = 75\%$). As mentioned in chapter 4, an AOM placed at the output of the I/O coupler allows us to switch from one detection to the other. Both probes are resonant with $|5S_{1/2}, F = 1, m_F = +1\rangle \rightarrow |5P_{1/2}, F' = 1, m_{F'} = +1\rangle$ and the science cavity. Notice that we did not lock the probe intensity because the characteristic response time of the lock is about 10 μs and we want to measure the Rydberg state as fast as possible compared to its lifetime, about a few tens of microseconds when we probe the system. The collective atom-cavity coupling is typically around $g = 2\pi \times 10$ MHz. On top of that, the second TiSa laser at 474 nm is used to open an EIT window on our atomic ensemble via a Rydberg state $|n_1\rangle = |n_1S, J = 1/2, m_J = +1/2\rangle$, as we discussed in chapter 5 and illustrated in figure 7.4. This beam comes from our second TiSa laser and it is injected in the other build-up cavity. The intensity of our D_1 probes and the Rabi frequency of the control laser beam are parameters of the detection and are optimized in the next section 7.2.2.

The sequence to prepare and detect a Rydberg excitation depends on the detection method. In both cases, the sequence starts by the preparation of the small atomic ensemble (~ 100 ms) as described in chapter 3. It is followed by a 100 μs optical pumping step to put all atoms in the ground state $|G\rangle = |5S_{1/2}, F = 1, m_F = +1\rangle$. For the phase-sensitive detection there is an additional step before the optical pumping to lock the relative phase between our LO and the probe in 400 μs⁽⁴⁾. We then send the two pulses (D_2 probe together with the TiSa

⁽⁴⁾The lock-and-hold phase lock and the pumping step are described in the chapter 4: 4.1.2 and (11)

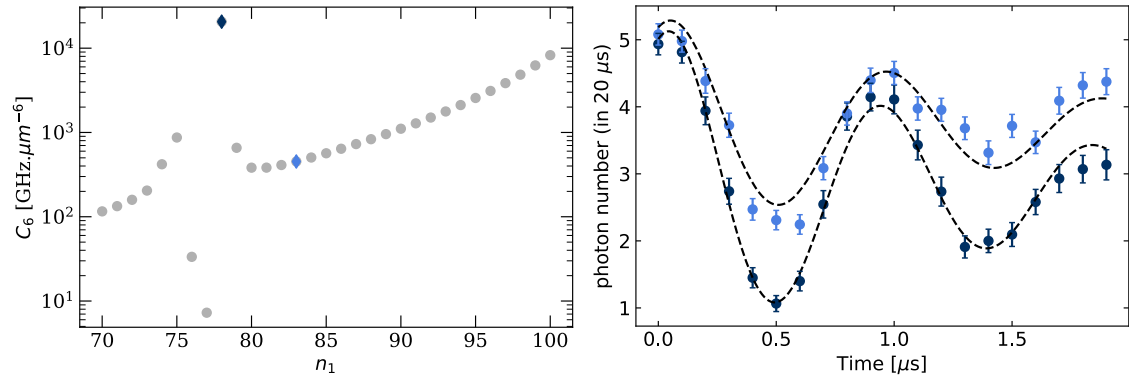


Figure 7.5: Increased visibility close to a Förster resonance. Left- C_6 coefficient absolute value between $n_2 = 109$ and $n_1 \in [70, 100]$. A resonance is visible for $n_1 = 78$. These data were perturbatively calculated with ARC [92]. Right- Rabi oscillations for $n_2 = 109$, a detection with $n_1 = 78$ (dark blue) and $n_1 = 83$ (light blue) all others things being equal (same Ω_2^R , $\sigma_{\text{cloud}} = 7 \mu\text{m}$). We observe a two-fold increase of the visibility due to a better Rydberg blockade between $n_1 = 78$ and $n_2 = 109$ close to a Förster resonance. This measurement was performed in transmission, see next section.

laser beam) to drive the superatom for a fixed period of time. Right afterwards, the D_1 probe and the control beam (Ω_D) are turned on during a few tens of microseconds to detect the state of our atomic cloud. Data are recorded by a DAI channel⁽⁵⁾ for SPCM measurements (typically with a $1 \mu\text{s}$ time bin) or a fast analog input channel (250 MHz acquisition rate) when we use the homodyne detection. The acquisition and control of the experiment were introduced in chapter 2, see section 2.3. This acquisition step plus the small repumping step are often repeated several times (about 10 loops) before restarting the whole experimental cycle. We are then free to scan a parameter between experimental cycles, for instance the duration of the Rabi pulses to observe oscillations through time.

Choice of the Rydberg pair

Let us now turn to the choice of Rydberg states as it is an important element for both our detection and the coherent control of the collective state. On one hand, we need a very-high interaction strength to drive the superatom between $|G\rangle$ and $|R\rangle$ and not the bath of multiply-excited states. On the other, we want to collect as many photons as possible in a given integration time as it should improve the fidelity of our detection⁽⁶⁾. The main issues related to the detection are the self-blockade of the probe and the transparency level which both depend on the control Rabi frequency ($\Omega_D \propto n_1^{*-3/2}$). Ideally, we would like to use a Low-Rydberg state for this purpose but the interaction with the other Rydberg state ($|R\rangle$, n_2) would decrease significantly and could compromise the blockade of the probe. In this context, it is interesting to work close to a Förster resonance to enhance the cross interaction between the two different Rydberg states. We investigated the magnitude of the cross interaction with the ARC calculator [92], left panel in figure 7.5. A 50-fold increase of the interaction strength (C_6 coefficient) is predicted for the pair $n_1 = 78$ and $n_2 = 109$ ⁽⁷⁾. In most of this chapter work, we will use this pair but with two distinct sizes for our atomic ensemble: $\sigma_c = 7 \mu\text{m}$ and $5 \mu\text{m}$ ⁽⁸⁾. In the first case, we observed an increase of the visibility of our Rabi oscillations on

⁽⁵⁾Digital time-binned edge-detection channel (DAI), see chapter 2, control setup

⁽⁶⁾This notion is defined later on in 7.2.1

⁽⁷⁾Notice that in practice, the van der Waals approximation is no longer valid but a complete diagonalization gives an interaction-induced frequency shift of $\sim 3.4 \text{ MHz}$ at the most likely distance $r = 2\sigma$ for the pair considered here.

⁽⁸⁾ $e^{-1/2}$ half-width.

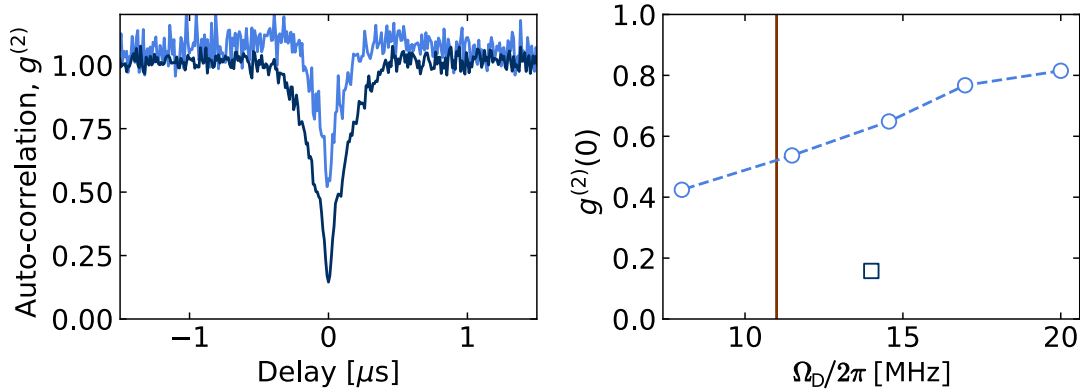


Figure 7.6: Second-order autocorrelation for $n_1 = 78$. Autocorrelation of the probe in transmission for $n_1 = 78$ and two cloud widths: $\sigma_c = 7 \mu\text{m}$ (light blue) and $5 \mu\text{m}$ (dark blue). Left-Autocorrelation versus time for the two configurations and a control frequency $\Omega_D \simeq 2\pi \times 14 \text{ MHz}$. The smaller cloud exhibits blockade at the single-photon level while the other can host a few excitations at the same time. Right- Autocorrelation at zero delay, for $\sigma_c = 5 \mu\text{m}$ (square) and $7 \mu\text{m}$ (circle) as a function of the Rabi frequency of the D_1 probe. The atom-cavity coupling is a good order of magnitude to reach for Ω_D in order to keep a high transparency ($> 75\%$ for $\Omega_D > g$).

the transmitted photon number ($\sim \times 2$) with respect to the pair $n_1 = 83$ and $n_2 = 109$ where no resonance is expected. This measurement is shown in figure 7.5, right plot, averaged over 110 shots. The autocorrelation of the probe was measured at $n_1 = 78$ with the two sizes, shown in figure 7.6. If we observe anti-bunching in both cases, the saturation at the single-photon level is not reached for $\sigma_c = 7 \mu\text{m}$ while it seems very close for $\sigma_c = 5 \mu\text{m}$. This volume reduction of our atomic ensemble is motivated by the increase of the blockade strength, for instance to reduce decoherence in our Rabi oscillations and also to improve another experiment⁽⁹⁾ in parallel to these measurements.

First observations

The optimization of our detection methods requires the control of the Rydberg superatom whereas the Rabi oscillations must be observed to affirm that we have obtained them. Overcoming this “chicken-and-egg” situation is possible by using long Rabi pulses ($\sim 10 \mu\text{s}$) with a high Rydberg state for both the detection and the control ($n_1, n_2 \simeq 100$). The main issue is to find the two-photon resonance because this resonance is light-shifted by the two driving beams. The frequency of the probe is scanned around the theoretical value and we use the transmission of the resonator for the detection. When the probe is resonant with the two-photon transition, we observe a decrease of the photon number collected by our SPCM due to a partial population of the Rydberg state that is at least visible on average, as shown in the left panel of figure 7.7 (averaged over 110 measurements). Once this first signal is obtained, we can adjust more precisely the frequency by looking at the point where the Rabi frequency is minimal as illustrated in the 2D plot on the right panel of this figure. Indeed, the Rabi oscillation for a two-level system, with a detuning δ , is given by:

$$P(t) = \frac{\Omega_R^2}{\Omega_R^2 + \delta^2} \sin\left(\sqrt{\Omega_R^2 + \delta^2} \frac{t}{2}\right)^2 \quad (7.16)$$

In figure 7.7, we both recover an increase of the Rabi frequency at a non-zero detuning but also a drop of the population in the Rydberg state out of resonance. This fine tuning is often

⁽⁹⁾We tried to observe a negative Wigner function for a ~ 1 photon pulse reflected on the cavity.

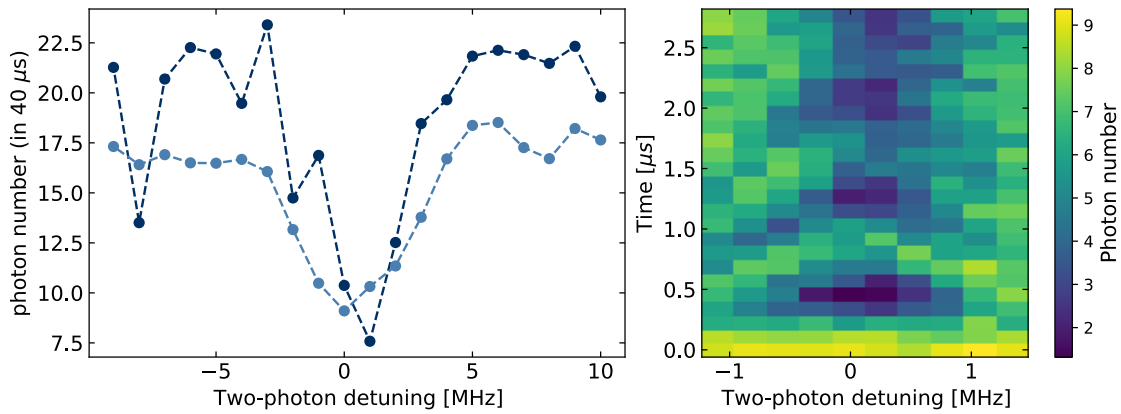


Figure 7.7: Two-photon spectroscopy. Spectroscopy to find the two-photon resonance for Rabi oscillations ($n_1 = 100, n_2 = 110$). It is first obtained by sending a long pulse ($\simeq 10 \mu\text{s}$) to partially populate the Rydberg state (dark blue). The transmission on the two-photon resonance is thus altered by the Rydberg excitation, resulting in a drop of the transmission. Notice that other resonances are present for a detuning of $\simeq -9 \text{ MHz}$ due to the coupling to the nearest Rydberg state ($|n_2S, I = 3/2, m_I = 3/2, J = 1/2, m_J = -1/2\rangle$) and $\simeq -3 \text{ MHz}$ due to residual atoms in the ground state $m_F = 0$. This measurement is repeated for a short pulse $\sim 250 \text{ ns}$ (light blue) to illustrate the difference of minimum with long Rabi pulses. Right- As a last check, a 2D scan is performed (pulse duration/detuning) to find the minimal value of the Rabi frequency.

necessary because, for long pulses and a positive detuning, the lasers can drive transitions towards multiply-excited states, which is visible on the plot.

7.1.3 Characterization of the collective driving

The coherence time is, as always with quantum systems [225–227], a crucial parameter in our experiment. This is especially true for experimental proposals based on the control of a collective Rydberg superatom [62, 170, 174]. We are now focusing on this parameter and this section compares our measurements to the sources of noise: a non-zero temperature, atom number fluctuations and an imperfect blockade.

The very peculiar feature of these Rabi oscillations is the collective increase of the Rabi frequency by the atom number. We will recover this important result in the last part of this section to demonstrate that we indeed drive the superatom.

Rydberg state

We discuss here the role of interactions in the damping of our superatom, equation 7.10. To this end, we characterized our Rabi oscillations for several principal quantum numbers for the superatom (n_2) to achieve a strong change in van der Waals interactions ($C_6 \propto n_2^{11}$). We first performed measurements with $n_2 = 101$ and then with $n_2 = 110$. This difference results in an increase by more than a factor of two in term of $n_2 - n_2$ van der Waals interactions:

$$\begin{aligned} C_6^{101S} &\simeq 65 \text{ THz } \mu\text{m}^6 \\ C_6^{110S} &\simeq 173 \text{ THz } \mu\text{m}^6 \end{aligned} \tag{7.17}$$

The Rabi oscillations were then detected via the transmission of the resonator with the $n_1 = 100$ Rydberg state. In this case, the C_6 coefficients for $n_1 - n_2$ interactions are:

$$\begin{aligned} C_6^{100S/101S} &\simeq 80 \text{ THz } \mu\text{m}^6 \\ C_6^{100S/110S} &\simeq 8 \text{ THz } \mu\text{m}^6 \end{aligned} \tag{7.18}$$

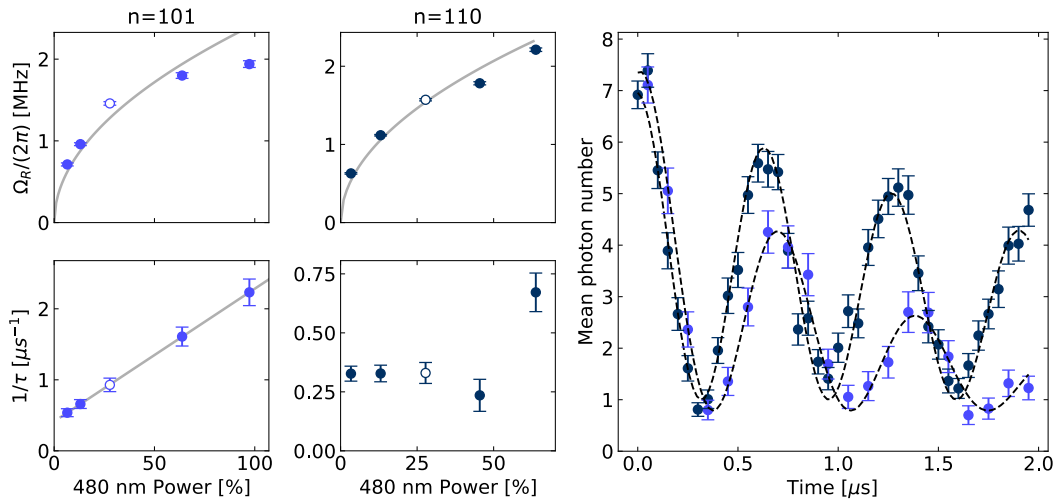


Figure 7.8: Imperfect blockade effects. Rabi oscillations versus 480 nm power for two Rydberg states $n_2 = 101, 110$. Left- Rabi frequency and damping rate as a function of this laser power for the 101 Rydberg state. The decoherence is limited by the interaction-induced dephasing characterized by the linearity between the damping and the power (fit: $aP + b$, where a, b are free parameters and P is the power). Middle- Same figures but for $n_2 = 110$. We observe a net improvement and the damping rate is not limited by interactions up to $\Omega_R = 2\pi \times 1.6$ MHz. Right- Rabi oscillations in the two configurations with almost the same Rabi frequency. The damping is clearly reduced by moving to a higher Rydberg state, with a fit function: $ae^{-t/\tau} \cos(\Omega t) + b$ where a, b, τ and Ω are free parameters.

Since these measurements were done with a $\sigma = 7 \mu\text{m}$ atomic ensemble⁽¹⁰⁾, the interaction between Rydberg atoms translates in a $h \times 1$ MHz shift for atoms separated by a distance of 2σ for the pair with the lowest interaction strength ($n_1 = 100, n_2 = 110$).

In order to compare the coherence time of our superatom for different Rydberg states, we recorded Rabi oscillations for several values of the control Rabi frequency. These measurements were first performed with $n_2 = 101$, $N \simeq 700$, $\Omega_1^R \simeq 2\pi \times 6$ MHz, a control Rabi frequency $\Omega_2^R \simeq 2\pi \times 15$ MHz, at maximum, and averaged over 110 detections. For the data set at $n_2 = 110$, the number of atoms marginally changed with $N \simeq 850$. On top of this, the maximum value of the control Rabi frequency is also slightly different with $\Omega_2^R \simeq 2\pi \times 16$ MHz.

Data are shown on figure 7.8. We recover the expected scaling law for the Rabi frequency with respect to the 480 nm beam power except for the drop-out of the highest Rabi frequency for $n_2 = 101$ that is probably caused by too weak interactions for the superatom relative to the increase of the effective linewidth of the transition given by $\Omega_R \propto \sqrt{\text{Power}}$. For the 101S Rydberg state, the decoherence rate is linear with the 480 nm beam power as we could expect for an interaction-dominated damping, equation 7.10. In this figure, data are fitted by an exponential decay rather than a Gaussian damping because the fit is more precise for the 101S Rydberg state but both methods provide a linear scaling for the damping rate.

When we turn to the second Rydberg state for the driving ($n_2 = 110$), we observe a decrease of this damping and more importantly this rate is almost flat up to $\Omega_R \simeq 2\pi \times 1.6$ MHz. In this range, interactions are not the main source of decoherence and the quality factor $Q = \Omega_R \tau$ is about 30 for the best configuration. After this threshold, the damping rate goes up and neglecting interactions is no longer possible. We illustrate this increase of coherence between the two Rydberg states dedicated to the driving (right plot) to highlight the significant gain obtained by simply increasing the interactions. Notice that the two oscillate almost at the same frequency. In the first case, light blue, the quality factor is $Q = 10$ while it is close to 30 when $n_2 = 110$.

⁽¹⁰⁾Gaussian half-width at $e^{-1/2}$: rms radius.

Scaling with the number of atoms

The signature of the collective nature of these Rabi oscillations is contained in the evolution of the Rabi frequency with respect to the number of atoms inside the blockade volume. As we emphasized in the theoretical derivation (equation 7.5) the collective Rabi frequency is expected to scale as \sqrt{N} with N the number of atoms in the blockade volume. In order to investigate this effect, we measured collective Rabi oscillations for several values of the atom number. The duration of the repumping beam in the optical pumping step⁽¹¹⁾ is changed in order to control the number of atoms in $5S_{1/2}, F = 1$. This parameter is then estimated via the collective vacuum Rabi splitting g proportional to \sqrt{N} . The data are plotted in figure 7.9, with the collective Rabi frequency (on the left), and the damping rate (on the right), as a function of the atom number. We clearly recover the expected scaling for the driving frequency, the data are indeed well fitted by a square root function. Some points in the graph are slightly above, this is probably due to a shift of the two-photon resonance (that increases the frequency) caused by electric field fluctuations⁽¹²⁾. Moreover, the damping rate seems to have a quadratic dependence with respect to the atom number as we expect in the interaction-dominated regime, equation 7.10. This is exactly what we observed with the Rabi oscillations as a function of the 480 nm power in figure 7.8, with a threshold at a frequency of $2\pi \times 1.5$ MHz.

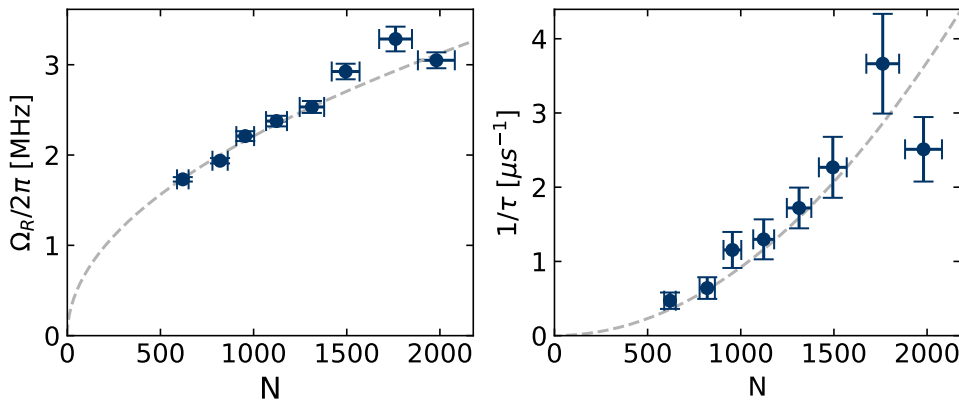


Figure 7.9: Collective Rabi oscillations vs. atom number. Left- Collective Rabi frequency (Ω_R) as a function of the atom number (N). A square root fit (grey dashed line) is plotted over the data (blue dots). Right- Damping rate ($1/\tau$) as a function of the atom number. Data are fitted by: aN^2 with a the only free parameter. The number of atoms is controlled via the pumping step and is estimated from the collective coupling parameter g . These measurements were obtained with $\Omega_2^R \simeq 14$ MHz, $n_1 = 100$ and $n_2 = 110$, a 7 μm atomic ensemble and averaged over 110 realizations.

Current limitations and possible improvements

The decoherence is dominated by two Gaussian damping processes through fluctuations of the atom number and temperature-induced dephasing but also by the van der Waals interactions with settings where the Rabi frequency exceed the interactions strength for a non-negligible part of the cloud. The first two give a coherence time⁽¹³⁾ of 4.5 μs and a driving frequency $\Omega_R \simeq 2\pi \times 1$ MHz if we assume 5% of fluctuations on the atom number and 4.7 μs for a temperature of 2 μK , respectively. The combination of both leads to an effective coherence time of $\simeq 3.2$ μs . We demonstrated that for $n_2 = 110$ and $\Omega_R \lesssim 2\pi \times 1.5$ MHz, the coherence

⁽¹¹⁾See chapter 4 for more details .

⁽¹²⁾At that time, we had trouble with the electric fields from the MOT coils but this is not a problem anymore.

⁽¹³⁾at e^{-1}

time is almost constant with a value around the expected 3 μ s. In this range, these observations indicate that we are mainly limited by the temperature and atom number fluctuations. The precise origin of the atom number fluctuations remains to be identified but the current stability already provides a quite good quality factor, around $Q = 30$, which allows us to prepare a Rydberg excitation with an efficiency of $e^{-(T_\pi/\tau)^2} = 99\%$.

Working with a smaller cloud, $\sigma_c = 5 \mu\text{m}$, could help to push back the limit in terms of Rabi frequency. We did not have time to explore this because of many issues with one of the TiSa lasers. We also increased the principal quantum number, especially with the ($n_2 = 120$)S Rydberg state, but we did not observe any improvement, certainly because of electric fields instabilities that we had at that time. This could be explored in more detail in the future. Reducing the temperature to 1 μK is possible but the gain is marginal if the fluctuations are kept at this magnitude (about $\sim 10\%$ increase for the quality factor). In order to reduce the fluctuations, dominated by the variations of the atom number, there is room for improvement. These fluctuations are certainly due to atomic transport, Raman cooling and pumping. It is perhaps possible to gain in stability in these steps, for instance by using a PID loop to stabilize the atom number via a measurement of the collective atoms-cavity coupling. A reduction by a factor of two together with a 1 μK temperature could lead to a 60% increase of the quality factor. However, lowering the temperature is only possible by reducing the trap depth or by using longer Raman steps, both of which could result in a decrease of the number of atoms. Currently, the $2\pi \times 10 \text{ MHz}$ coupling strength factor is close to the upper bound with a 5 μm atomic ensemble. Perhaps using a 6 μm ensemble is an interesting trade-off to lower the temperature while keeping a good blockade strength and enough coupling.

7.2 Detection of a Rydberg atom

This section is dedicated to the presentation of two methods for an efficient single-shot detection of a single Rydberg atom. Most of the time, the detection of Rydberg excitations is performed via ionization by counting ions or electrons [91]. Some alternative approaches have been studied: we can mention methods based on microwave measurements with high-Q cavity for the detection of Rydberg ensembles [228] or even down to the single excitation [229] but also via the recording of atomic losses in optical tweezers [224].

Electromagnetically induced transparency provides another non-destructive method to optically probe Rydberg excitations [99]. In the context of Rydberg blockade, the realization of an all-optical switch [42] or single-photon transistors [43, 44], in free space, indirectly demonstrated an efficient way to detect a single Rydberg excitation with fidelity of 72%. In our case and contrary to these pioneering experiments, we have a direct control of the superatom's state and our blockade in a cavity results in a 95% fidelity. In parallel to our work, colleagues from Vladan Vuletic's team [230] and Jian-Wei Pan's team [231] also performed similar experiments respectively in free-space and in a low-finesse cavity. Both of their methods rely on a change of transmission in the presence of a Rydberg excitation. In this section, we investigate a similar detection scheme with the cavity transmission as our colleagues did but on top of this, we perform an efficient phase-sensitive detection via the reflection of our science cavity. In this configuration, the superatom in a Rydberg state is enough to π -shift the reflection coefficient of the resonator. This leads to a state-dependent sign flip of the field quadratures that can be measured on our balanced homodyne detection.

Detection of a single atomic excitation in cavity is not new at all: several experiments performed such measurements with a single atom coupled to a high-finesse cavity [232, 233]. However, we draw attention to the fact that it is the first time that a single excitation is efficiently detected via a medium-finesse cavity, much easier to build than small-volume and high-finesses resonators. To our knowledge, it is also the first time that response of the phase is exploited to detect an atomic excitation and the first demonstration of a state-dependent π phase shift with a superatom strongly coupled to a cavity.

This detection step is crucial for the future of this experimental platform since several proposals require a measurement of the Rydberg superatom's state [62, 170, 174]. For instance, the deterministic generation of optical “Schrödinger kitten” states relies on our ability to measure the superatom's state in the final step of the experimental protocol. Errors in the detection would increase the loss budget for the reconstruction of the Wigner function and could prevent the observation of its negativity [157], one of the aims of this platform.

In this section, we start by defining what we mean by single-shot detection and how to characterize it. Then, we focus on the two complementary, in the quantum sense of the word, detection methods. In particular, for both approaches, we discuss the optimization and compare our observations to a simple model. We will conclude by discussing the current limitations and options toward future improvements.

7.2.1 Fidelity of a detector

The recent global pandemic has drawn public attention on the reliability of Covid19 tests [234, 235]. In such a detection of the disease, two kinds of errors matter. A false-positive error, in which case the tests outcome is positive while the patient is not carrying Covid19, and false-negative errors where the person is sick and the test is negative. This is exactly what we expect for a single-shot detector: each time a measurement is performed, the output is either positive or negative with residual false-negative and false-positive errors.

In our case, we will call false-positive the probability (e_0) to obtain the outcome “there is a Rydberg” while the atomic ensemble was in its ground state and a false-negative (e_r) the probability of the “no Rydberg” event for a superatom prepared in its Rydberg state. Moreover, the test output in our experiment is given by a digitized signal either from the homodyne detection or our SPCM. Therefore, we can note the output signal $x_k = x_1 k$ with k integer, x_1 being the vertical resolution. By convention, the detection outcome will be qualified as positive if k is below a given threshold k_t and negative otherwise. Finally, we will note the density distribution of this signal P_r when the superatom is in the Rydberg state and P_0 when the atomic ensemble is in its ground state. The threshold is then chosen to minimize the error in order to optimize the detector. For a given threshold, x_{k_t} , these two error probabilities are given by:

$$e_0(k_t) = \sum_{k \leq k_t} P_0(k), \text{ and } e_r(k_t) = \sum_{k > k_t} P_r(k) \quad (7.19)$$

Several definitions of the fidelity exist, for instance by considering the mean value [236], but the most conservative choice is to take the maximum of the two [237]:

$$\mathcal{F} = 1 - \max(e_0, e_1) \quad (7.20)$$

We see here the importance of controlling the state of our atomic cloud in order to obtain an estimation of the probability distribution with and without a Rydberg atom.

7.2.2 Transmission switch

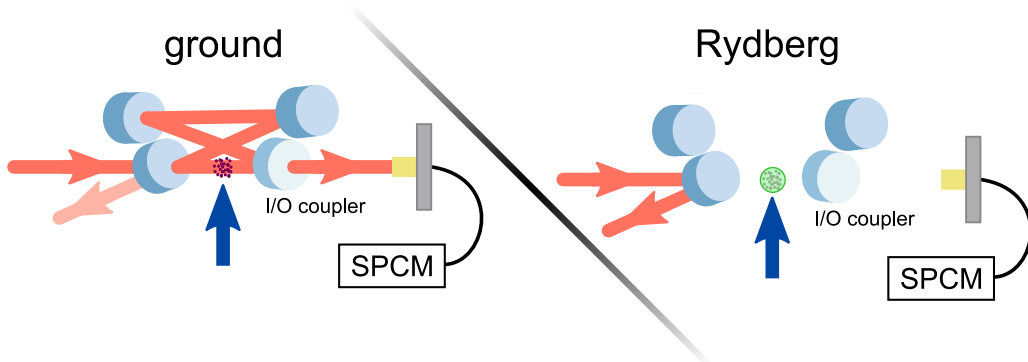


Figure 7.10: Transmission switch. In the blockade regime, the presence of a single Rydberg atom is able to stop the transmission of light through the resonator. We want to use this giant optical response to estimate the population in the Rydberg state. The light exits the cavity via the input/output coupler and is detected on a SPCM.

The first method we employed is based on the transparency drop of the cavity transmission in the presence of a highly excited Rydberg state. In this case, the state of the superatom acts like a switch for the photon stream, as it is shown in figure 7.10. This is the method we used for the characterization of the decoherence in the first part of this chapter. As a first example, the figure 7.11 shows a single-shot trace measured by the SPCM without (left plot) and with (right) a Rydberg atom stored in the atomic ensemble. In the second case, we clearly observe a transmission close to zero below 50 μ s that should allow to reach a high discrimination level between the two configurations. We discuss now the optimization of this detection method with respect to several parameters: the photon output rate detected with the SPCM, the integration time and the control Rabi frequency. This optimization is

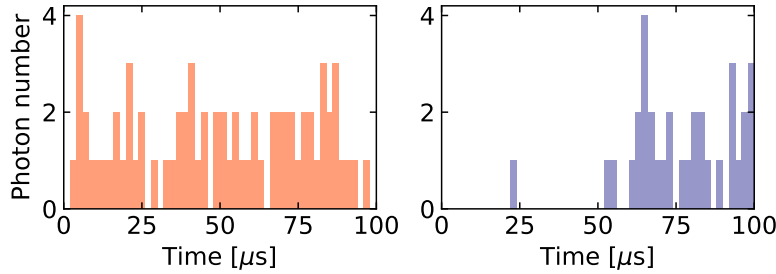


Figure 7.11: Single-shot measurements in transmission. The photon number in a $2\text{ }\mu\text{s}$ time bin measured with the SPCM as a function of time for the no-Rydberg case (left) and with a Rydberg excitation created at time zero (right). We observe a jump of the transmission on the right plot, indicating that the Rydberg is lost after $\simeq 50\text{ }\mu\text{s}$.

compared to a simple model taking into account the finite lifetime of the Rydberg atom. Finally, we present the best configuration and the associated detection fidelity.

Model

For the ground state situation, the distribution can be described by a Poisson distribution:

$$P_0(\phi_0 T, k) = (\phi_0 T)^k e^{-\phi_0 T} / k! \quad (7.21)$$

where k is the collected photon number, ϕ_0 is the SPCM photon flux (output) and T is the integration time. $\phi_0 T$ is thus the mean photon number detected by our SPCM.

This may seem odd as we showed in the first section that our probe features a sub-Poissonian statistic with an auto-correlation function below one at zero delay. The important point here is that this effect is visible on a $\leq 1\text{ }\mu\text{s}$ time scale while we will typically integrate the signal over $\sim 10\text{ }\mu\text{s}$, giving at least $\langle g^{(2)} \rangle \simeq 0.95$ after averaging over this duration.

On the other hand, the probability distribution for a Rydberg excitation in the atomic ensemble is given by

$$P_r(T, k) = e^{-T/\tau} P_0(T\phi_r, k) + \int_0^T \frac{e^{-t/\tau}}{\tau} P_0((T-t)\phi_0 + t\phi_r, k) dt \quad (7.22)$$

The first term is the probability distribution if we assume that a Rydberg atom is still present in our atomic ensemble after integration over a time T . This term is the product of the exponential decay due to the finite lifetime τ , times the Poisson probability to measure k photons after integration with a mean photon number $\phi_r T$. This distribution can thus take into account a residual flux ϕ_r to describe an imperfect blockade from the Rydberg atom. Even for a perfectly blockaded ensemble, there is still a small residual transmission given by $1/(1+2C)^2 \simeq 0.7\%$ for a coupling strength $g = 2\pi \times 10\text{ MHz}$. The second term encompasses the quantum jump of the Rydberg excitation at any time $0 < t < T$. For a jump at a time t , it is the product of the probability to lose the Rydberg excitation, times the probability to measure k photon after integration over T . The latter corresponds to the sum of two random variables that have a Poisson distribution of parameter $(T-t)\phi_0$ and $t\phi_r$. Therefore, this probability distribution also follows a Poisson law with a parameter $(T-t)\phi_0 + t\phi_r$.

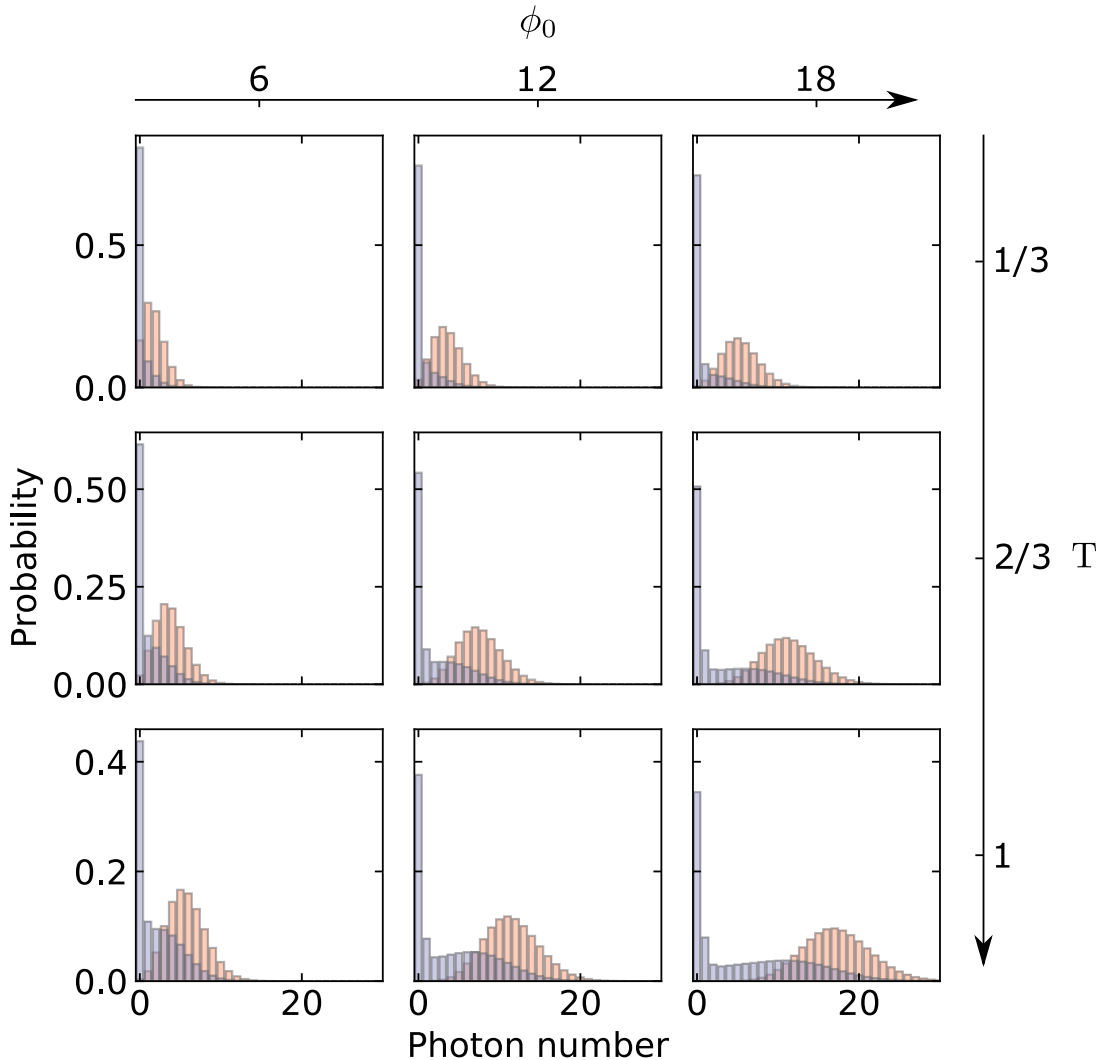


Figure 7.12: Simulated histograms vs integration time and output rate. Probability distributions with an integration time T at an output rate ϕ_0 (in unit of lifetime, $\tau = 1$). The no-Rydberg case (orange) is given by a Poisson distribution while the other distribution (purple) is a summation of Poisson distributions to take into account the Rydberg lifetime, see text.

Because we are dealing with a Poisson distribution, $P_0(\lambda, k) = \lambda^k e^{-\lambda} / k!$, we can simplify a bit the second term for $\delta_n = (\phi_0 - \phi_r)\tau > 1$. It leads to:

$$\begin{aligned} \int_0^T \frac{e^{-t/\tau}}{\tau k!} [(T-t)\phi_0 + t\phi_r]^k e^{-(T-t')\phi_0 - t\phi_r} dt = \\ \left(\frac{\delta_n}{\delta_n - 1} \right)^{k+1} \frac{e^{-T\phi_0/\delta_n}}{\delta_n k!} [\gamma_s(k+1, (1-1/\delta_n)T\phi_0) - \gamma_s(k+1, (1-1/\delta_n)T\phi_r)] \end{aligned} \quad (7.23)$$

where γ_s is the incomplete Gamma function defined as:

$$\gamma_s(k, x) = \int_0^x e^{-u} u^{k-1} du \quad (7.24)$$

such that in the limit $x \rightarrow +\infty$, one recovers the Gamma function $\gamma_s(k, +\infty) = \Gamma(k) = (k-1)!$, for k a positive integer.

In this model, we have three free parameters: the output photon rate detected on our

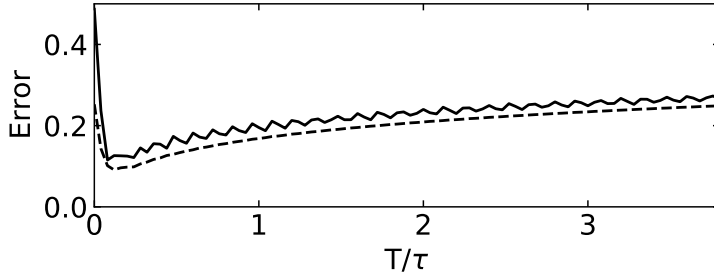


Figure 7.13: Mean and maximum error from our model. Errors as a function of the integration time for $\phi_0\tau = 18$. The mean error (dashed line) and the maximum of e_0, e_r are both minimal between $T/\tau = 0.1$ and 0.2 .

SPCM ϕ_0 , the integration time T and the residual transmission when a Rydberg atom is stored ϕ_r . The lifetime of the excitation is here considered as a constant. To illustrate this, the two histograms with or without a Rydberg atom are shown in figure 7.12 as a function of the input flux and the integration time. In that example, the residual leak rate is set to 1% of the output photon rate ϕ_0 close to what we expect to observe for a perfectly blockaded ensemble in the linear regime (transmission at $\simeq 90\%$). For a short integration time (compared to the Rydberg lifetime), the separation between the two distributions is $(\phi_0 - \phi_r)T$ while the width is given by $\sqrt{\phi_0 T}$ and $\sqrt{\phi_r T}$, respectively. As expected, this separation is all the more important as the output rate ϕ_0 is increased. However, the best acquisition duration is a trade-off between increasing the mean photon number for the no-Rydberg situation and the loss of the Rydberg excitation for the second distribution. In figure 7.12, the overlap between the two distributions grows monotonically for $T > \tau$. Of course, we cannot increase indefinitely the output rate because of the saturation of the transmission rate. It is possible to mitigate this phenomenon by reducing the principal quantum number in charge of the transparency window close to a Förster resonance to keep a strong cross interaction.

In what follows, we will only compute the detection error following our definition of the fidelity (equation 7.20) and we will focus on its optimization with respect to several parameters ($\phi_0, \phi_r, T, k_t, \dots$). The best configuration is then simply obtained by minimizing the error:

$$e_{\text{opt}} = \min_{p_1, \dots, p_M} [\max(e_0(p_1, \dots, p_M), e_r(p_1, \dots, p_M))] \quad (7.25)$$

where p_k is the k^{th} parameter among M . The error in a given configuration is thus $e = \max(e_0(p_1, \dots, p_M), e_r(p_1, \dots, p_M))$. However, it is convenient to reduce a little bit the size of the parameter space in order to obtain a simpler representation for the forthcoming optimization. Therefore, we will only show the error for the best threshold k_t with all other parameters fixed:

$$e_t(p_1, \dots, p_{M-1}) = \min_{k_t} [\max(e_0(p_1, \dots, p_{M-1}, k_t), e_r(p_1, \dots, p_{M-1}, k_t))] \quad (7.26)$$

Then, we only have to minimize it with respect to the parameter set. In order to illustrate this, the error is computed from the model as a function of the integration time in figure 7.13 with $\phi_0 = 18/\tau$. As a comparison, the mean error $(e_0 + e_r)/2$ is also plotted (dashed line). Most of the time, these two definitions are in fact very close as the best spot is often given by a configuration where $e_r \simeq e_0$. We recover that above $T = \tau$, the overlap of the detected photon distributions is growing, visible in the increase of the error.

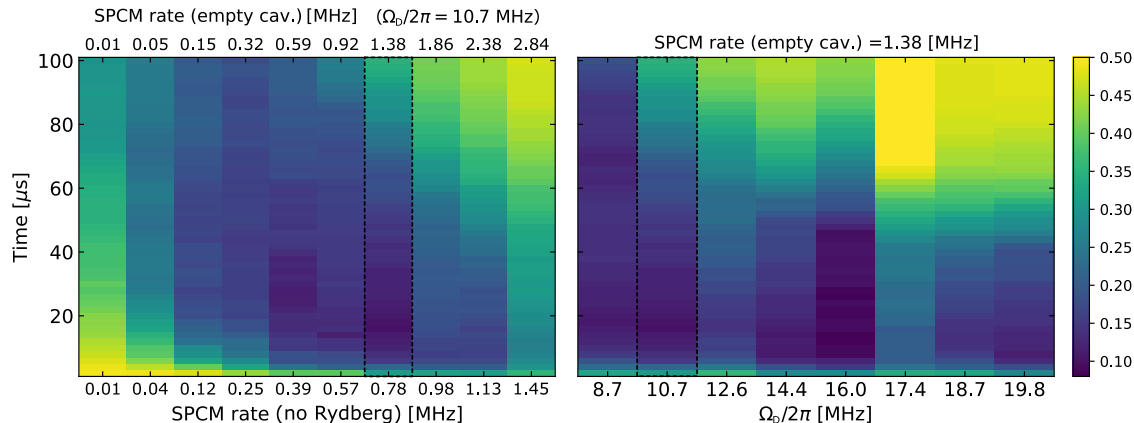


Figure 7.14: Error as a function of Ω_D , ϕ_0 , T . Left- One slice of the 3D optimization, the integration time versus the probe intensity at a constant control Rabi frequency $\Omega_D = 2\pi \times 10.7$ MHz. Right- Error as a function of the integration time and the control Rabi frequency.

Optimization

We now focus on the optimization of the real detection. The data presented here were measured with the pair $n_1 = 78$, $n_2 = 109$, a $7\text{ }\mu\text{m}$ atomic ensemble⁽¹⁴⁾ and a collective coupling close to $2\pi \times 10$ MHz. In particular, we measured the two distributions as a function of the integration time and the input photon rate with all other things equal. We also investigated the role of the control Rabi frequency (Ω_D) which has basically two effects on our detection. On one hand, increasing the control frequency improves the electromagnetically-induced transparency and thus enhances the output photon flux ϕ_0 . On the other hand, raising the control Rabi frequency decreases the Rydberg population in the polariton which can reduce the blockade efficiency (an increase of the residual flux ϕ_r). However, we do not expect to see a significant change in terms of blockade because the C_6 coefficient for this pair is close to the one for 100S-100S pair⁽¹⁵⁾ where we observed strong antibunching with similar parameters in chapter 5.

In figure 7.14, two cuts in the 3D optimization are shown after 210 measurements. On the left plot, the probe intensity and the integration time are scanned with a control Rabi frequency $\Omega_D = 2\pi \times 10.7$ MHz. The plot is given as a function of the SPCM rate for the superatom in the ground state and the SPCM rate for the empty cavity (no atoms at all). The output rate is a more natural parameter for the optimization of the detection but it is not linearly related to the input rate contrary to the output rate of the empty cavity. For instance, as the photon flux increases, the transparency is reduced from 90% to 50% for the data set shown on this plot. The color bar represents the detection error for the best photon number threshold, as previously discussed. The most striking difference with our first simulations is that the error seems to go up faster at high output photon rates. This suggests a dependence between the Rydberg lifetime and the photon flux.

The second plot shows the error as a function of the integration time and the control Rabi frequency. Again, we observe a change in the temporal response when we scan the control Rabi frequency. The transparency level goes from 50% up to 90% while the EIT linewidth increases by a factor of 3. The main effect is probably the modification of the transmission, equivalent to a change in the input rate, but a more careful analysis would be required. Anyway, we do not obtain a significant improvement by changing this parameter compared to the input photon rate. This also suggests that the blockade is already operating well for

⁽¹⁴⁾ $e^{-1/2}$ half-width.

⁽¹⁵⁾21 THz μm^6 for 78S-109S and 57 THz μm^6 for 100S-100S interactions

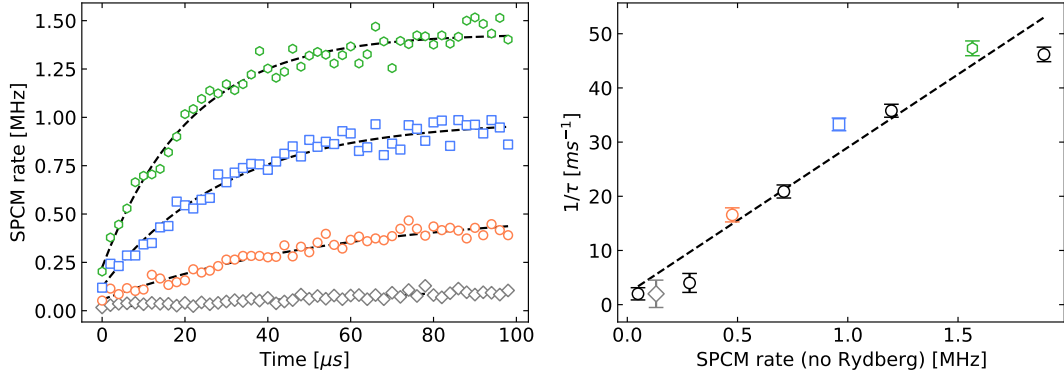


Figure 7.15: Rydberg lifetime vs SPCM rate. Left- SPCM rate in the presence of a Rydberg atom for several input intensities and a control frequency of $\Omega_D = 2\pi \times 14.4$ MHz. Data are fitted (dashed lines) by an exponential decay: $a(1 - b \exp(-t/\tau))$ where a, b, τ the three fitted parameters; a is the steady-state rate and τ is the Rydberg lifetime. The b parameter takes into account the initial transmission level ($\simeq 10\%$), it does not start at zero either because of an imperfect blockade or due to an imperfect Rydberg driving. Right- $1/\tau$ as a function of the SPCM rate without a Rydberg atom. The fit function (dashed line) is given by $aI + 1/\tau_0$ with a and τ_0 two free parameters while I is the probe intensity. We obtain a linear relation: $\phi_0\tau = 27 \pm 0.8$.

the detection. In this optimization we find an error close to 10 % for the best configuration comparable to the fidelity achieved by our colleagues in their studies [230, 231].

The lifetime as a function of the probe intensity is extracted from this data set to get more insight about the system. The data and fits are plotted in figure 7.15 for a control Rabi frequency $\Omega_D = 2\pi \times 14.4$ MHz close to the linear regime for the probe. We clearly observe a linear dependence between the output intensity and the loss rate giving $\phi_0\tau \simeq 30$, except perhaps for the three first points at very small input rates where the damping rate is almost flat. This linear scaling is observed for any control Rabi frequencies despite the change in the Rydberg interaction strength. This phenomenon may result from light-assisted collisions, that are difficult to estimate since we have several atoms within the Leroy radius. On top of that, we observe a non-zero transmission at zero delay, typically about 10%.

This residual transmission at zero delay, well above the 0.7% expected for a well-blockaded ensemble, can either be attributed to an imperfect blockade or to the preparation of a Rydberg excitation. The pulse duration is about 350 ns and the coherence time at e^{-1} is close to 3 μs. We can thus expect to have an efficiency close to $\eta_r \simeq 99\%$ for a Gaussian damping since we work here below the interaction-dominated regime. One way to confirm this is to look at the probability distributions with a short integration window ($T \ll \tau$). In this limit, the probability of losing the Rydberg atom is small and the distribution, when a Rydberg is present, is given by a Poisson distribution at the residual flux ϕ_r with a mean photon number around $T\phi_r$. If the state is not well prepared (efficiency η_r), the measured distribution is simply be the average between the case without Rydberg and the distribution in the presence of a Rydberg atom: $P_{\text{eff}} = \eta_r P_r + (1 - \eta_r)P_0$. In such case, we should observe a bump around the mean photon number $\phi_0 T$. This is shown in figure 7.16 for $T/\tau \simeq 0.2$ with the two measured distributions (with a Rydberg atom in purple and without in orange). Notice that the darkcount rate of our detector is ~ 300 Hz giving about 0.2% photon for this integration window, making its contribution completely negligible. In these plots no approximation is made and we directly use the full model. If we set $\eta_r = 90\%$, $\phi_r/\phi_0 = 1\%$ (red curve) we observe that the model gives a probability at bin 0 well above the measured distribution, below for $k > 0$ and almost equal near the mean photon number of the no-Rydberg distribution. On the contrary for $\eta_r = 100\%$, $\phi_r = 0.1\phi_0$ (blue curve), the probability from the model is close

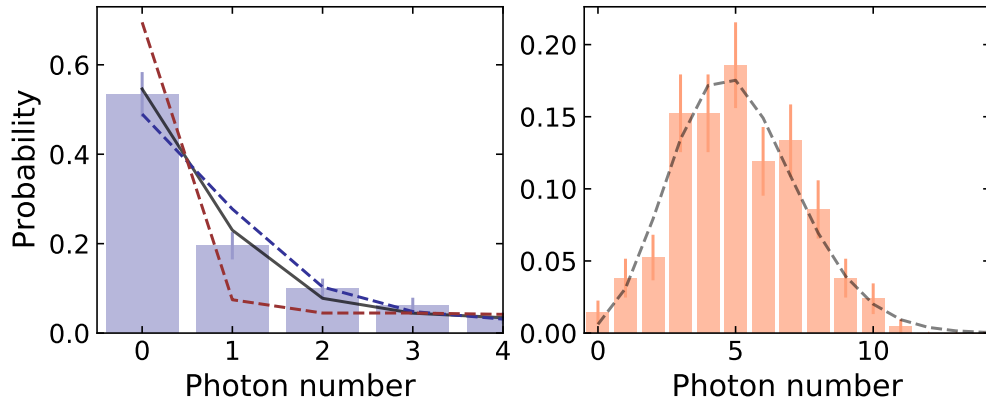


Figure 7.16: Fit of the probability distributions. Left- Estimated probability distribution with a Rydberg atom after a $8\ \mu\text{s}$ integration time (T), with a control frequency of $\Omega_D = 2\pi \times 14.4\ \text{MHz}$ and with a $\simeq 45\ \mu\text{s}$ lifetime. The data (purple) are fitted by the model described previously with the preparation efficiency η_r and the residual flux ϕ_r as free parameters (black curve). We find that the dominant effect comes from the residual flux $\phi_r/\phi_0 = 7 \pm 1\%$ ($\eta_r = 96 \pm 3\%$). The model assuming perfect blockade ($\phi_r/\phi_0 = 1\%$) and $\eta_r = 90\%$ is visible in red (dashed line) and the distribution with a perfect preparation ($\eta_r = 100\%$) and a residual rate $\phi_r/\phi_0 = 10\%$ is plotted in blue. The residual leak rate decreases significantly the population in 0 and inflates the neighbouring bins (around $T\phi_r$) while a preparation efficiency of 90% overestimates the first bin probability. Right- Probability distribution without Rydberg atom (orange). A Poisson distribution (dashed line) is adjusted with the mean photon number of the measured distribution.

to our experimental estimations for zero photon detected. It is significantly above for the following bins $k = 1$. A fit is also performed with ϕ_r and η_r the only two fitted parameters (black curve) and we find that the main contribution comes from the residual transmission with $\eta_r = 96 \pm 3\%$ while $\phi_r/\phi_0 = 7 \pm 1\%$ (transparency of 80%).

The optimization does not provide a unique point for the best configuration. For instance, changing the input flux directly impacts the lifetime of the excitation and leads to an additional constraint $\phi_0\tau \simeq 30$.

Single-shot fidelity

We have established that the best configuration is far from being unique when we scan the photon rate or the control Rabi frequency. In some regimes, the minimal error grows slowly when the integration time is extended, see for instance figure 7.13. In principle, one must take the preparation efficiency into account to compute the real error out of the estimated error: $\max(e_0, \eta_r e_r + (1 - \eta_r)e_0)$. If the output is $\eta_r e_r + (1 - \eta_r)e_0$, we are sure that $e_0 \leq \eta_r e_r + (1 - \eta_r)e_0 \leq e_r$, otherwise we correctly estimate the error. In the worst case scenario, we measure $s = \eta_r e_r + (1 - \eta_r)e_0$ with $e_0 \leq e_r$ then we can compute an upper bound: $e_r \leq s/\eta_r$ with our last data set, it yields $1/\eta_r \simeq 1.05$ and we can simply forget about this. Beside this, we use a single loop for the acquisition to avoid pollution from residual Rydberg excitations inside the cloud.

The best configuration yields a maximal error of $5.3 \pm 1.1\%$ and thus a fidelity of detection $\mathcal{F} = 94.7 \pm 1.1\%$. Both histograms are depicted in figure 7.17 with 400 realizations and the model is fitted with the preparation efficiency and the residual flux as free parameters giving $\eta_r = 100 \pm 5\%$ and $\phi_r/\phi_0 = 4.5 \pm 0.4\%$. Between the complete optimization presented previously and the measurement in this configuration, the size of the cloud was changed to $\sigma_c = 5\ \mu\text{m}$, in order to increase the blockade strength. In practice, it marginally reduced the residual flux but the damping rate of the Rydberg excitation is still linear with the photon

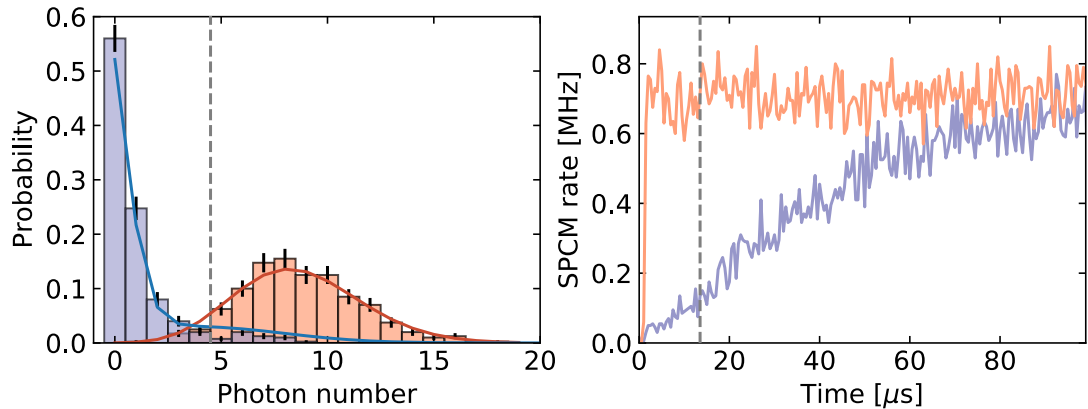


Figure 7.17: Single-shot fidelity in transmission. Left- The two histograms for the characterization of our detection, with a Rydberg atom in purple and without in orange. The configuration is the following: $T = 12 \mu\text{s}$, $\phi_0 = 0.71 \text{ MHz}$, $\tau = 42 \mu\text{s}$, $g = 2\pi \times 10.2 \text{ MHz}$, $\sigma_c = 5 \mu\text{m}$, $\Omega_D = 13.2 \text{ MHz}$ and the threshold (dashed line) is set to $n_t = 4$. The preparation efficiency is fitted to $100 \pm 5\%$ while the fitted residual leak rate is $\phi_r/\phi_0 = 4.5 \pm 0.4\%$. Right- Transmission versus time in the two configurations (same colors) with the integration time T (dashed line).

flux. Indeed, the photon flux is $\phi_0 \simeq 0.7 \text{ MHz}$ with a $\sim 42 \mu\text{s}$ lifetime giving $\phi_0\tau \simeq 29$ as previously observed with $\sigma_c = 7 \mu\text{m}$.

7.2.3 Detection via the reflected field

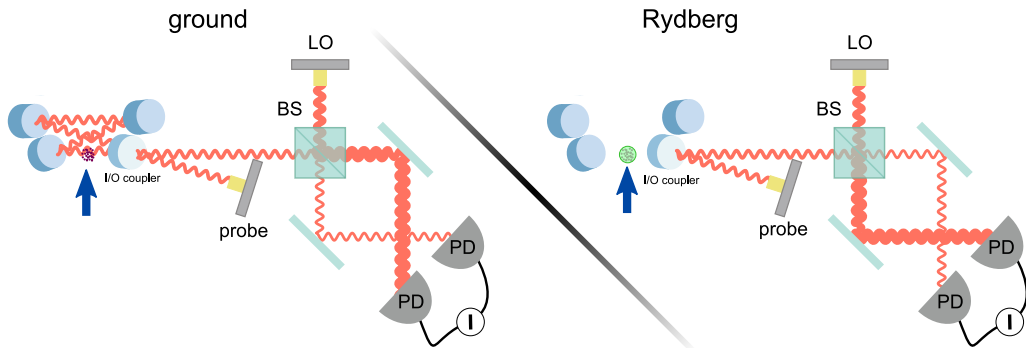


Figure 7.18: Detection via a π phase shift. Left- A probe beam (red) is injected from the I/O coupler of the science cavity. An EIT window is created via a control beam (Ω_D , blue arrow) such that the probe is propagating through the resonator. The relative phase with the Local Oscillator (LO) is adjusted to zero for a beam reflected off from a far off-resonant cavity (no intra-cavity field), see chapter 4. A homodyne detection is placed at the output of the cavity to measure the X quadrature, here negative. Right- The presence of a high Rydberg state in the atomic cloud prevents the propagation of light through the cavity. The probe is thus reflected off of the I/O mirror and the homodyne signal is consequently positive.

We now present a second approach to detect a Rydberg atom with our resonator. This method is based on the π phase shift of the reflection coefficient caused by a change of the superatom's state, as shown in figure 7.18. We described this mechanism in chapter 1, equation 1.54. This effect comes from the loss of transparency in our atomic ensemble induced by the interactions between Rydberg atoms.

In this part, we start by demonstrating a π phase shift induced by a single Rydberg excitation stored in our atomic ensemble. This new result of the Rydberg blockade mechanism leads to an efficient single-shot detection based on X-quadrature measurements. The characterization of the fidelity and the optimization of the detector are also discussed at the end of this subsection.

Observation of a conditional phase shift

As a first step towards a single-shot detection based on the sign-flip of the electromagnetic field, we performed measurements to demonstrate that a single Rydberg excitation is enough to obtain a π phase shift. This step is of first importance for photonic controlled phase gate proposals [170] or for the deterministic generation of optical “Schrödinger kitten” state. In both cases, the protocol is based on a π phase shift, of the electromagnetic field, induced by a change of the Rydberg superatom's state. Contrary to antibunching in transmission, this is the first time such a phase flip is observed with a superatom strongly coupled to a cavity.

The experimental sequence is equivalent to the single-shot detection in transmission. We calibrated the Rabi pulses to put our superatom in the Rydberg state ($T_\pi = 325$ ns). This measurement was done with $n_1 = 100$ and $n_2 = 101$. We then measured the mean value of \hat{X} and \hat{P} quadratures for a probe injected in reflection. This was done for the superatom in its ground state, without Rabi pulse, and in the Rydberg state after a π pulse. Data are shown in figure 7.19 in these two configurations and averaged over 420 measurements. The phase spectrum is depicted on the left while the quadratures are shown on the right. We clearly observe the expected shift on resonance when we drive the superatom to the Rydberg state (blue), with a phase $\phi_R = \pi(0.04 \pm 0.03)$ compared to the ground state situation (orange) with $\phi_G = \pi(0.91 \pm 0.04)$. For the superatom in the ground state, light sees the 100S Rydberg

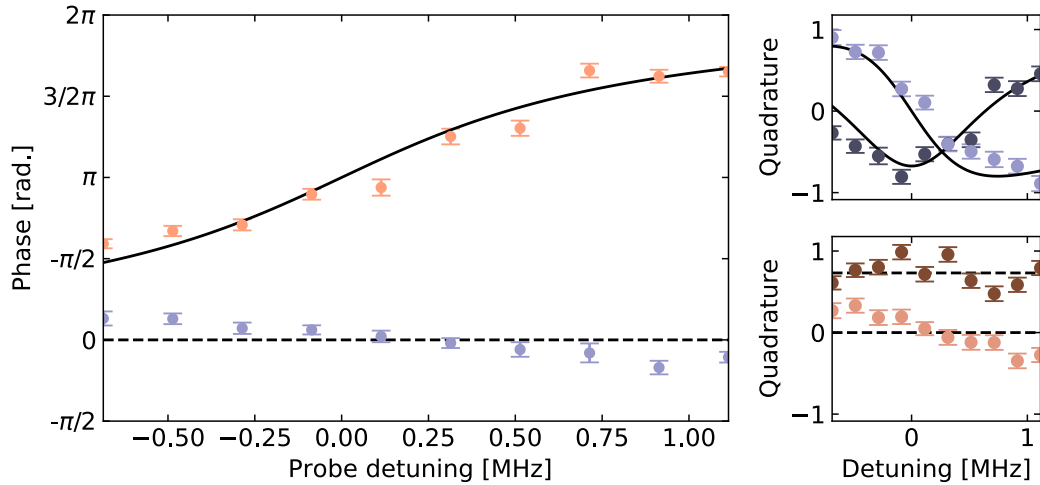


Figure 7.19: Rydberg-induced π phase shift. Left- Phase detected on the homodyne setup as a function of the probe detuning. For a superatom in its ground state, (orange dots) the phase spectrum is identical to an empty cavity with an effective width given by the EIT linewidth. When the superatom is in a Rydberg state (blue dots), the probe is reflected, the spectrum is flat and π -shifted on resonance compared to the ground state situation. Here, the phase spectrum is measured for $g = 2\pi \times 10.3$ MHz, $\Omega_D = 2\pi \times 12.3$ MHz, $\gamma_r \simeq 70$ kHz and the theoretical curve is indicated by the black solid line. Right- $\langle \hat{X} \rangle = \langle \hat{X}_0 \rangle$ (dark colors) and $\langle \hat{P} \rangle = \langle \hat{X}_{\pi/2} \rangle$ (light) quadratures for EIT in the linear regime (blue) and with one Rydberg excitation (red).

polariton resonance and the phases spectrum varies from 0 to 2π as the probe crosses this resonance. When the superatom is in the 101S Rydberg state, the resonance is shifted by the interactions. The phase spectrum is then flat as light is directly reflected off. This result is another smoking gun for the existence of strong interactions in our experimental platform as it demonstrates the implementation of a state-dependent optical π phase shift.

In figure 7.20, the separation between the signal with (right plot) and without (left) a Rydberg atom is visible at the single-shot level. This indicates that we should be able to obtain also an efficient single-shot detection with this approach and we now focus on the optimization of this new detection method.

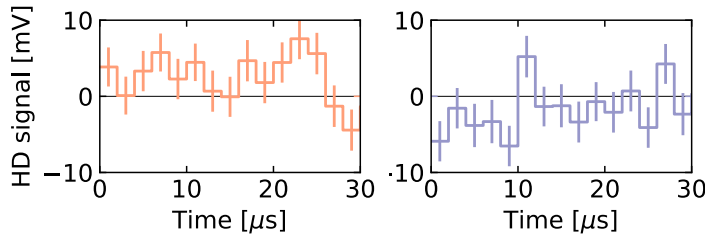


Figure 7.20: Single-shot HD signal. Single-shot homodyne signal for the X quadrature in the no-Rydberg case (left) and with a Rydberg excitation (right), for a 2 μ s time bin.

Model for the detection

Before going into the details of the optimization and discussing the fidelity, we need to adapt our transmission model with Gaussian distributions. We recall that the quadrature operator is given by:

$$\hat{X} = X_0 \int_0^T \hat{h}(t) dt \quad (7.27)$$

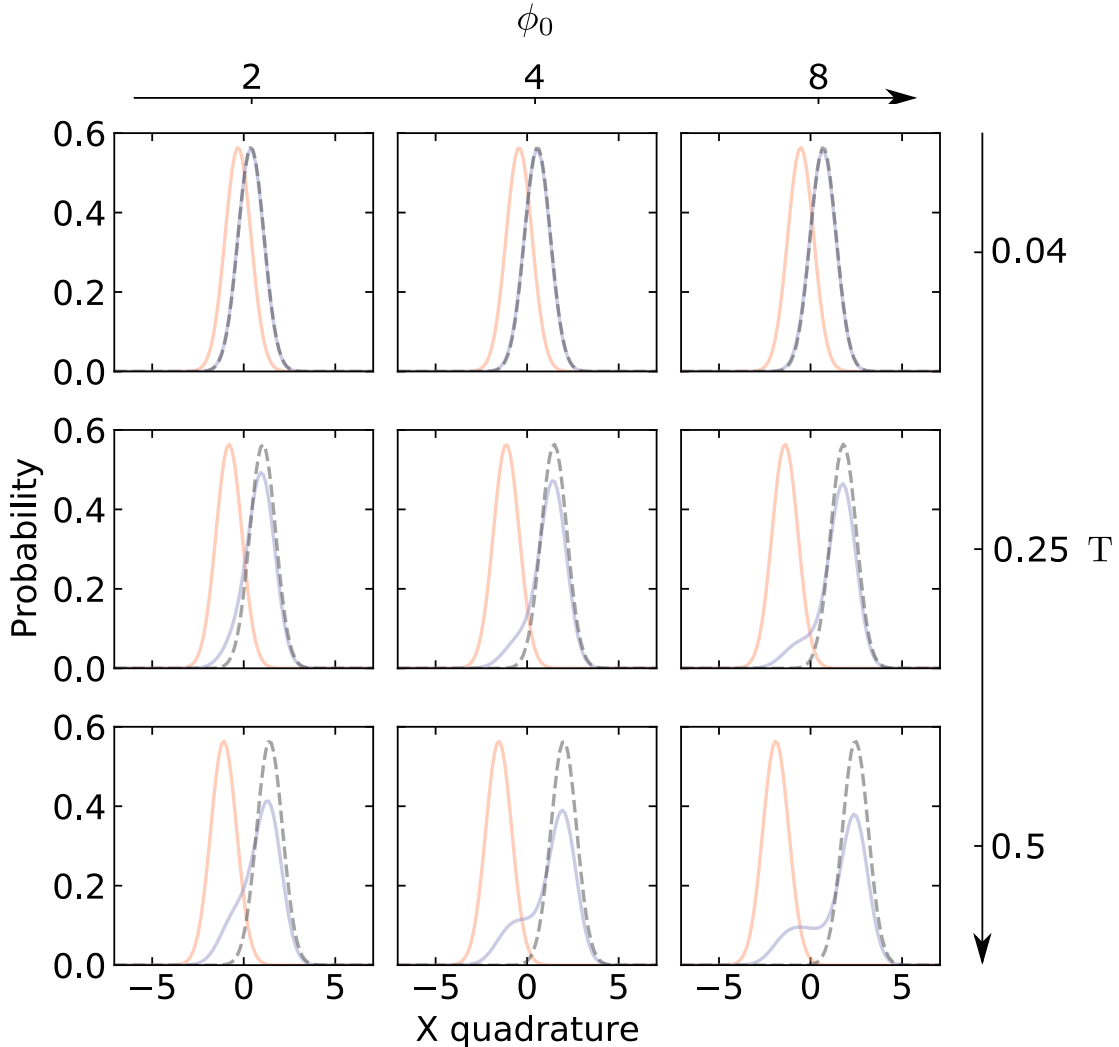


Figure 7.21: Simulated distributions vs integration time and output rate. Quadrature distributions after integration over a time T at an output rate ϕ_0 (in unit of lifetime, $\tau = 1$). The no-Rydberg case (orange) is given by a Gaussian distribution while the other case (purple) is a summation of Gaussian distributions to take into account the Rydberg lifetime, see text.

where \hat{h} is the homodyne signal, X_0 is a normalization factor to keep the rms width at a value of $\sigma_X = 1/\sqrt{2}$ for the vacuum state and we note $x_m = \langle \hat{X} \rangle$. For now on, the Gaussian distribution associated to the outcome x_k will be noted $G(x_m, x_k)$.

The probability distribution for the superatom in its ground state (G_0), after an integration time T and at an input flux ϕ_i , is centered on $-\sqrt{2\phi_i T R_{\text{EIT}}}$, where R_{EIT} is the reflectivity associated to EIT. On the contrary, if the superatom is excited to a Rydberg state, and if we assume that no jump has occurred during the acquisition window, the distribution is Gaussian and centered on $\sqrt{2T\phi_i R_{\text{Block}}}$ where R_{Block} is the reflectivity for a superatom in its Rydberg state. Otherwise, for a jump at a time $t < T$, the quadrature for this event is the sum of two Gaussian random variables: the first one with $\sigma_1 = \sqrt{t/(2T)}$ centered on $t\sqrt{2\phi_i/T R_{\text{Block}}}$ and the second one where $\sigma_2 = \sqrt{(T-t)/(2T)}$ with a mean value $-(T-t)\sqrt{2\phi_i/T R_{\text{EIT}}}$. As a result, the quadrature of the sum is also Gaussian and centered on $-(T-t)\sqrt{2\phi_i/T R_{\text{EIT}}} + t\sqrt{2\phi_i/T R_{\text{Block}}}$ with a rms width of $\sqrt{1/2}$. Finally, the complete distribution at x_k for the superatom in the Rydberg state is given by:

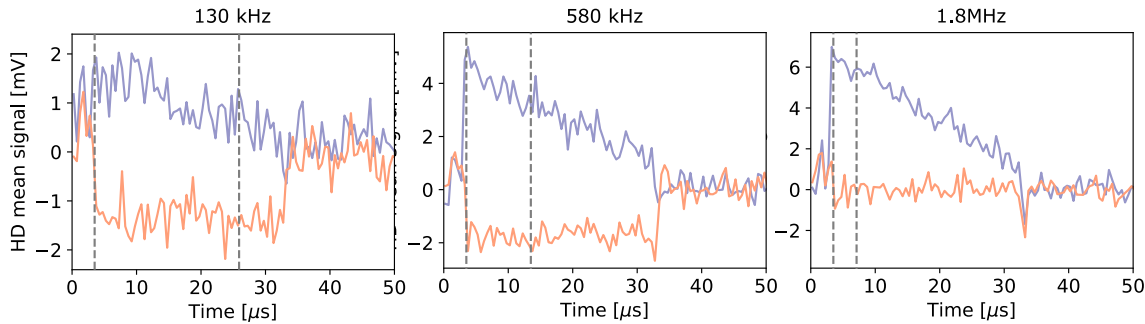


Figure 7.22: Mean homodyne signal. Signals of the homodyne detection with a Rydberg (purple) and without (orange) averaged over 400 realizations for three input fluxes. The grey dashed vertical lines mark the best integration time for each detection.

$$\begin{aligned} G_r(x_k) = & G(\sqrt{2T\phi_i R_{\text{Block}}}, x_k) e^{-T/\tau} \\ & + \int_0^T \frac{e^{-t/\tau}}{\tau} G_0(-(T-t)\sqrt{2\phi_i/TR_{\text{EIT}}} + t\sqrt{2\phi_i/TR_{\text{Block}}}, x_k) dt \end{aligned} \quad (7.28)$$

The ratio between the two reflectivities ($R_{\text{Block}} \simeq 75\%$ and $R_{\text{EIT}} \simeq 43\%$) is expected to be about 60% on resonance for $g = 2\pi \times 10 \text{ MHz}$, $\Omega_D = 2\pi \times 13 \text{ MHz}$ and $\gamma_r = 2\pi \times 100 \text{ kHz}$ assuming a perfectly blockaded ensemble and a preparation efficiency of $\eta_R = 100\%$.

We performed simulations of these two distributions following what we did for the transmission. Histograms are visible on figure 7.21 as a function of these two parameters. The ground-state situation is colored in orange while the distribution with a Rydberg excitation is in purple. As the integration time is increased, we observe a second bump on the “purple” histograms close to the no-Rydberg distribution. The damping of the Rydberg excitation thus increases the overlap between the distributions as expected. From this simulation, we expect to achieve a fidelity comparable to that of the first approach.

Optimization and fidelity

In the previous detection method, self-interaction effects of the 78S polaritons did not impact significantly the measured distributions. On the contrary, the reflection is rapidly modified by these effects and brings the ground superatom reflected field close to zero due to a partially randomized phase.

We optimized the detection for three input fluxes at 130 kHz, 580 kHz and 1.8 MHz to illustrate this effect, averaged over 400 shots. This data set was obtained with a 5 μm atomic ensemble, a collective coupling strength $g = 2\pi \times 10 \text{ MHz}$, $\Omega_D = 2\pi \times 13 \text{ MHz}$ and the Rydberg pair $n_1 = 78, n_2 = 109$.

These three values correspond to the linear regime, a probe close to the self-interaction limit and saturated, respectively. In figure 7.22, we show the mean HD signal as a function of time for these three configurations. In the first case, the lifetime of the Rydberg excitation is maximal but the probe is too weak to collect enough photons on the homodyne detection and the visibility is thus only $\sim 2 \text{ mV}$. At zero delay, the voltage ratio between the two configurations is about 80% giving a reflectivity ratio of $\simeq 60\%$. On contrary to transmission measurements, the lifetime is much shorter with about 50 μs even at this low input rate.

When we use a higher input rate, second plot on figure 7.22, the visibility is increased by a factor of 3. In this case, the voltage ratio is $\simeq 50\%$ giving a reflectivity ratio of 25% and

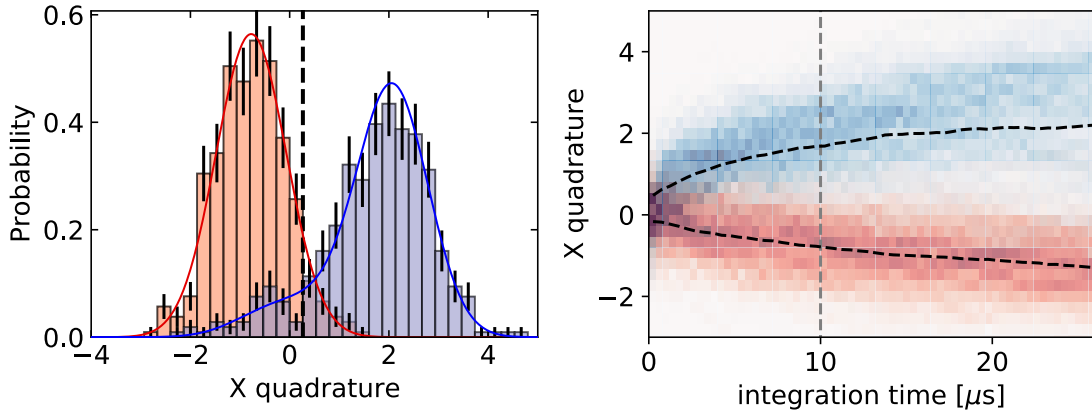


Figure 7.23: X quadratures histograms. Left- The best configuration for the detection with the no-Rydberg distribution (orange) and the one with a Rydberg atom (blue). They are both fitted by the model (solid lines), see text. Right- Evolution of the two distributions with the integration time, blue with a Rydberg and red without. Black dashed lines represent the mean value for both cases and the gray vertical dashed line gives the best integration time.

the lifetime is slightly reduced to 40 μs. For the highest input rate, the visibility is similar to the second plot ($\simeq 6$ mV) but the phase of light is randomized by self-interactions when the superatom is in its ground state and the lifetime falls to 21 μs. We give the integration window after optimization for the three input rates in dashed lines with a fidelity of 80% for the two extreme cases. The second situation (a 580 kHz photon rate) corresponds to the best configuration for this detection technique. In this case, we managed to reach a $89.9 \pm 1.5\%$ fidelity. The histogram and the evolution of the two distributions with the integration time are shown in figure 7.23. Data are fitted with two free parameters: the reflectivity with blockade $\mathcal{R}_R = 51 \pm 2\%$ and a preparation efficiency of $\eta_r = 99 \pm 2\%$. The latter is consistent with what we obtained in transmission and the coherence time of our Rabi oscillations.

Limitation and outlook for the detections

In the present case, the optimum configuration already provides an efficient detection method that benefits from a better single-photon detection efficiency than the transmission with photons collected by the SPCM. It is however possible to improve the transmission detection by removing the AOM switch where 75% of the light is deflected to the SPCM and by using a better counting module. For instance, superconducting nanowire single-photon detectors reach a $\geq 90\%$ efficiency, all in all resulting in a two-fold increase in terms of detected photons flux. Moreover, we have a relatively bad reflectivity on the cavity that can be increased by working with higher collective coupling factors g but the control Rabi frequency has to be risen as well in order to maintain, or even to enhance the transparency. This is surely an efficient way to improve the second detection method given that we currently have a 43% reflectivity for the superatom in the ground state. Perhaps the most efficient way to increase this transparency is to reduce the Rydberg linewidth. It can be done by turning off the dipole trap and going to lower temperatures close to 1 μK. The last option is to clean or replace the mirrors of our cavity to reduce the intrinsic losses of our resonator⁽¹⁶⁾.

⁽¹⁶⁾This was mentioned in chapter 2, more information about mirror losses are given there.

Conclusion

In this chapter we implemented a two-photon Rabi driving for our Rydberg superatom: the system oscillates between the ground state of our atomic ensemble and a single collective Rydberg excitation. We recovered the square root scaling law of the Rabi frequency with respect to the atom number, a clear signature of a collective effect. Besides this, we demonstrated our ability to obtain oscillations beyond the interaction-induced dephasing regime where the damping is dominated by the off-resonant coupling to doubly-excited states. The best quality factor for our Rabi oscillations is now close to 30 and could be further improved by increasing the Rydberg state, reducing the temperature of the atomic ensemble and the fluctuations of the atom number.

We then turned our attention to the detection of a single Rydberg superatom. As a first step, we demonstrated an efficient single-shot detection via the transmission of the resonator with a $94.7 \pm 1.1\%$ fidelity close to what our colleagues obtained in free space and in a low-finesse cavity [230, 231].

We presented a study of the reflection of our resonator. To begin with, we demonstrated an important result for this experimental platform: one Rydberg excitation is able to π phase shift a light beam injected from the I/O coupler of the cavity. This is the first time such a phase flip is observed with a superatom in cavity and it represents a promising tool for quantum information protocols. We then performed a second detection approach by taking advantage of this phase shift. In the best configuration, we managed to reach a $89.9 \pm 1.5\%$ fidelity.

The first detection method can be improved by using better photon counting modules (efficiency $\eta_{\text{det}} = 70\%$) and by removing the AOM for the detection switch ($\eta_{\text{AOM}} = 74\%$) but this is however not possible for experimental protocols mixing the two detection methods. The fidelity of the second approach could be increased by coupling more atoms to the cavity in order to rise the collective coupling factor g to obtain a better reflectivity (currently $\sim 70\%$), improving the EIT as well ($\sim 40\%$ reflection off of the cavity in EIT conditions) and cleaning the mirrors of our cavity.

As we mentioned in this chapter, this single-shot detection, the coherent control of our Rydberg superatom and the state-dependent π phase shift are important tools for the future experiments conducted with this platform, for the demonstration of an efficient controlled phase-gate or the deterministic generation of nonclassical states of light.

Conclusion

In this thesis we presented a new experimental platform that allowed us to reach strong interactions between photons in the optical domain. The chosen technique consists in injecting photons in a cavity strongly coupled to a small atomic cloud with interactions mediated by Rydberg excitations.

Overview

The first third of this manuscript (chapter 1 and 2) started by an introduction on the theoretical concepts related to this method, to highlight the experimental and technical constraints: strong collective coupling, high electromagnetically-induced transparency and strong Rydberg blockade. In this regard, we emphasized the crucial role of the Rydberg linewidth, but also the transmission of the input/output mirror, to achieve efficient interactions. We then described the new experimental platform, its assembly, and we justified our technical choices in light of the abovementioned constraints. In particular, this led us to opt for a medium-finesse cavity with an input/output mirror transmission of 0.9%, resulting in a cavity damping rate of $2\pi \times 2.9$ MHz (κ).

In a second part (chapter 3 to 5), we performed a characterization of the platform and implemented several atomic manipulation techniques for transport, cooling and trapping. These different steps finally allow us to obtain a small cold and dense atomic cloud inside our science cavity, characterized by a density of 4×10^{11} cm⁻³, a temperature of 2 µK and a 5 µm Gaussian radius. We obtained the collective strong coupling regime between this small atomic cloud and our optical cavity with a typical coupling strength of 10 MHz. We also achieved a high electromagnetically-induced transparency ($\simeq 90\%$) for a control Rabi frequency of 14 MHz, due to a limited broadening of the Rydberg linewidth, with a value of 80 kHz. Finally, we observed the saturation of the transmission rate and a strong photon antibunching with a zero-delay autocorrelation of 4%, thereby demonstrating the achievement of strong interactions between photons with our apparatus.

The last two chapters of this thesis focused on quantum optics experiments. In the first one, we used our experimental platform as a nonlinear quantum memory. We showed that this process can be seen as an efficient and on-demand single-photon source with a 37% efficiency and a high unicity with a zero-delay autocorrelation of 1.2%. In addition, we studied the quadratures of the output field and observed the truncation of a coherent state at one photon.

In the last chapter, we introduced the control and optical detection of our single Rydberg superatom. We used this coherent control to characterize our detection, establishing a high single-shot fidelity: 95% in transmission and 90% in reflection. In the latter case, the detection is based on a new kind of nonlinearity for a superatom in cavity: a change in the state of the superatom translates into a π phase shift of the electromagnetic field.

These experimental investigations conducted with our experimental platform support that the coupling of a small atomic ensemble with a cavity is a relevant approach to explore nonlinear quantum optics. In a couple of years, this hybrid platform allowed us to recover

some of the phenomena obtained with a single atom in cavity QED [179, 237, 238] or with the photon blockade of a free-space atomic ensemble [41, 42, 181]. These first results obtained with our platform, and presented in this manuscript, pave the way for more sophisticated experiments.

Outlook

Before discussing the prospects in terms of experiments, it is worth discussing the current limiting factors of our experimental platform:

- The first point concerns the stability of the experiment and its duty cycle. We currently have fluctuations on the atom number in our dipole trap, of the order of 5%, which limits the quality factor of our Rabi oscillations to 30. The second obstacle stems from the contamination by Rydberg pollutants [108] accumulated during the successive acquisitions within the same experimental cycle, that considerably reduces the duty cycle of our experiments. We are working on these two topics in order to limit these undesired effects.
- The second limiting factor is related to the effective Rydberg linewidth which, for example, sets the value of the transparency level. The broadening of this rate is dominated by the contributions of the Doppler effect and the differential lightshift of our dipole trap. Reducing the temperature by a factor of three should result in a narrowing of this linewidth to 50 kHz. In addition, turning the dipole trap off could further decrease this factor down to 20 kHz.
- The most critical parameter for our experimental platform is now the amount of losses in the cavity, with a reflectivity limited to 64%. These mirrors will probably be changed in the coming years to significantly improve the efficiency of future experiments.

Despite these concerns, the current platform already offers us the possibility to investigate new experimental protocols or to push further the experiments presented along this manuscript. This is for example the case for the nonlinear writing of an excitation discussed in chapter 6, by reducing the duration of the falling/rising edge of the control beam and understanding the exact role of Rydberg interactions in our platform for this protocol. This is also true for the off-resonance photon statistics in the continuum regime, discussed in chapter 5, through a more detailed study to isolate the dominant mechanism at stake in our observations of photon bunching.

There are many other short-term options: we can now investigate the entanglement between the Rydberg superatom and light or even directly between photons by mediating entanglement through the superatom [239]. Another approach consists in exploiting the control and detection tools to generate nonclassical states of light in a deterministic way, again via the entanglement between photons and the superatom [38]. One can also study many-body physics through the coupling of the cavity with several Rydberg superatoms to obtain long-range interactions between them, mediated by cavity photons [240]. In the mid-long term, it is also planned to use the different transverse modes of the cavity and their degeneracies to achieve multimode interactions directly inside the cavity [58].

Reflectivity of the science cavity

Cavity field with four mirrors

Our cavity is made of four mirrors, one input/output coupler with a transmission T and reflectivity R while each high-reflectivity mirror is characterized by a reflectivity R_{HR} . We do not assume here that $T + R = 1$ to take into account losses, $L = 1 - T - R$. The input field is E_i and the intra-cavity field after k round-trips is given by:

$$E_c^{(k)} = (R_{HR}^3 R)^{k/2} \sqrt{T} E_i e^{i\phi k} \quad (29)$$

The total intra-cavity field is then the sum of all these contributions:

$$E_c = \sum_k E_c^{(k)} = \frac{\sqrt{T} E_i}{1 - \sqrt{R_{HR}^3 R} e^{i\phi}} \quad (30)$$

The full width at half maximum, for the intensity of the field, is therefore:

$$\delta_f = \frac{\nu_{FSR}}{\pi} \frac{1 - \sqrt{R_{HR}^3 R}}{(R_{HR} R)^{1/4}} \quad (31)$$

where $\nu_{FSR} = c/\ell$ is the free spectral range and ℓ is the resonator length. Then, the finesse of the resonator is given by:

$$\mathcal{F} = \pi \frac{(R_{HR} R)^{1/4}}{1 - \sqrt{R_{HR}^3 R}} \quad (32)$$

The output field in reflection is the combination of the intra-cavity field transmitted through the input/output coupler plus the reflected field:

$$E_r = +\sqrt{R_{HR}^3 T} e^{i\phi} E_c - \sqrt{R} e^{i\phi} E_i = \frac{\sqrt{R_{HR}^3} e^{i\phi} (T + R) - \sqrt{R}}{1 - \sqrt{R_{HR}^3 R} e^{i\phi}} E_i \quad (33)$$

We now focus on the reflectivity on resonance, $e^{i\phi} = 1$ and introduce losses for our high-reflectivity mirrors $L_{HR} = 1 - R_{HR}$, where the residual transmission of these mirrors are considered here as losses. We further assume that the losses and transmission are small compared to 1, giving:

$$r_{cav} = \frac{E_r}{E_i} = \frac{\sqrt{(1 - L_{HR})^3 (1 - L)} - \sqrt{1 - T - L}}{1 - \sqrt{(1 - L_{HR})^3 (1 - L)}} \approx \frac{T - L_0}{T + L_0} \quad (34)$$

where $L_0 = 3L_{HR} + L$. This also results in a simple expression for the finesse and the damping rate:

$$\mathcal{F} \simeq \frac{2\pi}{T + L_0} \text{ and } K \simeq \nu_{FSR}(T + L_0) \quad (35)$$

We recover the expressions obtained with the derivation presented in chapter 1, equation 1.1.

Atoms in the resonator

One can take into account additional losses caused by the absorption of our atomic ensemble. The intra-cavity field after k round-trips is simply multiplied by a factor e^{-OD} . The reflectivity is then:

$$r_{cav} = \frac{E_r}{E_i} = \frac{\sqrt{(1 - L_{HR})^3 e^{-OD}}(1 - L) - \sqrt{1 - T - L}}{1 - \sqrt{(1 - L_{HR})^3}(1 - L)e^{-OD}} \quad (36)$$

when $OD \ll 1$, one recovers the previous approximation of the reflectivity but with corrected losses $L_1 = L_0 + OD$. In the limit where $OD \rightarrow +\infty$ one finds the reflectivity of the first mirror $|r_{cav}|^2 = R$.

Perturbative calculation of the second-order autocorrelation

This appendix provides the set of equations necessary for the numerical calculation presented in chapter 5, following the work of Grankin *et al.* [115]. The Hamiltonian for the atom-cavity system with a perfect Rydberg blockade was introduced in chapter 1 (equation 1.57):

$$H_{\text{EIT}} \simeq -\delta_a \hat{a}^\dagger \hat{a} - \delta_e \hat{P}^\dagger \hat{P} - \delta_r |R\rangle \langle R| + \frac{\Omega}{2} (|R\rangle \langle G| \hat{P} + |G\rangle \langle R| \hat{P}^\dagger) + g(\hat{P}^\dagger \hat{a} + \hat{P} \hat{a}^\dagger) + i\sqrt{2\kappa_0}\alpha(\hat{a}^\dagger - \hat{a}) \quad (37)$$

We also recall the linear steady-state equations for the operators \hat{a} , \hat{P} and \hat{S} :

$$\begin{aligned} \langle \hat{a} \rangle &= \frac{1}{\delta_a + i\kappa} \left(i\alpha\sqrt{2\kappa_0} + g\langle \hat{P} \rangle \right) \\ \langle \hat{P} \rangle &= \frac{1}{\delta_e + i\gamma} \left(g\langle \hat{a} \rangle + \frac{\Omega}{2}\langle \hat{S} \rangle \right) \\ \langle \hat{S} \rangle &= \frac{\Omega}{2(\delta_r + i\gamma_r)} \langle \hat{P} \rangle \end{aligned} \quad (38)$$

At the next order in the input flux, one finds the steady-state equations for the two-operator correlators at zero-delay:

$$\begin{aligned} \langle \hat{a}\hat{a} \rangle &= \frac{g}{\Delta_a} \langle \hat{a}\hat{P} \rangle + \frac{\alpha}{\Delta_a} \langle \hat{a} \rangle \\ \langle \hat{a}\hat{P} \rangle &= \frac{\Omega}{2(\Delta_a + \Delta_e)} \langle \hat{a}\hat{S} \rangle + \frac{g}{\Delta_a + \Delta_e} (\langle \hat{a}\hat{a} \rangle + \langle \hat{P}\hat{P} \rangle) + \frac{\alpha}{\Delta_a + \Delta_e} \langle \hat{P} \rangle \\ \langle \hat{a}\hat{S} \rangle &= \frac{\Omega}{2(\Delta_r + \Delta_e)} \langle \hat{a}\hat{P} \rangle + \frac{g}{\Delta_r + \Delta_e} \langle \hat{P}\hat{a} \rangle + \frac{\alpha}{\Delta_r + \Delta_e} \langle \hat{a} \rangle \\ \langle \hat{P}\hat{P} \rangle &= \frac{\Omega}{2\Delta_e} \langle \hat{P}\hat{S} \rangle + \frac{g}{\Delta_e} \langle \hat{a}\hat{P} \rangle \\ \langle \hat{P}\hat{S} \rangle &= \frac{\Omega}{2(\Delta_e + \Delta_r)} \langle \hat{P}\hat{P} \rangle + \frac{g}{\Delta_e + \Delta_r} \langle \hat{a}\hat{S} \rangle \end{aligned} \quad (39)$$

Finally, the two-operator correlators at a delay τ are obtained by propagation of the zero-delay equations:

$$\frac{d}{d\tau} \begin{pmatrix} \langle \hat{a}(t+\tau)\hat{a}(t) \rangle \\ \langle \hat{P}(t+\tau)\hat{a}(t) \rangle \\ \langle \hat{S}(t+\tau)\hat{a}(t) \rangle \end{pmatrix} = -i\alpha\langle \hat{a} \rangle \begin{pmatrix} 1 \\ 0 \\ 0 \end{pmatrix} - i \begin{pmatrix} -i\kappa - \delta_c & g & 0 \\ g & -i\gamma - \delta_e & \Omega/2 \\ 0 & \Omega/2 & -i\gamma_r - \delta \end{pmatrix} \begin{pmatrix} \langle \hat{a}(t+\tau)\hat{a}(t) \rangle \\ \langle \hat{P}(t+\tau)\hat{a}(t) \rangle \\ \langle \hat{S}(t+\tau)\hat{a}(t) \rangle \end{pmatrix} \quad (40)$$

Bibliography

- [1] M. Planck, “On the Theory of the Energy Distribution Law of the Normal Spectrum”, *Annalen der Physik* **4**, 553 (1900) (cit. on p. 1).
- [2] A. Einstein, “Concerning an heuristic point of view toward the emission and transformation of light”, *American Journal of Physics* **33**, 367 (1965) (cit. on p. 1).
- [3] N Bohr, “On the constitution of atoms and molecules”, *Niels Bohr Collected Works* **2**, 159–233 (1981) (cit. on p. 1).
- [4] M. H. Anderson, J. R. Ensher, M. R. Matthews, C. E. Wieman, and E. A. Cornell, “Observation of Bose-Einstein Condensation in a Dilute Atomic Vapor”, *Science* **269**, 198–201 (1995) (cit. on p. 1).
- [5] G. Binning, H. Rohrer, Ch. Gerber and E. Weibel, “Surface Studies by Scanning Tunneling Microscopy”, *Physical Review Letters* **49**, 57–61 (1982) (cit. on p. 1).
- [6] J. Bardeen and W. H. Brattain, “Transistor, a semiconductor triode”, *Physical Review* **74**, 230–231 (1948) (cit. on p. 1).
- [7] J. S. Bell, “on the Einstein Podolsky Rosen Paradox”, *Physics Physique Fizika* **1**, 195 (1964) (cit. on pp. 1, 123).
- [8] A. Aspect, P. Grangier, and G. Roger, “Experimental realization of Einstein-Podolsky-Rosen-Bohm Gedankenexperiment: A new violation of Bell’s inequalities”, *Physical Review Letters* **49**, 91–94 (1982) (cit. on pp. 1, 123).
- [9] A. Einstein, B. Podolsky, and N. Rosen, “Can quantum-mechanical description of physical reality be considered correct?”, *Foundations of Physics* **47**, 777–780 (1935) (cit. on p. 1).
- [10] R. Hydomako et al., “Antihydrogen detection in ALPHA”, *Hyperfine Interactions* **212**, 91–99 (2012) (cit. on p. 1).
- [11] L. V. Jørgensen, “The AEgIS antihydrogen gravity experiment”, *Hyperfine Interactions* **212**, 41–49 (2012) (cit. on p. 1).
- [12] P. Pérez et al., “The GBAR antimatter gravity experiment”, *Hyperfine Interactions* **233**, 21–27 (2015) (cit. on p. 1).
- [13] B. P. Abbott et al., “Observation of gravitational waves from a binary black hole merger”, *Physical Review Letters* **116**, 061102 (2016) (cit. on p. 1).
- [14] K. Beloy et al., “Frequency ratio measurements at 18-digit accuracy using an optical clock network”, *Nature* **591**, 564–569 (2021) (cit. on p. 1).
- [15] A. D. Ludlow, M. M. Boyd, J. Ye, E. Peik, and P. O. Schmidt, “Optical atomic clocks”, *Reviews of Modern Physics* **87**, 637–701 (2015) (cit. on p. 1).
- [16] V. Andreev, D. G. Ang, D. DeMille, J. M. Doyle, G. Gabrielse, J. Haefner, N. R. Hutzler, Z. Lasner, C. Meisenhelder, B. R. O’Leary, C. D. Panda, A. D. West, E. P. West, and X. Wu, “Improved limit on the electric dipole moment of the electron”, *Nature* **562**, 355–360 (2018) (cit. on p. 1).

- [17] M. S. Safronova, D. Budker, D. Demille, D. F. Kimball, A. Derevianko, and C. W. Clark, “Search for new physics with atoms and molecules”, *Reviews of Modern Physics* **90**, 25008 (2018) (cit. on p. 1).
- [18] R. Blatt and C. F. Roos, “Quantum simulations with trapped ions”, *Nature Physics* **8**, 277–284 (2012) (cit. on p. 2).
- [19] A. A. Houck, H. E. Türeci, and J. Koch, “On-chip quantum simulation with superconducting circuits”, *Nature Physics* **8**, 292–297 (2012) (cit. on p. 2).
- [20] I. M. Georgescu, S. Ashhab, and F. Nori, “Quantum simulation”, *Reviews of Modern Physics* **86**, 153–185 (2014) (cit. on p. 2).
- [21] K. Grover, “A fast quantum mechanical algorithm for database search”, *Proceedings of the twenty-eighth annual ACM symposium on Theory of computing*, 212–219 (1996) (cit. on p. 2).
- [22] P. W. Shor, “Polynomial-time algorithms for prime factorization and discrete logarithms on a quantum computer”, *SIAM Review* **41**, 303–332 (1999) (cit. on p. 2).
- [23] A. R. Calderbank and P. W. Shor, “Good quantum error-correcting codes exist”, *Physical Review A - Atomic, Molecular, and Optical Physics* **54**, 1098–1105 (1996) (cit. on p. 2).
- [24] M. I. Dyakonov, “When will we have a quantum computer?”, *Solid-State Electronics* **155**, 4–6 (2019) (cit. on p. 2).
- [25] J. Preskill, “Quantum computing in the NISQ era and beyond”, *Quantum* **2**, 79 (2018) (cit. on p. 2).
- [26] P. W. Shor and J. Preskill, “Simple proof of security of the BB84 quantum key distribution protocol”, *Physical Review Letters* **85**, 441–444 (2000) (cit. on p. 2).
- [27] W. K. Wootters and W. H. Zurek, “A single quantum cannot be cloned”, *Nature* **299**, 802–803 (1982) (cit. on p. 2).
- [28] S. Pirandola et al., “Advances in quantum cryptography”, *Advances in Optics and Photonics* **12**, 1012–1236 (2020) (cit. on p. 2).
- [29] H. J. Briegel, W. Dür, J. I. Cirac, and P. Zoller, “Quantum repeaters: The role of imperfect local operations in quantum communication”, *Physical Review Letters* **81**, 5932–5935 (1998) (cit. on p. 2).
- [30] N. Tomm, A. Javadi, N. O. Antoniadis, D. Najer, M. C. Löbl, A. R. Korsch, R. Schott, S. R. Valentin, A. D. Wieck, A. Ludwig, and R. J. Warburton, “A bright and fast source of coherent single photons”, *Nature Nanotechnology* **16**, 399–403 (2021) (cit. on pp. 3, 123).
- [31] D. V. Reddy, R. R. Nerem, S. W. Nam, R. P. Mirin, and V. B. Verma, “Superconducting nanowire single-photon detectors with 98% system detection efficiency at 1550 nm”, *Optica* **7**, 1649–1653 (2020) (cit. on p. 3).
- [32] J. L. O’Brien, G. J. Pryde, A. G. White, T. C. Ralph, and D. Branning, “Demonstration of an all-optical quantum controlled-NOT gate”, *Nature* **426**, 264–267 (2003) (cit. on p. 3).
- [33] C. Junge, D. O’Shea, J. Volz, and A. Rauschenbeutel, “Strong coupling between single atoms and nontransversal photons”, *Physical Review Letters* **110**, 213604 (2013) (cit. on p. 3).
- [34] T. Yoshie, A. Scherer, J. Hendrickson, G. Khitrova, H. M. Gibbs, G. Rupper, C. Ell, O. B. Shchekin, and D. G. Deppe, “Vacuum Rabi splitting with a single quantum dot in a photonic crystal nanocavity”, *Nature* **432**, 200–203 (2004) (cit. on p. 3).

- [35] A. Wallraff, D. I. Schuster, A. Blais, L. Frunzio, R. S. Huang, J. Majer, S. Kumar, S. M. Girvin, and R. J. Schoelkopf, “Strong coupling of a single photon to a superconducting qubit using circuit quantum electrodynamics”, *Nature* **431**, 162–167 (2004) (cit. on p. 3).
- [36] J. P. Reithmaier, G. Sek, A. Löffler, C. Hofmann, S. Kuhn, S. Reitzenstein, L. V. Keldysh, V. D. Kulakovskii, T. L. Reinecke, and A. Forchel, “Strong coupling in a single quantum dot-semiconductor microcavity system”, *Nature* **432**, 197–200 (2004) (cit. on p. 3).
- [37] E. Janitz, M. K. Bhaskar, and L. Childress, “Cavity quantum electrodynamics with color centers in diamond”, *Optica* **7**, 1232–1252 (2020) (cit. on p. 3).
- [38] B. Hacker, S. Welte, S. Daiss, A. Shaukat, S. Ritter, L. Li, and G. Rempe, “Deterministic creation of entangled atom–light Schrödinger-cat states”, *Nature Photonics* **13**, 110–115 (2019) (cit. on pp. 3, 35, 38, 83, 114, 142, 144, 174).
- [39] K.-J. Boller, A. Imamoglu and S. E. Harris, “Observation of Electromagnetically Induced Transparency”, *Open Physics* **66**, 2593–2596 (1991) (cit. on pp. 4, 20).
- [40] J. D. Pritchard, D. Maxwell, A. Gauguet, K. J. Weatherill, M. P. Jones, and C. S. Adams, “Cooperative atom-light interaction in a blockaded Rydberg ensemble”, *Physical Review Letters* **105**, 193603 (2010) (cit. on pp. 4, 25).
- [41] T. Peyronel, O. Firstenberg, Q. Y. Liang, S. Hofferberth, A. V. Gorshkov, T. Pohl, M. D. Lukin, and V. Vuletić, “Quantum nonlinear optics with single photons enabled by strongly interacting atoms”, *Nature* **488**, 57–60 (2012) (cit. on pp. 4, 25, 174).
- [42] S. Baur, D. Tiarks, G. Rempe, and S. Dürr, “Single-Photon Switch Based on Rydberg Blockade”, *Physical Review Letters* **112**, 073901 (2014) (cit. on pp. 4, 25, 158, 174).
- [43] D. Tiarks, S. Baur, K. Schneider, S. Dürr, and G. Rempe, “Single-photon transistor using a Förster resonance”, *Physical Review Letters* **113**, 053602 (2014) (cit. on pp. 4, 19, 158).
- [44] H. Gorniaczyk, C. Tresp, J. Schmidt, H. Fedder, and S. Hofferberth, “Single-photon transistor mediated by interstate Rydberg interactions”, *Physical Review Letters* **113**, 053601 (2014) (cit. on pp. 4, 25, 158).
- [45] O. Firstenberg, T. Peyronel, Q. Y. Liang, A. V. Gorshkov, M. D. Lukin, and V. Vuletić, “Attractive photons in a quantum nonlinear medium”, *Nature* **502**, 71–75 (2013) (cit. on pp. 4, 25, 112).
- [46] Q.-Y. Liang, A. V. Venkatramani, S. H. Cantu, T. L. Nicholson, M. J. Gullans, A. V. Gorshkov, J. D. Thompson, C. Chin, M. D. Lukin, and V. Vuletić, “Observation of three-photon bound States in a quantum nonlinear medium”, *Science* **359**, 783–786 (2018) (cit. on pp. 4, 25).
- [47] D. Tiarks, S. Schmidt, G. Rempe, and S. Dürr, “Optical π phase shift created with a single-photon pulse”, *Science Advances* **2**, e1600036 (2016) (cit. on pp. 4, 26).
- [48] M. Schlagmüller, T. C. Liebisch, F. Engel, K. S. Kleinbach, F. Böttcher, U. Hermann, K. M. Westphal, A. Gaj, R. Löw, S. Hofferberth, Pfau, and Tilman, “Ultracold Chemical Reactions of a Single Rydberg Atom in a Dense Gas”, *Physical Review X* **6**, 031020 (2016) (cit. on pp. 4, 26, 125).
- [49] O. Firstenberg, C. S. Adams, and S. Hofferberth, “Nonlinear quantum optics mediated by Rydberg interactions”, *Journal of Physics B: Atomic, Molecular and Optical Physics* **49**, 152003 (2016) (cit. on pp. 4, 26).

- [50] C. R. Murray and T. Pohl, “Quantum and Nonlinear Optics in Strongly Interacting Atomic Ensembles”, *Advances in Atomic, Molecular, and Optical Physics* **65**, 321–372 (2016) (cit. on p. 4).
- [51] M. Wallquist, K. Hammerer, P. Rabl, M. Lukin, and P. Zoller, “Hybrid quantum devices and quantum engineering”, *Physica Scripta* **T137**, 014001 (2009) (cit. on p. 4).
- [52] Z. L. Xiang, S. Ashhab, J. Q. You, and F. Nori, “Hybrid quantum circuits: Superconducting circuits interacting with other quantum systems”, *Reviews of Modern Physics* **85**, 623–653 (2013) (cit. on p. 4).
- [53] G. Kurizki, P. Bertet, Y. Kubo, K. Mølmer, D. Petrosyan, P. Rabl, and J. Schmiedmayer, “Quantum technologies with hybrid systems”, *Proceedings of the National Academy of Sciences of the United States of America* **112**, 3866–3873 (2015) (cit. on p. 4).
- [54] E. Bimbard, “Production and interaction of photons using atomic polaritons and Rydberg interactions”, PhD thesis (Institut d’Optique Graduate School, Université Paris Sud, 2015) (cit. on p. 4).
- [55] V. Parigi, E. Bimbard, J. Stanojevic, A. J. Hilliard, F. Nogrette, R. Tualle-Brouri, A. Ourjoumtsev, and P. Grangier, “Observation and measurement of interaction-induced dispersive optical nonlinearities in an ensemble of cold rydberg atoms”, *Physical Review Letters* **109**, 233602 (2012) (cit. on p. 4).
- [56] R. Boddeda, I. Usmani, E. Bimbard, A. Grankin, A. Ourjoumtsev, E. Brion, and P. Grangier, “Rydberg-induced optical nonlinearities from a cold atomic ensemble trapped inside a cavity”, *Journal of Physics B: Atomic, Molecular and Optical Physics* **49**, 084005 (2016) (cit. on p. 4).
- [57] N. Jia, N. Schine, A. Georgakopoulos, A. Ryou, L. W. Clark, A. Sommer, J. Simon, J. Ningyuan, N. Schine, A. Georgakopoulos, L. W. Clark, A. Sommer, and J. Simon, “A strongly interacting polaritonic quantum dot”, *Nature Physics* **14**, 550–554 (2018) (cit. on pp. 4, 29, 107, 111, 125, 142).
- [58] L. W. Clark, N. Schine, C. Baum, N. Jia, and J. Simon, “Observation of Laughlin states made of light”, *Nature* **582**, 41–45 (2020) (cit. on pp. 5, 12, 36, 40, 114, 174).
- [59] Q. Turchette, C. Hood, W. Lange, H. Mabuchi, and H. J. Kimble, “Measurement of Conditional Phase Shifts for Quantum Logic”, *Physical Review Letters* **75**, 4710–4713 (1995) (cit. on p. 8).
- [60] C. J. Hood, T. W. Lynn, H. Mabuchi, M. S. Chapman, J. Ye, and H. J. Kimble, “Real-time cavity QED with single atoms”, *Physical Review Letters* **80**, 4157–4160 (1998) (cit. on p. 8).
- [61] A. Ourjoumtsev, A. Kubanek, M. Koch, C. Sames, P. W. Pinkse, G. Rempe, and K. Murr, “Observation of squeezed light from one atom excited with two photons”, *Nature* **474**, 623–626 (2011) (cit. on p. 8).
- [62] B. Hacker, S. Welte, G. Rempe, and S. Ritter, “Letter”, *Nature* **536**, 193–196 (2016) (cit. on pp. 8, 142, 144, 154, 158).
- [63] M. Brune, F. Schmidt-Kaler, A. Maali, J. Dreyer, E. Hagley, J. M. Raimond, and S. Haroche, “Quantum rabi oscillation: A direct test of field quantization in a cavity”, *Physical Review Letters* **76**, 1800–1803 (1996) (cit. on pp. 8, 144).
- [64] P. Senellart and J. Bloch, “Nonlinear emission of microcavity polaritons in the low density regime”, *Physical Review Letters* **82**, 1233–1236 (1999) (cit. on p. 8).

- [65] N. V. Corzo, J. Raskop, A. Chandra, A. S. Sheremet, B. Gouraud, and J. Laurat, “Waveguide-coupled single collective excitation of atomic arrays”, *Nature* **566**, 359–362 (2019) (cit. on p. 8).
- [66] R. P. Emmanuele, M. Sich, O. Kyriienko, V. Shahnazaryan, F. Withers, A. Catanzaro, P. M. Walker, F. A. Benimetskiy, M. S. Skolnick, A. I. Tartakovskii, I. A. Shelykh, and D. N. Krizhanovskii, “Highly nonlinear trion-polaritons in a monolayer semiconductor”, *Nature Communications* **11**, 3589 (2020) (cit. on p. 8).
- [67] D. C. Dube, M. T. Lanagan, J. H. Kim, and S. J. Jang, “Dielectric measurements on substrate materials at microwave frequencies using a cavity perturbation technique”, *Journal of Applied Physics* **63**, 2466–2468 (1988) (cit. on p. 10).
- [68] J. M. Raimond, *Atoms and photons (Lecture)* (2019) (cit. on pp. 10, 105).
- [69] C. Cohen-Tannoudji, J. Dupont-Roc, and G. Grynberg, *Photons and Atoms - Introduction to Quantum Electrodynamics*, 1997 (cit. on p. 11).
- [70] A. J. Kollár, A. T. Papageorge, V. D. Vaidya, Y. Guo, J. Keeling, and B. L. Lev, “Supermode-density-wave-polariton condensation with a Bose-Einstein condensate in a multimode cavity”, *Nature Communications* **8**, 14386 (2017) (cit. on p. 12).
- [71] V. D. Vaidya, Y. Guo, R. M. Kroeze, K. E. Ballantine, A. J. Kollár, J. Keeling, and B. L. Lev, “Tunable-Range, Photon-Mediated Atomic Interactions in Multimode Cavity QED”, *Physical Review X* **8**, 011002 (2018) (cit. on p. 12).
- [72] C. W. Gardiner and M. J. Collett, “Input and output in damped quantum systems: Quantum stochastic differential equations and the master equation”, *Physical Review A* **31**, 3761–3774 (1985) (cit. on p. 12).
- [73] R. H. Dicke, “Coherence in spontaneous radiation processes”, *Physical Review* **93**, 99–110 (1954) (cit. on p. 13).
- [74] N. Skribanowitz, I. P. Herman, J. C. MacGillivray, and M. S. Feld, “Observation of dicke superradiance in optically pumped HF gas”, *Physical Review Letters* **30**, 309–312 (1973) (cit. on p. 13).
- [75] W. Dü, G. Vidal, and J. I. Cirac, “Three qubits can be entangled in two inequivalent ways W.”, *62*, 062314 (2000) (cit. on p. 14).
- [76] M. Eibl, N. Kiesel, M. Bourennane, C. Kurtsiefer, and H. Weinfurter, “Experimental Realization of a Three-Qubit Entangled W State Manfred”, *Physical Review Letters* **92**, 077901 (2004) (cit. on p. 14).
- [77] T. Elsässer, B. Nagorny, and A. Hemmerich, “Optical bistability and collective behavior of atoms trapped in a high-Q ring cavity”, *Physical Review A - Atomic, Molecular, and Optical Physics* **69**, 033403 (2004) (cit. on p. 14).
- [78] A. Dombi, A. Vukics, and P. Domokos, “Optical bistability in strong-coupling cavity QED with a few atoms”, *Journal of Physics B: Atomic, Molecular and Optical Physics* **46**, 224010 (2013) (cit. on p. 14).
- [79] K. M. M. Saffman, T. G. Walker, “Quantum information with Rydberg atoms”, *Reviews of Modern Physics* **82**, 2313–2363 (2010) (cit. on p. 16).
- [80] H. Labuhn, D. Barredo, S. Ravets, S. De Léséleuc, T. Macrì, T. Lahaye, and A. Browaeys, “Tunable two-dimensional arrays of single Rydberg atoms for realizing quantum Ising models”, *Nature* **534**, 667–670 (2016) (cit. on p. 16).
- [81] S. Ebadi, T. T. Wang, H. Levine, A. Keesling, G. Semeghini, A. Omran, D. Bluvstein, R. Samajdar, H. Pichler, W. W. Ho, S. Choi, S. Sachdev, M. Greiner, V. Vuletić, and M. D. Lukin, “Quantum phases of matter on a 256-atom programmable quantum simulator”, *Nature* **595**, 227–232 (2021) (cit. on pp. 16, 25, 144).

- [82] S. Haroche, “Nobel Lecture: Controlling photons in a box and exploring the quantum to classical boundary”, *Reviews of Modern Physics* **85**, 1083–1102 (2013) (cit. on p. 16).
- [83] R. Heidemann, U. Raitzsch, V. Bendkowsky, B. Butscher, R. Löw, Pfau, and Tilman, “Rydberg Excitation of Bose-Einstein Condensates”, *Physical Review Letters* **100**, 033601 (2008) (cit. on p. 16).
- [84] Y. N. Gnedin, A. A. Mihajlov, L. M. Ignjatović, N. M. Sakan, V. A. Srećković, M. Y. Zakharov, N. N. Bezuglov, and A. N. Klycharev, *Rydberg atoms in astrophysics*, 2009 (cit. on p. 16).
- [85] R. G. Cortiñas, M. Favier, B. Ravon, P. Méhaignerie, Y. Machu, J. M. Raimond, C. Sayrin, and M. Brune, “Laser Trapping of Circular Rydberg Atoms”, *Physical Review Letters* **124**, 123201 (2020) (cit. on p. 16).
- [86] M. J. Seaton, “Quantum defect theory”, *Reports on Progress in Physics* **46**, 167–257 (1983) (cit. on pp. 16–17).
- [87] E. Tiesinga, P. J. Mohr, D. B. Newell, and B. N. Taylor, “Codata recommended values of the fundamental physical constants: 2018”, *Reviews of Modern Physics* **93**, 025010 (2021) (cit. on p. 16).
- [88] W. Li, I. Mourachko, M. W. Noel, and T. F. Gallagher, “Millimeter-wave spectroscopy of cold Rb Rydberg atoms in a magneto-optical trap: Quantum defects of the ns, np, and nd series”, *Physical Review A - Atomic, Molecular, and Optical Physics* **67**, 052502 (2003) (cit. on pp. 17, 97).
- [89] M. Mack, F. Karlewski, H. Hattermann, S. Höckh, F. Jessen, D. Cano, and J. Fortágh, “Measurement of absolute transition frequencies of Rb87 to nS and nD Rydberg states by means of electromagnetically induced transparency”, *Physical Review A - Atomic, Molecular, and Optical Physics* **83**, 052515 (2011) (cit. on p. 17).
- [90] T. F. Gallagher, *Rydberg Atoms- Spectroscopy of alkali Rydberg states* (2009), pp. 340–364 (cit. on p. 17).
- [91] Gallagher T. F., *Rydberg Atoms* (Cambridge University Press, 2005) (cit. on pp. 17, 158).
- [92] N. Šibalić, J. D. Pritchard, C. S. Adams, and K. J. Weatherill, “ARC: An open-source library for calculating properties of alkali Rydberg atoms”, *Computer Physics Communications* **220**, 319–331 (2017) (cit. on pp. 17, 98, 152).
- [93] A Osterwalder and F Merkt, “Using high rydberg states as electric field sensors”, *Physical Review Letters* **82**, 1831–1834 (1999) (cit. on p. 18).
- [94] H. Q. Fan, S. Kumar, R. Daschner, H. Kübler, and J. P. Shaffer, “Subwavelength microwave electric-field imaging using Rydberg atoms inside atomic vapor cells”, *Optics Letters* **39**, 3030–3033 (2014) (cit. on p. 18).
- [95] C. G. Wade, N. Šibali, N. R. De Melo, J. M. Kondo, C. S. Adams, and K. J. Weatherill, “Real-time near-field terahertz imaging with atomic optical fluorescence”, *Nature Photonics* **11**, 40–43 (2017) (cit. on p. 18).
- [96] E. K. Dietsche, A. Larrouy, S. Haroche, J. M. Raimond, M. Brune, and S. Gleyzes, “High-sensitivity magnetometry with a single atom in a superposition of two circular Rydberg states”, *Nature Physics* **15**, 326–329 (2019) (cit. on p. 18).
- [97] H. Gorniaczyk, C. Tresp, P. Bienias, A. Paris-Mandoki, W. Li, I. Mirgorodskiy, H. P. Büchler, I. Lesanovsky, and S. Hofferberth, “Enhancement of Rydberg-mediated single-photon nonlinearities by electrically tuned Förster resonances”, *Nature Communications* **7**, 12480 (2016) (cit. on pp. 19, 25).

- [98] L. Béguin, A. Vernier, R. Chicireanu, T. Lahaye, and A. Browaeys, “Direct measurement of the van der waals interaction between two rydberg atoms”, Physical Review Letters **110**, 263201 (2013) (cit. on p. 19).
- [99] A. K. Mohapatra, T. R. Jackson, and C. S. Adams, “Coherent optical detection of highly excited rydberg states using electromagnetically induced transparency”, Physical Review Letters **98**, 113003 (2007) (cit. on pp. 20, 158).
- [100] M. D. Lukin and A. Imamoğlu, “Controlling photons using electromagnetically induced transparency”, Nature **413**, 273–276 (2001) (cit. on p. 22).
- [101] M. Fleischhauer, A. Imamoglu, and P. J. Marangos, “Electromagnetically induced transparency”, Reviews of Modern Physics **77**, 633–673 (2005) (cit. on p. 23).
- [102] D. Jaksch, J. I. Cirac, P. Zoller, S. L. Rolston, R. Côté, and M. D. Lukin, “Fast Quantum Gates for Neutral Atoms”, Physical Review Letters **85**, 2208–2211 (2000) (cit. on p. 25).
- [103] M. D. Lukin, M. Fleischhauer, R. Cote, L. M. Duan, D. Jaksch, J. I. Cirac, and P. Zoller, “Dipole blockade and quantum information processing in mesoscopic atomic ensembles”, Physical Review Letters **87**, 037901 (2001) (cit. on pp. 25, 142, 144).
- [104] A. Gaëtan, Y. Miroshnychenko, T. Wilk, A. Chotia, M. Viteau, D. Comparat, P. Pillet, A. Browaeys, and P. Grangier, “Observation of collective excitation of two individual atoms in the Rydberg blockade regime”, Nature Physics **5**, 115–118 (2009) (cit. on pp. 25, 142, 144).
- [105] E. Urban, T. A. Johnson, T. Henage, L. Isenhower, D. D. Yavuz, T. G. Walker, and M. Saffman, “Observation of Rydberg blockade between two atoms”, Nature Physics **5**, 110–114 (2009) (cit. on p. 25).
- [106] Y. O. Dudin, L. Li, F. Bariani, and A. Kuzmich, “Observation of coherent many-body Rabi oscillations”, Nature Physics **8**, 790–794 (2012) (cit. on pp. 25, 29, 114, 142, 144, 146–147).
- [107] Y. O. Dudin and A. Kuzmich, “Strongly interacting Rydberg excitations of a cold atomic gas”, Science **336**, 887–889 (2012) (cit. on p. 25).
- [108] V. Bendkowsky, B. Butscher, J. Nipper, J. P. Shaffer, R. Löw, and T. Pfau, “Observation of ultralong-range Rydberg molecules”, Nature **458**, 1005–1008 (2009) (cit. on pp. 26, 55, 174).
- [109] D. Tiarks, S. Schmidt-Eberle, T. Stolz, G. Rempe, and S. Dürr, “A photon–photon quantum gate based on Rydberg interactions”, Nature Physics **15**, 124–126 (2019) (cit. on p. 26).
- [110] A. Grankin, “Theoretical studies of optical non-linear effects in ultracold Rydberg gases”, (2016) (cit. on p. 28).
- [111] A. V. Gorshkov, J. Otterbach, M. Fleischhauer, T. Pohl, and M. D. Lukin, “Photon–photon interactions via Rydberg blockade”, Physical Review Letters **107**, 133602 (2011) (cit. on pp. 28, 107).
- [112] S. Sevinçli, N. Henkel, C. Ates, and T. Pohl, “Nonlocal nonlinear optics in cold Rydberg gases”, Physical Review Letters **107**, 153001 (2011) (cit. on pp. 28, 107).
- [113] A. V. Gorshkov, R. Nath, and T. Pohl, “Dissipative many-body quantum optics in rydberg media”, Physical Review Letters **110**, 153601 (2013) (cit. on pp. 28, 107).
- [114] A. Grankin, E. Brion, E. Bimbard, R. Boddeda, I. Usmani, A. Ourjoumtsev, and P. Grangier, “Quantum statistics of light transmitted through an intracavity Rydberg medium”, New Journal of Physics **16**, 043020 (2014) (cit. on pp. 28, 94, 107, 110, 112, 146).

- [115] A Grankin, E Brion, E Bimbard, R Boddeda, I Usmani, A Ourjoumtsev, and P Grangier, “Quantum-optical nonlinearities induced by Rydberg-Rydberg interactions: A perturbative approach”, *Physical Review A - Atomic, Molecular, and Optical Physics* **92**, 043841 (2015) (cit. on pp. 28, 94, 107, 177).
- [116] A. Grankin, E. Brion, R. Boddeda, S. Cük, I. Usmani, A. Ourjoumtsev, and P. Grangier, “Inelastic Photon Scattering via the Intracavity Rydberg Blockade”, *Physical Review Letters* **117**, 253602 (2016) (cit. on p. 28).
- [117] R. Calder and G. Lewin, “Reduction of stainless-steel outgassing in ultra-high vacuum”, *British Journal of Applied Physics* **18**, 1459–1472 (1967) (cit. on p. 33).
- [118] LIGO, “LIGO Vacuum Compatible Materials List”, *Laser Interferometer Gravitational Wave Observatory E960050-v1* (2014) (cit. on p. 33).
- [119] B. Hacker, “Two-Photon Gate and Creation of Optical Cat States using One Atom in a Cavity”, (2019) (cit. on pp. 35, 114).
- [120] N. Schine, A. Ryou, A. Gromov, A. Sommer, and J. Simon, “Synthetic Landau levels for photons”, *Nature* **534**, 671–675 (2016) (cit. on pp. 36, 40).
- [121] D. Gangloff, M. Shi, T. Wu, A. Bylinskii, B. Braverman, M. Gutierrez, R. Nichols, J. Li, K. Aichholz, M. Cetina, L. Karpa, B. Jelenković, I. Chuang, and V. Vuletić, “Preventing and reversing vacuum-induced optical losses in high-finesse tantalum (V) oxide mirror coatings”, *Optics Express* **23**, 18014–18028 (2015) (cit. on p. 37).
- [122] S. J. Habraken and G. Nienhuis, “Modes of a twisted optical cavity”, *Physical Review A - Atomic, Molecular, and Optical Physics* **75**, 033819 (2007) (cit. on pp. 38–40).
- [123] Y. Jie, L. Xingwu, L. Linmei, Z. Bin, W. Fei, and Z. Hongchang, “Nonplanar ring resonator modes: Generalized Gaussian beams”, *Applied Optics* **46**, 2980–2989 (2007) (cit. on pp. 38, 40).
- [124] T. Akagi et al., “Development of a three dimensional four mirror optical cavity for laser-Compton scattering”, *Nuclear Instruments and Methods in Physics Research, Section A: Accelerators, Spectrometers, Detectors and Associated Equipment* **724**, 63–71 (2013) (cit. on p. 38).
- [125] A. Noack, C. Bogan, and B. Willke, “Higher-order Laguerre–Gauss modes in (non-) planar four-mirror cavities for future gravitational wave detectors”, *Optics Letters* **42**, 751–754 (2017) (cit. on p. 38).
- [126] A. Sommer and J. Simon, “Engineering photonic Floquet Hamiltonians through Fabry-Pérot resonators”, *New Journal of Physics* **18**, 035008 (2016) (cit. on p. 40).
- [127] R. W. P. Drever, J. L. Hall, F. V. Kowalski, J. Hough, G. M. Ford, A. J. Munley, and H. Ward, “Laser Phase and Frequency Stabilization Using an Optical Resonator”, **31**, 97–105 (1983) (cit. on pp. 47, 95).
- [128] A. J. Wallard, “Frequency stabilization of the helium-neon laser by saturated absorption in iodine vapour”, *Journal of Physics E: Scientific Instruments* **5**, 926–930 (1972) (cit. on p. 47).
- [129] T. W. Hansch and B Couillaud, “Laser frequency stabilization by polarization spectroscopy of a reflecting reference cavity”, *Optics Communications* **35**, 441–444 (1980) (cit. on p. 47).
- [130] E. L. Raab, M. Prentiss, A. Cable, S. Chu, and D. E. Pritchard, “Trapping of Neutral Sodium Atoms with Radiation Pressure”, *Physical Review Letters* **59**, 2631–2634 (1987) (cit. on p. 57).
- [131] D. A. Steck, “Rubidium 87 D Line Data”, (2019) (cit. on p. 57).

- [132] P. D. Lett, R. N. Watts, C. I. Westbrook, W. D. Phillips, P. L. Gould, and H. J. Metcalf, “Observation of atoms laser cooled below the doppler limit”, *Physical Review Letters* **61**, 169–172 (1988) (cit. on p. 58).
- [133] Z. T. Lu, K. L. Corwin, M. J. Renn, M. H. Anderson, E. A. Comell, and C. E. Wieman, “Low-Velocity intense source of atoms from a magneto-optical trap”, *Collected Papers of Carl Wieman*, 420–423 (2008) (cit. on p. 58).
- [134] G. Reinaudi, T. Lahaye, Z. Wang, and D. Guéry-Odelin, “Strong saturation absorption imaging of dense clouds of ultracold atoms”, *Optics Letters* **32**, 3143–3145 (2007) (cit. on p. 60).
- [135] J. Dalibard and C. Cohen-Tannoudji, “Laser cooling below the Doppler limit by polarization gradients: simple theoretical models”, *Journal of the Optical Society of America B* **6**, 2023–2045 (1989) (cit. on p. 62).
- [136] A. Ashkin, “Acceleration and Trapping of Particles by Radiation Pressure”, *Physical Review Letters* **24**, 156–159 (1970) (cit. on p. 64).
- [137] D. Barredo, V. Lienhard, S. de Léséleuc, T. Lahaye, and A. Browaeys, “Synthetic three-dimensional atomic structures assembled atom by atom”, *Nature* **561**, 79–82 (2018) (cit. on p. 64).
- [138] H. Zhang and K. K. Liu, “Optical tweezers for single cells”, *Journal of the Royal Society Interface* **5**, 671–690 (2008) (cit. on p. 64).
- [139] R. Grimm and Y. B. Ovchinnikov, “Optical dipole traps for neutral atoms”, (1987) (cit. on p. 64).
- [140] D. Schrader, S. Kuhr, W. Alt, M. Müller, V. Gomer, and D. Meschede, “An optical conveyor belt for single neutral atoms”, *Applied Physics B: Lasers and Optics* **73**, 819–824 (2001) (cit. on p. 66).
- [141] R. Jáuregui, “Nonperturbative and perturbative treatments of parametric heating in atom traps”, *Physical Review A - Atomic, Molecular, and Optical Physics* **64**, 053408 (2001) (cit. on p. 67).
- [142] D. J. Han, S. Wolf, S. Oliver, C. McCormick, M. T. DePue, and D. S. Weiss, “3D Raman sideband cooling of cesium atoms at high density”, *Physical Review Letters* **85**, 724–727 (2000) (cit. on p. 69).
- [143] A. Urvoy, Z. Vendeiro, J. Ramette, A. Adiyatullin, and V. Vuletić, “Direct Laser Cooling to Bose-Einstein Condensation in a Dipole Trap”, *Physical Review Letters* **122**, 203202 (2019) (cit. on p. 69).
- [144] S. E. Hamann, D. L. Haycock, G. Klose, P. H. Pax, I. H. Deutsch, and P. S. Jessen, “Resolved-sideband raman cooling to the ground state of an optical lattice”, *Physical Review Letters* **80**, 4149–4152 (1998) (cit. on p. 70).
- [145] I. H. Deutsch and P. S. Jessen, “Quantum-state control in optical lattices”, *Physical Review A - Atomic, Molecular, and Optical Physics* **57**, 1972–1986 (1998) (cit. on p. 70).
- [146] R. H. Hadfield, M. J. Stevens, S. S. Gruber, A. J. Miller, R. E. Schwall, R. P. Mirin, and S. W. Nam, “Single photon source characterization with a superconducting single photon detector”, *Optics InfoBase Conference Papers* **13**, 10846–10853 (2005) (cit. on p. 76).
- [147] B. K. Lubsandorzhiev, “On the history of photomultiplier tube invention”, *Nuclear Instruments and Methods in Physics Research, Section A: Accelerators, Spectrometers, Detectors and Associated Equipment* **567**, 236–238 (2006) (cit. on p. 76).

- [148] R. Hambury Brown and R. Q. Twiss, "Correlation between photons in two coherent beams of light", *Nature* **177**, 27–32 (1956) (cit. on pp. 78, 103).
- [149] L. Mandel and E. Wolf, "Correlation in the fluctuating outputs from two square-law detectors illuminated by light of any state of coherence and polarization", *Physical Review* **124**, 1696–1702 (1961) (cit. on p. 78).
- [150] H. P. Yuen and V. W. Chan, "Noise in Homodyne and Heterodyne Detection.", *Optics Letters* **8**, 177–179 (1983) (cit. on p. 79).
- [151] G. L. Abbas, V. W. S. Chan, and T. K. Yee, "Local-oscillator excess-noise suppression for homodyne and heterodyne detection", *Optics Letters* **8**, 419–421 (1983) (cit. on p. 79).
- [152] U. Schnars, C. Falldorf, J. Watson, and W. Jüptner, *Digital holography and wavefront sensing: Principles, techniques and applications* (2015), pp. 1–226 (cit. on p. 79).
- [153] P. Bertet, A. Auffeves, P. Maioli, S. Osnaghi, T. Meunier, M. Brune, J. M. Raimond, and S. Haroche, "Direct Measurement of the Wigner Function of a One-Photon Fock State in a Cavity", *Physical Review Letters* **89**, 200402 (2002) (cit. on p. 80).
- [154] B. Vlastakis, G. Kirchmair, Z. Leghtas, S. E. Nigg, L. Frunzio, S. M. Girvin, M. Mirrahimi, M. H. Devoret, and R. J. Schoelkopf, "Deterministically encoding quantum information using 100-photon Schrödinger cat states", *Science* **342**, 607–610 (2013) (cit. on p. 80).
- [155] A. Ourjoumtsev, H. Jeong, R. Tualle-Brouri, and P. Grangier, "Generation of optical 'Schrödinger cats' from photon number states", *Nature* **448**, 784–786 (2007) (cit. on p. 80).
- [156] O. Morin, K. Huang, J. Liu, H. Le Jeannic, C. Fabre, and J. Laurat, "Remote creation of hybrid entanglement between particle-like and wave-like optical qubits", *Nature Photonics* **8**, 570–574 (2014) (cit. on p. 80).
- [157] U Leonhardt, *Measuring the quantum state of light* (Cambridge university press, 1997) (cit. on pp. 80, 158).
- [158] H. White, "Maximum Likelihood Estimation of Misspecified Models", *Econometrica* **50**, 1–25 (1982) (cit. on p. 81).
- [159] P. Diaconis, "The markov chain monte carlo revolution", *Bulletin of the American Mathematical Society* **46**, 179–205 (2009) (cit. on p. 81).
- [160] A. I. Lvovsky, "Iterative maximum-likelihood reconstruction in quantum homodyne tomography", *Journal of Optics B: Quantum and Semiclassical Optics* **6**, S556 (2004) (cit. on p. 81).
- [161] Y. Vardi and D. Lee, "From Image Deblurring to Optimal Investments : Maximum Likelihood Solutions for Positive Linear Inverse Problems", *Journal of the Royal Statistical Society. Series B (Methodological)* **55**, 569–612 (1993) (cit. on p. 82).
- [162] J. Appel, D. Hoffman, E. Figueroa, and A. I. Lvovsky, "Electronic noise in optical homodyne tomography", *Physical Review A - Atomic, Molecular, and Optical Physics* **75**, 035802 (2007) (cit. on p. 82).
- [163] C. Hamsen, K. N. Tolazzi, T. Wilk, and G. Rempe, "Two-Photon Blockade in an Atom-Driven Cavity QED System", *Physical Review Letters* **118**, 133604 (2017) (cit. on pp. 94, 110, 113).
- [164] J. Ningyuan, A. Georgakopoulos, A. Ryou, N. Schine, A. Sommer, and J. Simon, "Observation and characterization of cavity Rydberg polaritons", **93**, 041802 (2016) (cit. on p. 95).

- [165] A. Tauschinsky, R. M. Thijssen, S. Whitlock, H. B. Van LindenVanDenHeuvell, and R. J. Spreeuw, “Spatially resolved excitation of Rydberg atoms and surface effects on an atom chip”, *Physical Review A - Atomic, Molecular, and Optical Physics* **81**, 063411 (2010) (cit. on p. 95).
- [166] S. D. Hogan, J. A. Agner, F. Merkt, T. Thiele, S. Philipp, and A. Wallraff, “Driving Rydberg-Rydberg transitions from a coplanar Microwave Waveguide”, *Physical Review Letters* **108**, 063004 (2012) (cit. on p. 95).
- [167] A. Sommer, H. P. Büchler, and J. Simon, “Theory of interacting cavity Rydberg polaritons”, *4*, 014005 (2018) (cit. on pp. 107, 146).
- [168] B. Darquié, “Manipulation d’atomes dans des pièges dipolaires microscopiques et émission contrôlée de photons par un atome”, (2006) (cit. on p. 108).
- [169] T. Amthor, C. Giese, C. S. Hofmann, and M. Weidmüller, “Evidence of Antiblockade in an Ultracold Rydberg Gas”, *Physical Review Letters* **104**, 013001 (2010) (cit. on p. 112).
- [170] S. Das, A. Grankin, I. Iakourov, E. Brion, J. Borregaard, R. Boddeda, I. Usmani, A. Ourjoumtsev, P. Grangier, and A. S. Sørensen, “Photonic controlled- phase gates through Rydberg blockade in optical cavities”, *Physical Review A* **93**, 040303 (2016) (cit. on pp. 114, 142, 144, 154, 158, 167).
- [171] D. Maxwell, D. J. Szwer, D. Paredes-Barato, H. Busche, J. D. Pritchard, A. Gauguet, K. J. Weatherill, M. P. Jones, and C. S. Adams, “Storage and control of optical photons using Rydberg polaritons”, *Physical Review Letters* **110**, 103001 (2013) (cit. on pp. 114, 117).
- [172] E. Distante, P. Farrera, A. Padrón-Brito, D. Paredes-Barato, G. Heinze, and H. De Riedmatten, “Storing single photons emitted by a quantum memory on a highly excited Rydberg state”, *Nature Communications* **8**, 14072 (2017) (cit. on p. 114).
- [173] D. P. Ornelas-Huerta, A. N. Craddock, E. A. Goldschmidt, A. J. Hachtel, Y. Wang, P. Bienias, A. V. Gorshkov, S. L. Rolston, and J. V. Porto, “On-demand indistinguishable single photons from an efficient and pure source based on a Rydberg ensemble”, *Optica* **7**, 813 (2020) (cit. on pp. 114, 116–117, 123, 125).
- [174] L. Li, Y. O. Dudin, and A. Kuzmich, “Entanglement between light and an optical atomic excitation”, *Nature* **498**, 466–469 (2013) (cit. on pp. 114, 142, 144, 154, 158).
- [175] A. Miranowicz, M. Paprzycka, A. Pathak, and F. Nori, “Phase-space interference of states optically truncated by quantum scissors: Generation of distinct superpositions of qudit coherent states by displacement of vacuum”, *Physical Review A - Atomic, Molecular, and Optical Physics* **89**, 033812 (2014) (cit. on pp. 116, 131).
- [176] A. H. Kiilerich and K. Mølmer, “Input-Output Theory with Quantum Pulses”, *Physical Review Letters* **123**, 123604 (2019) (cit. on pp. 116, 119–120).
- [177] L. M. Duan, M. D. Lukin, J. I. Cirac, and P. Zoller, “Long-distance quantum communication with atomic ensembles and linear optics”, *Nature* **414**, 413–418 (2001) (cit. on p. 117).
- [178] A. D. Boozer, A. Boca, R. Miller, T. E. Northup, and H. J. Kimble, “Reversible state transfer between light and a single trapped atom”, *Physical Review Letters* **98**, 193601 (2007) (cit. on p. 117).
- [179] H. P. Specht, C. Nölleke, A. Reiserer, M. Uphoff, E. Figueroa, S. Ritter, and G. Rempe, “A single-atom quantum memory”, *Nature* **473**, 190–193 (2011) (cit. on pp. 117, 174).

- [180] E. Bimbard, R. Boddeda, N. Vitrant, A. Grankin, V. Parigi, J. Stanojevic, A. Ourjoumtsev, and P. Grangier, “Homodyne tomography of a single photon retrieved on demand from a cavity-enhanced cold atom memory”, *Physical Review Letters* **112**, 1–5 (2014) (cit. on p. 117).
- [181] L. Li and A. Kuzmich, “Quantum memory with strong and controllable Rydberg-level interactions”, *Nature Communications* **7**, 13618 (2016) (cit. on pp. 117, 174).
- [182] J. Honer, R. Löw, H. Weimer, T. Pfau, and H. P. Büchler, “Artificial atoms can do more than atoms: Deterministic single photon subtraction from arbitrary light fields”, *Physical Review Letters* **107**, 093601 (2011) (cit. on pp. 117, 140).
- [183] J. Stanojevic, V. Parigi, E. Bimbard, A. Ourjoumtsev, P. Pillet, and P. Grangier, “Generating non-Gaussian states using collisions between Rydberg polaritons”, *Physical Review A - Atomic, Molecular, and Optical Physics* **86**, 021403 (2012) (cit. on p. 117).
- [184] J. Combes, J. Kerckhoff, and M. Sarovar, “The SLH framework for modeling quantum input-output networks”, *Advances in Physics: X* **2**, 784–888 (2017) (cit. on p. 120).
- [185] C. K. Hong, Z. Y. Ou and L. Mandel, “Measurement of Subpicosecond Time Intervals between Two Photons by Interference”, *Physical Review Letters* **59**, 2044–2046 (1987) (cit. on p. 123).
- [186] P. Grangier, G. Roger, and A. Aspect, “Experimental evidence for a photon anticorrelation effect on a beam splitter: A new light on single-photon interferences”, *Epl* **1**, 173–179 (1986) (cit. on p. 123).
- [187] D. Bouwmeester, J. W. Pan, K. Mattle, M. Eibl, H. Weinfurter, and A. Zeilinger, “Experimental quantum teleportation”, *Nature* **390**, 575–579 (1997) (cit. on p. 123).
- [188] M. D. Jian-Wei Pan, Dik Bouwmeester, H. Weinfurter, and & A. Zeilinger, “Experimental test of quantum nonlocality in three-photon Greenberger-Horne-Zeilinger entanglement”, *Nature* **403**, 515–519 (2000) (cit. on p. 123).
- [189] A. Ourjoumtsev, R. Tualle-Brouri, J. Laurat, and P. Grangier, “Generating Optical Schrödinger Kittens for Quantum Information Processing”, *Science* **312**, 83–86 (2006) (cit. on p. 123).
- [190] M. Tillmann, B. Dakić, R. Heilmann, S. Nolte, A. Szameit, and P. Walther, “Experimental boson sampling”, *Nature Photonics* **7**, 540–544 (2013) (cit. on p. 123).
- [191] B. Darquié, M. Jones, J. Dingjan, J. Beugnon, S. Bergamini, Y. Sortais, G. Messin, A. Broways, and P. Grangier, “Controlled Single-Photon Emission from a Single Trapped Two-level Atom”, *Science* **309**, 454–455 (2005) (cit. on p. 123).
- [192] A. Beveratos, S. Kühn, R. Brouri, T. Gacoin, J. P. Poizat, and P. Grangier, “Room temperature stable single-photon source”, *European Physical Journal D* **18**, 191–196 (2002) (cit. on p. 123).
- [193] P. Maunz, D. L. Moehring, S. Olmschenk, K. C. Younge, D. N. Matsukevich, and C. Monroe, “Quantum interference of photon pairs from two remote trapped atomic ions”, *Nature Physics* **3**, 538–541 (2007) (cit. on p. 123).
- [194] Z. H. Peng, S. E. De Graaf, J. S. Tsai, and O. V. Astafiev, “Tunable on-demand single-photon source in the microwave range”, *Nature Communications* **7**, 12588 (2016) (cit. on p. 123).
- [195] R. S. Daveau, K. C. Balram, T. Pagnolato, J. Liu, E. H. Lee, J. D. Song, V. Verma, R. Mirin, S. W. Nam, L. Midolo, S. Stobbe, K. Srinivasan, and P. Lodahl, “Efficient fiber-coupled single-photon source based on quantum dots in a photonic-crystal waveguide”, *Optica* **4**, 178–184 (2017) (cit. on p. 123).

- [196] A. Kuhn, M. Hennrich, and G. Rempe, “Deterministic Single-Photon Source for Distributed Quantum Networking”, *Physical Review Letters* **89**, 067901 (2002) (cit. on p. 123).
- [197] M. Mücke, J. Bochmann, C. Hahn, A. Neuzner, C. Nölleke, A. Reiserer, G. Rempe, and S. Ritter, “Generation of single photons from an atom-cavity system”, *Physical Review A - Atomic, Molecular, and Optical Physics* **87**, 063805 (2013) (cit. on p. 123).
- [198] S. Thomas P. Senellart, “The race for the ideal single-photon source is on”, *Nature Nanotechnology* **16**, 367–368 (2021) (cit. on p. 123).
- [199] E. A. Goldschmidt, T. Boulier, R. C. Brown, S. B. Koller, J. T. Young, A. V. Gorshkov, S. L. Rolston, and J. V. Porto, “Anomalous Broadening in Driven Dissipative Rydberg Systems”, *Physical Review Letters* **116**, 113001 (2016) (cit. on p. 125).
- [200] F. Bariani, P. M. Goldbart, and T. A. Kennedy, “Dephasing dynamics of Rydberg atom spin waves”, *Physical Review A - Atomic, Molecular, and Optical Physics* **86**, 041802 (2012) (cit. on pp. 127, 146).
- [201] M. Barbieri, N. Spagnolo, M. G. Genoni, F. Ferreyrol, R. Blandino, M. G. Paris, P. Grangier, and R. Tualle-Brouri, “Non-Gaussianity of quantum states: An experimental test on single-photon-added coherent states”, *Physical Review A - Atomic, Molecular, and Optical Physics* **82**, 1–5 (2010) (cit. on p. 131).
- [202] C. H. Schulte, J. Hansom, A. E. Jones, C. Matthiesen, C. Le Gall, and M. Atature, “Quadrature squeezed photons from a two-level system”, *Nature* **525**, 222–225 (2015) (cit. on p. 131).
- [203] H. J. Carmichael, “Photon Antibunching and Squeezing for a Single Atom in a Resonant Cavity”, *Physical Review Letters* **55**, 539–539 (1985) (cit. on p. 131).
- [204] D. T. Pegg, L. S. Phillips, and S. M. Barnett, “Optical state truncation by projection synthesis”, *Physical Review Letters* **81**, 1604–1606 (1998) (cit. on p. 131).
- [205] S. A. Babichev, J. Ries, and A. I. Lvovsky, “Quantum scissors: Teleportation of single-mode optical states by means of a nonlocal single photon”, *Europhysics Letters* **64**, 1 (2003) (cit. on p. 131).
- [206] F. Ferreyrol, M. Barbieri, R. Blandino, S. Fossier, R. Tualle-Brouri, and P. Grangier, “Implementation of a nondeterministic optical noiseless amplifier”, *Physical Review Letters* **104**, 26–29 (2010) (cit. on p. 131).
- [207] H. Vahlbruch, M. Mehmet, K. Danzmann, and R. Schnabel, “Detection of 15 dB Squeezed States of Light and their Application for the Absolute Calibration of Photovoltaic Quantum Efficiency”, *Physical Review Letters* **117**, 110801 (2016) (cit. on p. 133).
- [208] N. Stiesdal, H. Busche, K. Kleinbeck, J. Kumlin, M. G. Hansen, H. P. Büchler, and S. Hofferberth, “Controlled multi-photon subtraction with cascaded Rydberg superatoms as single-photon absorbers”, *Nature Communications* **12**, 4328 (2021) (cit. on p. 140).
- [209] S. H. Cantu, A. V. Venkatramani, W. Xu, L. Zhou, B. Jelenković, M. D. Lukin, and V. Vuletić, “Repulsive photons in a quantum nonlinear medium”, *Nature Physics* **16**, 921–925 (2020) (cit. on p. 142).
- [210] R. Heidemann, U. Raitzsch, V. Bendkowsky, B. Butscher, R. Löw, L. Santos, and T. Pfau, “Evidence for coherent collective rydberg excitation in the strong blockade regime”, *Physical Review Letters* **99**, 163601 (2007) (cit. on p. 142).
- [211] Y. Nakamura, Y. A. Pashkin, and J. S. Tsai, “Rabi oscillations in a josephson-junction charge two-level system”, *Physical Review Letters* **87**, 246601 (2001) (cit. on p. 144).

- [212] J. M. Martinis, S. Nam, J. Aumentado, and C. Urbina, “Rabi Oscillations in a Large Josephson-Junction Qubit”, *Physical Review Letters* **89**, 9–12 (2002) (cit. on p. 144).
- [213] H. Kamada, H. Gotoh, J. Temmyo, T. Takagahara, and H. Ando, “Exciton rabi oscillation in a single quantum dot”, *Physical Review Letters* **87**, 246401 (2001) (cit. on p. 144).
- [214] M. Veldhorst, J. C. Hwang, C. H. Yang, A. W. Leenstra, B. De Ronde, J. P. Dehollain, J. T. Muhonen, F. E. Hudson, K. M. Itoh, A. Morello, and A. S. Dzurak, “An addressable quantum dot qubit with fault-tolerant control-fidelity”, *Nature Nanotechnology* **9**, 981–985 (2014) (cit. on p. 144).
- [215] P. Scholl, M. Schuler, H. J. Williams, A. A. Eberharter, D. Barredo, K. N. Schymik, V. Lienhard, L. P. Henry, T. C. Lang, T. Lahaye, A. M. Läuchli, and A. Browaeys, “Quantum simulation of 2D antiferromagnets with hundreds of Rydberg atoms”, *Nature* **595**, 233–238 (2021) (cit. on p. 144).
- [216] T. R. Gentile, B. J. Hughey, D. Kleppner, and T. W. Ducas, “Experimental Study of Two-Photon Rabi Oscillations”, *Coherence and Quantum Optics VI* **40**, 5103 (1990) (cit. on p. 144).
- [217] A. F. Linskens, I. Holleman, N. Dam, and J. Reuss, “Two-photon Rabi oscillations”, *Physical Review A - Atomic, Molecular, and Optical Physics* **54**, 4854–4862 (1996) (cit. on p. 144).
- [218] B. W. Shore, K. Bergmann, A. Kuhn, S. Schiemann, J. Oreg, and J. H. Eberly, “Laser-induced population transfer in multistate systems: A comparative study”, *Physical Review A* **45**, 5297–5300 (1992) (cit. on p. 144).
- [219] N. V. Vitanov, A. A. Rangelov, B. W. Shore, and K. Bergmann, “Stimulated Raman adiabatic passage in physics, chemistry, and beyond”, *Reviews of Modern Physics* **89**, 015006 (2017) (cit. on p. 144).
- [220] Z. Kis and F. Renzoni, “Qubit rotation by stimulated Raman adiabatic passage”, *Physical Review A - Atomic, Molecular, and Optical Physics* **65**, 032318 (2002) (cit. on p. 144).
- [221] I. I. Beterov, D. B. Tretyakov, V. M. Entin, E. A. Yakshina, I. I. Ryabtsev, C. McCormick, and S. Bergamini, “Deterministic single-atom excitation via adiabatic passage and Rydberg blockade”, *Physical Review A - Atomic, Molecular, and Optical Physics* **84**, 023413 (2011) (cit. on p. 144).
- [222] I. I. Beterov, M. Saffman, E. A. Yakshina, V. P. Zhukov, D. B. Tretyakov, V. M. Entin, I. I. Ryabtsev, C. W. Mansell, C. McCormick, S. Bergamini, and M. P. Fedoruk, “Quantum gates in mesoscopic atomic ensembles based on adiabatic passage and Rydberg blockade”, *Physical Review A - Atomic, Molecular, and Optical Physics* **88**, 010303 (2013) (cit. on p. 144).
- [223] U. Raitzsch, R. Heidemann, H. Weimer, B. Butscher, P. Kollmann, R. Löw, H. P. Büchler, and T. Pfau, “Investigation of dephasing rates in an interacting Rydberg gas”, *New Journal of Physics* **11**, 055014 (2009) (cit. on p. 146).
- [224] S. De Léséleuc, D. Barredo, V. Lienhard, A. Browaeys, and T. Lahaye, “Analysis of imperfections in the coherent optical excitation of single atoms to Rydberg states”, *Physical Review A* **97**, 053803 (2018) (cit. on pp. 149–150, 158).
- [225] M. Brune, E. Hagley, J. Dreyer, X. MaÎtre, A. Maali, C. Wunderlich, J. M. Raimond, and S. Haroche, “Observing the progressive decoherence of the “meter” in a quantum measurement”, *Physical Review Letters* **77**, 4887–4890 (1996) (cit. on p. 154).

- [226] H. De Riedmatten, J. Laurat, C. W. Chou, E. W. Schomburg, D. Felinto, and H. J. Kimble, “Direct measurement of decoherence for entanglement between a photon and stored atomic excitation”, *Physical Review Letters* **97**, 113603 (2006) (cit. on p. 154).
- [227] C. J. Myatt, B. E. King, Q. A. Turchette, C. A. Sackett, D. Kielpinski, W. M. Itano, C. Monroe, and D. J. Wineland, “Decoherence of quantum superpositions through coupling to engineered reservoirs”, *Nature* **403**, 269–273 (2000) (cit. on p. 154).
- [228] S. Garcia, M. Stammeier, J. Deiglmayr, F. Merkt, and A. Wallraff, “Single-Shot Non-destructive Detection of Rydberg-Atom Ensembles by Transmission Measurement of a Microwave Cavity”, *Physical Review Letters* **123**, 193201 (2019) (cit. on p. 158).
- [229] P. Maioli, T. Meunier, S. Gleyzes, A. Auffeves, G. Nogues, M. Brune, J. M. Raimond, and S. Haroche, “Nondestructive rydberg atom counting with mesoscopic fields in a cavity”, *Physical Review Letters* **94**, 113601 (2005) (cit. on p. 158).
- [230] W. Xu, A. V. Venkatramani, S. H. Cantú, T. Šumarák, V. Klüsener, M. D. Lukin, and V. Vuletić, “Fast Preparation and Detection of a Rydberg Qubit Using Atomic Ensembles”, *Physical Review Letters* **127**, 050501 (2021) (cit. on pp. 158, 164, 172).
- [231] C.-W. Yang, J. Li, M.-T. Zhou, X. Jiang, X.-H. Bao, and J.-W. Pan, “Single-shot measurement of a Rydberg superatom via collective photon burst”, Arxiv, 2106.10858 (2021) (cit. on pp. 158, 164, 172).
- [232] H. Mabuchi, Q. A. Turchette, M. S. Chapman, and H. J. Kimble, “Real-time detection of individual atoms falling through a high-finesse optical cavity”, *Optics Letters* **21**, 1393 (1996) (cit. on p. 158).
- [233] R. Gehr, J. Volz, G. Dubois, T. Steinmetz, Y. Colombe, B. L. Lev, R. Long, J. Estève, and J. Reichel, “Cavity-based single atom preparation and high-fidelity hyperfine state readout”, *Physical Review Letters* **104**, 203602 (2010) (cit. on p. 158).
- [234] H. Feng, Y. Liu, M. Lv, and J. Zhong, “A case report of COVID-19 with false negative RT-PCR test: necessity of chest CT”, *Japanese Journal of Radiology* **38**, 409–410 (2020) (cit. on p. 158).
- [235] C. Y. Johnson, “A ‘negative’ coronavirus test result doesn’t always mean you aren’t infected”, *The Washington Post* (2020) (cit. on p. 158).
- [236] R. P. Gehr, “Cavity based high-fidelity and non-destructive single atom detection on an atom chip”, (2011) (cit. on p. 159).
- [237] J. Bochmann, M. Mücke, C. Guhl, S. Ritter, G. Rempe, and D. L. Moehring, “Lossless state detection of single neutral atoms”, *Physical Review Letters* **104**, 203601 (2010) (cit. on pp. 159, 174).
- [238] K. M. Birnbaum, A. Boca, R. Miller, A. D. Boozer, T. E. Northup, and H. J. Kimble, “Photon blockade in an optical cavity with one trapped atom”, *Nature* **436**, 87–90 (2005) (cit. on p. 174).
- [239] T. Stolz, H. Hegels, M. Winter, B. Röhr, Y.-F. Hsiao, L. Husel, G. Rempe, and S. Dürr, “A quantum-logic gate between two optical photons with an efficiency above 40%”, Arxiv, 2111.09915 (2021) (cit. on p. 174).
- [240] H. Ritsch, P. Domokos, F. Brennecke, and T. Esslinger, “Cold atoms in cavity-generated dynamical optical potentials”, *Reviews of Modern Physics* **85**, 553–601 (2013) (cit. on p. 174).